Open Research Online

The Open University's repository of research publications
and other research outputs

Superfluidity and Superconductivity in Body-centred-cubic and Face-centred-cubic Systems

Thesis

oro.open.ac.uk

Superfluidity and Superconductivity

in Body-centred-cubic and

Face-centred-cubic Systems

Ganiyu Debo ADEBANJO

A THESIS SUBMITTED FOR THE DEGREE OF

Doctor of Philosophy

Department of Physics
School of Physical Sciences
The Open University
United Kingdom

December 2021

Declaration

I hereby declare that this thesis, written solely by me with guidance from my supervisor, presents original results (except otherwise cited) that have not been submitted to this or any other university as part of a degree or professional qualification.

G. D. Adebanjo
(2021)

Abstract

The microscopic description of phases in strongly correlated systems such as the fullerides (A_3C_{60}) is a challenge. In particular, how these strong interactions become attraction leading to a superconducting state remains a mystery. Understanding the mechanism(s) that drive(s) unconventional superconductivity is one of the most sought-after goals in many-body physics and indeed very complex to solve.

The aim of this thesis is, firstly, to investigate the conditions in which pairing may take place between two electrons in both body-centred cubic (BCC) and face-centred cubic (FCC) systems, and secondly, to examine the possibility for the emergence of a superconducting or superfluid state from paired electrons in three-dimensional (3D) systems. Here, pair properties are studied both in the anti-adiabatic and adiabatic limits. In the anti-adiabatic limit, we use a symmetrised approach, group theory analysis, and perturbation theory to exactly solve the two-body problem and analyse the properties of the electron pair. We also examine, using a continuous-time Monte Carlo algorithm (CTQMC), the effects of retarded electron-phonon interactions on the pair properties away from the anti-adiabatic limit. In the high-phonon frequency limit, the CTQMC also serves as a validation check for the anti-adiabatic analytic result and vice-versa (with both results showing perfect agreement).

Our result predicts that superfluidity can occur in BCC optical lattices up to a few tens of nanokelvin for fermionic lithium-6 atoms. Additionally, we found that, in the high-frequency limit, a paired state in an FCC lattice can be extremely light and small as compared to paired states on other 3D lattices. Such superlight states are expected to yield high transition temperatures under favourable circumstances. However, when the retardation effects arising from the electron-phonon interaction become important, bound pairs in the BCC lattice become lighter by orders of magnitude in a wide region

of the parameter space. We also found significant long-range effects due to the vibration of the alkali ions in the cesium-doped fulleride systems leading to the creation of light pairs in its BCC structure.

Dedication

This thesis is dedicated to God Almighty, my family, mentors (teachers and lecturers), and to those that walked with me through my academic journey up to this stage.

Acknowledgements

Contents

II   RESULTS AND DISCUSSIONS   61

4 Superfluidity in BCC Optical Lattices   62

5 Superlight States for High-T_c Superconductivity in FCC Lattices   103

III CONCLUSIONS   196

8 Conclusions   197

IV APPENDICES   201

A CTQMC Algorithm   202

B Supplementary Materials   205

C Publications   208

List of Figures

List of Tables

Part I

INTRODUCTION, MODELS AND

METHODS

Chapter 1

Introduction

This thesis begins with a brief introduction to the discovery of superconductivity and some of the theories that explain superconductivity. Then we talk about electronic strong correlations in solids and their impacts on our understanding of superconductivity. As this research is centred around the investigation of superfluidity and superconductivity in BCC and FCC systems, we then give a review of fulleride superconductors, and also briefly discuss optical lattices formed using ultra-cold atoms and how they can be used to demonstrate some of the results in this thesis. Finally, this chapter is concluded with our objectives and the overall outline of the thesis.

1.1   Superconductivity

Superconductivity is a phenomenon where materials (known as *superconductors*) exhibit complete loss of electrical resistance and expulsion of magnetic fields when cooled below a characteristic temperature, as was first discovered in 1911 by Heike Kamerlingh Onnes [1]. The first successful microscopic explanation of this amazing phenomenon only came about five decades later (in 1957) following the joint effort of Bardeen, Cooper, and Schrieffer to create the popularly known BCS theory [2, 3]. The BCS theory explains that weak attraction between electrons mediated by lattice vibrations leads to the formation of Cooper pairs and thus superconductivity. The earliest superconductors were well described in the BCS scheme. The mechanism of superconductivity was believed to be fully understood until 1986 when superconductivity was also observed at unusually high temperatures in materials that are strongly correlated [4]. This discovery raised the question: How is Cooper pairing possible when the repulsion between electrons is very large and dominant?

To understand why this question is raised, it is important to understand the idea behind the BCS formalism. BCS theory relies on the Landau–Fermi liquid theory (LFLT), which shows that a gas of weakly interacting electrons can be treated as non-interacting quasiparticles with renormalised mass [5]. Hence, the LFLT explains why a metal, despite having electrons that are interacting, can be described with free-electron models. However, the BCS trio understood that for superconductivity to occur, a source of attraction is needed for the pairing of electrons. This was achieved via retarded electron-phonon interactions (EPIs), and no matter how small the attraction is, superconductivity will happen since there is no repulsion between the quasiparticles – this summarises the BCS description. To understand the importance of the question above, we need to also ex-

amine the situation where the LFLT breaks down and thus the BCS theory. This leads us to our next discussion on strong correlation.

1.2   Strong Correlation in Superconductors

Even though the LFLT has been very successful in treating some of the complexities in condensed matter systems, we know that there are limits to its simplifications. It cannot apply to non-Fermi liquids [6] as well as as strongly interacting systems. Though models such as the Hubbard model [7] and formalisms such as the dynamical mean-field approximation [8, 9] have been useful, the field of strong correlations remains a challenge for physicists.

In the limit where the Coulomb interactions between particles become large, the LFLT fails. As a result, materials with strong correlation deviate from metallic states and display non-Fermi liquid behaviours such as anti-ferromagnetism and a Mott insulating state. High-temperature superconductors (HTS), also known as unconventional superconductors, have these non-Fermi liquid states in their phase diagrams (e.g. see Ref. [10]) which means that correlation effects cannot be ignored. Therefore, it is necessary to consider other ways of creating pairs between strongly correlated particles that interact via strong local Coulomb repulsion. Alternatives include very strong local or intersite EPIs that can overcome the electrostatic repulsions to create local pairs.

For local pairs, it has been proposed that superconductivity can be described in the Bose-Einstein condensation (BEC) framework. Interacting bosonic systems at low temperatures undergo BEC, a phase where the ground state has high occupation [11, 12, 13, 14]. Local pairs of fermions have integer spin and act like bosons. The BEC framework for superconductivity involves the condensation of small, preformed local

pairs. Unlike in the BCS theory where pairs are large and their condensation occurs immediately upon pair formation, the bound pairs are small and their condensation occurs at a lower temperature than the pair binding temperature in the BEC framework. This thesis explores BEC superconductivity which we shall use to estimate transition temperatures.

1.3 BCC and FCC Superconductors: Doped Fullerides

The discovery of high T_c superconductors generated a lot of interest in the search for other materials that could superconduct at high temperatures. Among them is the solid form of buckminsterfullerene (fullerenes for short) [15], a molecular solid made from carbon C_{60} molecules [16]. The majority of the fullerenes are closely packed into an FCC structure with the C_{60} molecules occupying the lattice sites [17]. Band structure calculations show that the valence electrons in an undoped C_{60} molecule are below the Fermi level and the h_u level which is the highest occupied molecular orbital (HOMO) is completely filled while the lowest unoccupied molecular orbital (LUMO) t_{lu} (with 3 degenerate states that can occupy up to 6 electrons) is empty (see Figure 1.1).

While the undoped C_{60} solid is an insulator [18], doping the solid with alkali and alkali-earth metals can significantly alter its electronic properties to become a metallic conductor or even a superconductor. The alkali atoms donate electrons that occupy the LUMO level. Amongst the doped solids, the trivalent-doped family (A_3C_{60}), such as Cs_3C_{60}, Rb_3C_{60} and K_3C_{60}, are unconventional superconductors with high transition temperatures (up to 38 K [19]), large Coulomb repulsion, and Jahn–Teller coupling. The cesium-doped solid (Cs_3C_{60}) is particularly special since it can be synthesised into BCC
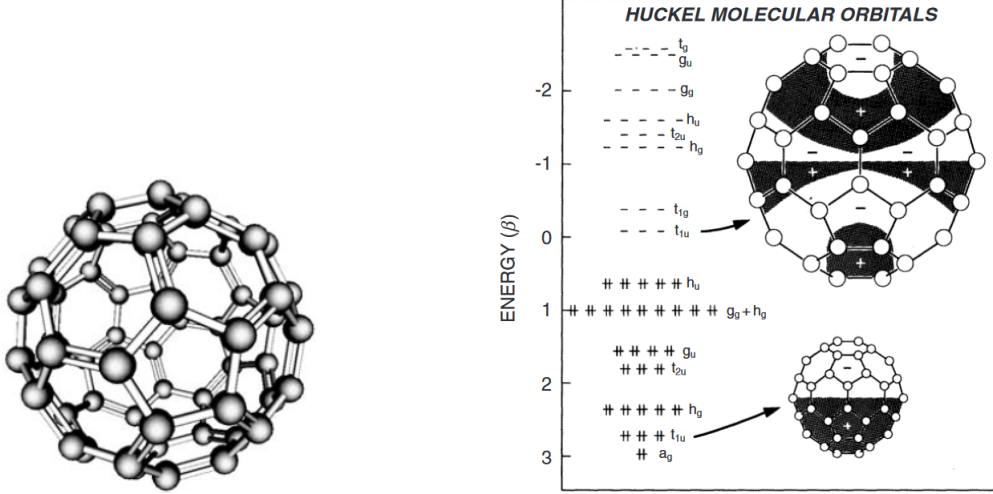
Figure 1.1: The structure (left panel) and the Hückel molecular orbitals (right panel) of a free C_{60} molecule. Reproduced from Ref. [18] with permission.

(cubic A15) and FCC structures which both superconduct at similar temperatures under the application of pressure [19, 20, 21].

For these compounds, the bandwidth energy W is on the order of 0.5 eV. The high-frequency intramolecular vibron modes, $\hbar\omega_{\mathrm{ph}}/W \sim 0.1-0.4$, play a key role in the resulting high critical temperatures. Also, the Jahn–Teller coupling in these compounds is quite large, with an electron-phonon coupling of $\lambda \sim 0.5 - 1$. The competition between the Jahn–Teller coupling and the Hund's rule is significant and determines where and how electrons are distributed within the LUMO. The Coulomb repulsion in A_3C_{60} supercon-ductors is also large with the ratio of Hubbard U to the bandwidth W, $1.5 \lesssim U/W \lesssim 2.5$ [22, 17]. Typical values for the onsite and nearest-neighbour Coulomb potentials range from about $1 - 1.5$ eV and $0.25 - 0.4$ eV, respectively [23, 24, 25, 26, 27]. Despite having an s-wave order parameter, there are signatures of unconventional superconductivity such as the proximity of Mott and superconducting states (see Figure 1.2) [28], suggesting that the BCS-like theories, for example Migdal-Eliashberg, are insufficient to explain the superconducting mechanism in these compounds [29, 30, 31]. So, fullerides are un-usual materials with features similar to the cuprates and thus interesting to explore for

better understanding of unconventional pairing in superconductors.
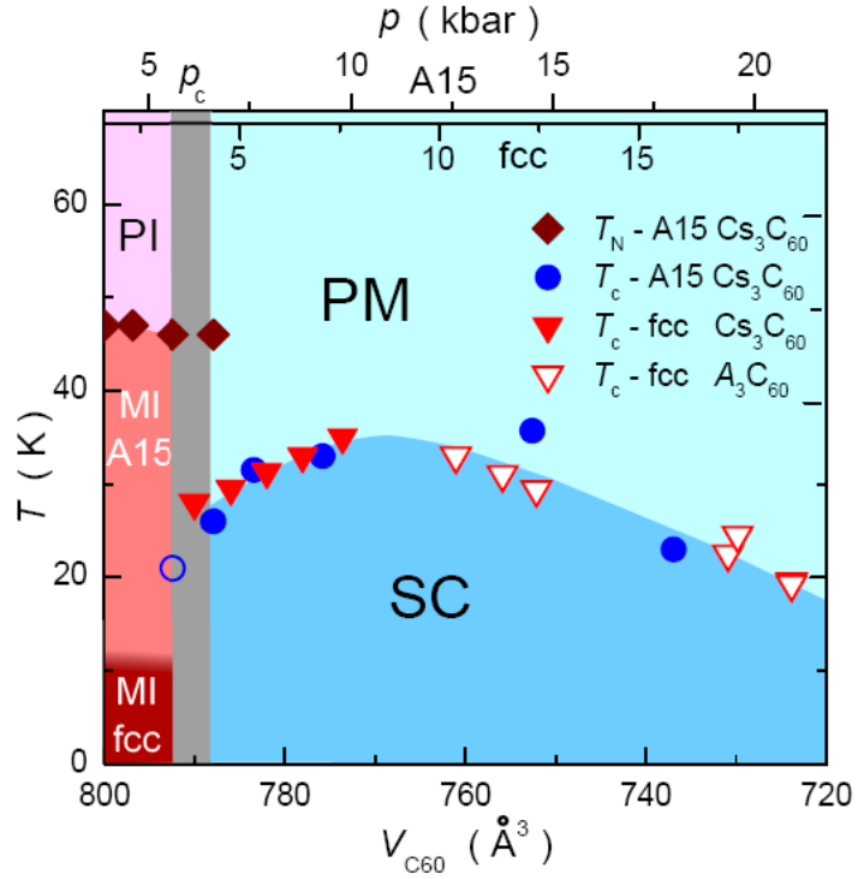
Figure 1.2: Phase diagram of trivalent-doped fullerides (A_3C_{60}). The plot shows the change in the transition temperature as a function of volume and pressure. The prominent feature is the dome-shaped superconducting phase next to a Mott-insulating state for both BCC and FCC structures. This phase diagram is similar to that of the cuprates - indicating that strongly correlated electrons are also important in A_3C_{60} solids. Reproduced from Ref. [28].

1.4   BCC and FCC Optical Lattices

Optical lattices are created through the interference of laser beams [32]. By varying the

angle of overlap, standing waves which correspond to a variety of optical (Bravais) lattices

can be experimentally realised. For example, the simplest one-dimensional optical lattice

can be generated by using two counter-propagating beams. Similarly, by superimposing

two or three orthogonal counter-propagating beams, one can realise the square and simple

cubic optical lattices, respectively.

There are several ways of generating BCC and FCC lattices using different laser ge-

ometry [33, 34]. In contrast to the orthogonal beam arrangement for the construction

of the simple cubic optical lattice, the BCC and FCC optical lattices are obtained from

non-orthogonal arrangements of multiple beams. Using a variety of methods, for example

the magneto-optical trap technique [35], atoms can be cooled, trapped, and manipulated

in the optical lattices in a precise and controlled manner. As a result, ultra-cold atoms

in optical systems have become the perfect environment for practical quantum simula-

tions which allows for the exploration of low-temperature phenomena such as BEC and

superfluidity, and Mott-Hubbard transitions [36, 37, 38].

1.5   Objectives and Aims of this Thesis

In the wider context of theoretical condensed matter physics research, the complexity of

models grow with lattice dimension d. Theoretical models are well studied on the chain

lattice. However, for $d > 1$, the problem becomes more complex and typically cannot be

exactly solved.

BEC occurs only in quasi-2D or three dimensional (3D) systems, so, it is imperative

to concentrate our effort on these systems rather than lower dimensions. While the

simple cubic lattice has been given the most attention (both theoretical and experimental investigations) amongst 3D systems, the BCC and FCC lattices on the other hand are often neglected. Our objectives for this study include:

- Exploring local pairing scenarios in relatively complex and unexplored lattices than were previously investigated.

- Understanding the onset of pair formation and the condensation temperatures in lattices with substantial signatures of both electron-phonon interaction and strong electron correlations.

- Develop a realistic model Hamiltonian to study the A_3C_{60} compounds (a family of molecular superconductors).

The aim of this thesis is to gain a better insight into realistic mechanisms responsible for superconductivity and superfluidity resulting from preformed local pairs in strongly interacting systems beyond the weak attraction described by the BCS theory.

1.6   Thesis Outline

This thesis contains eight chapters and is divided into three parts. Part I: Introduction, models and methods consists of three chapters. Part II: Results and discussions containing four chapters. Part III: Conclusions. The breakdown of each part is explained below.

Part I :   There are three chapters in this part, the first being the current (introduction) chapter. In chapter two, we will present the models used in this thesis. Chapter three is the methodology chapter discussing all the methods we have employed for this work.

Part II : This part consists of four chapters reporting all the new results in this work. The properties of bound pairs including the superfluid state in a BCC optical lattice (which is now published in Ref. [39]) is reported in chapter four. In chapter five, we report the superconducting properties of fermion particles in an FCC lattice (these results have been submitted for peer review, Ref. [40]). Since the A_3C_{60} compounds have BCC and FCC structures, we develop a Hamiltonian to study possible pairing mechanisms and examine any structural effects in these materials in the sixth chapter. Chapter seven is the last in this part and we report data from the simulation of bound pairs using a continuous-time quantum Monte Carlo algorithm.

Part III : This thesis ends with summary and conclusions in the eighth chapter. We also make suggestions for the direction of future work.

Chapter 2

Models of Interaction

2.1 Summary

In the introductory chapter, we discussed strong correlation in fermionic systems, its consequences for the Landau–Fermi liquid theory, and the challenge of strong correlation in our understanding of superconductivity. The aim of this chapter is to present some models that are used to study these correlated systems. We start with the description of the Bloch states of a free electron and Hubbard models, and then extend to other models which consider non-static lattices to describe the interplay between electrons and phonons. We also discuss the (bi)polaron problem and how bipolarons form in materials. Lastly, we derive an effective UV model using a canonical transformation.

2.2   Preliminaries

Many-body systems have very complicated physics because the behaviour of one particle depends on the relative positions or behaviours of other particles within the system. This leads to correlated behaviour (see Section 1.2 of Chapter 1). This is particularly true for a system of charged particles like the electron gas, interacting via Coulomb forces. These correlation effects make many-body physics challenging, but there are many approximations that can be made to understand the basic principles at a fundamental level. One such approximation is the mean-field theory where a particle is assumed to be interacting with an average field of other particles. Building on these simplifications, the acoustic, optical and thermal properties of a solid can be inferred. We will introduce both the conceptual ideas and the mathematical descriptions of models that are relevant to this thesis in the next sections.

2.3   Bloch States of an Electron

Given a simple system (Figure 2.1) of an isolated electron in a periodic lattice potential $V(\boldsymbol{r})$, the solution to the Schrödinger equation gives rise to Bloch states [41]. By periodicity, we mean that the potential $V(\boldsymbol{r} + \boldsymbol{R}) = V(\boldsymbol{r})$, where $\boldsymbol{R}$ is the Bravais lattice vector, i.e. a translation vector of the lattice in real-space. The Bloch function has the form

$$\psi_{\boldsymbol{k}}(\boldsymbol{r}) = e^{i\boldsymbol{k}\cdot\boldsymbol{r}} u_{\boldsymbol{k}}(\boldsymbol{r}) \tag{2.1}$$

where ψ is the wavefunction or eigenstate of the electron, $\boldsymbol{k}$ is the wave vector of the lattice, $\boldsymbol{r}$ is the real-space position vector of the lattice (atomic site) and $u_{\boldsymbol{k}}(\boldsymbol{r})$ is a function that has the periodicity of the lattice. (We note that in this chapter, nuclei and ions are used interchangeably). Sometimes, electrons are localised on atomic orbitals,

which is often the case in solids. In such a localised scenario, an electron would spend a considerable amount of time on a single site and occasionally hop to other atomic sites. Due to this observation in many solids, the tight-binding model was developed.
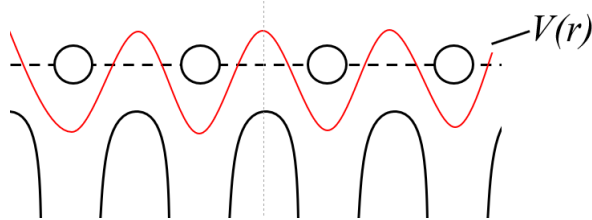
Figure 2.1: Periodic potential in 1D (one dimension). Circles represent lattice ions.

2.4 The Tight-Binding Model

The tight-binding approximation (TBA), based on the LCAO (linear combination of atomic orbitals) approximation, provides an understanding of the behaviour of electrons in localised atomic orbitals [42]. In its simplest form, it is a toy model used to demonstrate the movement of electrons in solids. In the model, the following assumptions are made: (1) the nuclei are static (Born–Oppenheimer approximation), (2) a single atomic orbital is considered, and (3) the electrons are situated only on atomic sites (not in between two sites) and are allowed to hop to the nearest-neighbour nuclei sites.

To derive the Hamiltonian of this model, we first define Wannier functions ϕ in terms of the Bloch function (2.1) via the transformation

$$\psi_{\boldsymbol{k}}(\boldsymbol{r}) = \frac{1}{\sqrt{N}} \sum_j e^{i\boldsymbol{k}\cdot\boldsymbol{R}_j} \phi(\boldsymbol{r} - \boldsymbol{R}_j) \tag{2.2}$$

where $\phi(\boldsymbol{r} - \boldsymbol{R}_j)$ is the Wannier function for lattice vector $\boldsymbol{R}$ located at the j-th atomic site and N is the number of primitive unit cells. The one-electron Hamiltonian in this periodic, non-vibrating crystal is

$$\mathcal{H} = -\frac{\hbar^2}{2m}\nabla^2 + V(\boldsymbol{r}) \tag{2.3}$$

and the corresponding total energy is

$$\varepsilon_{\boldsymbol{k}} = \int d^3 r \psi_{\boldsymbol{k}}^\dagger(\boldsymbol{r}) \mathcal{H} \psi_{\boldsymbol{k}}(\boldsymbol{r}) \equiv \varepsilon_{jl} = \frac{1}{N} \sum_{j,l} e^{i\boldsymbol{k}\cdot(\boldsymbol{R}_j - \boldsymbol{R}_l)} \int d^3 r \phi^*(\boldsymbol{r} - \boldsymbol{R}_l) \mathcal{H} \phi(\boldsymbol{r} - \boldsymbol{R}_j) \quad (2.4)$$

To express the Hamiltonian using second quantised notation, we define the wavefunction

and its conjugate in terms of a basis set as,

$$\psi(\boldsymbol{r}) = \sum_j c_{j\sigma} \phi_j \tag{2.5}$$

$$\psi^\dagger(\boldsymbol{r}) = \sum_j c_{j\sigma}^\dagger \phi_j^* \tag{2.6}$$

where j represents the lattice site, c ($c^\dagger$) is the annihilation (creation) operator*. Hence,

the effective Hamiltonian for the TBA, after some algebraic steps, is

$$H = \sum_{jl\sigma} \varepsilon_{jl} c_{j\sigma}^\dagger c_{l\sigma} \equiv \sum_{\langle jl\rangle\sigma} t_{jl} c_{j\sigma}^\dagger c_{l\sigma} \tag{2.7}$$

where we have introduced σ to represent the electron spin index, $\langle \ldots \rangle$ implies the sum is

on nearest-neighbour sites only, and ε_{jl} is the energy defined in Equation (2.4). The case

for which $j = l$ represents the onsite energy and has been absorbed into the chemical

potential. Equation (2.7) represents a hopping process where electron jumps from site l

to a nearest-neighbour site j and t_{jl} is the hopping integral defined as

$$t_{jl} = \int d^3 r \phi^*(\boldsymbol{r} - \boldsymbol{R}_l) \left[-\frac{\hbar^2}{2m} \nabla^2 + V(\boldsymbol{r}) \right] \phi(\boldsymbol{r} - \boldsymbol{R}_j) \tag{2.8}$$

2.5   Hubbard Hamiltonian

As the TBA is only used to examine the properties of an isolated, non-interacting par-

ticle, it is a simple model and can be solved exactly. Hubbard in 1963 [7] added a

---

*These are fermion operators and the anti-commutation rules apply: $\{c_i, c_j^\dagger\} = \delta_{ij}$, $\{c_i, c_j\} = 0$,
$\{c_i^\dagger, c_j^\dagger\} = 0$, $c_j^\dagger c_j = n_j$. Here, n_j is the fermion occupation number operator with index j.

Coulomb onsite interaction to the tight-binding Hamiltonian to study electron correlation effects in narrow-band materials. Hubbard made an assumption that this narrow band can be represented by an *s* molecular orbital. Using this assumption, he developed a Hamiltonian of the form

$$H = \sum_{\langle jl \rangle \sigma} t_{jl} c_{j\sigma}^{\dagger} c_{l\sigma} + U_{\mathrm{H}} \sum_{j} n_{j\uparrow} n_{j\downarrow} \qquad (2.9)$$

where the first term represents the TBA discussed earlier, U_{H} represents the Coulomb-mediated onsite interaction between two electrons situated on the same lattice site j, $\uparrow$ and $\downarrow$ are the spins of the two electrons (spins in the same direction do not contribute due to Pauli exclusion), and $n_{j\sigma} = c_{j\sigma}^{\dagger} c_{j\sigma}$ is the fermion number operator. The onsite interaction U_{H} is primarily taken to be repulsive as in Hubbard's original work, but attractive U_{H} cases are also considered (for example, Refs. [43, 44]). Other treatments of the Hubbard Hamiltonian extend the Coulomb interaction to neighbouring sites where the intersite interaction potential is denoted V_{H}. Such considerations are sometimes called extended-Hubbard models or UV-models and have a Hamiltonian of the form

$$H = \sum_{\langle jl \rangle \sigma} t_{jl} c_{j\sigma}^{\dagger} c_{l\sigma} + U_{\mathrm{H}} \sum_{j} n_{j\uparrow} n_{j\downarrow} + V_{\mathrm{H}} \sum_{j \neq l, \sigma\sigma'} n_{j\sigma} n_{l\sigma'} \qquad (2.10)$$

where the first and second terms are from Equation (2.9) and V_{H} is the Coulomb-mediated intersite interaction. Note that $j = l$ is excluded from the summation in the third term.

2.5.1 Mott-Hubbard Insulator

Inspecting carefully, we see that some characteristics of a material can be examined by considering which term is dominant in Equation (2.9). Sir Nevill Mott studied correlation effects in a lattice at half filling (i.e. one electron per lattice site) [45]. The physics goes thus: when the electrons are strongly correlated (i.e. very strong Coulomb repulsion is present), the hopping is suppressed and electrons predominantly sit on their original

lattice sites. On the other hand, they can move around if the repulsion is insignificant. This description is what distinguishes a metal (where electric current can be transferred by electrons due to their motion) from a Mott insulator (where the large onsite Coulomb repulsion disfavours double occupancy in a way that inhibits electron motions).

2.6   Phonons

In the discussions so far, the models used an approximation of static nuclei. In reality, atoms that make up the lattice vibrate about their fixed positions. *Phonons*, which represent a collective vibration of nuclei in a solid, can interact with electrons thereby turning an electron into a quasiparticle with either slightly or significantly different properties [41]. It is also possible for the same phonon to travel to another electron and interact with it. Phonons play essential roles in describing many phenomena observed in condensed matter systems. We shall briefly talk about the description of a system with vibrating ions only, and, in subsequent sections, we will look at the consequences for the Hamiltonian of the overall system (ions and electrons).

The phonon Hamiltonian H_{ph} can be treated classically like the harmonic oscillator [46] whereby the atoms, separated by lattice constant b, are assumed to be linked by elastic springs.

$$H_{\mathrm{ph}} = \sum_j \left[\frac{K}{2} \left(x_j - x_{j-1} \right)^2 + \frac{1}{2M} p_j^2 \right], \tag{2.11}$$

$$[p_j, x_{j'}] = \frac{\hbar}{i} \delta_{j,j'} \tag{2.12}$$

where M is the mass of the atoms, K is the spring constant, x_j is the displacement of the atom at site j, and p_j is the momentum of the atom located at site j.

In Fourier-space, x and p can be expressed as

$$x_j = \frac{1}{\sqrt{N}} \sum_{\boldsymbol{k}} x_{\boldsymbol{k}}\, e^{i\boldsymbol{k}\cdot\boldsymbol{R}_j} \quad : \quad x_{\boldsymbol{k}} = \frac{1}{\sqrt{N}} \sum_{j} x_j\, e^{-i\boldsymbol{k}\cdot\boldsymbol{R}_j} \tag{2.13}$$

$$p_j = \frac{1}{\sqrt{N}} \sum_{\boldsymbol{k}} p_{\boldsymbol{k}}\, e^{i\boldsymbol{k}\cdot\boldsymbol{R}_j} \quad : \quad p_{\boldsymbol{k}} = \frac{1}{\sqrt{N}} \sum_{j} p_j\, e^{-i\boldsymbol{k}\cdot\boldsymbol{R}_j} \tag{2.14}$$

where $\boldsymbol{k}$ is the wave vector in momentum-space. Straightforward substitutions of Equations (2.13) and (2.14) into the original Hamiltonian (2.11) gives

$$H_{\mathrm{ph}} = \sum_{\boldsymbol{k}} \left[\frac{M\omega_{\boldsymbol{k}}^2}{2} x_{\boldsymbol{k}} x_{-\boldsymbol{k}} + \frac{1}{2M} p_{\boldsymbol{k}} p_{-\boldsymbol{k}} \right] \tag{2.15}$$

where $\omega_{\boldsymbol{k}} = \sqrt{\frac{K}{M}} \times 2 \left| \sin \frac{kb}{2} \right|$ is a momentum-dependent vibrational frequency.

We may introduce the annihilation and creation operators as

$$a_{\boldsymbol{k}} = \left(\frac{M\omega_{\boldsymbol{k}}}{2\hbar} \right)^{1/2} \left(x_{\boldsymbol{k}} + \frac{ip_{-\boldsymbol{k}}}{M\omega_{\boldsymbol{k}}} \right) \tag{2.16}$$

$$a_{\boldsymbol{k}}^{\dagger} = \left(\frac{M\omega_{\boldsymbol{k}}}{2\hbar} \right)^{1/2} \left(x_{-\boldsymbol{k}} - \frac{ip_{\boldsymbol{k}}}{M\omega_{\boldsymbol{k}}} \right) \tag{2.17}$$

and the solution to the Hamiltonian can be re-written, in terms of operators, as

$$H_{\mathrm{ph}} = \sum_{\boldsymbol{k}} \hbar\omega_{\boldsymbol{k}} \left(a_{\boldsymbol{k}}^{\dagger} a_{\boldsymbol{k}} + \frac{1}{2} \right) = \sum_{\boldsymbol{k}} \hbar\omega_{\boldsymbol{k}} \left(n_{\boldsymbol{k}} + \frac{1}{2} \right) \quad . \tag{2.18}$$

Note that $a_{\boldsymbol{k}}$ and $a_{\boldsymbol{k}}^{\dagger}$ obey the boson commutation relation $[a_{\boldsymbol{k}}, a_{\boldsymbol{k}'}^{\dagger}] = \delta_{\boldsymbol{k},\boldsymbol{k}'}$, and $a_{\boldsymbol{k}}^{\dagger} a_{\boldsymbol{k}} = n_{\boldsymbol{k}}$ is the boson occupation number.

In the remaining part of this thesis, however, we will be using a non-dispersive Hamiltonian which has the form, in real-space,

$$H_{\mathrm{ph}} = \hbar\omega_0 \sum_{j} \left(a_j^{\dagger} a_j + \frac{1}{2} \right) = \hbar\omega_0 \sum_{j} \left(n_j + \frac{1}{2} \right) \quad , \tag{2.19}$$

where ω_0 is the frequency of the optical branch of the phonon modes (assumed flat), to describe the phonon subsystem.
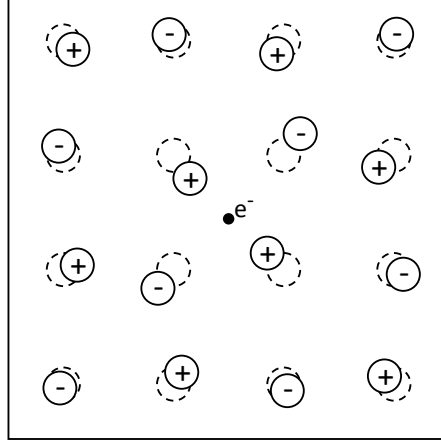
Figure 2.2: Illustration of an electron (small black dot) interacting with lattice ions (big circles). If the lattice is highly deformable, the positive ions will be strongly pulled towards the electron and negative ions strongly repelled. Dashed-line circles represent the original (equilibrium) ions' positions.

2.7   Electron-Phonon Interaction (EPI)

Since electrons can interact with ions via Coulomb-like interactions as in Figure 2.2, we will derive the Hamiltonian for the EPI in this section. Let us say the ith electron interacts with the jth ion via a potential V_{el-ion}, the Hamiltonian reads

$$H_{el-ion} = -e \int d\boldsymbol{r}_i \rho_{el}(\boldsymbol{r}_i) \sum_j V_{el-ion}(\boldsymbol{r}_i - \boldsymbol{R}_j) \qquad (2.20)$$

where e is the charge of the electron, ρ_{el} is the electron density, $\boldsymbol{r}_i$ and $\boldsymbol{R}_j$ represents the vector position of the electron and ion, respectively.

If we perturb the ion to move a small distance $\boldsymbol{\xi}_j$ from its equilibrium position $\boldsymbol{R}_j^{(0)}$, then we can express $\boldsymbol{R}_j$ in terms of the displacement as $\boldsymbol{R}_j = \boldsymbol{R}_j^{(0)} + \boldsymbol{\xi}_j$. Thus, we have

$$H_{el-ion} = -e \int d\boldsymbol{r}_i \rho_{el}(\boldsymbol{r}_i) \sum_j V_{el-ion}(\boldsymbol{r}_i - \boldsymbol{R}_j^{(0)} - \boldsymbol{\xi}_j) \qquad (2.21)$$

The Taylor expansion of the right-hand-side of Equation (2.21) gives

$$V_{el-ion}(\boldsymbol{r}_i - \boldsymbol{R}_j^{(0)} - \boldsymbol{\xi}_j) = V_{el-ion}(\boldsymbol{r}_i - \boldsymbol{R}_j^{(0)}) - \boldsymbol{\xi}_j \cdot \nabla V_{el-ion}(\boldsymbol{r}_i - \boldsymbol{R}_j^{(0)}) + \mathcal{O}(\boldsymbol{\xi}_j^2) \qquad (2.22)$$

so that if we neglect $\mathcal{O}(\boldsymbol{\xi}_j^2)$ and higher-order terms, our Hamiltonian becomes

$$H_{\text{el-ion}} = -e \int d\boldsymbol{r}_i \rho_{\text{el}}(\boldsymbol{r}_i) \sum_j V_{\text{el-ion}}(\boldsymbol{r}_i - \boldsymbol{R}_j^{(0)})$$

$$+ e \int d\boldsymbol{r}_i \rho_{\text{el}}(\boldsymbol{r}_i) \sum_j \boldsymbol{\xi}_j \cdot \nabla V_{\text{el-ion}}(\boldsymbol{r}_i - \boldsymbol{R}_j^{(0)})$$

(2.23)

The first term (zeroth-order) in $\boldsymbol{\xi}_j$ is the periodic potential which leads to Bloch states (see Section 2.3). The second term is the main ingredient of the EPI as it describes the force experienced by an electron when an ion moves away from its equilibrium position. Higher-order terms in ξ are usually small and can be neglected in our case. However, higher terms in the series (2.22) may be relevant to the treatment of high temperature systems [47].

In a simple 1D case, the EPI can be expressed as

$$H_{\text{el-ph}}^{(1)} = \int d\boldsymbol{r}_i \rho_{\text{el}}(\boldsymbol{r}_i) \left\{ \sum_j e\, \boldsymbol{\xi}_j \cdot \nabla V_{\text{el-ion}}(\boldsymbol{r}_i - \boldsymbol{R}_j) \right\} \equiv \sum_{ij} f_{ij} \boldsymbol{\xi}_j (n_{i\uparrow} + n_{i\downarrow}) \qquad (2.24)$$

where f_{ij} represents the force experienced by an electron at a position i and an ion located at a position j.

If we combine the EPI with the TBA, we end up with more comprehensive models of electron motion. We note here that the EPI can be long range or local: by local we mean that only electrons nearest to the displaced ion are considered while long-range EPI implies that the ion vibration can have effects on distant electrons.

2.8 Long-range Electron-Phonon Interaction

In the previous two sections, we mentioned that phonons propagate through solids and we have also developed the basic Hamiltonian describing interaction of this vibration with an electron (i.e. the EPI). A full Hamiltonian which incorporates the phononic and electronic contributions has the general form

$$H = H_{\text{el}} + H_{\text{el}-\text{ph}} + H_{\text{ph}} \tag{2.25}$$

where H_{el} represents the tight-binding electron subsystem Hamiltonian, $H_{\text{el}-\text{ph}}$ is the interaction between electron and the vibrating lattice, and H_{ph} is the Hamiltonian describing the phonon subsystem.

This model of long-range electron-phonon interaction (EPI), also known as the Fröhlich model [48], in real-space is written as

$$H = \sum_{\langle ii' \rangle \sigma} t_{ii'} c_{i\sigma}^{\dagger} c_{i'\sigma} + \frac{\hbar}{\sqrt{2M\omega_0}} \sum_{ij\sigma} g_{ij} n_{i\sigma}(a_j^{\dagger} + a_j) + \hbar\omega_0 \sum_j (a_j^{\dagger} a_j + \frac{1}{2}) \tag{2.26}$$

where g_{ij} is a parameter that represents the coupling of an electron on site i to the phonon at site j, all other variables are explained in earlier equations. Equation (2.26) captures all the information that is needed to describe the behaviour of a *single* electron in a lattice (Note: up to this point, we still assume that our system contains just one valence electron). However, the strength of the EPI decreases with distance. When the Coulomb interactions between electrons are added in the Hamiltonian, the Fröhlich model can be used to study various phenomena in condensed matter physics including superconductivity - the main focus of this thesis.

2.9 Holstein Model

The Holstein model is identical to Fröhlich's in that they both describe electrons in a deformable lattice but differ by the extent and strength of the coupling parameter g_{ij}. The Hamiltonian reads

$$H = \sum_{\langle ii' \rangle \sigma} t_{ii'} c_{i\sigma}^{\dagger} c_{i'\sigma} + \frac{\hbar g}{\sqrt{2M\omega_0}} \sum_{i\sigma} n_{i\sigma}(a_i^{\dagger} + a_i) + \hbar\omega_0 \sum_i (a_i^{\dagger} a_i + \frac{1}{2}) \tag{2.27}$$

We see that the Hamiltonian focuses only on electrons and ions that are at the same location i. Hence Holstein's model is often referred to as local EPI. In Holstein's original work [49], he studied the EPI, describing electron self-trapping (i.e. the possibility of an electron being trapped in a potential it has created).

2.10 Polaron and Bipolaron

Generally speaking, when charge carriers (valence electrons or holes) travel through a solid, they interact with the lattice phonons. We continue our discussion assuming that the charge carriers are electrons and we neglect the Coulomb repulsion between these electrons. At finite temperature, the EPI often has two major consequences. Firstly, electrons are scattered by the vibrating atoms which brings about electrical resistance, particularly in semiconductors and insulators [50]. Secondly, the phonon alters the characteristic properties of the electron [41].

In 1933, Landau reported how the properties of a free electron can change due to lattice polarisation and postulated the possibility of self-trapping of an electron at low temperature [51]. His explanation can be summarised thus: when an electron is present in a polarisable medium such as an ionic lattice, the surrounding ions are attracted or pulled towards the electron (as in Figure 2.2) thereby creating *virtual* phonons with low frequency. The motions of the ions leads to the distortion of the underlying lattice and a dense phonon cloud forms around the electron - sometimes referred to as "*electron dressing*". It turns out that the electron interacts with the polarised field, and as coupling between the electron and this polarisation increases, the energy of the whole system is lowered. In Landau's picture, when the electron moves from one point to another, the phonon cloud appears to adiabatically follow the trajectory of the passing electron.

2.10.1   Polaron

The dressed electron described by Landau is a quasiparticle which is known today as a

polaron: a name coined by Pekar in 1946 [52]. Pekar argued that in solids, electrons do

not always move freely but as polarons instead [52]. Today, we know that polarons exist

in range of media and materials including high temperature superconductors, ultracold

atoms and plasmas [53, 54, 55]. Fundamentally, a polaron has significantly different

properties from the original band carrier. It is characterised by its self-energy, E_{pol},

an enhanced effective mass, m_{pol}, and its characteristic response to external electric

and magnetic fields [56]. These properties are in principle determined by factors which

include the type of phonon, the strength of coupling and the dimensionality of the system

[57].

Some terminology used in polaron problems

Polaron studies are categorised based on the polaron size, coupling strength and phonon

frequencies etc.

1. If the polaron radius r_{pol} is compared with the lattice spacing b, we can have

   - A small polaron: when $r_{\text{pol}} \approx b$.

   - A large polaron: when $r_{\text{pol}} \gg b$.

2. The Fröhlich polaron can be studied at different coupling strengths. The cou-

   pling parameter α, which is related to the number of phonons in the cloud [58], is

   expressed as [59, 60]

$$\alpha = \frac{e^2}{\hbar} \sqrt{\frac{m_{\text{pol}}}{2\hbar\omega_{LO}}} \left(\frac{1}{\varepsilon_\infty} - \frac{1}{\varepsilon_0} \right) \tag{2.28}$$

   where m_{pol} is the effective mass of the polaron (to be discussed shortly), ω_{LO} being

   the plasma frequency (usually represented by an Einstein phonon i.e. $\omega_{LO} \equiv \omega_0$),

ε_∞ and ε_0 are the high-frequency and static dielectric constants, respectively. Note that α and g defined in Equations (2.26) and (2.27) are directly related: $\alpha \propto g^2$ [61]. The three regimes are

- Weak-coupling regime when $\alpha \ll 1$.

- Strong-coupling regime when $\alpha \gg 1$.

- Intermediate coupling where $\alpha \sim 1$.

3. The ratio of the phonon frequency $\hbar\omega_{\mathrm{ph}}$, and the half-bandwidth W, is also significant. The polaron problem is regarded as in the

- Adiabatic limit if $W \gg \hbar\omega_{\mathrm{ph}}$.

- Anti-adiabatic (non-adiabatic) limit if $W \ll \hbar\omega_{\mathrm{ph}}$.

2.10.1.1   Weak-Coupling Regime

In the weak-coupling limit, the electron-phonon coupling (EPI) term in Equation (2.26) can be treated as a perturbation [60]. While there is not an exact solution to this problem yet [56], the polaron wavefunctions and the lattice distortions spreads over many lattice sites, and the problem can be solved perturbatively. To first order in the coupling constant α, the polaron self-energy in the Fröhlich model is obtained as [56]

$$E_{\mathrm{pol}} = -\alpha\hbar\omega_0 \tag{2.29}$$

with an effective mass

$$m_{\mathrm{pol}} = \frac{m^*}{1 - \frac{\alpha}{6}} \tag{2.30}$$

where ω_0 is the phonon frequency, m^* is the bare electron band mass. Equations (2.29) and (2.30) are the results obtained from the Rayleigh-Schrödinger perturbation theory

[60]. The increase in the effective mass is due to the fact that the electron is self-trapped (which means it spends a lot of time polarising its surrounding, forming a bound state with the polarisation while occupying a local state) and for it to move, it requires extra energy to drag this deformation along. Looking at Equation (2.30), one might immediately ask: what happens when $\alpha = 6$? At $\alpha = 6$, the mass diverges and the polaron becomes completely localised (non-itinerant). Hence, the validity of Equation (2.30) as a weak-coupling solution means that the coupling must be much smaller than a critical value ($\alpha < \alpha_c = 6$).

The weak-coupling expansions [56] yield the polaron energy

$$E_{\text{pol}} = -\hbar\omega_0(\alpha + 0.015919\alpha^2 + 0.000806\alpha^3 + \dots,) \tag{2.31}$$

with mass given as

$$m_{\text{pol}} = m^*(1 + \frac{\alpha}{6} + 0.0236276\alpha^2 + \dots,) \tag{2.32}$$

This expression for the polaron mass is identical to that obtained in Ref. [62]: $m_{\text{pol}} \approx m^*(1 + \alpha/6)$ when $\alpha \to 0$. As the coupling diminishes, a very large polaron is formed and its motion is related to the half-bandwidth zt where z is the coordination number and t is the hopping parameter.

2.10.1.2   Strong-Coupling Regime

The strong-coupling treatment was first carried out in the pioneering work of Landau and Pekar [63]. In this limiting case, the Holstein Hamiltonian (2.27) describes the problem in such a way that the tight-binding term can be treated as a perturbation. This means that the bandwidth is small compared to the EPI term. The polaron radius is on the order of the lattice spacing (small polaron). A variational calculation using a Gaussian

wavefunction yields polaron self-energy [56]

$$E_{\text{pol}} = -\frac{\alpha^2 \hbar \omega_0}{3\pi} = -0.106\alpha^2 \hbar \omega_0 \tag{2.33}$$

Unlike the weak-coupling limit, the energy is proportional to the square of the coupling parameter. The expansion for the polaron energy in the strong-coupling limit, obtained in Miyake's work [64], is

$$E_{\text{pol}} = -\hbar \omega_0 \left(0.108513\alpha^2 + 2.836 + \mathcal{O}(1/\alpha^2) \right) \qquad , \tag{2.34}$$

with the polaron mass given as

$$m_{\text{pol}} = m^* \left(1 + 0.0227019\alpha^4 \right) \tag{2.35}$$

As can be seen in Equation (2.35), the enhanced mass is proportional to the fourth-power in α which means it can be very large. For example, the polaron mass is heavier by several orders of magnitude than the bare electron mass [63]. The spatial extent of the polaron wavefunction in the strong-coupling limit can be determined using the formula

$$r_{\text{pol}}^{-1} = \frac{\alpha}{3} \sqrt{\frac{4\omega_0 m^*}{\pi \hbar}} \tag{2.36}$$

which is the inverse radius. The polaron ground state energy in the weak- and strong-coupling limits is shown in Figure 2.3. It summarises that the Rayleigh-Schrödinger perturbation theory is sufficient at small values of α while the strong-coupling calculation is valid when α gets very large. We can see that at a coupling constant of about $\alpha \approx 5$, both plots almost converge. Therefore, the value for $\alpha \sim 5$ may be considered the crossover between the weak- and strong-coupling theories.
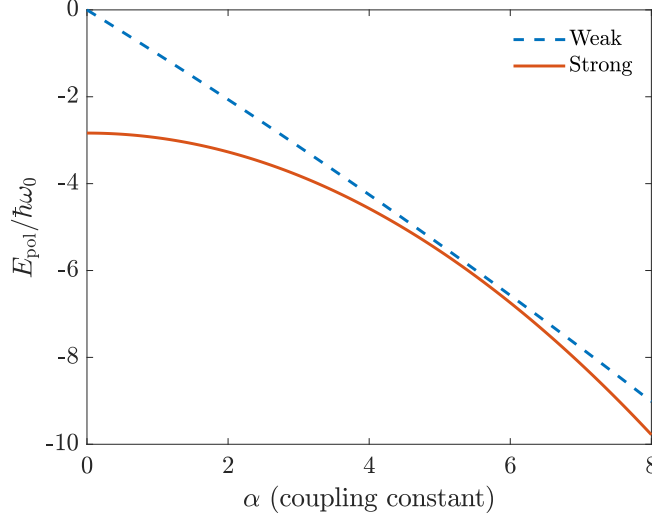
Figure 2.3: Comparing the polaron energy in the weak and strong-coupling expansion limits according to Equations (2.31) and (2.34), respectively. Both curves almost touch around $\alpha \approx 5$ and, hence, this value of α may be considered the crossover point between the weak- and strong-coupling theories.

2.10.1.3   All-Coupling Result

No exact solution exists for the polaron mass at arbitrary coupling values, but the best approximation so far was determined by Feynman using his path integral formalism [62]. Figure 2.4 shows a summary of his result which agrees quite well both in the weak- and strong-coupling regimes. The key difference between Figures 2.3 and 2.4 is that the constant term 2.836 (from Equaton (2.34)) has been neglected in the α expansion of Feynman's all-coupling result.

All categories or types of polaron (for example, see Table 3 in Ref. [65]) are formed in a similar way; an ion vibration creates a potential well for the charge carrier. The transport mechanisms for small polarons are distinct in the limits of high and low phonon frequencies [66]. In the adiabatic limit $W \gg \hbar\omega_{\mathrm{ph}}$, where the motion of an electron is fast with respect to the ions' motions, the electron hops when the distortions in the neighbouring sites are about the same size as the occupied state. This enables the electron to move many times within a unit cell. Also, this leads to scattering as the
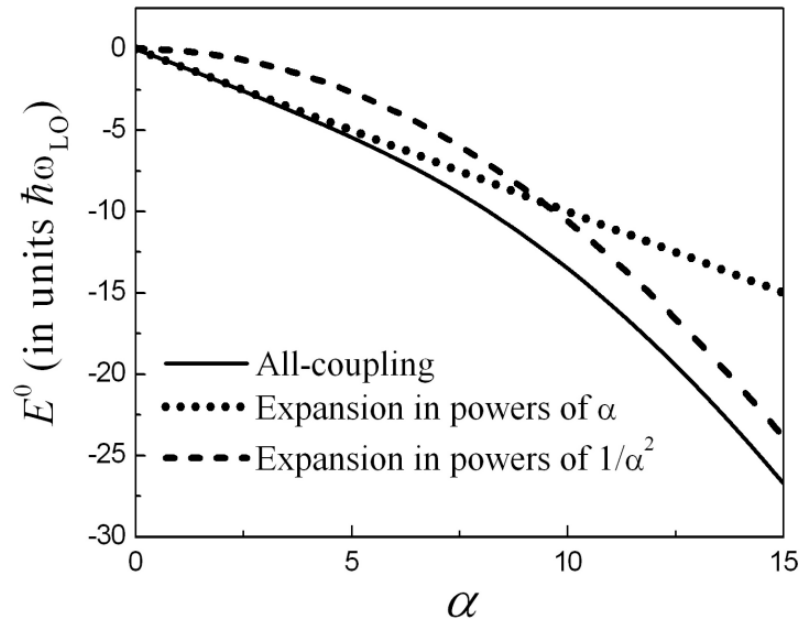
Figure 2.4: Polaron energy at arbitrary coupling from Feynman's all-coupling theory (solid line) compared with some weak-coupling (dotted line) result and strong-coupling (dashed line) results. Reproduced from Ref. [57].

electron interacts with the new distortion [59]. During a hopping event, the scattering process is considered inelastic if the number of phonons N_{ph} changes, whilst it is elastic if N_{ph} is unaltered [49]. In contrast, when $W \ll \hbar\omega_{ph}$, the ion motion is faster than the electron hopping. In this case, the lattice relaxation rate is fast.

Experimentally, a polaron can be observed in the optical absorption spectrum. It corresponds to the peak in the spectrum when the energy of the incident light (in the THz frequency range) is comparable with the Debye frequency ω_D [57, 67]. It is worth mentioning that, even though they may appear different at first glance, the Fröhlich and Holstein Hamiltonians have similar properties over a wide range of parameters in the polaron treatments, and both can lead to small or large polarons [68].

2.10.2   Bipolaron

As complex as they are, the polaron theories discussed above consider a single electron in a polarisable environment. We can extend the treatment to a more realistic situation

where there is more than one electron. Let us consider a system with only two electrons. Two electrons can experience an attractive force via the phonons as long as the EPI strength dominates over the Coulomb repulsion. Therefore, if the EPI is dominant two polarons can bind into a single quasiparticle known as *bipolaron*, which behaves as a charged boson. The ground state of bipolarons generally forms a singlet with an *s*-wave symmetry (sometimes the onsite and intersite singlets are referred to as $s0$ and $s1$, respectively). In addition, other states with *p*-, *d*- and *f*- symmetries can be realised too. All the terminologies discussed previously for polarons apply to bipolarons too, except that there are now two particles. Thus, a bipolaron can be small or large, treated in the weak-, intermediate- or strong-coupling regimes, as well as in the adiabatic or non-adiabatic limits. Below a critical onsite repulsion U_c (which depends on the lattice), a stable onsite bipolaron can be formed for finite EPI. When $U = 0$, bipolarons are stable in 1D for an arbitrary non-zero EPI, but a critical EPI has to be reached to form stable bipolarons in higher dimensions [57]. The formation process of both small and large bipolarons is the same but their properties greatly differ [59].

Bipolaron properties vary depending on the dimension and the structure of the lattice. In the extreme case of strong EPI, two small localised polarons can bind to form a small bipolaron with a heavy effective mass that scales as the square of the polaron hopping integral t or alternatively as the square of single polaron mass (i.e. $m_{\mathrm{bip}} \propto (m_{\mathrm{pol}})^2$) [69]. A second-order bipolaron tunnelling manifests in lattices such as chain [70, 71], square [72] and simple cubic [73]. Conversely, in the weak-coupling limit where large bipolarons can be formed, the bipolaron has a relatively light mass with a first-order hopping dependence (i.e. $m_{\mathrm{bip}} \propto m_{\mathrm{pol}}$). This is due to a partially pre-existing lattice deformation that spans over many sites, so that one of the polaron pair can hop without breaking the pairing. First-order tunnelling of bipolarons can exist at strong coupling in

systems such as the staggered ladder [69] and triangular lattices [74, 72]. In fact, in some cases, superlight bipolarons [69] can be formed: meaning that the bipolarons would be slightly heavier than a single polaron only by a factor between 2 and 6.

We mentioned in Chapter 1 that small bound polaron pairs can form a condensate which may lead to superconductivity or superfluidity upon lowering the temperature of the system. Since the discovery of HTS, an explanation to the superconductivity mechanism has been attempted in the context of strongly bound bipolarons [75, 76, 77, 78, 79]. The two main conditions for bipolaronic superconductivity are: (1) The polaron (and thus the bipolaron) density must not be high, otherwise, a charge-density wave may occur. We, however, note that the charge carriers in the majority of the superconductors are not dilute. (2) The bipolarons should be strongly coupled (i.e. a pair of polaron binds via strong EPI), small and must not be strongly interacting to hinder superconductivity.

Polarons are well-established in nearly all media, but bipolarons have a lesser occurrence [65]. It is hoped that with advancing technologies, experimental observation of bipolaron signatures will become possible. The main ingredients of the method and approximations that I applied in this thesis will be discussed in the next section.

2.11   Lang-Firsov Canonical Transformation

The EPI models described above, and by extension phonon-mediated superconductivity, are very difficult to treat exactly because contributions from both the electrons and phonons are intertwined. However, it is possible to decouple the EPI term (electron and phonon operators) into standalone terms representing electron and phonon subsystems while retaining the underlying physics of the EPI.

The Lang-Firsov (LF) canonical transformation [80] is a powerful technique one can

employ to disentangle the subsystem operators. This leads to a transformed Hamiltonian with a transformed wavefunction $|\Psi\rangle_{\text{LF}} = e^{-S}|\Psi\rangle$. To demonstrate how the transformation works in the present context, let us examine the generalised EPI of Holstein type:

$$H = \sum_{\langle ii'\rangle} t_{ii'} c_i^\dagger c_{i'} + \sum_{ij} \gamma_{ij} c_i^\dagger c_i (a_j^\dagger + a_j) + \hbar\omega \sum_j (a_j^\dagger a_j + \frac{1}{2}) \tag{2.37}$$

where $t_{ii'}$, ω and γ_{ij} are constant parameters. Next, we perform a canonical operation with a new (transformed) Hamiltonian as

$$\tilde{H} = e^S H e^{-S} = H + [S, H] + \frac{1}{2!}[S, [S, H]] + \frac{1}{3!}[S, [S, [S, H]]] + \dots \tag{2.38}$$

where $S = -\frac{\gamma_{ij}}{\hbar\omega} c_i^\dagger c_i (a_j^\dagger - a_j)$ is an anti-hermitian operator such that $S^\dagger = -S$ to preserve the physical observables [80]. Then, we can derive the commutation relations for the series in Equation (2.38). For example

$$[S, c_i] = -\frac{\gamma_{ij}}{\hbar\omega} c_i^\dagger c_i c_i (a_j^\dagger - a_j) + \frac{\gamma_{ij}}{\hbar\omega} c_i c_i^\dagger c_i (a_j^\dagger - a_j)$$
$$= 0 + \frac{\gamma_{ij}}{\hbar\omega} c_i (1 - c_i c_i^\dagger)(a_j^\dagger - a_j) = -\frac{\gamma_{ij}}{\hbar\omega} c_i (a_j^\dagger - a_j) \tag{2.39}$$

$$[S, [S, c_i]] = -\frac{\gamma_{ij}}{\hbar\omega}(a_j^\dagger - a_j)[S, c_i] = c_i \left[-\frac{\gamma_{ij}}{\hbar\omega}(a_j^\dagger - a_j) \right]^2 \tag{2.40}$$

$$[S, a_j] = -\frac{\gamma_{ij}}{\hbar\omega} c_i^\dagger c_i (a_j^\dagger - a_j) a_j + \frac{\gamma_{ij}}{\hbar\omega} c_i^\dagger c_i a_j (a_j^\dagger - a_j) \tag{2.41}$$
$$= -\frac{\gamma_{ij}}{\hbar\omega} c_i c_i^\dagger ([a_j^\dagger, a_j] + a_j a_j - a_j a_j) = \frac{\gamma_{ij}}{\hbar\omega} c_i^\dagger c_i$$

$$[S, [S, a_j]] = 0 \tag{2.42}$$

We also define new (transformed) electron and phonon operators below.

$$c_i \to \tilde{c}_i = c_i \exp\left[\sum_j \frac{\gamma_{ij}}{\hbar\omega}(a_j^\dagger - a_j)\right], \quad c_i^\dagger \to \tilde{c}_i^\dagger = c_i^\dagger \exp\left[-\sum_j \frac{\gamma_{ij}}{\hbar\omega}(a_j^\dagger - a_j)\right] \tag{2.43}$$

$$a_j \to \tilde{a}_j = a_j - \sum_i \frac{\gamma_{ij}}{\hbar\omega} c_i^\dagger c_i \ , \qquad a_j^\dagger \to \tilde{a}_j^\dagger = a_j^\dagger - \sum_i \frac{\gamma_{ij}}{\hbar\omega} c_i^\dagger c_i \tag{2.44}$$

Then setting $\hbar = 1$ for convenience, the transformed Hamiltonian can be expressed in terms of Equations (2.43) and (2.44) as

$$
\begin{aligned}
\tilde{H} =& e^S \left[\sum_{\langle ii' \rangle} t_{ii'} c_i^\dagger c_{i'} + \sum_{ij} \gamma_{ij} c_i^\dagger c_i (a_j^\dagger + a_j) + \omega \sum_j \left(a_j^\dagger a_j + \frac{1}{2} \right) \right] e^{-S} \\
=& \sum_{\langle ii' \rangle} t_{ii'} \tilde{c}_i^\dagger \tilde{c}_{i'} + \sum_{ij} \gamma_{ij} \tilde{c}_i^\dagger \tilde{c}_i (\tilde{a}_j^\dagger + \tilde{a}_j) + \omega \sum_j \left(\tilde{a}_j^\dagger \tilde{a}_j + \frac{1}{2} \right) \\
=& \sum_{\langle ii' \rangle} \tilde{t}_{ii'} c_i^\dagger c_{i'} + \sum_{ij} \gamma_{ij} c_i^\dagger c_i \left(a_j^\dagger + a_j - 2 \sum_{i'} \frac{\gamma_{i'j}}{\omega} c_{i'}^\dagger c_{i'} \right) \\
& + \omega \sum_j \left[\left(a_j^\dagger - \sum_i \frac{\gamma_{ij}}{\omega} c_i c_j^\dagger \right) \left(a_j - \sum_{i'} \frac{\gamma_{i'j}}{\omega} c_{i'}^\dagger c_{i'} \right) + \frac{1}{2} \right] \\
=& \sum_{\langle ii' \rangle} \tilde{t}_{ii'} c_i^\dagger c_{i'} - \sum_{ii'} c_i^\dagger c_i c_{i'}^\dagger c_{i'} \sum_j \frac{\gamma_{ij} \gamma_{i'j}}{\omega} + \omega \sum_j \left(a_j^\dagger a_j + \frac{1}{2} \right)
\end{aligned}
$$

$$(2.45)$$

$$(2.46)$$

We can now see that the electron and phonon operators are completely decoupled by this transformation. This means that the EPI term splits into a polaron and phonon decoupled system such that the polaron moves with a renormalised electron hopping matrix $\tilde{t}$ *.

2.11.1 Transformed Hamiltonian in the Atomic Limit

Consider the atomic limit where the hopping term is set to zero $\tilde{t}_{ii'} \to 0$, the relevant terms are the phonon and interaction parts

$$
\tilde{H}_{at} = - \sum_{ii'} n_i n_{i'} \sum_j \frac{f_{ij} f_{i'j}}{2 \omega^2 M} + \omega \sum_j \left(a_j^\dagger a_j + \frac{1}{2} \right)
$$

$$(2.47)$$

where we have introduced $\gamma_{ij} = \frac{f_{ij}}{\sqrt{2M\omega}}$: f_{ij} is the force felt by an electron located at the ith site from a phonon at j^{th} site, M is the mass of the ion. From here we can define an interaction function Φ which represents the total interaction between the electron and

---

*The Coulomb part remains unchanged because the electron number operators are unchanged upon transformation.

the surrounding phonons.

$$\Phi_{ii'} = \sum_j f_{ij} f_{i'j} \tag{2.48}$$

We define a dimensionless parameter $\lambda = E_{\text{pol}}/W$ which measures the coupling strength between the electron and the phonon, where $W = zt$ is the half-bandwidth. The self energy of the polaron E_{pol} is found when $i = i'$, so that

$$E_{\text{pol}} = \frac{1}{2\omega^2 M} \sum_j f_{0j}^2 = \frac{\Phi_{00}}{2\omega^2 M} \tag{2.49}$$

Hence,

$$\tilde{H}_{at} = -\sum_{ii'} n_i n_{i'} \lambda W \frac{\Phi_{ii'}}{\Phi_{00}} + \omega \sum_j (a_j^\dagger a_j + \frac{1}{2}) \tag{2.50}$$

In this limit, we have a simplified Hamiltonian which is proportional to the ratio of two interaction functions and the coupling parameter λ.

2.11.2   Transformation of the Tight-Binding Hamiltonian

The first term in Equation (2.45) represents the electron hopping term

$$\tilde{H}_{tb} = \sum_{\langle ii' \rangle} \tilde{t}_{ii'} c_i^\dagger c_{i'} \tag{2.51}$$

where

$$\tilde{t}_{ii'} = t_{ii'} \exp\left[-\sum_j \frac{\gamma_{ij}}{\omega}(a_j^\dagger - a_j) \right] \exp\left[\sum_j \frac{\gamma_{i'j}}{\omega}(a_j^\dagger - a_j) \right] \tag{2.52}$$

Using the identity

$$e^A e^B e^{-[A,B]/2} = e^{A+B} \qquad , \tag{2.53}$$

which is valid if $[A, B]$ commutes with A and B respectively. We can also write Equation (2.53) as: $e^A e^B = e^{A+B} e^{[A,B]/2}$. We use the last (equivalent) expression by taking $A = -\sum_j \frac{\gamma_{ij}}{\omega}(a_j^\dagger - a_j)$ and $B = \sum_j \frac{\gamma_{i'j}}{\omega}(a_j^\dagger - a_j)$. We note that $[A, B] = 0$, therefore

$$\tilde{t}_{ii'} = t_{ii'} \exp\left[\frac{1}{(\omega)^2}\left\{ \sum_j (\gamma_{i'j} - \gamma_{ij})a_j^\dagger - \sum_j (\gamma_{i'j} - \gamma_{ij})a_j \right\} \right] \tag{2.54}$$

Re-using Equation (2.53) in its original form by choosing

$A = \sum_j (\gamma_{i'j} - \gamma_{ij})a_j^\dagger$ and $B = -\sum_j (\gamma_{i'j} - \gamma_{ij})a_j$, then,

$[A, B] = \sum_j (\gamma_{i'j} - \gamma_{ij})(\gamma_{i'j} - \gamma_{ij}) = \sum_j (\gamma_{i'j}^2 - 2\gamma_{i'j}\gamma_{ij} + \gamma_{ij}^2).$

After some algebra, with the substitution of $\gamma_{ij} = \frac{f_{ij}}{\sqrt{2M\omega}}$ as we defined earlier, we arrive at

$$\tilde{t}_{ii'} = t_{ii'} \exp\left[-\frac{\lambda W}{\omega}\left(1 - \frac{\Phi_{ii'}}{\Phi_{00}}\right)\right] \exp\left(\sum_j (\gamma_{i'j} - \gamma_{ij})a_j^\dagger\right)$$
$$\times \exp\left(\sum_j (\gamma_{i'j} - \gamma_{ij})a_j\right)$$

(2.55)

The original hopping integral $t_{ii'}$ becomes modified by the EPI through the parameters $\Phi_{ii'}/\Phi_{00}$ and λ, similar to Equation (2.50). Equation (2.55) also provides valuable information particularly due to the order of the creation and annihilation operators. In the anti-adiabatic limit where there are no real phonons, the phonon operators are set to zero and the hopping integral reduces [81] to

$$\tilde{t}_{ii'} = t_{ii'} \exp\left[-\frac{\lambda W}{\omega}\left(1 - \frac{\Phi_{ii'}}{\Phi_{00}}\right)\right] . \qquad (2.56)$$

2.12 *UV* Models

Above, the decoupling of the electron and phonon operators was successfully achieved through the canonical transformation, and it was noted that the electron in the electronic part of the Hamiltonian becomes a phonon-dressed electron. If we re-introduce the Coulomb potential between electrons and consider the bipolaron problem in the anti-adiabatic, strong-coupling regime ($\hbar\omega \gg t, \lambda \gg 1$) [71, 72, 81, 82], then the effective Hamiltonian for the Hubbard-Fröhlich model has the form [81]

$$H = -\sum_{nn'\sigma} \tilde{t}_{nn'} c_{n\sigma}^\dagger c_{n'\sigma} - E_{\text{pol}} \sum_n c_{n\sigma}^\dagger c_{n\sigma} + \tilde{U} \sum_n c_{n\uparrow}^\dagger c_{n\downarrow}^\dagger c_{n\downarrow} c_{n\uparrow} + \sum_{nn'}' \sum_{\sigma\sigma'} \tilde{V}_{nn'} c_{n\sigma}^\dagger c_{n\sigma} c_{n'\sigma'}^\dagger c_{n'\sigma'}$$

(2.57)

where the prime in the last summation excludes self-interaction, and the renormalised

onsite and intersite interactions respectively are

$$\tilde{U} \to U = U_\text{H} - 2W\lambda \tag{2.58}$$

$$\tilde{V} \to V = V_\text{H} - 2W\lambda \frac{\Phi_{nn'}}{\Phi_{00}} \tag{2.59}$$

where U_H and V_H are typical Hubbard interactions. Equations (2.10) and (2.57) are

similar except for the renormalised U and V in the latter. Restricting n' to the nearest-

neighbours of n, the Hamiltonian defines the UV model which is often referred to as the

extended-Hubbard model (EHM) [70, 83]. It is possible to extend the intersite interaction

to next-nearest-neighbour distances [84], but the studies in this thesis only consider the

nearest-neighbour interactions.

Chapter 3

Methodology

3.1 Summary

In this chapter, we discuss the methods that are used in this thesis. Firstly, we find a solution to the UV Hamiltonian derived in Chapter 2. Then, we review group theory analysis which will be used for the identification of pairing symmetries. Next, we discuss the standard Rayleigh–Schrödinger perturbation theory. Finally, we conclude by introducing a quantum Monte-Carlo algorithm which can be used to simulate bipolarons.

3.2   Preliminaries

The methods applied in this work can be split into four types and they will be presented in the following order.

Method I: Solution to the UV model. This involves solving a two-particle Schrödinger equation for the UV Hamiltonian. The solution yields a self-consistent equation which can be found in Section 3.3.1. Because the dimension of the secular equation increases with the lattice coordination number z (and thus the number of pairing states), we will introduce a symmetrisation approach (Section 3.3.2) which helps categorise the pair symmetries. The steps and the benefits of using the symmetrised solutions will be discussed.

Method II: Group theory. This method can be very helpful in the simplification of physics problems. Amongst other things, it can be used for transformations, to analyse symmetries, and in the construction of the band structure of a crystal [85]. We review basic concepts of group theory analysis relevant to this work in Section 3.4. They include the representation theory, symmetry operations, the character table, eigenvalue problem and block-diagonalisation of secular matrices.

Method III: Perturbation theory. The degenerate Rayleigh-Schrödinger time-independent perturbation theory is discussed in Section 3.5. The purpose of this method is to validate our UV results in certain limits.

Method IV: Monte-Carlo simulation. Numerical simulation is advantageous where certain approximations become invalid. We introduce how bipolaron properties can be obtained using a Monte-Carlo algorithm in Section 3.6.1.

3.3 The Standard *UV* Model

We have previously derived an effective *UV* model in Section 2.12 of Chapter 2. Here, we will focus on the general form of the model Hamiltonian and demonstrate how it can be used to solve a problem of two spin-$\frac{1}{2}$ fermions in a single orbital. The Hamiltonian has the form

$$H = \sum_{\langle \boldsymbol{n}, \boldsymbol{a} \rangle \sigma} \tilde{t}_{\boldsymbol{a}} c^{\dagger}_{\boldsymbol{n}+\boldsymbol{a}\sigma} c_{\boldsymbol{n}\sigma} + U \sum_{\boldsymbol{n}} \hat{\rho}_{\boldsymbol{n}\uparrow} \hat{\rho}_{\boldsymbol{n}\downarrow} + V \sum_{\langle \boldsymbol{n}, \boldsymbol{a} \rangle} \hat{\rho}_{\boldsymbol{n}+\boldsymbol{a}} \hat{\rho}_{\boldsymbol{n}} \tag{3.1}$$

where $c^{\dagger}$ (c) is the creation (annihilation) operator, σ is the electron spin, $\hat{\rho}_{\boldsymbol{n}} = \hat{\rho}_{\boldsymbol{n}\uparrow} + \hat{\rho}_{\boldsymbol{n}\downarrow}$ ($\hat{\rho}_{\boldsymbol{n}\sigma}$ is the number operator for electrons on site $\boldsymbol{n}$ with spin σ), $\boldsymbol{a}$ the intersite lattice vector, and $\tilde{t}_{\boldsymbol{a}}$ is the intersite hopping parameter. U and V are the effective onsite and intersite interactions, respectively.

3.3.1 Solution to the *UV* Model

To solve Equation (3.1) for the case of two particles, we construct a real-space Schrödinger equation. The two-body wavefunction $\Psi(\boldsymbol{n}_1 \, \boldsymbol{n}_2)$ must satisfy:

$$\sum_{\boldsymbol{a}} \tilde{t}_{\boldsymbol{a}} \left[\Psi(\boldsymbol{n}_1 + \boldsymbol{a}, \boldsymbol{n}_2) + \Psi(\boldsymbol{n}_1, \boldsymbol{n}_2 + \boldsymbol{a}) \right] + \sum_{\boldsymbol{a}} \hat{V}_{\boldsymbol{a}} \, \delta_{\boldsymbol{n}_1 - \boldsymbol{n}_2, \boldsymbol{a}} \Psi(\boldsymbol{n}_1, \boldsymbol{n}_2) = E\Psi(\boldsymbol{n}_1, \boldsymbol{n}_2) \tag{3.2}$$

where $\boldsymbol{n}_1$ and $\boldsymbol{n}_2$ are the spatial coordinates, the interaction terms have been combined into a single function (i.e. $\hat{V}_{\boldsymbol{a}=0} = U$ and $\hat{V}_{\boldsymbol{a}\neq0} = V$), E is the total energy of the system. We will drop the subscript from $\tilde{t}_{\boldsymbol{a}}$ for brevity.

Equation (3.2) can be solved as follows. We define the Fourier-space wavefunction

$$\psi_{\boldsymbol{k}_1 \boldsymbol{k}_2} = \frac{1}{N} \sum_{\boldsymbol{n}_1 \boldsymbol{n}_2} \Psi(\boldsymbol{n}_1, \boldsymbol{n}_2) \, e^{-i\boldsymbol{k}_1 \cdot \boldsymbol{n}_1 - i\boldsymbol{k}_2 \cdot \boldsymbol{n}_2} \tag{3.3}$$

where N is the total number of lattice sites. If we multiply Equation (3.2) by $\frac{1}{N} e^{-i\boldsymbol{k}_1 \cdot \boldsymbol{n}_1} \times$

$e^{-i\mathbf{k}_2 \cdot \mathbf{n}_2}$ and sum over $\mathbf{n}_1$ and $\mathbf{n}_2$, we get

$$\frac{1}{N} \sum_a \tilde{t} \left[\sum_{\mathbf{n}_1 \mathbf{n}_2} e^{-i\mathbf{k}_1 \cdot \mathbf{n}_1 - i\mathbf{k}_2 \cdot \mathbf{n}_2} \{ \Psi(\mathbf{n}_1 + \mathbf{a}, \mathbf{n}_2) + \Psi(\mathbf{n}_1, \mathbf{n}_2 + \mathbf{a}) \} \right]$$

$$+ \frac{1}{N} \sum_a \hat{V}_a \sum_{\mathbf{n}_1 \mathbf{n}_2} e^{-i\mathbf{k}_1 \cdot \mathbf{n}_1 - i\mathbf{k}_2 \cdot \mathbf{n}_2} \delta_{\mathbf{n}_1 - \mathbf{n}_2, a} \Psi(\mathbf{n}_1, \mathbf{n}_2) \tag{3.4}$$

$$= \frac{1}{N} E \sum_{\mathbf{n}_1 \mathbf{n}_2} e^{-i\mathbf{k}_1 \cdot \mathbf{n}_1 - i\mathbf{k}_2 \cdot \mathbf{n}_2} \Psi(\mathbf{n}_1, \mathbf{n}_2)$$

Since the summation $\sum_{\mathbf{n}_1 \mathbf{n}_2}$ is independent of $\mathbf{a}$, we can define new variables $\mathbf{m}_1 = \mathbf{n}_1 + \mathbf{a}$, and $\mathbf{m}_2 = \mathbf{n}_2 + \mathbf{a}$. Then we have

$$\sum_a \tilde{t} e^{i\mathbf{k}_1 \cdot \mathbf{a}} \frac{1}{N} \sum_{\mathbf{m}_1 \mathbf{n}_2} e^{-i\mathbf{k}_1 \cdot \mathbf{m}_1 - i\mathbf{k}_2 \cdot \mathbf{n}_2} \Psi(\mathbf{m}_1, \mathbf{n}_2) + \sum_a \tilde{t} e^{i\mathbf{k}_2 \cdot \mathbf{a}} \frac{1}{N} \sum_{\mathbf{n}_1 \mathbf{m}_2} e^{-i\mathbf{k}_1 \cdot \mathbf{n}_1 - i\mathbf{k}_2 \cdot \mathbf{m}_2} \Psi(\mathbf{n}_1, \mathbf{m}_2)$$

$$+ \frac{1}{N} \sum_{a\mathbf{P}} \hat{V}_a e^{-i\mathbf{P} \cdot \mathbf{a}} \frac{1}{N} \sum_{\mathbf{n}_1 \mathbf{n}_2} e^{-i(\mathbf{k}_1 - \mathbf{P}) \cdot \mathbf{n}_1} e^{-i(\mathbf{k}_2 + \mathbf{P}) \cdot \mathbf{n}_2} \Psi(\mathbf{n}_1, \mathbf{n}_2)$$

$$= \frac{1}{N} E \sum_{\mathbf{n}_1 \mathbf{n}_2} e^{-i\mathbf{k}_1 \cdot \mathbf{n}_1 - i\mathbf{k}_2 \cdot \mathbf{n}_2} \Psi(\mathbf{n}_1, \mathbf{n}_2)$$

$$\tag{3.5}$$

where we have replaced the Dirac-delta function as $\delta_{\mathbf{m},\mathbf{n}} = \frac{1}{N} \sum_{\mathbf{P}} e^{i\mathbf{P} \cdot (\mathbf{m}-\mathbf{n})}$. Using the definition in Equation (3.3) and expressing $\mathbf{P} = \mathbf{k}_1 - \mathbf{q}$, we arrive at

$$(E - \varepsilon_{\mathbf{k}_1} - \varepsilon_{\mathbf{k}_2}) \psi_{\mathbf{k}_1 \mathbf{k}_2} = \frac{1}{N} \sum_{a\mathbf{q}} \hat{V}_a \, e^{i(\mathbf{q} - \mathbf{k}_1) \cdot \mathbf{a}} \, \psi_{\mathbf{q}, \mathbf{k}_1 + \mathbf{k}_2 - \mathbf{q}} \quad , \tag{3.6}$$

where

$$\varepsilon_{\mathbf{k}} = \sum_a \tilde{t} \, e^{i\mathbf{k} \cdot \mathbf{a}} \tag{3.7}$$

is the dispersion relation for one particle with momentum $\mathbf{k}$.

Next, we define a new wavefunction Φ_a

$$\Phi_a(\mathbf{k}_1 + \mathbf{k}_2) = \Phi_a(\mathbf{P}) \equiv \frac{1}{N} \sum_{\mathbf{q}} e^{i\mathbf{q} \cdot \mathbf{a}} \, \psi_{\mathbf{q}, \mathbf{P} - \mathbf{q}} \tag{3.8}$$

where $\mathbf{P} = \mathbf{k}_1 + \mathbf{k}_2$ is the total momentum of the particle pair. After the substitution of Φ_a, Equation (3.6) may be re-written as

$$\psi_{\mathbf{k}_1 \mathbf{k}_2} = \sum_a \hat{V}_a \frac{e^{-i\mathbf{k}_1 \cdot \mathbf{a}}}{E - \varepsilon_{\mathbf{k}_1} - \varepsilon_{\mathbf{k}_2}} \Phi_a(\mathbf{P}) \quad . \tag{3.9}$$

Lastly, we substitute Equation (3.9) back into Equation (3.8) to get

$$\Phi_{\boldsymbol{a}}(\boldsymbol{P}) = -\sum_{\boldsymbol{a'}} \hat{V}_{\boldsymbol{a'}} \, \mathcal{G}_{\boldsymbol{aa'}}(E, \boldsymbol{P}) \, \Phi_{\boldsymbol{a'}}(\boldsymbol{P}) \qquad (3.10)$$

where $\mathcal{G}_{\boldsymbol{aa'}}(E, \boldsymbol{P})$ is the Green's function defined as

$$\mathcal{G}_{\boldsymbol{aa'}}(E, \boldsymbol{P}) = \frac{1}{N} \sum_{\boldsymbol{q}} \frac{e^{i\boldsymbol{q}\cdot(\boldsymbol{a}-\boldsymbol{a'})}}{-E + \varepsilon_{\boldsymbol{q}} + \varepsilon_{\boldsymbol{P}-\boldsymbol{q}}} \qquad . \qquad (3.11)$$

Note that the sign of E in the denominator has been flipped and this is done for convenience only. The set of linear equations generated from (3.10)

$$\det | -\hat{V}_{\boldsymbol{a'}} \, \mathcal{G}_{\boldsymbol{aa'}}(E, \boldsymbol{P}) - \delta_{\boldsymbol{aa'}} | = 0 \qquad , \qquad (3.12)$$

determines the energy $E(\boldsymbol{P})$ of the system as a function of the pair's total momentum. Equation (3.12) is solved self-consistently to obtain the general solution of the two-body problem.

3.3.2 Symmetrised and Anti-symmetrised Solutions

In general, Equation (3.10) generates a square matrix of size $z + 1$, where z is the coordination number of the lattice. As a result, we would have (3×3), (5×5), (7×7), (7×7), (9×9) and (13×13) matrices for the two-particle problem in chain, square, triangular, simple cubic, body-centred cubic, and face-centred cubic lattices respectively. Hence, it is helpful to apply a symmetrisation approach that reduces the matrix size to about half. In the following, we shall demonstrate how this is done.

The two-particle wavefunction has to be symmetric or anti-symmetric under spatial exchange $\Psi(\boldsymbol{n}_1, \boldsymbol{n}_2) = \pm\Psi(\boldsymbol{n}_2, \boldsymbol{n}_1)$ which relates to the singlet $(+)$ and triplet $(-)$ spin states. To express the symmetrised wavefunctions, we permute $\boldsymbol{k}_1 \to \boldsymbol{k}_2$ in Equation (3.6) and then we add/subtract the resulting equation from the unpermuted version of

Equation (3.6). Doing this yields

$$(E - \varepsilon_{\boldsymbol{k}_1} - \varepsilon_{\boldsymbol{k}_2})(\psi_{\boldsymbol{k}_1\boldsymbol{k}_2} \pm \psi_{\boldsymbol{k}_2\boldsymbol{k}_1}) = \frac{1}{N} \sum_{\boldsymbol{a}\boldsymbol{q}} \hat{V}_{\boldsymbol{a}} \left\{ e^{i(\boldsymbol{q}-\boldsymbol{k}_1)\cdot\boldsymbol{a}} \pm e^{i(\boldsymbol{q}-\boldsymbol{k}_2)\cdot\boldsymbol{a}} \right\} \psi_{\boldsymbol{q},\boldsymbol{k}_1+\boldsymbol{k}_2-\boldsymbol{q}} \quad (3.13)$$

We can re-write the (anti-)symmetrised pair wavefunctions on the left-hand side of Equation (3.13) as

$$\phi^{\pm}_{\boldsymbol{k}_1\boldsymbol{k}_2} = \psi_{\boldsymbol{k}_1\boldsymbol{k}_2} \pm \psi_{\boldsymbol{k}_2\boldsymbol{k}_1}. \quad (3.14)$$

where $\phi^{+}_{\boldsymbol{k}_1\boldsymbol{k}_2}$ and $\phi^{-}_{\boldsymbol{k}_1\boldsymbol{k}_2}$ respectively are the singlet and the triplet wavefunctions. So, Equation (3.13) becomes

$$(E - \varepsilon_{\boldsymbol{k}_1} - \varepsilon_{\boldsymbol{k}_2})\phi^{\pm}_{\boldsymbol{k}_1\boldsymbol{k}_2} = \frac{1}{N} \sum_{\boldsymbol{q}\boldsymbol{a}} \hat{V}_{\boldsymbol{a}} \left\{ e^{i(\boldsymbol{q}-\boldsymbol{k}_1)\cdot\boldsymbol{a}} \pm e^{i(\boldsymbol{q}-\boldsymbol{k}_2)\cdot\boldsymbol{a}} \right\} \psi_{\boldsymbol{q},\boldsymbol{k}_1+\boldsymbol{k}_2-\boldsymbol{q}} \quad (3.15)$$

Notice that on the right-hand side, we still have ψ. The summation over the lattice vector $\boldsymbol{a}$, in Equation (3.15) can be split into two sets ($\{\boldsymbol{a}_+\}$ for singlets, and $\{\boldsymbol{a}_-\}$ for triplets) which thus allows us to write Equation (3.15) in terms of $\phi^{\pm}$ instead of ψ. To do this, we define $\{\boldsymbol{a}_+\}$ and $\{\boldsymbol{a}_-\}$ to be a set of near-neighbour lattice vectors, and also include the zero vector in the case of singlets. Neither of the new vectors should contain member pairs that are related by inversion. Otherwise, there are no specific rules of selection. Let us illustrate this on a square lattice. The lattice vectors for the onsite and all nearest-neighbour sites are $\{(0,0), (1,0), (0,1)(-1,0), (0,-1)\}$. So, an acceptable combination can be $\{\boldsymbol{a}_+\} = \{(0,0), (1,0), (0,1)\}$ for the singlet, and $\{\boldsymbol{a}_-\} = \{(1,0), (0,1)\}$ for the triplet. But we cannot have, say, $\{\boldsymbol{a}_+\} = \{(0,0), (1,0), (-1,0)\}$ because the second and third elements are related by inversion.

Once the singlet and triplet vectors have been correctly chosen, we can express Equation (3.15) as

$$(E - \varepsilon_{\boldsymbol{k}_1} - \varepsilon_{\boldsymbol{k}_2})\phi^{\pm}_{\boldsymbol{k}_1\boldsymbol{k}_2} = \frac{1}{N} \sideset{}{'}\sum_{\boldsymbol{q}\boldsymbol{a}_{\pm}} \hat{V}_{\boldsymbol{a}_{\pm}} \left\{ e^{i(\boldsymbol{q}-\boldsymbol{k}_1)\cdot\boldsymbol{a}_{\pm}} \pm e^{i(\boldsymbol{q}-\boldsymbol{k}_2)\cdot\boldsymbol{a}_{\pm}} \right\} \phi^{\pm}_{\boldsymbol{q},\boldsymbol{k}_1+\boldsymbol{k}_2-\boldsymbol{q}} \quad (3.16)$$

where the primed summation in Equation (3.16) above means that a factor of $\frac{1}{2}$ should be included for the case $\boldsymbol{a}_+ = \boldsymbol{0}$ to account for double counting of onsite pairs. Following similar steps in Equations $(3.8)-(3.11)$, we obtain

$$\Phi^{\pm}_{\boldsymbol{a}_\pm}(\boldsymbol{P}) = -\sum_{\boldsymbol{a}'_\pm} \hat{V}_{\boldsymbol{a}_\pm} \mathcal{G}^{\pm}_{\boldsymbol{a}_\pm \boldsymbol{a}'_\pm}(E, \boldsymbol{P})\, \Phi^{\pm}_{\boldsymbol{a}'_\pm}(\boldsymbol{P}) \tag{3.17}$$

where the Green's function is now

$$\mathcal{G}^{\pm}_{\boldsymbol{a}_\pm \boldsymbol{a}'_\pm}(E, \boldsymbol{P}) = \frac{1}{N} \sum_{\boldsymbol{q}} \frac{e^{i\boldsymbol{q}\cdot(\boldsymbol{a}_\pm - \boldsymbol{a}'_\pm)} \pm e^{i[\boldsymbol{q}\cdot\boldsymbol{a}_\pm - (\boldsymbol{P}-\boldsymbol{q})\cdot\boldsymbol{a}'_\pm]}}{-E + \varepsilon_{\boldsymbol{q}} + \varepsilon_{\boldsymbol{P}-\boldsymbol{q}}} \tag{3.18}$$

Hence, Equations $(3.15)-(3.18)$ are used to obtain the (anti-)symmetrised solutions.

Some advantages of using (anti-)symmetrised solutions include

- Reduction in the size of the self-consistent equation. For example, the matrix equation for the BCC case would reduce to *two* (5×5) and (4×4) matrices instead of *one* (9×9) matrix equation, and for the FCC case, we will have (7×7) and (6×6) matrices instead of (13×13) matrix equation.

- Improvements in both the numerical stability and computational speed of calculations.

- Lack of ambiguity in identifying singlet and triplet states. Since the matrix equations for the singlets and triplets are completely separated, their properties are obtained independently, thus eliminating any form of ambiguity.

In addition to applying the symmetrised approach, we can obtain further simplification using group theory. Hence, we will briefly discuss the application of group theory relevant to this work.

3.4   Group Theory Analysis

Group theory finds a lot of applications in quantum physics via the representation theory. For every physical observable, there exists a corresponding Hermitian operator with a complete set of eigenfunctions. Hence, the state of a system can be represented by a linear combination of these eigenfunctions. The representation theory is useful when a set of operators acting on a Hilbert space have common properties and thus form a group. In this thesis, we take advantage of the fact that when operators belonging to a group act on a system and the system remains physically invariant, a linear combination of basis which represents the states of the system can be obtained to simplify the two-particle problem. The details will become clear in Chapters 4 and 5 when this is applied. In what follows, some mathematical concepts of group theory will be introduced.

Mathematically, a set G of elements is called a *"group"* if the four conditions below are satisfied.

1. A group must obey the *closure* property such that if we multiply any two elements A and B of G, the result C must also be an element of G. That is,

$$A \cdot B = C \in G \qquad \qquad . \qquad \qquad (3.19)$$

2. G contains an element I or E called the *identity* element such that for every element $A \in G$,

$$A \cdot E = E \cdot A = A \qquad \qquad . \qquad \qquad (3.20)$$

3. For any element $A \in G$, there exists an inverse element $B = A^{-1} \in G$ such that

$$A \cdot B = E \qquad \qquad (3.21)$$

4. For three elements A, B and $C \in G$, the law of *associativity* must hold i.e.

$$A \cdot (B \cdot C) = (A \cdot B) \cdot C \qquad \qquad (3.22)$$

Before proceeding, we will briefly define some of the commonly used terms in group theory.

- Conjugate Elements: Element B' is conjugate to the element B if

$$B' = XBX^{-1} \qquad \text{where } B, B' \text{and } X \in G \qquad (3.23)$$

  Note that any element B is also conjugate to itself, for example, $B = EBE^{-1}$.

- Classes: A class of a group G is the collection of elements of G that are conjugate to each other. Put in another way, when each element $X \in G$ is applied to the RHS of Equation (3.23), the set of distinct results for an element B forms a class. Note that: no element of G can be a member of two different classes; the identity element is a class on its own.

- Similarity transformation: The equation of the form (3.23) is known as the *"similarity transformation"* and will be used many times in this work. We can use this expression to diagonalise a matrix equation into block-diagonal form.

3.4.1 Groups of Coordinate Transformations

In quantum physics problems, we often apply transformations to reduce the complexity of a Hamiltonian. The transformation must be chosen in a way that the physical representation (e.g. symmetry) of the system will not be compromised. Examples of symmetry transformations are rotation, reflection, translation, permutation, and so on. Meanwhile, the set of all the transformations which leave the system physically invariant constitutes a group [85]. The set of coordinate transformations that leave the Hamiltonian invariant form a group usually called *"the group of the Schrödinger equation"*, but sometimes referred to as *"the invariance group of the Hamiltonian operator"* [86]. In the next section, we will briefly describe some symmetry transformations.

Our application of group theory in this work involves performing rotations of rigid bodies about different axes and orientations. We note that the symmetry of the system remains conserved in all cases.

Suppose that we have a point P in a three-dimensional Euclidean space $\mathbb{R}^3$, in an orthogonal XYZ coordinate and we rotate about OX to a new orthogonal coordinate system $X'Y'Z'$. It is possible to describe the point P in the new coordinate system. This is done by mapping the new coordinate onto the old coordinate.

In a compact form, we can write

$$\mathbf{r}' = \mathbf{R}(T)\mathbf{r} \tag{3.24}$$

where $\mathbf{r}'$ and $\mathbf{r}$ represent the new and old coordinates, respectively, and the rotation operator

$$\mathbf{R}(T) = \begin{bmatrix} 1 & 0 & 0 \\ 0 & \cos\theta & \sin\theta \\ 0 & -\sin\theta & \cos\theta \end{bmatrix} \tag{3.25}$$

depends on the rotation T but is independent of the position P. $\mathbf{R}(T)$ obeys the orthogonality rule

$$[\mathbf{R}(T)]^T = [\mathbf{R}(T)]^{-1} \tag{3.26}$$

and

$$\det |\, \mathbf{R}(T) \,| = 1 \tag{3.27}$$

The product of two rotations T_1 and T_2 is

$$\mathbf{R}(T_1 T_2) = \mathbf{R}(T_1)\mathbf{R}(T_2) \qquad , \tag{3.28}$$

but in general, $\mathbf{R}(T_1)\mathbf{R}(T_2) \neq \mathbf{R}(T_2)\mathbf{R}(T_1)$.

Translation symmetry is achieved by simply moving a body in $\mathbb{R}^3$ (without rotation). Inversion and reflection are similar in that they involve the rearrangement (or swapping)

of identical points of a body in space while the system remains physically unchanged.

3.4.2 Representation Theory of Finite Groups

The two main reasons for applying group theory in this work are for further simplification of analytic calculations and the classification of the symmetries of bound pairs. Even though we can use the symmetrised solution to separate singlets from triplets, group theory further helps to identify the sub-symmetries within these separate classes. In other words, it is possible to identify s-wave and d-wave singlets and, similarly, we can distinguish between p-wave and f-wave triplets. We note that identification of states using this method is most useful at the Brillouin zone centre because states of the same symmetry class (e.g different singlets or different triplets) can mix away from the zone centre. We will introduce some mathematical concepts of representation theory below.

If each element A of a group G can be assigned a non-singular square matrix $\Gamma(A)$ such that $\Gamma(A_1 A_2) = \Gamma(A_1)\Gamma(A_2) \in G$ for every pair A_1 and A_2 of the group, then, the set of matrices $\{\Gamma(A_1), \Gamma(A_2), \ldots, \Gamma(A_n)\}$ is said to be the representation of G and the order of these matrices gives the dimension of the representation.

3.4.2.1 Equivalent Representation

Let Γ be a d-dimensional representation of a group G and let S be any non-singular $d \times d$ matrix. If for each element $A \in G$ we can define a $d \times d$ matrix $\Gamma'(A)$ such that

$$\Gamma'(A) = S \cdot \Gamma(A) \cdot S^{-1} \qquad\qquad , \qquad\qquad (3.29)$$

then the set $\{\Gamma'(A_1), \Gamma'(A_2), \ldots, \Gamma'(A_n)\}$ also forms a d-dimensional representation of G. Hence, both representations Γ and Γ' are said to be equivalent. Note that Equation (3.29) is a similarity transformation (see Section 3.4).

3.4.2.2   Unitary Representation

If there is a representation Γ_u in which the matrices $\Gamma_u(A)$ are unitary for every $A \in G$, such a representation is called a *"unitary representation"*. For a unitary matrix U, the identity $U^\dagger U = I = UU^\dagger$ holds. Similarly, a unitary representation obeys the identity relation

$$\Gamma_u(A)^\dagger \Gamma_u(A) = \Gamma_u(A)\Gamma_u(A)^\dagger = \mathbf{1} \qquad . \qquad (3.30)$$

Furthermore, a unitary transformation obeys the similarity transformation

$$\Gamma'_u(A) = S \cdot \Gamma_u(A) \cdot S^{-1} \qquad , \qquad (3.31)$$

if S is a unitary matrix. In essence, when Equation (3.31) is valid, Γ'_u and Γ_u are equivalent unitary representations.

3.4.3   Reducible & Irreducible Representations

In this work, we will make use of the irreducible representations to identify the symmetries of bound states and to determine linear combinations of the orthogonal basis. The irreducible representations of crystallographic point groups can be found in standard textbooks (e.g. Cornwell [86]). However, we will only explain the general procedures for obtaining the irreducible representations from the reducible ones.

Partitioned Matrix: Sometimes a matrix M may be partitioned into smaller matrices in the form

$$M = \begin{bmatrix} m_{11} & m_{12} & m_{13} & m_{14} \\ m_{21} & m_{22} & m_{23} & m_{24} \\ m_{31} & m_{32} & m_{33} & m_{34} \end{bmatrix} \equiv \begin{bmatrix} M^{11} & M^{12} & M^{13} \\ M^{21} & M^{22} & M^{23} \end{bmatrix} \qquad (3.32)$$

where

$$M^{11} = \begin{bmatrix} m_{11} \\ m_{12} \end{bmatrix}, \, M^{12} = \begin{bmatrix} m_{12} & m_{13} \\ m_{22} & m_{23} \end{bmatrix}, \, M^{13} = \begin{bmatrix} m_{14} \\ m_{24} \end{bmatrix},$$

$$M^{21} = \begin{bmatrix} m_{31} \end{bmatrix}, \, M^{22} = \begin{bmatrix} m_{32} & m_{33} \end{bmatrix}, \, M^{23} = \begin{bmatrix} m_{34} \end{bmatrix}$$

then each sub-matrix has some independent characteristics of the original matrix.

3.4.3.1   Reducible Representations

Suppose that we partition a d-dimensional representation Γ of a group G as

$$\Gamma(T) = \left[\begin{array}{c|c} \Gamma_{11}(T) & X(T) \\ \hline \mathbf{0} & \Gamma_{22}(T) \end{array} \right] \qquad : \text{ for all } T \in G \qquad (3.33)$$

where $\Gamma_{11}(T)$, $X(T)$, $\Gamma_{22}(T)$ and the zero matrix $\mathbf{0}$ have dimensions $s_1 \times s_1$, $s_1 \times s_2$, $s_2 \times s_2$ and $s_2 \times s_1$ respectively. (Here $s_1 + s_2 = d$, $s_1 \geq 1$, $s_2 \geq 1$ and s_1 and s_2 are the same for all $T \in G$.) Then, the product $\Gamma(T_1)\Gamma(T_2)$ must have the form (3.33)

$$\Gamma(T_1)\Gamma(T_2) = \begin{bmatrix} \Gamma_{11}(T_1)\Gamma_{11}(T_2) & \Gamma_{11}(T_1)X(T_2) + X(T_1)\Gamma_{22}(T_2) \\ \mathbf{0} & \Gamma_{22}(T_1)\Gamma_{22}(T_2) \end{bmatrix} \qquad (3.34)$$

so that

$$\Gamma_{11}(T_1 T_2) = \Gamma_{11}(T_1)\Gamma_{11}(T_2)$$

$$\Gamma_{22}(T_1 T_2) = \Gamma_{22}(T_1)\Gamma_{22}(T_2) \qquad (3.35)$$

$$\text{and} \quad X(T_1 T_2) = \Gamma_{11}(T_1)X(T_2) + X(T_1)\Gamma_{22}(T_2)$$

The first two expressions in (3.35) mean that $\Gamma_{11}(T)$ and $\Gamma_{22}(T)$ are both representations of G. From this, we understand that (quoting from Ref. [86]):

> *"A representation of a group G is said to be 'reducible' if it is equivalent to a representation Γ that has the form of Equation (3.33) for all $T \in G$."*

3.4.3.2   Irreducible Representations

It may be possible that the representations $\Gamma_{11}(T_1T_2)$ and $\Gamma_{22}(T_1T_2)$ in Equations (3.35)

can be reduced further. The reduction process proceeds by selecting a suitable matrix

S (usually unitary) where one performs similarity transformations $S \cdot \Gamma(T) \cdot S^{-1}$ until

all the matrices of a representation are no longer reducible. As such, the irreducible

representation of Γ would finally be composed of diagonal blocks of matrices that are

themselves non-reducible

$$\Gamma''(T) = \begin{bmatrix} \Gamma''_{11}(T) & 0 & 0 & \dots & 0 \\ 0 & \Gamma''_{22}(T) & 0 & \dots & 0 \\ 0 & 0 & \Gamma''_{33}(T) & \dots & 0 \\ \vdots & \vdots & \vdots & \ddots & \vdots \\ 0 & 0 & 0 & \dots & \Gamma''_{nn}(T) \end{bmatrix} \tag{3.36}$$

Thus, $\Gamma''_{11}, \dots \Gamma''_{nn}$, form the irreducible representations of the group G.

3.4.4   The Orthogonality Theorem

If $\phi_1^p(\mathbf{r})$, $\phi_2^p(\mathbf{r}), \dots$, and $\psi_1^q(\mathbf{r})$, $\psi_2^q(\mathbf{r})$ are respectively basis functions for the *unitary irre-*

ducible representations Γ^p and Γ^q of a group of coordinate transformations G, while Γ^p

and Γ^q are not equivalent if $p \neq q$ (but are identical if $p = q$), then

$$(\phi_m^p, \psi_n^q) = \delta_{p,q}\delta_{m,n} \qquad . \tag{3.37}$$

In the process of finding a set of basis functions for the two-particle problem, all the

basis functions representing the bound states must obey the orthogonality rule. The

basis used in this thesis conforms with this rule.

3.4.5 Character & Character Table

The character table via the irreducible representations is probably the most important tool in the application of group theory in this work. It allows the construction of a reduction formula in conjunction with the irreducible representations which is then used to identify the symmetries of the bound states. The following concepts are most relevant.

Character χ: this is the trace of an irreducible matrix i.e.

$$\chi(T) = \text{tr}\,[\Gamma(T)] = \sum_{j=1}^{d} \Gamma(T)_{jj} \qquad . \tag{3.38}$$

For example, the character of the identity representation of dimension d is $\chi(E) = d$.

Character Table: this is a tabular presentation of the character (χ) for each class of a group G.

3.4.6 Eigenvalue Problem

Suppose that an operator T acts on a set of basis functions ϕ_n, this operation can be expressed as

$$T\phi_n = \sum_{m} \phi_m T_{mn} \qquad , \tag{3.39}$$

which represents a set of linear equations, one for each value of n. The choice of the set of the basis $\{\phi_n\}$ is not unique. If we choose a set of orthonormal basis functions $\{\psi_n\}$ such that the non-vanishing term only occurs when $m = n$, this gives a simple equation

$$T\psi_n = T_{nn}\psi_n \equiv t_n\psi_n \tag{3.40}$$

where t_n is a scalar for every n. Any non-zero vector ψ_n which satisfies Equation (3.40) is called an *eigenvector* or *eigenfunction* of the operator T and t_n is the corresponding

eigenvalue. Equation (3.40) has a non-trivial solution if and only if

$$\det(T_{nn} - t_n) = 0 \qquad (3.41)$$

and this form of expression is referred to as the *eigenvalue problem* or sometimes called the *secular equation.* This is the form of the UV solution in Equation (3.12).

3.4.7   Procedure as used in this Thesis

Below is the systematic procedure used in this work and the steps are to be followed in this order.

1. Perform all symmetry operations of the crystallographic point group and construct a reducible character table (also called the reduction formula).

2. Decompose the reducible representations in step 1 into irreducible representations and identify the symmetries.

3. Define a set of unitary, orthogonal bases while omitting the normalisation constants.

4. Using the bases defined in step 3, apply the similarity transformation to block-diagonalise the matrix equations.

3.5   Perturbation Theory (PT)

The two-particle solution of the UV model obtained in Section (3.3.1) is exact, so we can, for example, calculate the eigenvalues and eigenfunctions in the ground state and extract some properties of the pair. Meanwhile, we sometimes want to gain quantitative information on the dynamics of the two-body problem when the the system is perturbed. For example, we may want to know how a bound pair moves in a lattice.

Perturbation theory (PT) is an effective tool that we can use to understand how a well-known system changes when it is slightly disturbed. Perturbative treatments can be applied both in the degenerate and non-degenerate situations. A dedicated chapter on perturbation theory in quantum mechanics with practical examples can be found in Sakurai and Napolitano [87]. In addition, many online resources (e.g. [88, 89]) can be found discussing perturbation theory. Here, we mainly discuss the degenerate Rayleigh-Schrödinger perturbation theory as it is used in this thesis. However, we will briefly talk about the non-degenerate case up to first order so as to make some remarks on the perturbation series when degeneracy is present.

Let us assume that a system with a known solution is described by the eigenequation

$$\hat{H}_0 \left|\psi_n^{(0)}\right\rangle = E_n^{(0)} \left|\psi_n^{(0)}\right\rangle \tag{3.42}$$

where $\hat{H}_0$ is the unperturbed Hamiltonian, $\psi_n^{(0)}$ is the unperturbed, discrete eigenstate, and $E_n^{(0)}$ is the corresponding eigenvalue (unperturbed energy). If we introduce an external perturbation described by a Hamiltonian $\epsilon H'$ to the physical system, then the (new) Hamiltonian describing the perturbed system is the sum of the contributing Hamiltonians

$$\hat{H} \equiv \hat{H}(\epsilon) = \hat{H}_0 + \epsilon \hat{H}' \qquad : \epsilon \ll 1 \tag{3.43}$$

where ϵ is the strength of the introduced perturbation. In addition to the new Hamiltonian $\hat{H}$, we have new eigenstates $\left|\psi_n\right\rangle_\epsilon$ such that

$$\hat{H} \left|\psi_n\right\rangle_\epsilon = E_n' \left|\psi_n\right\rangle_\epsilon \tag{3.44}$$

where

$$\left|\psi_n\right\rangle_\epsilon = \left|\psi_n^{(0)}\right\rangle + \left|\Delta\psi_n\right\rangle = \left|\psi_n^{(0)}\right\rangle + \epsilon \left|\psi_n^{(1)}\right\rangle + \epsilon^2 \left|\psi_n^{(2)}\right\rangle + \dots \tag{3.45}$$

$$E_n' \equiv E_n(\epsilon) = E_n^{(0)} + \Delta E_n = E_n^{(0)} + \epsilon E_n^{(1)} + \epsilon^2 E_n^{(2)} + \dots \tag{3.46}$$

$|\psi_n\rangle_\epsilon$ and E'_n are the eigenstate and the total energy, respectively, in the perturbed state.

Up to first-order in perturbation, the correction to energy and the corresponding eigenstate is respectively

$$E'_n = E_n^{(0)} + \epsilon \left\langle \psi_n^{(0)} \middle| \hat{H}' \middle| \psi_n^{(0)} \right\rangle + \mathcal{O}(\epsilon^2) \tag{3.47}$$

$$|\psi_n\rangle_\epsilon = \left| \psi_n^{(0)} \right\rangle + \epsilon \sum_{k \neq n} \frac{H'_{kn}}{E_n^{(0)} - E_k^{(0)}} \left| \psi_k^{(0)} \right\rangle + \mathcal{O}(\epsilon^2) \tag{3.48}$$

Remarks

1. The correction up to the first order Equation (3.47) for the ground state energy overestimates the true ground state energy due to the variational principle.

2. When there is (unlifted) degeneracy such that $E_n^{(0)} = E_k^{(0)}$, Equation (3.48) diverges and becomes unsolvable for those degenerate states. This is also true for higher-orders in the perturbation as they all contain energy differences in the denominator. To circumvent the divergence problem, we will consider the degenerate case.

3.5.1   Degenerate PT

The second remark above requires us to treat degenerate states specially. Suppose that $\hat{H}_0$ possesses N degenerate eigenstates $|\psi_r^{(0)}\rangle$ with eigenvalues $E_r^{(0)}$, where the subscript $r = 1, 2, 3, \ldots, N$. Having degeneracy adds another layer of complexity when treating a system perturbatively. Our primary aim will be to examine the effect of perturbation on the degenerate subspace of $\hat{H}_0$.

For this degenerate subspace, we have

$$|\psi_r\rangle_\epsilon = \left| \psi_r^{(0)} \right\rangle + \epsilon \left| \psi_r^{(1)} \right\rangle + \epsilon^2 \left| \psi_r^{(2)} \right\rangle + \ldots \tag{3.49}$$

$$E_r(\epsilon) = E_r^{(0)} + \epsilon E_r^{(1)} + \epsilon^2 E_r^{(2)} + \ldots \tag{3.50}$$

The implication of Equation (3.50) in particular is that the degeneracy becomes totally lifted to first-order if all $E_r^{(1)}$ are different for the new eigenstates. Sometimes, however, some of the states may still have the same energy and partial degeneracy is retained.

Then the Schrödinger equation due to the perturbation becomes

$$
\left[\hat{H}_0 + \epsilon \hat{H}'\right]\left[\left|\psi_r^{(0)}\right\rangle + \epsilon\left|\psi_r^{(1)}\right\rangle + \epsilon^2\left|\psi_r^{(2)}\right\rangle + \dots\right] =
$$
$$
\left[E_r^{(0)} + \epsilon E_r^{(1)} + \epsilon^2 E_r^{(2)} + \dots\right]\left[\left|\psi_r^{(0)}\right\rangle + \epsilon\left|\psi_r^{(1)}\right\rangle + \epsilon^2\left|\psi_r^{(2)}\right\rangle + \dots\right]
$$
(3.51)

First-order: ϵ^1

Up to first-order in Equation (3.51), we have

$$
\hat{H}_0\left|\psi_r^{(1)}\right\rangle + \hat{H}'\left|\psi_r^{(0)}\right\rangle = E_r^{(0)}\left|\psi_r^{(1)}\right\rangle + E_r^{(1)}\left|\psi_r^{(0)}\right\rangle
$$
$$
(\hat{H}_0 - E_r^{(0)})\left|\psi_r^{(1)}\right\rangle = (E_r^{(1)} - \hat{H}')\left|\psi_r^{(0)}\right\rangle
$$
(3.52)

To find the energy due to the perturbation, we define new basis sets which are linear superpositions of the degenerate eigenstates

$$
\left|\psi_r^{(0)}\right\rangle = \sum_{s=1}^{N}\left|\phi_s^{(0)}\right\rangle\left\langle\phi_s^{(0)}\middle|\psi_r^{(0)}\right\rangle = \sum_{s=1}^{N} C_{rs}\left|\phi_s^{(0)}\right\rangle
$$
(3.53)

$$
\left|\psi_r^{(1)}\right\rangle = \sum_{p=1}^{N} A_{rp}^{(1)}\left|\psi_p^{(0)}\right\rangle
$$
(3.54)

where C_{rs} and A_{rp} are unknown constants. From (3.52), we obtain

$$
\sum_{p=1}^{N} A_{rp}^{(1)}(\hat{H}_0 - E_r^{(0)})\left|\psi_p^{(0)}\right\rangle = \sum_{s=1}^{N} C_{rs}(E_r^{(1)} - \hat{H}')\left|\phi_s^{(0)}\right\rangle
$$
(3.55)

Taking the inner product of Equation (3.55) with $\left\langle\phi_u^{(0)}\right|$ for $u = 1, 2, 3, \dots, N$, the LHS vanishes, thus we have

$$
\sum_{s,u=1}^{N} C_{rs}\left\langle\phi_u^{(0)}\middle|(E_r^{(1)} - \hat{H}')\middle|\phi_s^{(0)}\right\rangle = 0 \qquad .
$$
(3.56)

The interpretation of this expression is that the perturbed Hamiltonian must be diagonal in the degenerate subspace by the choice of a "good" basis in Equation (3.53).

We also note that the energy correction to first order in both the non-degenerate and degenerate cases (i.e. Equations (3.47) and (3.56), respectively) look very similar (though they are not practically the same). The solution to Equation (3.56) is obtained by finding the determinant of the matrix

$$
\begin{vmatrix}
H'_{11} - E^{(1)} & H'_{12} & H'_{13} & \ldots & H'_{1N} \\
H'_{21} & H'_{22} - E^{(1)} & H'_{23} & \ldots & H'_{2N} \\
\vdots & \vdots & \vdots & \ddots & \vdots \\
H'_{N1} & H'_{N2} & H'_{N3} & \ldots & H'_{NN} - E^{(1)}
\end{vmatrix} = 0 \qquad (3.57)
$$

which has N roots (energy). If the roots are distinct, then the degeneracy is completely lifted. Degeneracy is partial or not lifted at all if some or all of the roots are equal.

Unlike in the non-degenerate case where the eigenstate to first-order is obtained easily (see Equation (3.48)), the first-order eigenstate correction in the degenerate case could have contributions both from within the degenerate subspace as well as from other states [87, 88]. We can find the component of $\left|\psi_r^{(1)}\right\rangle$ along other states $\left\langle\psi_q^{(0)}\right|$ (i.e. states outside the degenerate subspace and we will do that first) and within the degenerate subspace. For the first case, we perform the scalar product of Equation (3.55) with $\left\langle\psi_q^{(0)}\right|$. Doing this yields

$$
\left|\psi_r^{(1)}\right\rangle_{\notin \mathrm{deg}} = \sum_{q \neq r} \frac{\left\langle\psi_q^{(0)}\right| \hat{H} \left|\psi_r^{(0)}\right\rangle}{E_r^{(0)} - E_q^{(0)}} \left|\psi_q^{(0)}\right\rangle = \sum_{q \neq r} \frac{H_{qr}}{E_r^{(0)} - E_q^{(0)}} \left|\psi_q^{(0)}\right\rangle \qquad (3.58)
$$

The subscript "$\notin$ deg" implies that these are states outside the degenerate subspace. However, for components of these eigenstates within the degenerate subspace, we have to use the second-order expression and it turns out that if we perform the scalar product with $\left\langle\psi_l^{(0)}\right|$ for $l = 1, 2, 3, \ldots, N$, the eigenstate along the degenerate subspace $\left|\psi_r^{(1)}\right\rangle_{\in \mathrm{deg}}$ does not vanish only if the degeneracy is lifted to first order but vanishes if otherwise.

In the non-vanishing case, we obtain

$$\left|\psi_r^{(1)}\right\rangle_{\in\text{deg}} = \sum_{l\neq r} \frac{\left\langle\psi_l^{(0)}\right|\hat{H}\left|\psi_r^{(1)}\right\rangle_{\notin\text{deg}}}{E_l^{(0)} - E_r^{(0)}}\left|\psi_l^{(0)}\right\rangle \tag{3.59}$$

Similarly, we see that we will encounter divergence problem if degeneracy (i.e. $l = r$) still exists after first-order perturbation. Hence, Equation (3.59) is only useful when the degeneracy is completely lifted to first-order.

Second-order: ϵ^2

After some algebra, the energy to second-order correction has the form of Equation (3.56) and is given as

$$\sum_{s=1}^{N}(M_{us}^{(2)} - E_r^{(2)}\delta_{u,s})C_{rs} = 0 \tag{3.60}$$

where

$$M_{us}^{(2)} = \sum_{p\neq r}\frac{H_{up}H_{ps}}{E_r^{(0)} - E_p^{(0)}} \tag{3.61}$$

The second-order correction to energy $E_r^{(2)}$ is obtained by solving the determinant of the matrix equation (3.60). In general, second-order perturbation calculations are usually considered if degeneracy is not lifted by the first-order correction or in cases where first-order perturbation does not take the system to a state of interest. In this thesis, for example, we will be interested in finding the energy of a bound pair perturbatively. If to first-order the particles become unbound, we will go higher in perturbation. The calculations carried out in this thesis are limited to second-order.

3.6   Monte-Carlo Simulation

While analytic methods can give exact solutions, they can be cumbersome and laborious. Equally, not all problems are analytically solvable, and thus, sometimes, we have to rely on computational methods. In computational research, the term *Monte–Carlo* generally means stochastic simulations where new configurations of a system are suggested and generated randomly based on a set of rules. It involves starting with an initial configuration and a move is made to change to a different configuration. Based on an acceptance rule that ensures ergodicity, the new configuration is either accepted or rejected. If the move is rejected, another attempt will be made. This continues until a fixed number of updates has been made.

3.6.1   Continuous-time Quantum Monte-Carlo (CTQMC)

So far we have considered purely analytic methods (UV approximation and group theory analysis) that we will be using in our study. We note that the UV model, through the Lang-Firsov transformation, is an approximation that does not provide much, if any, information about the phonon degrees of freedom. It means that some inherent information about lattice vibrations could be lost.

Fortunately, the dynamics of the system resulting from the EPI can be investigated using a continuous-time quantum Monte-Carlo algorithm (CTQMC) [90]. The algorithm has been used extensively to study properties of polarons and bipolarons in 1D to 3D lattices [69, 71, 72, 73, 81, 91, 92, 93, 94] but not for bipolarons in the BCC and FCC lattices. In this thesis, I have used the algorithm to simulate properties of two fermions in BCC lattices and extended it for FCC lattices.

The CTQMC algorithm works using path integral formalism [95] whereby the path
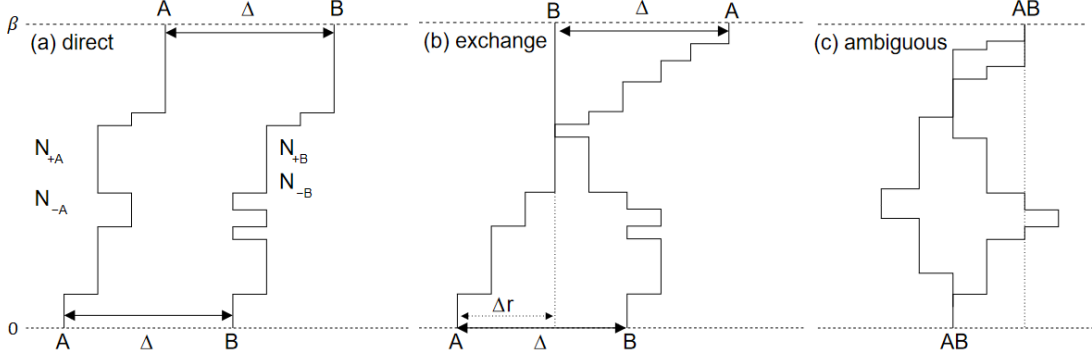
Figure 3.1: Illustration of two-electron paths in a 1D system after imaginary time evolution $0 \to \bar{\beta}$. (a) Paths do not cross each other. N_{+i} and N_{-i} are total kinks of a certain type on path i. The kinks are introduced by an acceptance rule. (b) An exchanged configuration where paths interact on a particular site and then particles continue to meander. (c) Paths end on the same site in an ambiguous configuration. (Reproduced from Ref. [71])

of a particle exists in imaginary time τ. Figure 3.1 shows an example of two-particle paths. The value of τ ranges between 0 and the inverse temperature $\bar{\beta} = 1/k_B T$. The partition function Z determines the number of accessible paths in a configuration. In quantum statistical problems, the partition function, which is independent of the choice of representation, can simply be written as the trace over the state space [96]

$$Z = \text{tr}\left[e^{-\bar{\beta}H}\right] = \sum_{\boldsymbol{R}} \langle \boldsymbol{R}|e^{-\bar{\beta}H}|\boldsymbol{R}\rangle \tag{3.62}$$

where $|\boldsymbol{R}\rangle$ represents a complete set of orthonormal basis states in real space. In path integral form, Z can be expressed as

$$Z = \int \mathcal{D}r e^{-A[r(\tau)]} \tag{3.63}$$

where $\mathcal{D}$ represents the integral over all the possible paths, and

$$A[r(\tau)] = \int_0^{\bar{\beta}} d\tau \mathcal{L}\left[r(\tau)\right] \tag{3.64}$$

is the phonon-induced action parameter which contains all the information about the path $r(\tau)$ via the Lagrangian $\mathcal{L}\left[r(\tau)\right]$ [97]. $\mathcal{L}$ describes all the interactions within the system, and, hence, information such as the hopping of a particle (represented by a kink)

can be understood during a path update. The bipolaron action used in this work has

the form [90]

$$A[r(\tau)] = A_0[r(\tau)] + A_{\Delta r}[r(\tau)] - V(r_1, r_2)$$

$$= \sum_{s=1}^{p} \sum_{n} \frac{\hbar}{4M_s\omega_s} \int_0^{\bar{\beta}} \int_0^{\bar{\beta}} d\tau_1 d\tau_2 \frac{\cosh \hbar\omega_s \left(\frac{\bar{\beta}}{2} - |\tau_1 - \tau_2|\right)}{\sinh \hbar\omega_s \frac{\bar{\beta}}{2}} F_{ns}(\tau_1) F_{ns}(\tau_2) \quad (3.65)$$

$$+ \sum_{s=1}^{p} \sum_{n} \frac{\hbar}{2M_s\omega_s} B_{ns} \left(C_{n+\Delta r,s} - C_{ns}\right) - \int_0^{\beta} V[r_1(\tau), r_2(\tau)] d\tau$$

where

$$B_{ns} \equiv \int_0^{\bar{\beta}} d\tau \frac{\sinh \hbar\omega_s \left(\bar{\beta} - \tau\right)}{\sinh \hbar\omega_s \bar{\beta}} F_{ns}(\tau) \quad , \tag{3.66}$$

$$C_{ns} \equiv \int_0^{\bar{\beta}} d\tau \frac{\sinh \hbar\omega_s \tau}{\sinh \hbar\omega_s \bar{\beta}} F_{ns}(\tau) \quad , \tag{3.67}$$

$$F_{ns}(\tau) = f_{ns}[r_1(\tau)] + f_{ns}[r_2(\tau)] \quad . \tag{3.68}$$

$F_{ns}(\tau)$ describes the total force (contributed by two particles) acting at the s-th oscillator

(with frequency ω_s and mass M_s) in the n-th unit cell at time τ. Also, $r_1(\tau)$ and $r_2(\tau)$

are the respective locations of the paths (i.e. particles) at time τ.

Note that in Equation (3.65), the first term $A_0[r(\tau)]$ corresponds to bipolaron action

under a periodic boundary condition in time such that $\xi_m(0) = \xi_m(\bar{\beta})$. The second term

$A_{\Delta r}[r(\tau)]$ corresponds to bipolaron action with a twisted boundary condition such that

$\xi_m(0) = \xi_{m+\Delta r}(\bar{\beta})$. The twisted boundary condition is needed for the estimation of the

pair mass [92]. $\Delta r = r(\bar{\beta}) - r(0)$ is the offset distance between the endpoints of the paths

in a non-exchange configuration, $V[r_1(\tau), r_2(\tau)]$ is an instantaneous Coulomb interaction

which can take the Hubbard form $V[r_1(\tau), r_2(\tau)] = U\delta_{r_1, r_2}$.

The estimators used to calculate the thermodynamic properties of bipolarons are

defined below [97]

1. **Total Energy:** The total ground state energy is given as

$$E_{\text{bip}} = -\lim_{\bar{\beta} \to \infty} \left[\left\langle \frac{\delta A}{\delta \bar{\beta}} \right\rangle + \frac{1}{\bar{\beta}} \left\langle \sum_i N_i \right\rangle \right] \tag{3.69}$$

2. **Number of Phonons:** The total number of excited phonons in the system can be estimated as

$$N_{\mathrm{ph}} = - \lim_{\bar{\beta} \to \infty} \frac{1}{\bar{\beta}} \left\langle \left. \frac{\delta A}{\delta \bar{\omega}} \right|_{\lambda \bar{\omega}} \right\rangle \tag{3.70}$$

3. **Bipolaron Mass:** We estimate the inverse mass using the relation

$$\frac{1}{m_{\mathrm{bip}}} = - \lim_{\bar{\beta} \to \infty} \frac{\langle (\Delta r_i)^2 \rangle}{\bar{\beta} \hbar^2} \tag{3.71}$$

4. **Bipolaron Radius:** The radius is calculated as

$$R_{\mathrm{bip}} = \left\langle \sqrt{\frac{1}{\bar{\beta}} \int_0^{\bar{\beta}} \Delta r_{12}(\tau)^2 \delta \tau} \right\rangle \tag{3.72}$$

All other parameters have their meanings and definitions declared in previous equations.

Other technical details on the CTQMC can be found in Appendix A.

To end this chapter, we give a summary of the bipolaron simulation.

1. The required parameters must be defined and fed into the algorithm. The code flags error(s) if any of these parameters are not properly set.

2. At the start, each particle has a straight path and a few kinks are randomly inserted into these paths.

3. As per the binary update rules (see Appendix A), kink (or anti-kink) insertion or removal is proposed. In addition to the existing updates used prior to the commencement of this work, I have introduced additional update rules which will be discussed in Chapter 7.

4. Accept or reject updates in step 3 based on the Metropolis acceptance algorithm.

5. After a warm-up period, calculate physical observables (such as the ground-state energy, average number of excited phonons, effective mass and bipolaron size) and estimate errors in measurements using the bootstrap re-sampling method.

6. Repeat steps 2–5 depending on a pre-determined number of measurements. More accurate results are obtained with increased simulation time.

End of Part I

This chapter completes Part I of this thesis. We believe we have set the stage to discuss our results in the next part (Part II). The solution to the UV model on BCC and FCC lattice is reported in Chapters 4 and 5, respectively, where we apply the symmetrised and anti-symmetrised solutions, group theory analysis and degenerate perturbation theory. In Chapter 6, we apply the (anti-)symmetrised UV solution after deriving an effective UV Hamiltonian for the fulleride compounds. The properties of bipolarons both on the BCC and FCC lattices from the CTQMC are reported in Chapter 7.

Part II

RESULTS AND DISCUSSIONS

Chapter 4

Superfluidity in BCC Optical

Lattices

4.1 Summary

We analytically study the properties of bound pairs in a BCC optical lattice using the UV model derived in Chapter 3. We begin this chapter with a preliminary discussion of how the UV model can be applied to fermions in a BCC lattice, then we obtained the self-consistent equations for the spin-singlet and spin-triplet states using the (anti-)symmetrisation method. Next, pair properties like the total energy, critical binding interaction, dispersion, effective mass, and effective radius are calculated in that order. The procedures for each calculation are discussed in detail. We also compute the BEC transition temperatures of fermion pairs in the ultra-cold regime and in the dilute limit. Finally, we end this chapter with a discussion of our findings.

4.2 Preliminaries

The coordination number in a BCC lattice is 8 as shown in Figure 4.1, thus there are nine possible configurations for onsite and intersite pairing in the unit cell. With a lattice constant b, the lattice vectors, including the central site, are $(0,0,0)$, $(\frac{b}{2}, \frac{b}{2}, \frac{b}{2})$, $(-\frac{b}{2}, \frac{b}{2}, \frac{b}{2})$, $(\frac{b}{2}, -\frac{b}{2}, \frac{b}{2})$, $(\frac{b}{2}, \frac{b}{2}, -\frac{b}{2})$, $(-\frac{b}{2}, -\frac{b}{2}, -\frac{b}{2})$, $(\frac{b}{2}, -\frac{b}{2}, -\frac{b}{2})$, $(-\frac{b}{2}, \frac{b}{2}, -\frac{b}{2})$, $(-\frac{b}{2}, -\frac{b}{2}, \frac{b}{2})$.
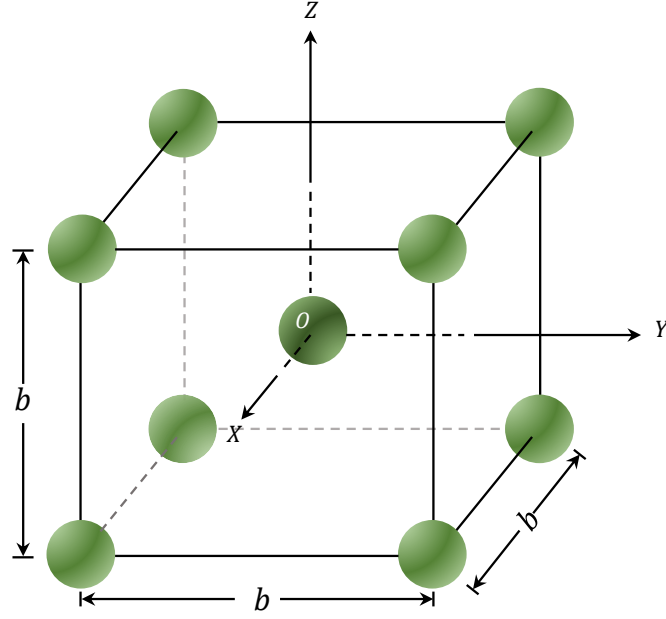
Figure 4.1: A BCC lattice showing the 8 nearest-neighbour sites.

We recall from Chapter 3 that the (anti-)symmetrised solution is

$$(E - \varepsilon_{\boldsymbol{k}_1} - \varepsilon_{\boldsymbol{k}_2})\phi^{\pm}_{\boldsymbol{k}_1 \boldsymbol{k}_2} = \frac{1}{N} \sum_{\boldsymbol{q}\boldsymbol{a}_\pm}' \hat{V}_{\boldsymbol{a}_\pm} \left\{ e^{i(\boldsymbol{q}-\boldsymbol{k}_1)\,\boldsymbol{a}_\pm} \pm e^{i(\boldsymbol{q}-\boldsymbol{k}_2)\,\boldsymbol{a}_\pm} \right\} \phi^{\pm}_{\boldsymbol{q},\boldsymbol{k}_1+\boldsymbol{k}_2-\boldsymbol{q}} \tag{4.1}$$

where $\phi^{+}_{\boldsymbol{q},\boldsymbol{k}_1+\boldsymbol{k}_2-\boldsymbol{q}}$ and $\phi^{-}_{\boldsymbol{q},\boldsymbol{k}_1+\boldsymbol{k}_2-\boldsymbol{q}}$ are respectively the singlet and triplet wavefunctions. The free-particle dispersion in a BCC lattice for negative hopping integral $(-t)$ between nearest-neighbour vectors $\boldsymbol{a}$ is

$$\varepsilon_{\boldsymbol{k}} = \sum_{\boldsymbol{a}} t\, e^{i\boldsymbol{k}\cdot\boldsymbol{a}} = -8t \cos\frac{k_x b}{2} \cos\frac{k_y b}{2} \cos\frac{k_z b}{2} \tag{4.2}$$

Next, we define vector sets $\{\boldsymbol{a}_+\}$ and $\{\boldsymbol{a}_-\}$, and then substitute them into Equation (4.1). By doing so, we will have (5×5) and (4×4) matrices for the singlets and triplet

states, respectively. The respective vectors may be chosen as *

$$\{\boldsymbol{a}_+\} = \{\boldsymbol{a}_0^+, \boldsymbol{a}_1^+, \boldsymbol{a}_2^+, \boldsymbol{a}_3^+, \boldsymbol{a}_4^+\} = \{(0,0,0), (\frac{b}{2}, \frac{b}{2}, \frac{b}{2}), (-\frac{b}{2}, \frac{b}{2}, \frac{b}{2}), (\frac{b}{2}, -\frac{b}{2}, \frac{b}{2}), (\frac{b}{2}, \frac{b}{2}, -\frac{b}{2})\}$$

(4.3)

$$\{\boldsymbol{a}_-\} = \{\boldsymbol{a}_1^-, \boldsymbol{a}_2^-, \boldsymbol{a}_3^-, \boldsymbol{a}_4^-\} = \{(\frac{b}{2}, \frac{b}{2}, \frac{b}{2}), (-\frac{b}{2}, \frac{b}{2}, \frac{b}{2}), (\frac{b}{2}, -\frac{b}{2}, \frac{b}{2}), (\frac{b}{2}, \frac{b}{2}, -\frac{b}{2})\} \qquad (4.4)$$

We now proceed with finding the separate solutions to the singlet and triplet states. Note that when we say singlet or triplet states we are referring to spin-singlet and spin-triplet states.

4.2.1 Solution for Singlets

For the singlets, we use the vectors $\{\boldsymbol{a}_+\}$ in Equation (4.1). Doing this we have †

$$
\begin{aligned}
(E - \varepsilon_{\boldsymbol{k}_1} - \varepsilon_{\boldsymbol{k}_2})\phi_{\boldsymbol{k}_1\boldsymbol{k}_2}^+ =& \frac{1}{N}\sum_{\boldsymbol{q}} \Bigg[\frac{1}{2}U(e^{i(\boldsymbol{q}-\boldsymbol{k}_1)\boldsymbol{a}_0^+} + e^{i(\boldsymbol{q}-\boldsymbol{k}_2)\boldsymbol{a}_0^+}) + V(e^{i(\boldsymbol{q}-\boldsymbol{k}_1)\boldsymbol{a}_1^+} + e^{i(\boldsymbol{q}-\boldsymbol{k}_2)\boldsymbol{a}_1^+}) \\
& + V(e^{i(\boldsymbol{q}-\boldsymbol{k}_1)\boldsymbol{a}_2^+} + e^{i(\boldsymbol{q}-\boldsymbol{k}_2)\boldsymbol{a}_2^+}) + V(e^{i(\boldsymbol{q}-\boldsymbol{k}_1)\boldsymbol{a}_3^+} + e^{i(\boldsymbol{q}-\boldsymbol{k}_2)\boldsymbol{a}_3^+}) \\
& + V(e^{i(\boldsymbol{q}-\boldsymbol{k}_1)\boldsymbol{a}_4^+} + e^{i(\boldsymbol{q}-\boldsymbol{k}_2)\boldsymbol{a}_4^+}) \Bigg] \phi_{\boldsymbol{q},\boldsymbol{k}_1+\boldsymbol{k}_2-\boldsymbol{q}}^+ \\
=& \frac{1}{N}\sum_{\boldsymbol{q}} \Bigg[U + V\, e^{i(\frac{q_x}{2}+\frac{q_y}{2}+\frac{q_z}{2})}(e^{-i\boldsymbol{k}_1\boldsymbol{a}_1^+} + e^{-i\boldsymbol{k}_2\boldsymbol{a}_1^+}) \\
& + V\, e^{i(\frac{-q_x}{2}+\frac{q_y}{2}+\frac{q_z}{2})}(e^{-i\boldsymbol{k}_1\boldsymbol{a}_2^+} + e^{-i\boldsymbol{k}_2\boldsymbol{a}_2^+}) \\
& + V\, e^{i(\frac{q_x}{2}-\frac{q_y}{2}+\frac{q_z}{2})}(e^{-i\boldsymbol{k}_1\boldsymbol{a}_3^+} + e^{-i\boldsymbol{k}_2\boldsymbol{a}_3^+}) \\
& + V\, e^{i(\frac{q_x}{2}+\frac{q_y}{2}-\frac{q_z}{2})}(e^{-i\boldsymbol{k}_1\boldsymbol{a}_4^+} + e^{-i\boldsymbol{k}_2\boldsymbol{a}_4^+}) \Bigg] \phi_{\boldsymbol{q},\boldsymbol{k}_1+\boldsymbol{k}_2-\boldsymbol{q}}^+
\end{aligned}
$$

(4.5)

---

*We ensure that no set of vectors is related by inversion and that $\boldsymbol{a}_0^+$ belongs to the singlets.
†Reminder that $\boldsymbol{a}_+ = \boldsymbol{0}$ term must be multiplied by $\frac{1}{2}$ to account for double occupancy.

We can then represent some basis functions as follows:

$$\Phi_0^+(\boldsymbol{P}) = \frac{1}{N}\sum_{\boldsymbol{q}} \phi_{\boldsymbol{q},\boldsymbol{P}-\boldsymbol{q}}^+ \quad , \qquad\qquad \Phi_1^+(\boldsymbol{P}) = \frac{1}{N}\sum_{\boldsymbol{q}} e^{i(\frac{q_x}{2}+\frac{q_y}{2}+\frac{q_z}{2})}\,\phi_{\boldsymbol{q},\boldsymbol{P}-\boldsymbol{q}}^+$$

$$\Phi_2^+(\boldsymbol{P}) = \frac{1}{N}\sum_{\boldsymbol{q}} e^{i(\frac{-q_x}{2}+\frac{q_y}{2}+\frac{q_z}{2})}\,\phi_{\boldsymbol{q},\boldsymbol{P}-\boldsymbol{q}}^+ \quad , \quad \Phi_3^+(\boldsymbol{P}) = \frac{1}{N}\sum_{\boldsymbol{q}} e^{i(\frac{q_x}{2}-\frac{q_y}{2}+\frac{q_z}{2})}\,\phi_{\boldsymbol{q},\boldsymbol{P}-\boldsymbol{q}}^+ \quad (4.6)$$

$$\Phi_4^+(\boldsymbol{P}) = \frac{1}{N}\sum_{\boldsymbol{q}} e^{i(\frac{q_x}{2}+\frac{q_y}{2}-\frac{q_z}{2})}\,\phi_{\boldsymbol{q},\boldsymbol{P}-\boldsymbol{q}}^+$$

where $\boldsymbol{P} = \boldsymbol{k}_1 + \boldsymbol{k}_2$. Hence, Equation (4.5) can be written in a more generalised form

$$\phi_{\boldsymbol{k}_1\boldsymbol{k}_2}^+ = \frac{1}{(E-\varepsilon_{\boldsymbol{k}_1}-\varepsilon_{\boldsymbol{k}_2})}\Big\{ U\Phi_0^+(\boldsymbol{P}) + V\,\Phi_1^+(\boldsymbol{P})(e^{-i\boldsymbol{k}_1\boldsymbol{a}_1^+} + e^{-i\boldsymbol{k}_2\boldsymbol{a}_1^+})$$

$$+ V\,\Phi_2^+(\boldsymbol{P})(e^{-i\boldsymbol{k}_1\boldsymbol{a}_2^+} + e^{-i\boldsymbol{k}_2\boldsymbol{a}_2^+}) + V\,\Phi_3^+(\boldsymbol{P})(e^{-i\boldsymbol{k}_1\boldsymbol{a}_3^+} + e^{-i\boldsymbol{k}_2\boldsymbol{a}_3^+}) \qquad (4.7)$$

$$+ V\,\Phi_4^+(\boldsymbol{P})(e^{-i\boldsymbol{k}_1\boldsymbol{a}_4^+} + e^{-i\boldsymbol{k}_2\boldsymbol{a}_4^+}) \Big\}$$

We apply Equation (4.7) to each basis function $\Phi_0^+(\boldsymbol{P})$, $\Phi_1^+(\boldsymbol{P})$, $\Phi_2^+(\boldsymbol{P})$, $\Phi_3^+(\boldsymbol{P})$, $\Phi_4^+(\boldsymbol{P})$ and replace the variable q_j as: $q_j = q_j' + \frac{P_j}{2}$. A simple substitution would yield five equations for $\Phi_i^+(\boldsymbol{P})$: $i = 0, 1, 2, 3, 4$.

$$\Phi_0^+(\boldsymbol{P}) = \frac{1}{N}\sum_{\boldsymbol{q}'} \frac{1}{E - \varepsilon_{\frac{\boldsymbol{P}}{2}+\boldsymbol{q}'} - \varepsilon_{\frac{\boldsymbol{P}}{2}-\boldsymbol{q}'}}\Big\{ U\Phi_0^+(\boldsymbol{P})$$

$$+ V\Phi_1^+(\boldsymbol{P})\,e^{-i(\frac{P_x}{4}+\frac{P_y}{4}+\frac{P_z}{4})}\Big[e^{i(\frac{q_x'}{2}+\frac{q_y'}{2}+\frac{q_z'}{2})} + e^{-i(\frac{q_x'}{2}+\frac{q_y'}{2}+\frac{q_z'}{2})}\Big]$$

$$+ V\Phi_2^+(\boldsymbol{P})\,e^{i(\frac{P_x}{4}-\frac{P_y}{4}-\frac{P_z}{4})}\Big[e^{i(\frac{q_x'}{2}-\frac{q_y'}{2}-\frac{q_z'}{2})} + e^{-i(\frac{q_x'}{2}-\frac{q_y'}{2}-\frac{q_z'}{2})}\Big] \qquad (4.8)$$

$$+ V\Phi_3^+(\boldsymbol{P})\,e^{-i(\frac{P_x}{4}-\frac{P_y}{4}+\frac{P_z}{4})}\Big[e^{i(\frac{q_x'}{2}-\frac{q_y'}{2}+\frac{q_z'}{2})} + e^{-i(\frac{q_x'}{2}-\frac{q_y'}{2}+\frac{q_z'}{2})}\Big]$$

$$+ V\Phi_4^+(\boldsymbol{P})\,e^{-i(\frac{P_x}{4}+\frac{P_y}{4}-\frac{P_z}{4})}\Big[e^{i(\frac{q_x'}{2}+\frac{q_y'}{2}-\frac{q_z'}{2})} + e^{-i(\frac{q_x'}{2}+\frac{q_y'}{2}-\frac{q_z'}{2})}\Big] \Big\}$$

$$\Phi_1^+(\boldsymbol{P}) = \frac{1}{N}\sum_{\boldsymbol{q}'} \frac{1}{E - \varepsilon_{\frac{\boldsymbol{P}}{2}+\boldsymbol{q}'} - \varepsilon_{\frac{\boldsymbol{P}}{2}-\boldsymbol{q}'}}\Big\{ U\Phi_0^+(\boldsymbol{P})\,e^{i(\frac{P_x}{4}+\frac{P_y}{4}+\frac{P_z}{4})}e^{i(\frac{q_x'}{2}+\frac{q_y'}{2}+\frac{q_z'}{2})}$$

$$+ V\Phi_1^+(\boldsymbol{P})\Big[1 + e^{2i(\frac{q_x'}{2}+\frac{q_y'}{2}+\frac{q_z'}{2})}\Big] + V\Phi_2^+(\boldsymbol{P})e^{i\frac{P_x}{2}}\Big[e^{2i(\frac{q_x'}{2})} + e^{2i(\frac{q_y'}{2}+\frac{q_z'}{2})}\Big]$$

$$+ V\Phi_3^+(\boldsymbol{P})e^{i\frac{P_y}{2}}\Big[e^{2i(\frac{q_y'}{2})} + e^{2i(\frac{q_x'}{2}+\frac{q_z'}{2})}\Big] + V\Phi_4^+(\boldsymbol{P})e^{i\frac{P_z}{2}}\Big[e^{2i(\frac{q_z'}{2})} + e^{2i(\frac{q_x'}{2}+\frac{q_y'}{2})}\Big] \Big\}$$

$$(4.9)$$

$$\Phi_2^+(\boldsymbol{P}) = \frac{1}{N}\sum_{\boldsymbol{q}'}\frac{1}{E - \varepsilon_{\frac{\boldsymbol{P}}{2}+\boldsymbol{q}'} - \varepsilon_{\frac{\boldsymbol{P}}{2}-\boldsymbol{q}'}}\left\{U\Phi_0^+(\boldsymbol{P})\,e^{-i(\frac{P_x}{4}-\frac{P_y}{4}-\frac{P_z}{4})}\,e^{-i(\frac{q_x'}{2}-\frac{q_y'}{2}-\frac{q_z'}{2})}\right.$$

$$+ V\Phi_1^+(\boldsymbol{P})\,e^{-i\frac{P_x}{2}}\left[e^{-2i(\frac{q_x'}{2})} + e^{2i(\frac{q_y'}{2}+\frac{q_z'}{2})}\right] + V\Phi_2^+(\boldsymbol{P})\left[1 + e^{-2i(\frac{q_x'}{2}-\frac{q_y'}{2}-\frac{q_z'}{2})}\right]$$

$$+ V\Phi_3^+(\boldsymbol{P})\,e^{-i(\frac{P_x}{2}-\frac{P_y}{2})}\left[e^{-2i(\frac{q_x'}{2}-\frac{q_y'}{2})} + e^{2i(\frac{q_z'}{2})}\right]$$

$$\left.+ V\Phi_4^+(\boldsymbol{P})\,e^{-i(\frac{P_x}{2}-\frac{P_z}{2})}\left[e^{-2i(\frac{q_x'}{2}-\frac{q_z'}{2})} + e^{2i(\frac{q_y'}{2})}\right]\right\}$$

(4.10)

$$\Phi_3^+(\boldsymbol{P}) = \frac{1}{N}\sum_{\boldsymbol{q}'}\frac{1}{E - \varepsilon_{\frac{\boldsymbol{P}}{2}+\boldsymbol{q}'} - \varepsilon_{\frac{\boldsymbol{P}}{2}-\boldsymbol{q}'}}\left\{U\Phi_0^+(\boldsymbol{P})\,e^{i(\frac{P_x}{4}-\frac{P_y}{4}+\frac{P_z}{4})}\,e^{i(\frac{q_x'}{2}-\frac{q_y'}{2}+\frac{q_z'}{2})}\right.$$

$$+ V\Phi_1^+(\boldsymbol{P})\,e^{-i\frac{P_y}{2}}\left[e^{-2i(\frac{q_y'}{2})} + e^{2i(\frac{\mathbf{q_x'}}{2}+\frac{\mathbf{q_z'}}{2})}\right] + V\Phi_2^+(\boldsymbol{P})\,e^{i(\frac{P_x}{2}-\frac{P_y}{2})}\left[e^{2i(\frac{q_x'}{2}-\frac{q_y'}{2})} + e^{2i(\frac{q_z'}{2})}\right]$$

$$\left.+ V\Phi_3^+(\boldsymbol{P})\left[1 + e^{2i(\frac{q_x'}{2}-\frac{q_y'}{2}+\frac{q_z'}{2})}\right] + V\Phi_4^+(\boldsymbol{P})\,e^{-i(\frac{P_y}{2}-\frac{P_z}{2})}\left[e^{-2i(\frac{q_y'}{2}-\frac{q_z'}{2})} + e^{2i(\frac{q_x'}{2})}\right]\right\}$$

(4.11)

$$\Phi_4^+(\boldsymbol{P}) = \frac{1}{N}\sum_{\boldsymbol{q}'}\frac{1}{E - \varepsilon_{\frac{\boldsymbol{P}}{2}+\boldsymbol{q}'} - \varepsilon_{\frac{\boldsymbol{P}}{2}-\boldsymbol{q}'}}\left\{U\Phi_0^+(\boldsymbol{P})\,e^{i(\frac{P_x}{4}+\frac{P_y}{4}-\frac{P_z}{4})}\,e^{i(\frac{q_x'}{2}+\frac{q_y'}{2}-\frac{q_z'}{2})}\right.$$

$$+ V\Phi_1^+(\boldsymbol{P})\,e^{-i\frac{P_z}{2}}\left[e^{-2i(\frac{q_z'}{2})} + e^{2i(\frac{q_x'}{2}+\frac{q_y'}{2})}\right] + V\Phi_2^+(\boldsymbol{P})\,e^{i(\frac{P_x}{2}-\frac{P_z}{2})}\left[e^{2i(\frac{q_x'}{2}-\frac{q_z'}{2})} + e^{2i(\frac{q_y'}{2})}\right]$$

$$\left.+ V\Phi_3^+(\boldsymbol{P})e^{i(\frac{P_y}{2}-\frac{P_z}{2})}\left[e^{2i(\frac{\mathbf{q_y'}}{2}-\frac{\mathbf{q_z'}}{2})} + e^{2i(\frac{\mathbf{q_x'}}{2})}\right] + V\Phi_4^+(\boldsymbol{P})\left[1 + e^{2i(\frac{q_x'}{2}+\frac{q_y'}{2}-\frac{q_z'}{2})}\right]\right\}$$

(4.12)

Each of these equations (4.8)–(4.12) can be re-written in a simple form. For example,

$$\tilde{\Phi}_0^+(\boldsymbol{P}) = U\mathcal{G}_{(0,0,0)}(\boldsymbol{P})\tilde{\Phi}_0^+(\boldsymbol{P}) + V\left[\mathcal{G}_{(1,1,1)}(\boldsymbol{P}) + \mathcal{G}_{(\bar{1},\bar{1},\bar{1})}(\boldsymbol{P})\right]\tilde{\Phi}_1^+(\boldsymbol{P})$$

$$+ V\left[\mathcal{G}_{(1,\bar{1},\bar{1})}(\boldsymbol{P}) + \mathcal{G}_{(\bar{1},1,1)}(\boldsymbol{P})\right]\tilde{\Phi}_2^+(\boldsymbol{P}) + V\left[\mathcal{G}_{(1,\bar{1},1)}(\boldsymbol{P}) + \mathcal{G}_{(\bar{1},1,\bar{1})}(\boldsymbol{P})\right]\tilde{\Phi}_3^+(\boldsymbol{P})$$

$$+ \left[\mathcal{G}_{(1,1,\bar{1})}(\boldsymbol{P}) + \mathcal{G}_{(\bar{1},\bar{1},1)}(\boldsymbol{P})\right]\tilde{\Phi}_4^+(\boldsymbol{P})$$

(4.13)

where a new function $\tilde{\Phi}_i^+(\boldsymbol{P}) = e^{\frac{-i}{2}(\boldsymbol{P}\boldsymbol{a}_i^+)}\Phi_i^+$ (where $i = 0, 1, 2, 3, 4$) containing a phase factor that describes the centre-of-mass motion of the pair has been introduced. In

addition, $\mathcal{G}$ is the momentum-dependent Green's function defined as

$$\mathcal{G}_{(l,m,n)}(\boldsymbol{P}) = \frac{1}{N} \sum_{\boldsymbol{q}'} \frac{e^{i(l\frac{q'_x}{2} + m\frac{q'_y}{2} + n\frac{q'_z}{2})}}{E - \varepsilon_{\frac{P}{2}+\boldsymbol{q}'} - \varepsilon_{\frac{P}{2}-\boldsymbol{q}'}}$$

$$= -\int_{-2\pi}^{2\pi}\int_{-2\pi}^{2\pi}\int_{-2\pi}^{2\pi} \frac{dq'_x dq'_y dq'_z}{(4\pi)^3} \frac{\cos\left(l\frac{q'_x}{2} + m\frac{q'_y}{2} + n\frac{q'_z}{2}\right)}{|E| + \varepsilon_{\frac{P}{2}+\boldsymbol{q}'} + \varepsilon_{\frac{P}{2}-\boldsymbol{q}'}}$$

(4.14)

where l, m, and n are integers $\in [0 \pm 1 \pm 2]$. We will place a bar above a negative integer subscript for compactness. For instance, $\mathcal{G}_{(1,-1,-1)} \equiv \mathcal{G}_{1\bar{1}\bar{1}}$; $\mathcal{G}_{(-2,0,2)} \equiv \mathcal{G}_{\bar{2}02}$. Finally, we combine all these equations to form a (5×5) matrix equation for the spin-singlets at arbitrary pair momentum as:

$$\begin{bmatrix} U\mathcal{G}_{000} & V(\mathcal{G}_{111} + \mathcal{G}_{\bar{1}\bar{1}\bar{1}}) & V(\mathcal{G}_{\bar{1}11} + \mathcal{G}_{1\bar{1}\bar{1}}) & V(\mathcal{G}_{1\bar{1}1} + \mathcal{G}_{\bar{1}1\bar{1}}) & V(\mathcal{G}_{11\bar{1}} + \mathcal{G}_{\bar{1}\bar{1}1}) \\ U\mathcal{G}_{111} & V(\mathcal{G}_{000} + \mathcal{G}_{222}) & V(\mathcal{G}_{200} + \mathcal{G}_{022}) & V(\mathcal{G}_{020} + \mathcal{G}_{202}) & V(\mathcal{G}_{002} + \mathcal{G}_{220}) \\ U\mathcal{G}_{\bar{1}11} & V(\mathcal{G}_{\bar{2}00} + \mathcal{G}_{022}) & V(\mathcal{G}_{000} + \mathcal{G}_{\bar{2}22}) & V(\mathcal{G}_{\bar{2}20} + \mathcal{G}_{002}) & V(\mathcal{G}_{\bar{2}02} + \mathcal{G}_{020}) \\ U\mathcal{G}_{1\bar{1}1} & V(\mathcal{G}_{0\bar{2}0} + \mathcal{G}_{202}) & V(\mathcal{G}_{2\bar{2}0} + \mathcal{G}_{002}) & V(\mathcal{G}_{000} + \mathcal{G}_{2\bar{2}2}) & V(\mathcal{G}_{0\bar{2}2} + \mathcal{G}_{200}) \\ U\mathcal{G}_{11\bar{1}} & V(\mathcal{G}_{00\bar{2}} + \mathcal{G}_{220}) & V(\mathcal{G}_{20\bar{2}} + \mathcal{G}_{020}) & V(\mathcal{G}_{02\bar{2}} + \mathcal{G}_{200}) & V(\mathcal{G}_{000} + \mathcal{G}_{22\bar{2}}) \end{bmatrix} \begin{bmatrix} \tilde{\Phi}_0^+ \\ \tilde{\Phi}_1^+ \\ \tilde{\Phi}_2^+ \\ \tilde{\Phi}_3^+ \\ \tilde{\Phi}_4^+ \end{bmatrix} = \begin{bmatrix} \tilde{\Phi}_0^+ \\ \tilde{\Phi}_1^+ \\ \tilde{\Phi}_2^+ \\ \tilde{\Phi}_3^+ \\ \tilde{\Phi}_4^+ \end{bmatrix}$$

(4.15)

4.2.2   Solution for Triplets

Using $\{\mathbf{a}_-\}$ in Equation (4.1), the anti-symmetrised equation is

$$
(E - \varepsilon_{\mathbf{k}_1} - \varepsilon_{\mathbf{k}_2})\phi^-_{\mathbf{k}_1\mathbf{k}_2} = \frac{1}{N}\sum_{\mathbf{q}}\Bigg[V\,e^{i(\frac{q_x}{2}+\frac{q_y}{2}+\frac{q_z}{2})}\big(e^{-i\mathbf{k}_1\mathbf{a}_1^-} - e^{-i\mathbf{k}_2\mathbf{a}_1^-}\big)
$$
$$
+ V\,e^{i(\frac{-q_x}{2}+\frac{q_y}{2}+\frac{q_z}{2})}\big(e^{-i\mathbf{k}_1\mathbf{a}_2^-} - e^{-i\mathbf{k}_2\mathbf{a}_2^-}\big)
$$
$$
+ V\,e^{i(\frac{q_x}{2}-\frac{q_y}{2}+\frac{q_z}{2})}\big(e^{-i\mathbf{k}_1\mathbf{a}_3^-} - e^{-i\mathbf{k}_2\mathbf{a}_3^-}\big)
$$
$$
+ V\,e^{i(\frac{q_x}{2}+\frac{q_y}{2}-\frac{q_z}{2})}\big(e^{-i\mathbf{k}_1\mathbf{a}_4^-} - e^{-i\mathbf{k}_2\mathbf{a}_4^-}\big)\Bigg]\phi^-_{\mathbf{q},\mathbf{k}_1+\mathbf{k}_2-\mathbf{q}}
\tag{4.16}
$$

Our spin-triplet basis functions are obtained similarly to the singlet case as:

$$
\Phi^-_1(\mathbf{P}) = \frac{1}{N}\sum_{\mathbf{q}} e^{i(\frac{q_x}{2}+\frac{q_y}{2}+\frac{q_z}{2})}\,\phi^-_{\mathbf{q},\mathbf{P}-\mathbf{q}} \quad,\quad \Phi^-_2(\mathbf{P}) = \frac{1}{N}\sum_{\mathbf{q}} e^{i(\frac{-q_x}{2}+\frac{q_y}{2}+\frac{q_z}{2})}\,\phi^-_{\mathbf{q},\mathbf{P}-\mathbf{q}}
$$
$$
\Phi^-_3(\mathbf{P}) = \frac{1}{N}\sum_{\mathbf{q}} e^{i(\frac{q_x}{2}-\frac{q_y}{2}+\frac{q_z}{2})}\,\phi^-_{\mathbf{q},\mathbf{P}-\mathbf{q}} \quad,\quad \Phi^-_4(\mathbf{P}) = \frac{1}{N}\sum_{\mathbf{q}} e^{i(\frac{q_x}{2}+\frac{q_y}{2}-\frac{q_z}{2})}\,\phi^-_{\mathbf{q},\mathbf{P}-\mathbf{q}}
\tag{4.17}
$$

Going through a procedure similar to the spin-singlets, the set of self-consistent equations for the triplets are

$$
\Phi^-_1(\mathbf{P}) = \frac{1}{N}\sum_{\mathbf{q}'}\frac{1}{E - \varepsilon_{\frac{\mathbf{P}}{2}+\mathbf{q}'} - \varepsilon_{\frac{\mathbf{P}}{2}-\mathbf{q}'}}\Bigg\{ V\Phi^-_1(\mathbf{P})\Big[1 - e^{2i(\frac{q'_x}{2}+\frac{q'_y}{2}+\frac{q'_z}{2})}\Big]
$$
$$
+ V\Phi^-_2(\mathbf{P})\,e^{2i(\frac{P_x}{4})}\Big[e^{2i(\frac{q'_x}{2})} - e^{2i(\frac{q'_y}{2}+\frac{q'_z}{2})}\Big] + V\Phi^-_3(\mathbf{P})\,e^{2i(\frac{P_y}{4})}\Big[e^{2i(\frac{q'_y}{2})} - e^{2i(\frac{q'_x}{2}+\frac{q'_z}{2})}\Big]
$$
$$
+ V\Phi^-_4(\mathbf{P})\,e^{2i(\frac{P_z}{4})}\Big[e^{2i(\frac{q'_z}{2})} - e^{2i(\frac{q'_x}{2}+\frac{q'_y}{2})}\Big]\Bigg\}
$$
$$
= V\Phi^-_1(\mathbf{P})\Big[\mathcal{G}_{000} - \mathcal{G}_{222}\Big] + V\Phi^-_2(\mathbf{P})\,e^{i\frac{P_x}{2}}\Big[\mathcal{G}_{200} - \mathcal{G}_{022}\Big]
$$
$$
+ V\Phi^-_3(\mathbf{P})\,e^{i\frac{P_y}{2}}\Big[\mathcal{G}_{020} - \mathcal{G}_{202}\Big] + V\Phi^-_4(\mathbf{P})\,e^{i\frac{P_z}{2}}\Big[\mathcal{G}_{002} - \mathcal{G}_{220}\Big]
\tag{4.18}
$$

$$
\Phi^-_2(\mathbf{P}) = V\Phi^-_1(\mathbf{P})\,e^{-i\frac{P_x}{2}}\Big[\mathcal{G}_{\bar{2}00} - \mathcal{G}_{022}\Big] + V\Phi^-_2(\mathbf{P})\Big[\mathcal{G}_{000} - \mathcal{G}_{\bar{2}22}\Big]
$$
$$
+ V\Phi^-_3(\mathbf{P})\,e^{-i(\frac{P_x}{2}-\frac{P_y}{2})}\Big[\mathcal{G}_{\bar{2}20} - \mathcal{G}_{002}\Big] + V\Phi^-_4(\mathbf{P})\,e^{-i(\frac{P_x}{2}-\frac{P_z}{2})}\Big[\mathcal{G}_{\bar{2}02} - \mathcal{G}_{020}\Big]
\tag{4.19}
$$

$$
\Phi^-_3(\mathbf{P}) = V\Phi^-_1(\mathbf{P})\,e^{-i\frac{P_y}{2}}\Big[\mathcal{G}_{0\bar{2}0} - \mathcal{G}_{202}\Big] + V\Phi^-_2(\mathbf{P})\,e^{i(\frac{P_x}{2}-\frac{P_y}{2})}\Big[\mathcal{G}_{2\bar{2}0} - \mathcal{G}_{002}\Big]
$$
$$
+ V\Phi^-_3(\mathbf{P})\Big[\mathcal{G}_{000} - \mathcal{G}_{2\bar{2}2}\Big] + V\Phi^+_4(\mathbf{P})\,e^{-i(\frac{P_y}{2}+\frac{P_z}{2})}\Big[\mathcal{G}_{0\bar{2}2} - \mathcal{G}_{200}\Big]
\tag{4.20}
$$

$$\Phi_4^-(\boldsymbol{P}) = V\Phi_1^-(\boldsymbol{P})\, e^{-i\frac{P_z}{2}}\Big[\mathcal{G}_{00\bar{2}} - \mathcal{G}_{220}\Big] + V\Phi_2^-(\boldsymbol{P})\, e^{i(\frac{P_x}{2}-\frac{P_z}{2})}\Big[\mathcal{G}_{20\bar{2}} - \mathcal{G}_{020}\Big]$$
$$+ V\Phi_3^-(\boldsymbol{P})e^{i(\frac{P_y}{2}-\frac{P_z}{2})}\Big[\mathcal{G}_{02\bar{2}} - \mathcal{G}_{200}\Big] + V\Phi_4^-(\boldsymbol{P})\Big[\mathcal{G}_{000} - \mathcal{G}_{22\bar{2}}\Big]$$

(4.21)

We also re-write the triplet equations above to contain the centre-of-mass motion as we did for the singlets. For example, Equation (4.18) becomes

$$\tilde{\Phi}_1^-(\boldsymbol{P}) = V\Big[\mathcal{G}_{000} - \mathcal{G}_{222}\Big]\tilde{\Phi}_1^-(\boldsymbol{P}) + V\Big[\mathcal{G}_{200} - \mathcal{G}_{022}\Big]\tilde{\Phi}_2^-(\boldsymbol{P})$$
$$+ V\Big[\mathcal{G}_{020} - \mathcal{G}_{202}\Big]\tilde{\Phi}_3^-(\boldsymbol{P}) + V\Big[\mathcal{G}_{002} - \mathcal{G}_{220}\Big]\tilde{\Phi}_4^-(\boldsymbol{P})$$

(4.22)

The matrix equation for the spin-triplet at arbitrary momentum is thus:

$$\begin{bmatrix} V(\mathcal{G}_{000} - \mathcal{G}_{222}) & V(\mathcal{G}_{200} - \mathcal{G}_{022}) & V(\mathcal{G}_{020} - \mathcal{G}_{202}) & V(\mathcal{G}_{002} - \mathcal{G}_{220}) \\ V(\mathcal{G}_{\bar{2}00} - \mathcal{G}_{022}) & V(\mathcal{G}_{000} - \mathcal{G}_{\bar{2}22}) & V(\mathcal{G}_{\bar{2}20} - \mathcal{G}_{002}) & V(\mathcal{G}_{\bar{2}02} - \mathcal{G}_{020}) \\ V(\mathcal{G}_{0\bar{2}0} - \mathcal{G}_{202}) & V(\mathcal{G}_{2\bar{2}0} - \mathcal{G}_{002}) & V(\mathcal{G}_{000} - \mathcal{G}_{2\bar{2}2}) & V(\mathcal{G}_{0\bar{2}2} - \mathcal{G}_{200}) \\ V(\mathcal{G}_{00\bar{2}} - \mathcal{G}_{220}) & V(\mathcal{G}_{20\bar{2}} - \mathcal{G}_{020}) & V(\mathcal{G}_{02\bar{2}} - \mathcal{G}_{200}) & V(\mathcal{G}_{000} - \mathcal{G}_{22\bar{2}}) \end{bmatrix} \begin{bmatrix} \tilde{\Phi}_1^- \\ \tilde{\Phi}_2^- \\ \tilde{\Phi}_3^- \\ \tilde{\Phi}_4^- \end{bmatrix} = \begin{bmatrix} \tilde{\Phi}_1^- \\ \tilde{\Phi}_2^- \\ \tilde{\Phi}_3^- \\ \tilde{\Phi}_4^- \end{bmatrix}$$

(4.23)

and the Green's function $\mathcal{G}$ is defined in Equation (4.14). Equations (4.15) and (4.23) are the respective eigenequations that are solved to obtain pair properties for the singlets and triplets.

In the next section, we will discuss the properties of bound pairs in a BCC lattice.

4.3 Pair Properties

In this section, we examine the properties of two bound fermions in BCC optical lattices. The properties of interest include the total energy, pairing diagram, dispersion, pair effective mass, effective radius, and estimate of Bose-Einstein condensation (BEC) transition temperatures. The main discussion focuses on the s-states (onsite and extended). Nonetheless, other pairing symmetries (p-, d- and f- states) will be briefly discussed too.

4.3.1 Total Energy

The total energy in the ground state provides the most vital information about the system. With the total energy, one can tell whether the particles are bound or not. However, to create a bound pair, a minimum threshold of attraction is required. The attraction can either be onsite U or intersite V. As noted earlier in the preliminary discussion, we can determine the total energy of a pair at an arbitrary pair momentum $\boldsymbol{P}$.

4.3.1.1 Energy of an Unbound Pair at $\boldsymbol{P} = 0$

The minimum energy of *one* free particle (also called the half-bandwidth W) from Equation (4.2) $\varepsilon_{\min} \equiv W = -8t$ is obtained when $\boldsymbol{k} = 0$. Thus, the total energy of *two* free-particles, each at zero momentum, is $-16t$. However, binding only occurs when there is sufficient attraction, and if the particles bind, the energy of the system has to drop. So in the simplest case of *zero* total momentum ($\boldsymbol{P} = 0$), we consider the transition from unbound free-particles to a bound pair to occur when the total energy drops below $-16t$.

4.3.1.2 Energy of a Bound Pair at $\boldsymbol{P} = 0$

To calculate the total energy at *zero* pair momentum, we set $\boldsymbol{P} = 0$ in Equation (4.15). For $\boldsymbol{P} = 0$ which corresponds to the Γ point (the centre of the Brillouin zone (BZ)), there is a simplification of the Green's function (4.14), and the BCC lattice possesses O_h point symmetry. It means that we can apply group theory analysis.

Simplification at the Γ point

At the BZ centre, the Green's function from Equation (4.14) becomes

$$
\begin{aligned}
\mathcal{G}_{lmn}(0) &= -\int_{-2\pi}^{2\pi}\int_{-2\pi}^{2\pi}\int_{-2\pi}^{2\pi}\frac{dq'_x dq'_y dq'_z}{(4\pi)^3}\frac{\cos\left(l\frac{q'_x}{2}\right)\,\cos\left(m\frac{q'_y}{2}\right)\,\cos\left(n\frac{q'_z}{2}\right)}{|E| + 2\varepsilon_{\boldsymbol{q}'}}\\
&= -\frac{1}{(2\pi)^3}\int_{-\pi}^{\pi}\int_{-\pi}^{\pi}\int_{-\pi}^{\pi}\frac{\cos\left(lq''_x\right)\cdot\cos\left(mq''_y\right)\cdot\cos\left(nq''_z\right)}{|E| - 16t\cos(q''_x)\cdot\cos(q''_y)\cdot\cos(q''_z)}dq''_x\,dq''_y dq''_z \quad : \quad (q''_j = \frac{q'_j}{2})
\end{aligned}
$$

(4.24)

and the following relations hold

$$\mathcal{G}_{000}(0) \equiv \mathcal{G}_0$$

$$\mathcal{G}_{111}(0) = \mathcal{G}_{\bar{1}11}(0) = \mathcal{G}_{1\bar{1}1}(0) = \mathcal{G}_{11\bar{1}}(0) = \mathcal{G}_{\bar{1}1\bar{1}}(0) = \mathcal{G}_{\bar{1}\bar{1}1}(0) = \mathcal{G}_{1\bar{1}\bar{1}}(0) \equiv \mathcal{G}_1$$

$$\mathcal{G}_{222}(0) = \mathcal{G}_{\bar{2}22}(0) = \mathcal{G}_{2\bar{2}2}(0) = \mathcal{G}_{22\bar{2}}(0) = \mathcal{G}_{\bar{2}2\bar{2}}(0) = \mathcal{G}_{\bar{2}\bar{2}2}(0) = \mathcal{G}_{2\bar{2}\bar{2}}(0) \equiv \mathcal{G}_2 \qquad (4.25)$$

$$\mathcal{G}_{200}(0) = \mathcal{G}_{0\bar{2}0}(0) = \mathcal{G}_{002}(0) = \mathcal{G}_{\bar{2}00}(0) = \mathcal{G}_{0\bar{2}0}(0) = \mathcal{G}_{00\bar{2}}(0) \equiv \mathcal{G}_3$$

$$\mathcal{G}_{220}(0) = \mathcal{G}_{022}(0) = \mathcal{G}_{202}(0) \equiv \mathcal{G}_4$$

Then, Equations (4.15) and (4.23) respectively become (note that $\tilde{\Phi}_i^{\pm} \equiv \Phi_i^{\pm}$ since $\boldsymbol{P} = 0$)

$$
\underbrace{\begin{bmatrix} U\mathcal{G}_0 & 2V\mathcal{G}_1 & 2V\mathcal{G}_1 & 2V\mathcal{G}_1 & 2V\mathcal{G}_1 \\ U\mathcal{G}_1 & V(\mathcal{G}_0 + \mathcal{G}_2) & V(\mathcal{G}_3 + \mathcal{G}_4) & V(\mathcal{G}_3 + \mathcal{G}_4) & V(\mathcal{G}_3 + \mathcal{G}_4) \\ U\mathcal{G}_1 & V(\mathcal{G}_3 + \mathcal{G}_4) & V(\mathcal{G}_0 + \mathcal{G}_2) & V(\mathcal{G}_4 + \mathcal{G}_3) & V(\mathcal{G}_4 + \mathcal{G}_3) \\ U\mathcal{G}_1 & V(\mathcal{G}_3 + \mathcal{G}_4) & V(\mathcal{G}_4 + \mathcal{G}_3) & V(\mathcal{G}_0 + \mathcal{G}_2) & V(\mathcal{G}_4 + \mathcal{G}_3) \\ U\mathcal{G}_1 & V(\mathcal{G}_3 + \mathcal{G}_4) & V(\mathcal{G}_4 + \mathcal{G}_3) & V(\mathcal{G}_4 + \mathcal{G}_3) & V(\mathcal{G}_0 + \mathcal{G}_2) \end{bmatrix}}_{\hat{H}_{\text{singlet}}}\underbrace{\begin{bmatrix} \Phi_0^+ \\ \Phi_1^+ \\ \Phi_2^+ \\ \Phi_3^+ \\ \Phi_4^+ \end{bmatrix}}_{\hat{\Phi}_{\text{singlet}}} = \underbrace{\begin{bmatrix} \Phi_0^+ \\ \Phi_1^+ \\ \Phi_2^+ \\ \Phi_3^+ \\ \Phi_4^+ \end{bmatrix}}_{\hat{\Phi}_{\text{singlet}}} \qquad (4.26)
$$

$$
\underbrace{\begin{bmatrix} V(\mathcal{G}_0 - \mathcal{G}_2) & V(\mathcal{G}_3 - \mathcal{G}_4) & V(\mathcal{G}_3 - \mathcal{G}_4) & V(\mathcal{G}_3 - \mathcal{G}_4) \\ V(\mathcal{G}_3 - \mathcal{G}_4) & V(\mathcal{G}_0 - \mathcal{G}_2) & V(\mathcal{G}_4 - \mathcal{G}_3) & V(\mathcal{G}_4 - \mathcal{G}_3) \\ V(\mathcal{G}_3 - \mathcal{G}_4) & V(\mathcal{G}_4 - \mathcal{G}_3) & V(\mathcal{G}_0 - \mathcal{G}_2) & V(\mathcal{G}_4 - \mathcal{G}_3) \\ V(\mathcal{G}_3 - \mathcal{G}_4) & V(\mathcal{G}_4 - \mathcal{G}_3) & V(\mathcal{G}_4 - \mathcal{G}_3) & V(\mathcal{G}_0 - \mathcal{G}_2) \end{bmatrix}}_{\hat{H}_{\text{triplet}}}\underbrace{\begin{bmatrix} \Phi_1^- \\ \Phi_2^- \\ \Phi_3^- \\ \Phi_4^- \end{bmatrix}}_{\hat{\Phi}_{\text{triplet}}} = \underbrace{\begin{bmatrix} \Phi_1^- \\ \Phi_2^- \\ \Phi_3^- \\ \Phi_4^- \end{bmatrix}}_{\hat{\Phi}_{\text{triplet}}} \qquad (4.27)
$$

The matrix equations above can be written in a compact form as

$$\hat{H}_{s,t}\,\hat{\Phi}_{s,t} = \mu_{s,t}\,\hat{\Phi}_{s,t} \qquad (4.28)$$

thus forming an eigenvalue problem. $\hat{H}_s$ and $\hat{H}_t$ are the singlet and triplet dispersion matrices, μ_s and μ_t being the eigenvalues corresponding to singlet $\hat{\Phi}_s$ and triplet $\hat{\Phi}_t$ eigenvectors respectively. So, the values of E (in the denominator of the Green's function) corresponding to the pair's total energy are found by searching for eigenvalues of $\mu_{s,t} = 1$.
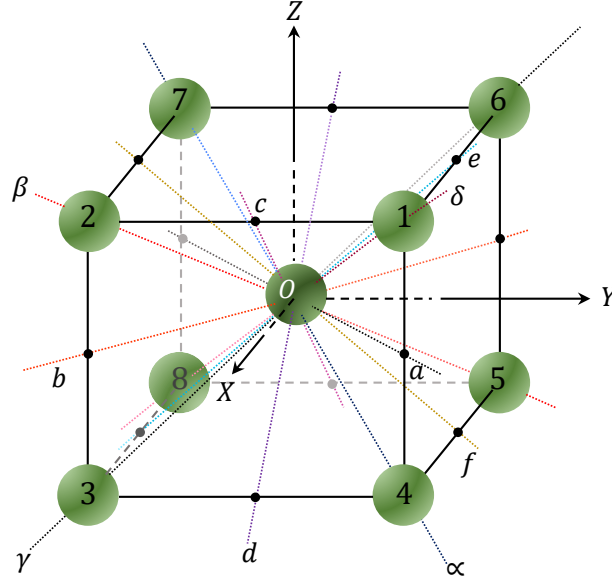
Figure 4.2: A basic BCC lattice showing the axes of the O_h operations. The axes are OX, OY, OZ, Oa, Ob, Oc, Od, Oe, Of, $O\alpha$, $O\beta$, $O\gamma$, and $O\delta$.

Application of Group Theory

In addition to the simplified Green's function at the zone centre, the system of equations (4.26) and (4.27) can be further reduced by following the procedure listed in Section 3.4.7 of Chapter 3 where the symmetry operations, in this case, are those belonging to the O_h group. After going through the steps, we will have the s, p, d, and f symmetries in block-diagonal form. A breakdown of these steps follows:

Step 1: Using the site labels in Figure 4.2, we perform the 48 operations on the system
and then find the character of the input representation (sometimes called the reduction
formula): this is labelled Red. rep (the second row in Table 4.1).

O_h group	E	$8C_2$	$3C_3$	$6C_4$	$6C_5$	C_6	$8C_7$	$3C_8$	$6C_9$	$6C_{10}$		
Red. rep (Γ_t^{bcc})	8	2	0	0	0	0	0	0	0	4	$\sum$	$\sum/48$
A_{1g}	8	16	0	0	0	0	0	0	0	24	48	1
A_{2g}	8	16	0	0	0	0	0	0	0	-24	0	0
E_g	16	-16	0	0	0	0	0	0	0	0	0	0
T_{1g}	24	0	0	0	0	0	0	0	0	-24	0	0
T_{2g}	24	0	0	0	0	0	0	0	0	24	48	1
A_{1u}	8	16	0	0	0	0	0	0	0	-24	0	0
A_{2u}	8	16	0	0	0	0	0	0	0	24	48	1
E_u	16	-16	0	0	0	0	0	0	0	0	0	0
T_{1u}	24	0	0	0	0	0	0	0	0	24	48	1
T_{2u}	24	0	0	0	0	0	0	0	0	-24	0	0

Table 4.1: Constructing irreducible representation from O_h point group using the reduc-
tion formula in a BCC lattice. The symmetry classes and the matrices for irreducible
representations of each symmetry operation are provided in Appendix B.

Step 2: We obtain the irreducible representations (irred. reps.) by looking at the
non-zero contributions in the last column of Table 4.1. Hence the sought irreducible
representations for both the singlet and triplet states are

$$\Gamma_{\text{singlet}}^{\text{bcc}} = A_{1g} \oplus T_{2g} \tag{4.29}$$

$$\Gamma_{\text{triplet}}^{\text{bcc}} = T_{1u} \oplus A_{2u} \tag{4.30}$$

whence A_{1g}, T_{2g}, A_{2u} and T_{2u} forms the *s*-, *d*-, *p*- and *f*- states respectively. From
here, we can find the linear combinations of bases that represent these symmetries. For

instance, the singlets, $\Gamma^{\text{bcc}}_{\text{singlet}}$, can have the combinations

$$\chi^{A_{1g}} = \Phi_1^+ + \Phi_2^+ + \Phi_3^+ + \Phi_4^+ \tag{4.31}$$

$$\chi^{T_{2g}} = \begin{cases} \Phi_1^+ + \Phi_2^+ - \Phi_3^+ - \Phi_4^+ \\ \\ \Phi_1^+ - \Phi_2^+ \\ \\ \Phi_3^+ - \Phi_4^+ \end{cases} \tag{4.32}$$

and the triplets, $\Gamma^{\text{bcc}}_{\text{triplet}}$, can have the combinations

$$\chi^{T_{1u}} = \begin{cases} \Phi_1^- - \Phi_2^- + \Phi_3^- + \Phi_4^- \\ \\ \Phi_1^- + \Phi_2^- \\ \\ \Phi_3^- - \Phi_4^- \end{cases} \tag{4.33}$$

$$\chi^{A_{2u}} = \Phi_1^- - \Phi_2^- - \Phi_3^- - \Phi_4^- \tag{4.34}$$

Step 3: If we combine Equation (4.31) with Φ_0^+ (the onsite basis), we transform to a new basis [‡,§]

$$\hat{\Phi}_s = \begin{bmatrix} \Phi_0 \\ \Phi_s \\ \Phi_{d_1} \\ \Phi_{d_2} \\ \Phi_{d_3} \end{bmatrix} = \begin{bmatrix} 1 & 0 & 0 & 0 & 0 \\ 0 & 1 & 1 & 1 & 1 \\ 0 & 1 & 1 & -1 & -1 \\ 0 & 1 & -1 & 0 & 0 \\ 0 & 0 & 0 & 1 & -1 \end{bmatrix} \begin{bmatrix} \Phi_0^+ \\ \Phi_1^+ \\ \Phi_2^+ \\ \Phi_3^+ \\ \Phi_4^+ \end{bmatrix} \equiv \hat{\chi}_s \begin{bmatrix} \Phi_0^+ \\ \Phi_1^+ \\ \Phi_2^+ \\ \Phi_3^+ \\ \Phi_4^+ \end{bmatrix} \tag{4.35}$$

$$\hat{\Phi}_t = \begin{bmatrix} \Phi_{p_1} \\ \Phi_{p_2} \\ \Phi_{p_3} \\ \Phi_f \end{bmatrix} = \begin{bmatrix} 1 & -1 & 1 & 1 \\ 1 & 1 & 0 & 0 \\ 0 & 0 & 1 & -1 \\ 1 & -1 & -1 & -1 \end{bmatrix} \begin{bmatrix} \Phi_1^- \\ \Phi_2^- \\ \Phi_3^- \\ \Phi_4^- \end{bmatrix} \equiv \hat{\chi}_t \begin{bmatrix} \Phi_1^- \\ \Phi_2^- \\ \Phi_3^- \\ \Phi_4^- \end{bmatrix} \tag{4.36}$$

[‡]Remember that we have omitted the normalisation factors of the new symmetrised basis.

[§]The subscript s has been used twice: $\hat{\Phi}_s$ means all possible singlet states $(s, d, \dots)$ while Φ_s means an extended s-state.

$\hat{\chi}_i$ (where $i = s, t$) is derived by performing the symmetry operations or by a trial and error method. Note that these bases are orthogonal.

Step 4: We can diagonalise the matrix equation using the similarity transformation

$$\hat{H}_i^{\text{diag}} = \hat{\chi}_i \cdot \hat{H}_i \cdot \hat{\chi}_i^{-1} \tag{4.37}$$

By applying Equation (4.37), the new symmetrised bases $\hat{\chi}_s$ and $\hat{\chi}_t$ respectively block-diagonalise the matrices $\hat{H}_s$ and $\hat{H}_t$ as follows

$$\begin{bmatrix} U\mathcal{G}_0 & 2V\mathcal{G}_1 & 0 & 0 & 0 \\ 4U\mathcal{G}_1 & \mathcal{K}_s & 0 & 0 & 0 \\ 0 & 0 & \mathcal{K}_d & 0 & 0 \\ 0 & 0 & 0 & \mathcal{K}_d & 0 \\ 0 & 0 & 0 & 0 & \mathcal{K}_d \end{bmatrix} \begin{bmatrix} \Phi_0 \\ \Phi_s \\ \Phi_{d_1} \\ \Phi_{d_2} \\ \Phi_{d_3} \end{bmatrix} = \begin{bmatrix} \Phi_0 \\ \Phi_s \\ \Phi_{d_1} \\ \Phi_{d_2} \\ \Phi_{d_3} \end{bmatrix} \tag{4.38}$$

$$\begin{bmatrix} \mathcal{K}_p & 0 & 0 & 0 \\ 0 & \mathcal{K}_p & 0 & 0 \\ 0 & 0 & \mathcal{K}_p & 0 \\ 0 & 0 & 0 & \mathcal{K}_f \end{bmatrix} \begin{bmatrix} \Phi_{p_1} \\ \Phi_{p_2} \\ \Phi_{p_3} \\ \Phi_f \end{bmatrix} = \begin{bmatrix} \Phi_{p_1} \\ \Phi_{p_2} \\ \Phi_{p_3} \\ \Phi_f \end{bmatrix} \tag{4.39}$$

where

$$\mathcal{K}_s = V(\mathcal{G}_0 + \mathcal{G}_2 + 3\mathcal{G}_3 + 3\mathcal{G}_4) \tag{4.40}$$

$$\mathcal{K}_d = V(\mathcal{G}_0 + \mathcal{G}_2 - \mathcal{G}_3 - \mathcal{G}_4) = 1 \tag{4.41}$$

$$\mathcal{K}_p = V(\mathcal{G}_0 - \mathcal{G}_2 + \mathcal{G}_3 - \mathcal{G}_4) = 1 \tag{4.42}$$

$$\mathcal{K}_f = V(\mathcal{G}_0 - \mathcal{G}_2 - 3\mathcal{G}_3 + 3\mathcal{G}_4) = 1 \tag{4.43}$$

In (4.38), the top-left 2×2 block corresponds to the s-symmetrical states (having contributions from both the onsite and intersite interactions) while the other three 1×1 blocks are d-symmetrical states which are triply degenerate (when $\boldsymbol{P} = 0$). Similarly, in Equation (4.39), the p-states are 3-fold degenerate and there is a single f-state.

The total energy measured in terms of the half-bandwidth W is shown in Figure 4.3. The flat region of the curve corresponds to the total energy of two unbound particles (the threshold energy $E^{\mathrm{Th}} = -2W$). The energy drops below $-2W$ as the attraction gets stronger, indicating that a bound pair has been formed. Pairs are highly stable (well bound) at large attractive coupling. The symmetries of the pairs are indicated. The p- and d-states are both three-fold degenerate, and the s- and f-states have degeneracy 1.

Figure 4.3a and 4.3b respectively, show a shift in the critical U (V) required to form stable s-symmetric pair when modifying the intersite (onsite) repulsion. A stable s-symmetric pair is guaranteed to form if $U \leq -2W$ or $V \leq -0.8858W$ (more details in the next section 4.3.2). For infinite attractive V, the particles form deep, localised pairs and the energies associated with all the intersite pairing symmetries converge, on a single value i.e. $E \to -|V|$ (inset plots in Figure 4.3). For non-s pairing symmetries, the critical interaction is independent of U. For the onsite s-pair, $E \to -|U|$ as $U \to -\infty$. In these large interaction limits, binding energies and thus binding temperatures can be very large.
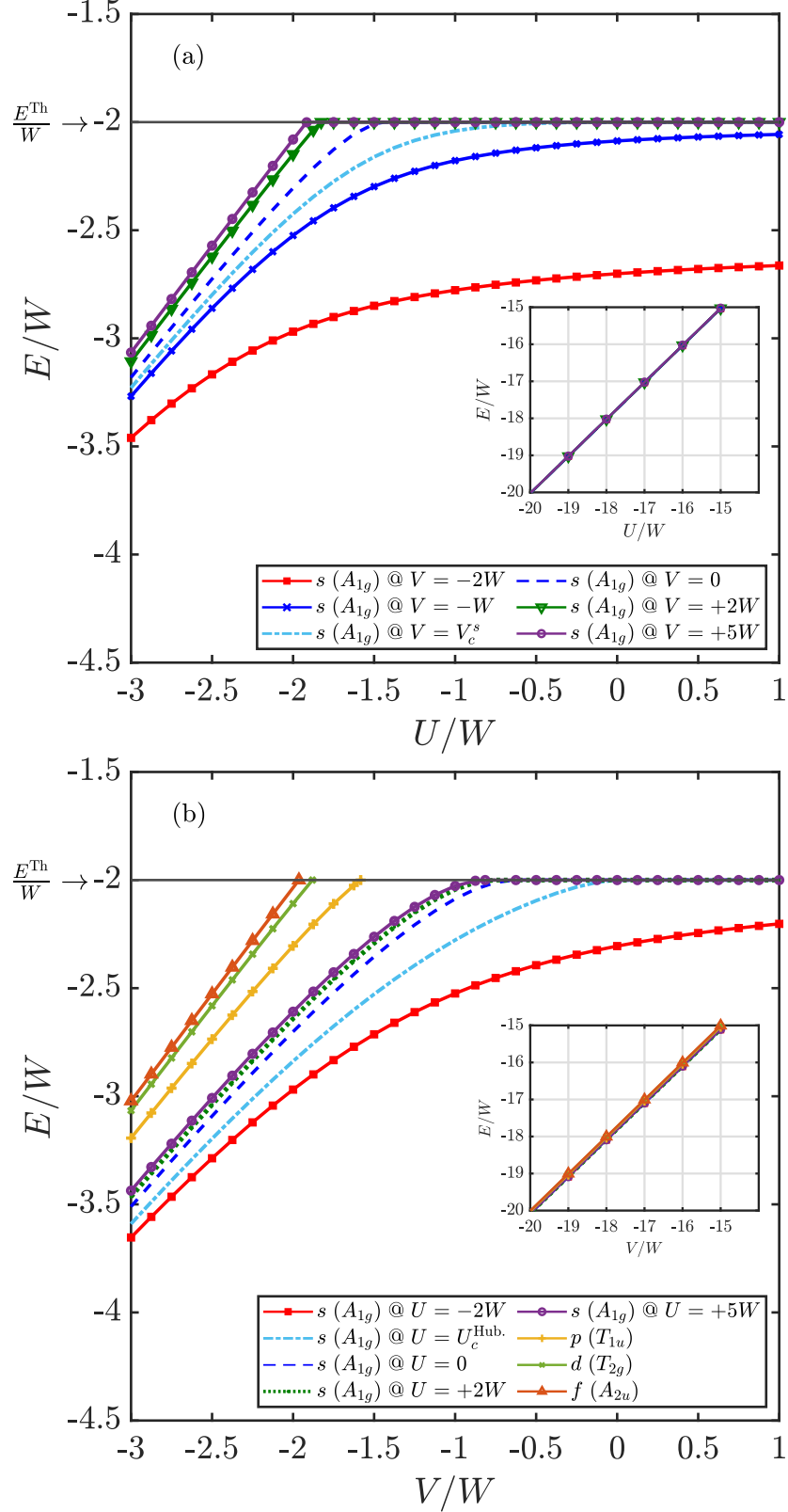
Figure 4.3: The total energy of bound pairs on the BCC optical lattice at $\boldsymbol{P} = 0$, $T = 0$. The s-state forms the ground state. The critical Hubbard attraction for $V = 0$ is $U_c^{\text{Hub.}}(0) = -1.4355W$ and for $U = 0$, $V_c^s(0) = -0.6358W$. The p-, d- and f- states are not dependent on U (this means that a change in U only affects the total energy of the s-state). For large onsite, $|U| \gg |V|, t$ (intersite, $|V| \gg |U|, t$) attraction, $E \rightarrow -|U|$ ($E \rightarrow -|V|$) for all the states (inset plots). The corresponding symmetry of each state is also indicated.

4.3.2　Binding Criteria

Once the equations have been diagonalised, it is possible to calculate the critical binding threshold by setting the energy of the system equal to the energy of *two* free-particles $E \to -2W = -16t$. These critical binding values are exact and accurate because one can obtain exact analytic solutions to the Green's functions at $\boldsymbol{P} = 0$. For this purpose, it is convenient to re-write the singlet and triplet determinant matrices (4.38) and (4.39), and remove redundant elements. Doing this gives the respective states:

$$s: \quad \begin{bmatrix} 1 - U\mathcal{G}_0 & -2V\mathcal{G}_1 \\ -4U\mathcal{G}_1 & 1 - \mathcal{K}_s \end{bmatrix} = 0 \tag{4.44}$$

$$d: \quad 1 - \mathcal{K}_d = 0 \tag{4.45}$$

$$p: \quad 1 - \mathcal{K}_p = 0 \tag{4.46}$$

$$f: \quad 1 - \mathcal{K}_f = 0 \tag{4.47}$$

The Green's function (4.25) can be expressed in terms of the elliptic integral of the first kind [98] as

$$\mathcal{G}_0 = -\frac{K_0^2}{4\pi^2 t} = \frac{-0.087075245605354804}{t} \tag{4.48}$$

$$\mathcal{G}_1 = \frac{1}{16t} - \frac{K_0^2}{4\pi^2 t} = \frac{1}{16t} + \mathcal{G}_0 \tag{4.49}$$

$$\mathcal{G}_2 = \frac{1}{2t} - \frac{K_0^2}{\pi^2 t} - \frac{9}{16tK_0^2} = \frac{1}{2t} + 4\mathcal{G}_0 + \frac{9}{64\pi^2 t^2 \mathcal{G}_0} \tag{4.50}$$

$$\mathcal{G}_3 = -\frac{1}{16tK_0^2} = \frac{1}{64\pi^2 t^2 \mathcal{G}_0} \tag{4.51}$$

$$\mathcal{G}_4 = -\frac{K_0^2}{4\pi^2 t} + \frac{1}{4tK_0^2} = \mathcal{G}_0 - \frac{1}{16\pi^2 t^2 \mathcal{G}_0} = \mathcal{G}_0 - 4\mathcal{G}_3 \tag{4.52}$$

where $K_0 = K\left(\frac{1}{\sqrt{2}}\right) = 1.85407467\ldots$ is the complete elliptic integral of the first kind.

Expanding the determinant (4.44) gives the critical binding for the s-states

$$V_c^s \le V(U) = \frac{U\mathcal{G}_0 - 1}{U\mathcal{G}_0\mathcal{C} - \mathcal{C} - 8U\mathcal{G}_1^2} \tag{4.53}$$

where $\mathcal{C} = \mathcal{G}_0 + \mathcal{G}_2 + 3\mathcal{G}_3 + 3\mathcal{G}_4 = 8\mathcal{G}_0 + \frac{1}{2t} = -0.19660196484283837/t$.

Therefore,

$$V_c^s(U = 0) = -5.0864191t \approx -0.6358W \tag{4.54}$$

$$V_c^s(U \to +\infty) = -7.0864191t \approx -0.8858W \tag{4.55}$$

$$U_c(V = 0) = -11.4843202t \approx -1.4355W \tag{4.56}$$

$$U_c(V \to +\infty) = -16t = -2W \tag{4.57}$$

Similarly, (4.45) - (4.47) respectively yields

$$V_c^d = -15.0428185t \approx -1.8804W \tag{4.58}$$

$$V_c^p = -12.6624416t \approx -1.5828W \tag{4.59}$$

$$V_c^f = -15.7113739t \approx -1.9639W \tag{4.60}$$

By identifying the point at which the total energy drops below $-2W$, the binding diagram at $\boldsymbol{P} = 0$ can be constructed (see Figure 4.4). From Equations (4.58)–(4.60), it is clear that for any pairing symmetry with a node at the origin, binding of the particles is independent of U.

Within the U-V parameter space, pairing is found at large, attractive U/W and/or V/W. The kinetic energy of the particles in the BCC lattice is high (relative to 1D, 2D, and simple cubic lattices) due to the higher coordination number and, as a result, U or V must be large and attractive to form a bound state. For a negative-U Hubbard model with no intersite interaction, the critical binding is $U_c^s(V{=}0){\approx}{-}1.4355W$. Also, $V_c^s(U{=}0){\approx}{-}0.6358W$ is required to bind particles when the onsite interaction is absent. An intersite strength $V_c^s(+\infty){\approx}{-}0.8858W$ is sufficient to maintain a bound state even if the Hubbard repulsion is infinite while $U_c^s(V \to +\infty){=}{-}2W$. Figure 4.4 also shows the binding thresholds of the p-, d- and f-states respectively occurring at large intersite attractions, that is, $V_c^p{=}{-}1.5828W$, $V_c^d{=}{-}1.8804W$, $V_c^f{=}{-}1.9639W$.
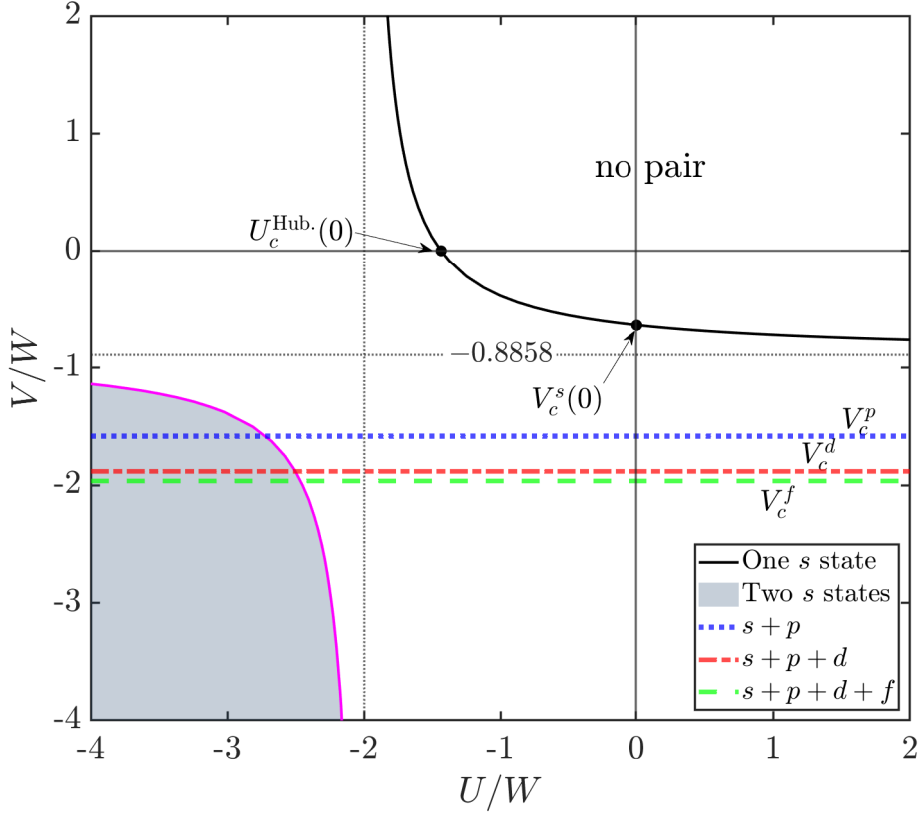
Figure 4.4: Binding diagram for pair formation when $\boldsymbol{P} = 0$ (temperature $T = 0$) on the BCC lattice. The top curved solid line shows the formation of one bound s-state pair (singlet), the shaded region enclosed by the curved magenta solid line indicates the region of formation of two s-states, the blue dotted line shows the onset of triply degenerate p-states (three p-wave triplets), the red dash-dotted line shows the binding of the three-fold degenerate d-states (three d-wave singlets) and the green dashed line indicates the formation of a pair with f-symmetry (one f-wave triplet). The p-, d- and f- states begin to appear at critical intersite attractions $-1.5828W$, $-1.8803W$ and $-1.9639W$ respectively. The smaller dotted vertical and horizontal lines are the asymptotes ($V^s_{\text{asym.}} \approx -0.8858\text{W}$ and $U^{\text{Hub.}}_{\text{asym.}} = -2W$) and for potentials equal to or more attractive than these values, the creation of an s-state bound pair is guaranteed.

4.3.3 Dispersion

The energy of a bound pair can be constructed across the entire BZ using Equations (4.15) and (4.23). To produce a band structure that shows all the pairing symmetries, we consider intersite attraction sufficient to bind the most energetic f-state at the zone centre (i.e. Γ point). One of the benefits of the dispersion calculation is that we can compute the pair *effective mass* (section 4.3.4) which is required for the estimation of the *condensation temperature* (section 4.3.6). Examples of dispersions are plotted in
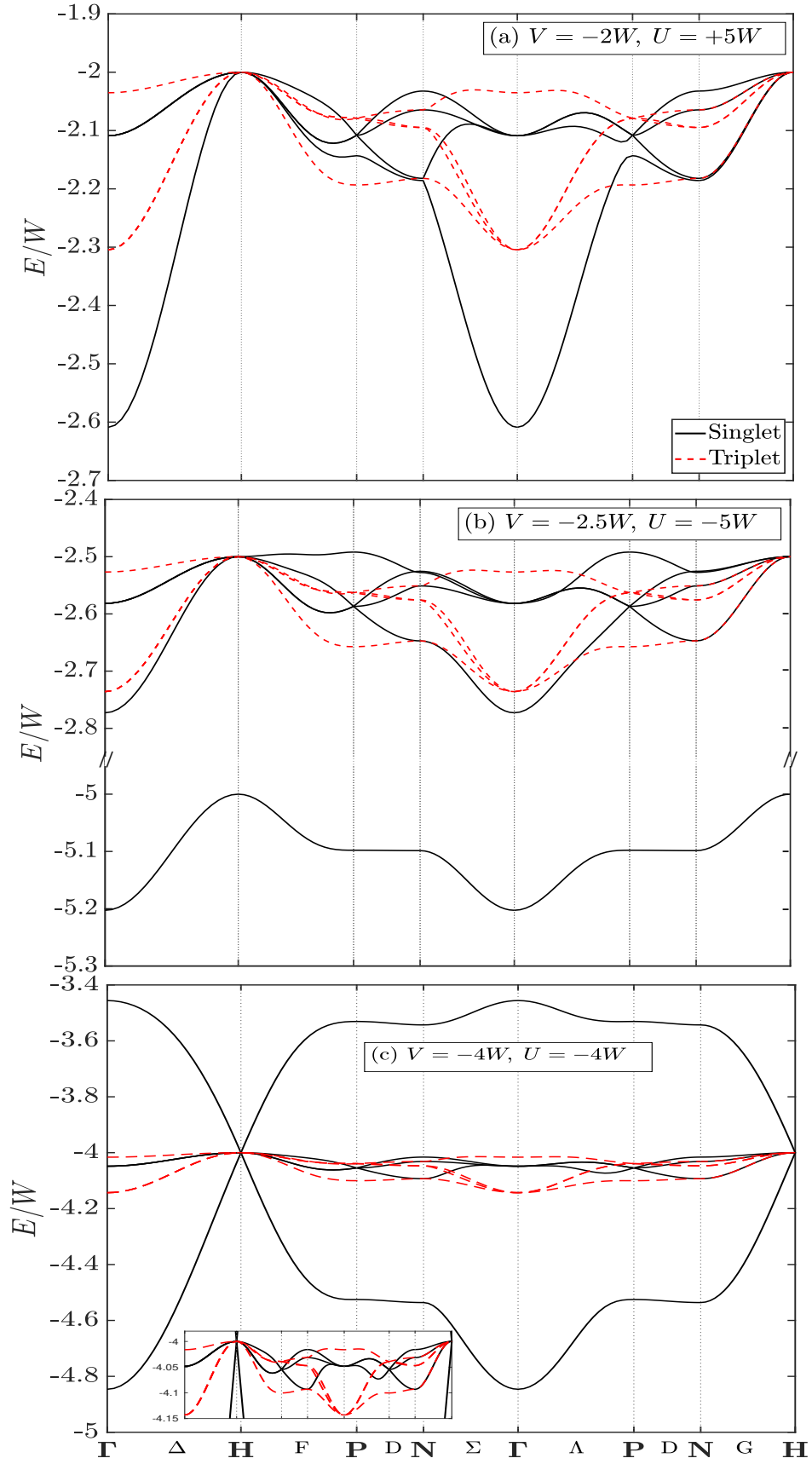
Figure 4.5: Examples of dispersions with (a) repulsive U and attractive V, (b) U and V are both attractive but dominant U, (c) competing attractions where both U and V are attractive and equal. Solid (red dotted) lines are the singlet (triplet) states. In (b) there is a low-lying onsite state. Note the axis re-scaling in (b).

Figure 4.5. The dispersion for two free particles is not shown but lies in the range $-2 \leq E/W \leq 2$. The singlet s-symmetric pair has the lowest energy around the BZ centre but this is not always the case at other high symmetry points. There is a high level of degeneracy on the Γ-H line; all states with the same symmetry class are degenerate and the simplification at the Γ point (refer to Section 4.3.1.2) applies too. The momentum contribution only renormalises the hopping parameter t along the Γ-H line.

Away from the Γ-H line, states with different symmetries mix. Although the singlet and triplet states can be unambiguously classified because the (anti-)symmetrised solution separates singlets from triplets. From the dispersion calculations, we note that away from the Γ point, there is a possibility of forming bound pairs with vanishingly small attraction. This provides further insights into pair formation and stability at different attractive U and V values. Across the BZ, there are singlet-triplet crossings, especially along N-H.

At the H point where the total pair momentum is maximal, there is some special behaviour. Firstly, the bound onsite s-state has an energy equal to U and all other states (which are bound by the intersite potential) have energy V (as long as the relevant potential is non-zero and attractive). Secondly, for repulsive U, the extended-s state becomes completely independent of the Hubbard U repulsion (Figure 4.6, panels (a) and (b)). Thirdly, a vanishingly small attraction ($U \to 0^{(-)}$ and $V \to 0^{(-)}$) is sufficient to bind pairs (Figure 4.6c).

When U is repulsive, the band structure gets narrower as the intersite attraction V increases, consistent with an increase in the effective mass. Whereas in the situation of competing attractions (i.e. when U and V are both attractive and equal), the bandwidth increases (Figure 4.5c), and the singlet pair becomes highly mobile because its movement is a first-order effect. Since we expect convergence of bound states at the H point for

any attractive U and/or V (see last paragraph and Figure 4.6c), the dispersion in Figure 4.5c is reminiscent of the conical band structure of monolayer graphene [99] with point H similar in form to the Dirac points in graphene. This condition $U = V$ (such that both are sufficiently attractive) is the superlight limit where the bound pair has a light mass and hence higher mobility in the BCC lattice. This may be analogous to the very high mobility of charge carriers found in graphene as a material with massless fermions [100].
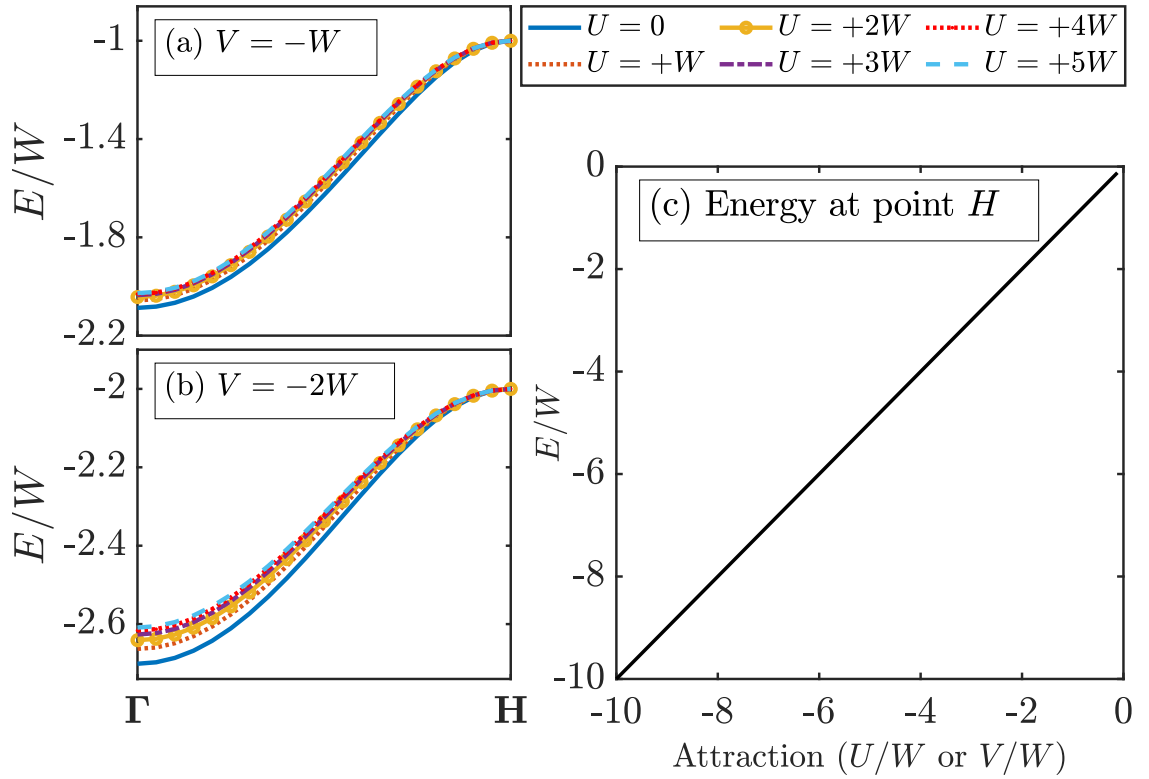
Figure 4.6: Panels (a) and (b): Dispersion of the extended s-state only on the Γ-H line showing that it is independent of repulsive U at the H point. Panel (c): energy of all bound states at point H (N.B. extended-s, d, p and f states are only bound if V is attractive, and the onsite s state is only bound if U is attractive). (c) shows that a pair, whatever the symmetry, can be formed at the H point at a very weak attraction, in contrast to the critical attractions U_c, V_c (refer to Section 4.3.2 or Figure 4.4), required at the Γ point. The legends for the plots in (a) and (b) are at the top-right.

4.3.3.1 Application of Second-Order Perturbation Theory (SOPT)

We validate the dispersion results in the strong-coupling limits where we will introduce kinetic hopping of particles in the system as a perturbation. Firstly, we consider the strongly attractive Hubbard limit: $U \to -\infty$, $|U| \gg t$, $V = 0$. Secondly, we compute the dispersion in the limit $U \to +\infty$, $V < 0$, $|V| \gg t$.

To do this, we define *four* nearest-neighbour vectors (see Figure 4.7)

$$\boldsymbol{a}_1 = \left\{\frac{b}{2}, \frac{b}{2}, \frac{b}{2}\right\}, \boldsymbol{a}_2 = \left\{\frac{b}{2}, \frac{b}{2}, -\frac{b}{2}\right\}, \boldsymbol{a}_3 = \left\{\frac{b}{2}, -\frac{b}{2}, \frac{b}{2}\right\}, \boldsymbol{a}_4 = \left\{\frac{b}{2}, -\frac{b}{2}, -\frac{b}{2}\right\}, \quad (4.61)$$

where b is the BCC lattice constant. Next, we define the Fourier-space vectors below

$$A_{\boldsymbol{n}} = \sum_{\boldsymbol{P}} e^{i\boldsymbol{P}\boldsymbol{n}} A_{\boldsymbol{P}} \ , \qquad A_{\boldsymbol{n}+\boldsymbol{a}} = \sum_{\boldsymbol{P}} e^{i\boldsymbol{P}(\boldsymbol{n}+\boldsymbol{a})} A_{\boldsymbol{P}} = e^{i\boldsymbol{P}\boldsymbol{a}} A_{\boldsymbol{n}} \qquad (4.62)$$

where $\boldsymbol{P}$ is the pair total momentum.
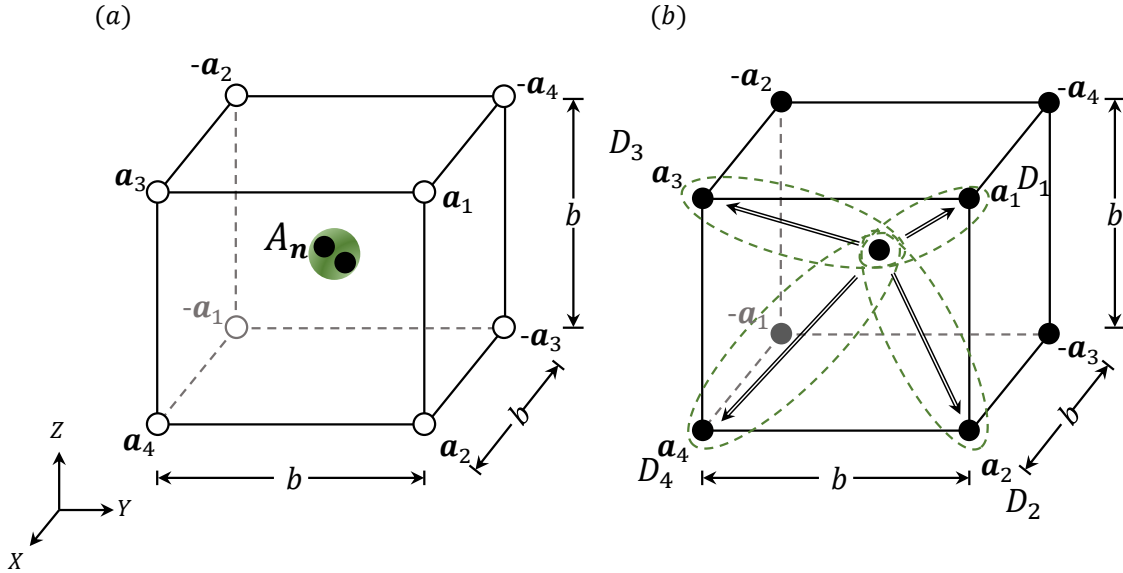
Figure 4.7: BCC nearest-neighbour vectors and dimer basis for: (a) Onsite attraction - note that $\boldsymbol{P} = 0$ in the initial configuration $A_{\boldsymbol{n}}$. (b) Intersite attraction - D_1, D_2, D_3 and D_4 are pre-defined intersite configurations. In (b) we use the central lattice site as the anchor point, the double-line arrow shows the anchor direction which is important in analysing the hopping of triplet states. The need for this is to help determine the sign arising from particle exchange.

Strongly bound onsite pair

In the limit of large attractive U, $V = 0$, the UV Hamiltonian only contains the kinetic and the Hubbard terms. The perturbation H' is the hopping of particles, and since we are performing second-order perturbation theory (SOPT) calculation, there are two hopping events via t . However, the energy at the intermediate step is zero because the particles occupy different lattice sites and $V = 0$, and, thus, the energy due to the perturbation is proportional to t^2/U. If the initial configuration is $A_{\boldsymbol{n}}$ as in Figure 4.7a, then the perturbed Hamiltonian matrix is

$$\hat{H}' \cdot A_{\boldsymbol{n}} = -\frac{16t^2}{|U|} A_{\boldsymbol{n}} - \frac{2t^2}{|U|}(A_{\boldsymbol{n}+\boldsymbol{a}_1} + A_{\boldsymbol{n}-\boldsymbol{a}_1} + A_{\boldsymbol{n}+\boldsymbol{a}_2} + A_{\boldsymbol{n}-\boldsymbol{a}_2} + A_{\boldsymbol{n}+\boldsymbol{a}_3} + A_{\boldsymbol{n}-\boldsymbol{a}_3} + A_{\boldsymbol{n}+\boldsymbol{a}_4} + A_{\boldsymbol{n}-\boldsymbol{a}_4})$$

$$(4.63)$$

The substitution of Equation (4.62) into Equation (4.63) gives the second-order energy perturbation

$$
\begin{aligned}
E_n^{(2)} &= -\frac{16t^2}{|U|} - \frac{2t^2}{|U|}(e^{i\boldsymbol{P}\boldsymbol{a}_1} + e^{-i\boldsymbol{P}\boldsymbol{a}_1} + e^{i\boldsymbol{P}\boldsymbol{a}_2} + e^{-i\boldsymbol{P}\boldsymbol{a}_2} + e^{i\boldsymbol{P}\boldsymbol{a}_3} + e^{-i\boldsymbol{P}\boldsymbol{a}_3} + e^{i\boldsymbol{P}\boldsymbol{a}_4} + e^{-i\boldsymbol{P}\boldsymbol{a}_4}) \\
&= -\frac{16t^2}{|U|} - \frac{16t^2}{|U|} \cdot \cos\frac{P_x b}{2} \cdot \cos\frac{P_y b}{2} \cdot \cos\frac{P_z b}{2}
\end{aligned}
$$

$$(4.64)$$

Therefore, the only bound state in the strong attractive U limit has the dispersion

$$E(\boldsymbol{P}) = -|U| - \frac{16t^2}{|U|}\left(1 + \cos\frac{P_x b}{2} \cdot \cos\frac{P_y b}{2} \cdot \cos\frac{P_z b}{2}\right) \qquad (4.65)$$

where the first and the second terms correspond to the unperturbed and the perturbed energy, respectively.

We plot the result obtained from Equation (4.15) versus Equation (4.65) in Figure 4.8. Both results are in perfect agreement. The dispersion resembles that of a *free* particle in a BCC BZ. This means that even though the two particles form a bound state, the pair behaves like a single particle moving across the zone.
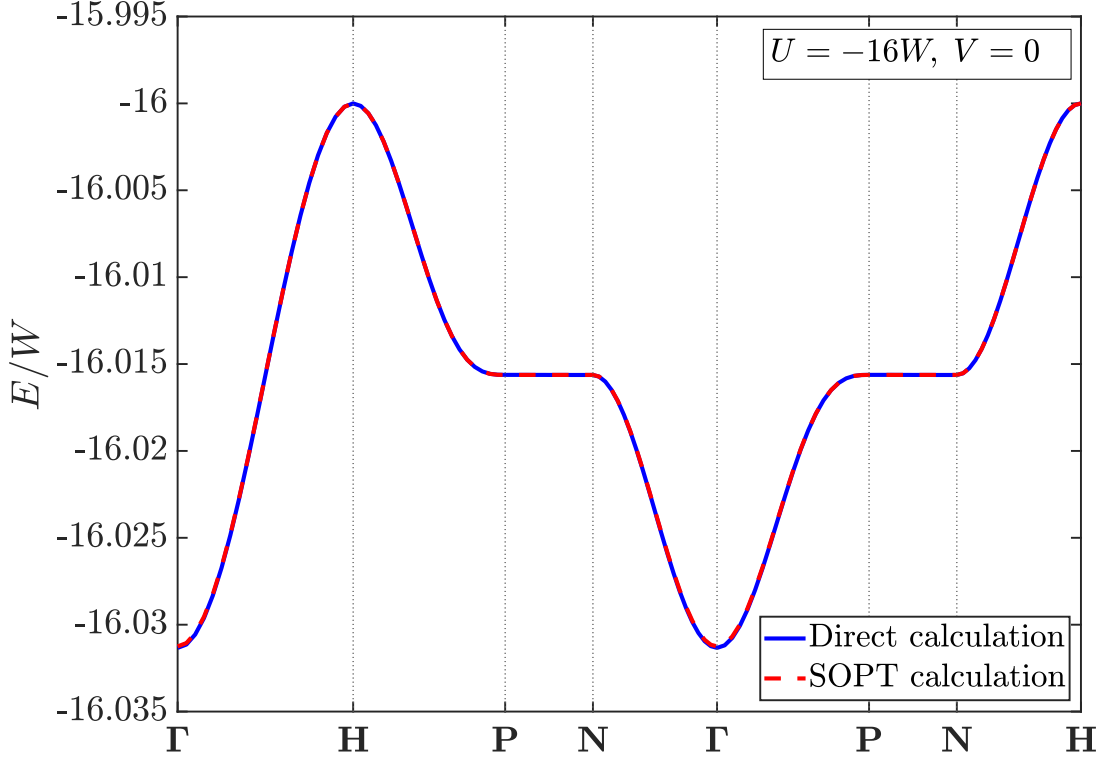
Figure 4.8: Comparing the dispersion of a strongly bound onsite pair ($U = -16W$, $V = 0$) obtained from Equation (4.15) against the second-order perturbation calculation Equation (4.65). The blue solid line is the direct calculation and the red dashed line is for the SOPT result. There is an excellent agreement between both results.

Strongly bound pairs requiring intersite attraction

In the limit $U = +\infty$, $V < 0$, $V \gg t$, the pair is made of two particles occupying a pair of nearest-neighbour sites with the zeroth-order binding energy $-|V|$. Due to the strong onsite repulsion, the hopping processes exclude double occupation on a site and the relevant energy scale is therefore

$$\tilde{t} = \frac{t^2}{|V|} \ .\tag{4.66}$$

We can also define an auxiliary function

$$\tilde{\varepsilon}_{\boldsymbol{P}} \equiv -8\tilde{t} \cdot \cos\frac{P_x b}{2} \cdot \cos\frac{P_y b}{2} \cdot \cos\frac{P_z b}{2} \ ,\tag{4.67}$$

where $\boldsymbol{P}$ is the total pair momentum.

Next, we define four dimer basis states for the singlets and triplets, respectively, as

$$D_{i,\boldsymbol{n}}^{s} = \frac{1}{\sqrt{2}} \left(|\uparrow\rangle_{\boldsymbol{n}} |\downarrow\rangle_{\boldsymbol{n}+\boldsymbol{a}_i} + |\downarrow\rangle_{\boldsymbol{n}} |\uparrow\rangle_{\boldsymbol{n}+\boldsymbol{a}_i} \right) \quad , \tag{4.68}$$

$$D_{i,\boldsymbol{n}}^{t} = |\uparrow\rangle_{\boldsymbol{n}} |\uparrow\rangle_{\boldsymbol{n}+\boldsymbol{a}_i} \quad . \tag{4.69}$$

Note that for the triplet states, $D_{i,\boldsymbol{n}}^{t} = -D_{i,\boldsymbol{n}-\boldsymbol{a}_i}^{t}$. The second-order Hamiltonian matrices are quite complicated in comparison to Equation (4.63). Meanwhile, the Fourier transform yields a matrix equation of the form:

$$E_1(\boldsymbol{P}) \cdot D_{1,\boldsymbol{P}} = B_{11} \cdot D_{1,\boldsymbol{P}} + B_{12} \cdot D_{2,\boldsymbol{P}} + B_{13} \cdot D_{3,\boldsymbol{P}} + B_{14} \cdot D_{4,\boldsymbol{P}} \tag{4.70}$$

$$E_2(\boldsymbol{P}) \cdot D_{2,\boldsymbol{P}} = B_{21} \cdot D_{1,\boldsymbol{P}} + B_{22} \cdot D_{2,\boldsymbol{P}} + B_{23} \cdot D_{3,\boldsymbol{P}} + B_{24} \cdot D_{4,\boldsymbol{P}} \tag{4.71}$$

$$E_3(\boldsymbol{P}) \cdot D_{3,\boldsymbol{P}} = B_{31} \cdot D_{1,\boldsymbol{P}} + B_{32} \cdot D_{2,\boldsymbol{P}} + B_{33} \cdot D_{3,\boldsymbol{P}} + B_{34} \cdot D_{4,\boldsymbol{P}} \tag{4.72}$$

$$E_4(\boldsymbol{P}) \cdot D_{4,\boldsymbol{P}} = B_{41} \cdot D_{1,\boldsymbol{P}} + B_{42} \cdot D_{2,\boldsymbol{P}} + B_{43} \cdot D_{3,\boldsymbol{P}} + B_{44} \cdot D_{4,\boldsymbol{P}} \,, \tag{4.73}$$

where for the singlet states

$$B_{11} = -14\,\tilde{t} + 2\,\tilde{\varepsilon}_{\boldsymbol{P}} + 2\tilde{t}\cos{(\boldsymbol{P}\boldsymbol{a}_1)} - |V| \tag{4.74}$$

$$B_{12} = -2\tilde{t}\,(1 + e^{i\boldsymbol{P}\boldsymbol{a}_1})(1 + e^{-i\boldsymbol{P}\boldsymbol{a}_2}) - 2\tilde{t}\,(1 + e^{i\boldsymbol{P}\boldsymbol{a}_3})(1 + e^{-i\boldsymbol{P}\boldsymbol{a}_4}) \tag{4.75}$$

$$B_{13} = -2\tilde{t}\,(1 + e^{i\boldsymbol{P}\boldsymbol{a}_1})(1 + e^{-i\boldsymbol{P}\boldsymbol{a}_3}) - 2\tilde{t}\,(1 + e^{i\boldsymbol{P}\boldsymbol{a}_2})(1 + e^{-i\boldsymbol{P}\boldsymbol{a}_4}) \tag{4.76}$$

$$B_{14} = -2\tilde{t}\,(1 + e^{i\boldsymbol{P}\boldsymbol{a}_1})(1 + e^{-i\boldsymbol{P}\boldsymbol{a}_4}) - 2\tilde{t}\,e^{i\boldsymbol{P}\boldsymbol{a}_1}(1 + e^{-i\boldsymbol{P}\boldsymbol{a}_2})(1 + e^{-i\boldsymbol{P}\boldsymbol{a}_3}) \,, \tag{4.77}$$

$$B_{21} = -2\tilde{t}\,(1 + e^{-i\boldsymbol{P}\boldsymbol{a}_1})(1 + e^{i\boldsymbol{P}\boldsymbol{a}_2}) - 2\tilde{t}\,(1 + e^{-i\boldsymbol{P}\boldsymbol{a}_3})(1 + e^{i\boldsymbol{P}\boldsymbol{a}_4}) \tag{4.78}$$

$$B_{22} = -14\,\tilde{t} + 2\,\tilde{\varepsilon}_{\boldsymbol{P}} + 2\tilde{t}\cos{(\boldsymbol{P}\boldsymbol{a}_2)} - |V| \tag{4.79}$$

$$B_{23} = -2\tilde{t}\,(1 + e^{i\boldsymbol{P}\boldsymbol{a}_2})(1 + e^{-i\boldsymbol{P}\boldsymbol{a}_3}) - 2\tilde{t}\,e^{i\boldsymbol{P}\boldsymbol{a}_2}(1 + e^{-i\boldsymbol{P}\boldsymbol{a}_1})(1 + e^{-i\boldsymbol{P}\boldsymbol{a}_4}) \tag{4.80}$$

$$B_{24} = -2\tilde{t}\,(1 + e^{i\boldsymbol{P}\boldsymbol{a}_2})(1 + e^{-i\boldsymbol{P}\boldsymbol{a}_4}) - 2\tilde{t}\,(1 + e^{i\boldsymbol{P}\boldsymbol{a}_1})(1 + e^{-i\boldsymbol{P}\boldsymbol{a}_3}) \,, \tag{4.81}$$

$$B_{31} = -2\tilde{t}\,(1 + e^{-i\boldsymbol{P}\boldsymbol{a}_1})(1 + e^{i\boldsymbol{P}\boldsymbol{a}_3}) - 2\tilde{t}\,(1 + e^{-i\boldsymbol{P}\boldsymbol{a}_2})(1 + e^{i\boldsymbol{P}\boldsymbol{a}_4}) \tag{4.82}$$

$$B_{32} = -2\tilde{t}\,(1 + e^{-i\boldsymbol{P}\boldsymbol{a}_2})(1 + e^{i\boldsymbol{P}\boldsymbol{a}_3}) - 2\tilde{t}\,e^{i\boldsymbol{P}\boldsymbol{a}_3}(1 + e^{-i\boldsymbol{P}\boldsymbol{a}_1})(1 + e^{-i\boldsymbol{P}\boldsymbol{a}_4}) \tag{4.83}$$

$$B_{33} = -14\,\tilde{t} + 2\,\tilde{\varepsilon}_{\boldsymbol{P}} + 2\tilde{t}\cos\left(\boldsymbol{P}\boldsymbol{a}_3\right) - |V| \tag{4.84}$$

$$B_{34} = -2\tilde{t}\,(1 + e^{i\boldsymbol{P}\boldsymbol{a}_1})(1 + e^{-i\boldsymbol{P}\boldsymbol{a}_2}) - 2\tilde{t}\,(1 + e^{i\boldsymbol{P}\boldsymbol{a}_3})(1 + e^{-i\boldsymbol{P}\boldsymbol{a}_4}), \tag{4.85}$$

$$B_{41} = -2\tilde{t}\,(1 + e^{-i\boldsymbol{P}\boldsymbol{a}_1})(1 + e^{i\boldsymbol{P}\boldsymbol{a}_4}) - 2\tilde{t}\,e^{i\boldsymbol{P}\boldsymbol{a}_4}(1 + e^{-i\boldsymbol{P}\boldsymbol{a}_2})(1 + e^{-i\boldsymbol{P}\boldsymbol{a}_3}) \tag{4.86}$$

$$B_{42} = -2\tilde{t}\,(1 + e^{-i\boldsymbol{P}\boldsymbol{a}_1})(1 + e^{i\boldsymbol{P}\boldsymbol{a}_3}) - 2\tilde{t}\,(1 + e^{-i\boldsymbol{P}\boldsymbol{a}_2})(1 + e^{i\boldsymbol{P}\boldsymbol{a}_4}) \tag{4.87}$$

$$B_{43} = -2\tilde{t}\,(1 + e^{-i\boldsymbol{P}\boldsymbol{a}_1})(1 + e^{i\boldsymbol{P}\boldsymbol{a}_2}) - 2\tilde{t}\,(1 + e^{-i\boldsymbol{P}\boldsymbol{a}_3})(1 + e^{i\boldsymbol{P}\boldsymbol{a}_4}) \tag{4.88}$$

$$B_{44} = -14\,\tilde{t} + 2\,\tilde{\varepsilon}_{\boldsymbol{P}} + 2\tilde{t}\cos\left(\boldsymbol{P}\boldsymbol{a}_4\right) - |V|, \tag{4.89}$$

whereas, for the triplets

$$B_{11} = -14\,\tilde{t} + 2\,\tilde{\varepsilon}_{\boldsymbol{P}} + 2\tilde{t}\cos\left(\boldsymbol{P}\boldsymbol{a}_1\right) - |V| \tag{4.90}$$

$$B_{12} = -2\tilde{t}\,(1 + e^{i\boldsymbol{P}\boldsymbol{a}_3})(1 + e^{-i\boldsymbol{P}\boldsymbol{a}_4}) \tag{4.91}$$

$$B_{13} = -2\tilde{t}\,(1 + e^{i\boldsymbol{P}\boldsymbol{a}_2})(1 + e^{-i\boldsymbol{P}\boldsymbol{a}_4}) \tag{4.92}$$

$$B_{14} = 2\tilde{t}\,e^{i\boldsymbol{P}\boldsymbol{a}_1}(1 + e^{-i\boldsymbol{P}\boldsymbol{a}_2})(1 + e^{-i\boldsymbol{P}\boldsymbol{a}_3}), \tag{4.93}$$

$$B_{21} = -2\tilde{t}\,(1 + e^{-i\boldsymbol{P}\boldsymbol{a}_3})(1 + e^{i\boldsymbol{P}\boldsymbol{a}_4}) \tag{4.94}$$

$$B_{22} = -14\,\tilde{t} + 2\,\tilde{\varepsilon}_{\boldsymbol{P}} + 2\tilde{t}\cos\left(\boldsymbol{P}\boldsymbol{a}_2\right) - |V| \tag{4.95}$$

$$B_{23} = 2\tilde{t}\,e^{i\boldsymbol{P}\boldsymbol{a}_2}(1 + e^{-i\boldsymbol{P}\boldsymbol{a}_1})(1 + e^{-i\boldsymbol{P}\boldsymbol{a}_4}) \tag{4.96}$$

$$B_{24} = -2\tilde{t}\,(1 + e^{i\boldsymbol{P}\boldsymbol{a}_1})(1 + e^{-i\boldsymbol{P}\boldsymbol{a}_3}), \tag{4.97}$$

$$B_{31} = -2\tilde{t}\,(1 + e^{-i\boldsymbol{P}\boldsymbol{a}_2})(1 + e^{i\boldsymbol{P}\boldsymbol{a}_4}) \tag{4.98}$$

$$B_{32} = 2\tilde{t}\,e^{i\boldsymbol{P}\boldsymbol{a}_3}(1 + e^{-i\boldsymbol{P}\boldsymbol{a}_1})(1 + e^{-i\boldsymbol{P}\boldsymbol{a}_4}) \tag{4.99}$$

$$B_{33} = -14\,\tilde{t} + 2\,\tilde{\varepsilon}_{\boldsymbol{P}} + 2\tilde{t}\cos\left(\boldsymbol{P}\boldsymbol{a}_3\right) - |V| \tag{4.100}$$

$$B_{34} = -2\tilde{t}\,(1 + e^{i\boldsymbol{P}\boldsymbol{a}_1})(1 + e^{-i\boldsymbol{P}\boldsymbol{a}_2}), \tag{4.101}$$

$$B_{41} \quad = \quad 2\tilde{t}\,e^{i\boldsymbol{P}\boldsymbol{a}_4}(1+e^{-i\boldsymbol{P}\boldsymbol{a}_2})(1+e^{-i\boldsymbol{P}\boldsymbol{a}_3}) \tag{4.102}$$

$$B_{42} \quad = \quad -2\tilde{t}\,(1+e^{-i\boldsymbol{P}\boldsymbol{a}_1})(1+e^{i\boldsymbol{P}\boldsymbol{a}_3}) \tag{4.103}$$

$$B_{43} \quad = \quad -2\tilde{t}\,(1+e^{-i\boldsymbol{P}\boldsymbol{a}_1})(1+e^{i\boldsymbol{P}\boldsymbol{a}_2}) \tag{4.104}$$

$$B_{44} \quad = \quad -14\,\tilde{t} + 2\,\tilde{\varepsilon}_{\boldsymbol{P}} + 2\tilde{t}\cos\left(\boldsymbol{P}\boldsymbol{a}_4\right) - |V| \quad . \tag{4.105}$$

We note that our perturbation approach separates the singlet states from the triplet states like the (anti-)symmetrised solutions. Therefore, in the limit $U \to +\infty$, $V \to -\infty$, there are four bound singlet states with corresponding energies $E_1(\boldsymbol{P})$, $E_2(\boldsymbol{P})$, $E_3(\boldsymbol{P})$, and $E_4(\boldsymbol{P})$, and similarly, there are four bound triplet states with corresponding energies $E_1(\boldsymbol{P})$, $E_2(\boldsymbol{P})$, $E_3(\boldsymbol{P})$, and $E_4(\boldsymbol{P})$. These solutions are valid at arbitrary total pair momentum $\boldsymbol{P}$: this means that the BZ dispersion can be calculated in the strong coupling limit.

We compute the dispersion from direct UV solutions (4.15) and (4.23) and then compare it with the perturbative dispersion (4.70)–(4.73) with the parameters $V = -16W$, $U = +\infty$. The results are plotted in Figure 4.9. We note that these results are qualitatively and quantitatively consistent. With increasing intersite attraction V while considering higher-order contributions in perturbation, perhaps the dispersions would become replicas.
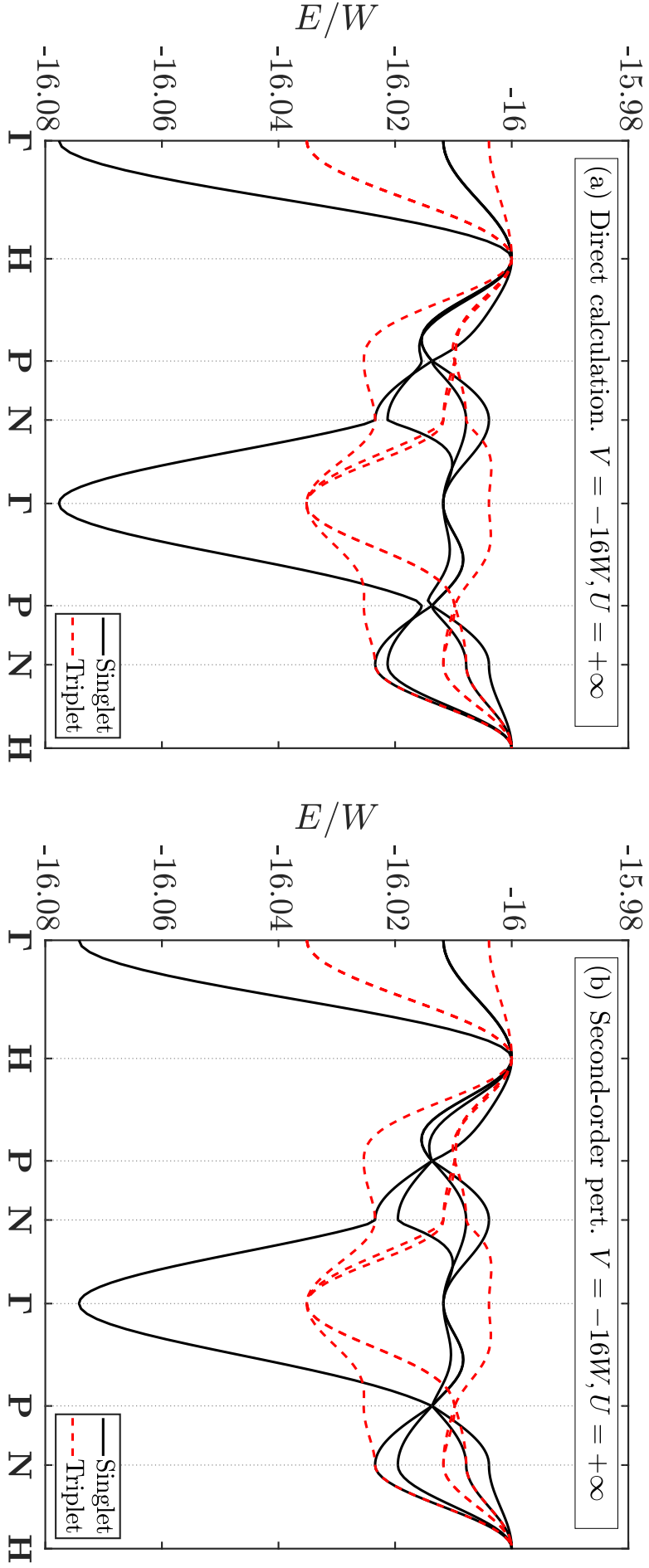
Figure 4.9: Direct calculation vs. second-order perturbation dispersion at $V = -16W$, $U = +\infty$.
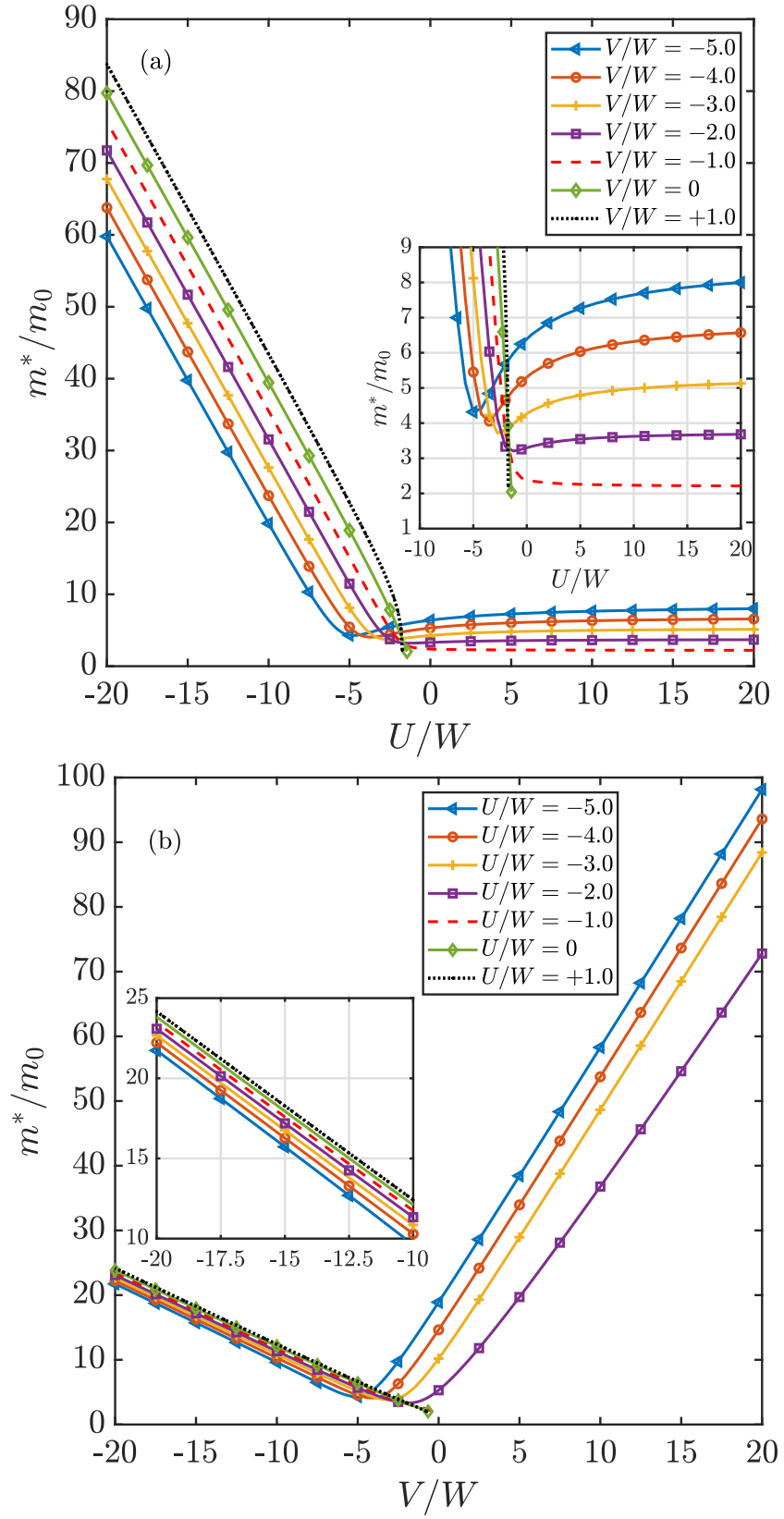
Figure 4.10: The pair mass expressed in the unit of a *free* particle mass. $m_0 = \hbar^2/(2b^2 t)$ is the bare mass of one free particle in the BCC lattice (see derivation in Appendix B).

4.3.4 Effective Mass

The pair mass denoted m^*, can be calculated from the second derivative of the dispersion within the standard effective mass approximation as

$$[m_i^*]^{-1} = \frac{1}{\hbar^2} \frac{\partial^2 E}{\partial P_i^2}. \tag{4.106}$$

where E and P is the pair total energy and momentum respectively.

The effective masses, measured relative to m_0, can be seen in Figure 4.10. Weakly bound pairs are light (about $2m_0$ when pair energy approaches the threshold energy E^{Th}) and get heavier as the binding attraction is increased. Note that $m_0 = \hbar^2/(2b^2 t)$ is the effective bare mass of *one* free particle in the BCC lattice (see derivation in Appendix B).

Pairs with strong intersite attraction are much lighter in comparison to their counterpart pairs with strong onsite attraction (for example, compare the masses at $U = -20W$ in Figure 4.10a and for $V = -20W$ in Figure 4.10b). This occurs since large attractive U confines the pair to the same site thereby suppressing the probability of particles hopping to other sites (the suppression is even greater when V is repulsive).

When U and V are both attractive and of similar magnitude, we find superlight pairs (minima in Figure 4.10a and 4.10b). These correspond to the situation where particles can move without passing through a high-energy intermediate state. Figure 4.11 demonstrates this superlight process where the pair travels through the lattice in a crawler motion [69]. The process of movement can be summarised in three main steps: (i) the particles interact via attractive V; (ii) one particle hops to interact with the other via an attractive U; (iii) either of the particles can hop so interaction is intersite again. While it moves around, the pair's total energy remains unchanged in all the configurations.
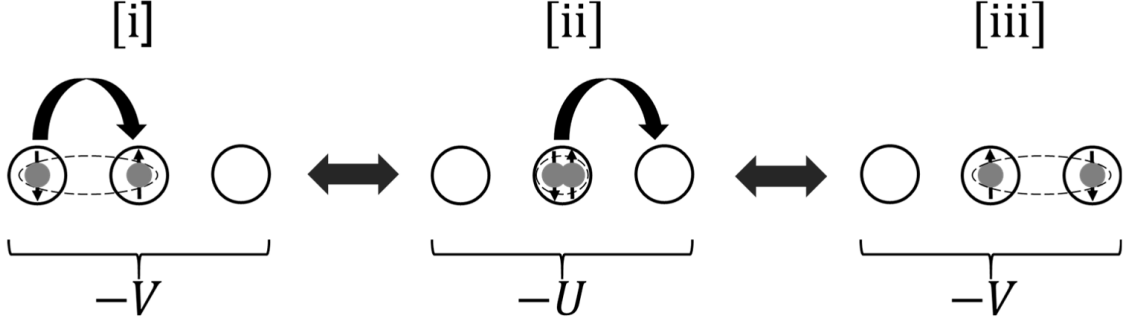
Figure 4.11: One-dimensional schematic of superlight behaviour of a singlet when U and V are comparable and sufficiently attractive. The big circle, grey ball (with vertical arrow), and the dashed line oval represent lattice site, particle (spin) and bonding, respectively. The two-way arrow indicates that the total energy of the pair E, is the same, thus hopping between configurations comes with no energy penalty.

4.3.5 Radius

The effective radius has been calculated using the relation

$$\langle r^* \rangle = \sqrt{\frac{\sum_{\boldsymbol{n}} \boldsymbol{n}^2 \Psi^*(\boldsymbol{n}_1, \boldsymbol{n}_2)\Psi(\boldsymbol{n}_1, \boldsymbol{n}_2)}{\sum_{\boldsymbol{n}} \Psi^*(\boldsymbol{n}_1, \boldsymbol{n}_2)\Psi(\boldsymbol{n}_1, \boldsymbol{n}_2)}} \quad , \tag{4.107}$$

where $\boldsymbol{n} = \boldsymbol{n}_1 - \boldsymbol{n}_2$ is the spatial separation between the particles and $\Psi(\boldsymbol{n}_1, \boldsymbol{n}_2)$ is the pair wavefunction in real-space.

The procedure for calculating the radius of a bound s-state is as follows. Firstly, we calculate the energy of the bound pair and obtain the eigenvectors using Equation (4.15). Then we create a basis set for the reciprocal lattice which in the case of a real-space BCC lattice has an FCC structure. Using a three-dimensional fast-Fourier-transform (FFT) algorithm, for example [101], we transform the k-space wavefunction $\phi^+_{\boldsymbol{k}_1 \boldsymbol{k}_2}$ in Equation (4.7) into its real-space counterpart $\Psi(\boldsymbol{n}_1, \boldsymbol{n}_2)$. Finally, we calculate $\boldsymbol{n}$, the relative position of the particles, and apply Equation (4.107) above.

Figure 4.12 shows the radius of a bound pair. Near the threshold energy ($E \to E^{\mathrm{Th}}$), the particles form a large pair: a consequence of the delocalisation of the pair wavefunction. At intermediate U and V (both attractive), the pair's size is on the order of

the near-neighbour distance, a (the horizontal line in Figure 4.12). In a pairing scenario where V is fixed and U is tuned to be highly attractive, the two bound particles are localised and held on the same site. The pair is also local for large intersite attractions, but the size levels off to the nearest-neighbour distance at large attractive V. By local, we mean bound pairs that are not larger than the lattice constant. Notice how a shoulder is formed when the onsite and intersite attraction are equal. This happens because the pair fluctuates between onsite and intersite configurations.
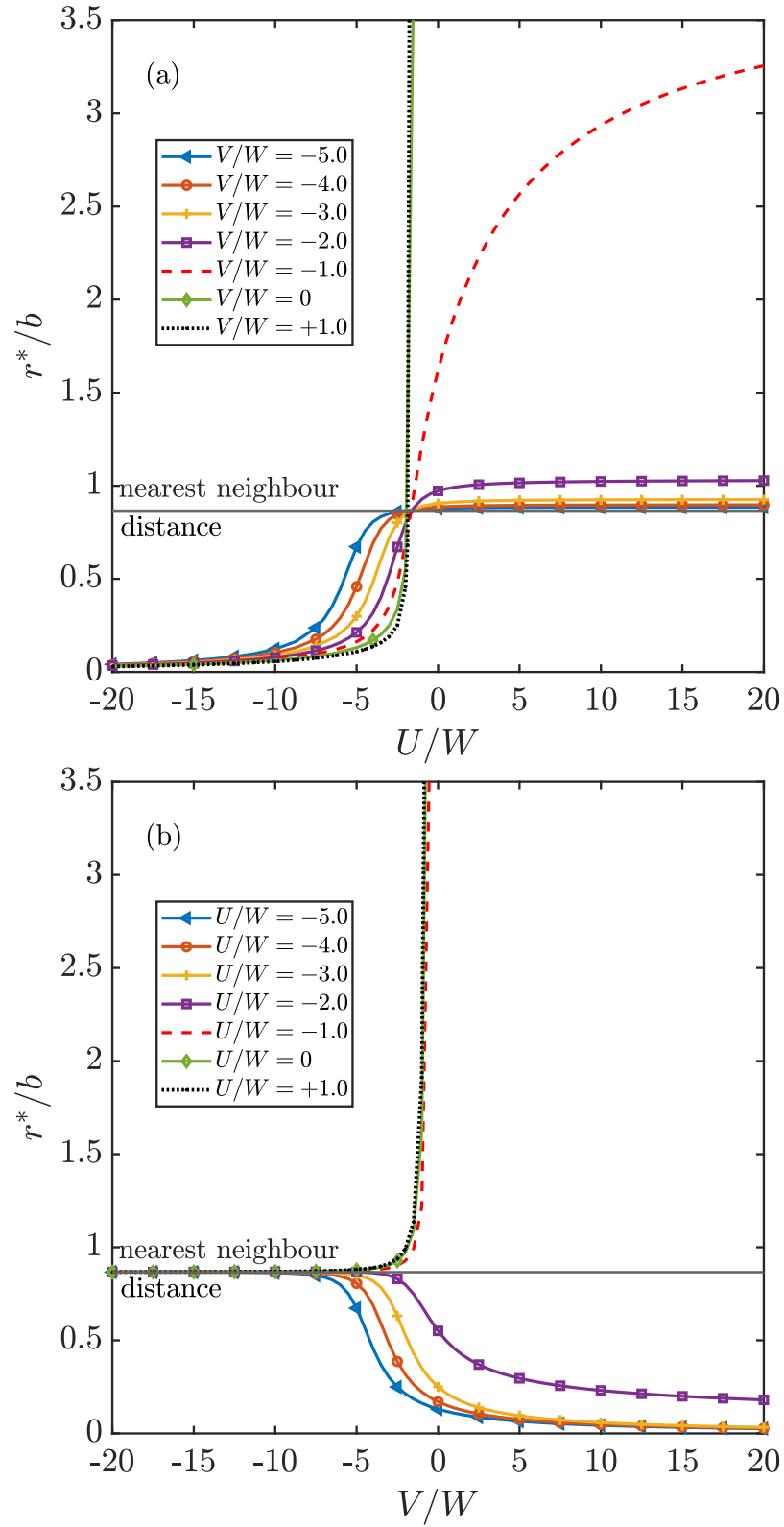
Figure 4.12: Effective radius for various U and V. The thin solid horizontal lines represent the nearest-neighbour distance $a = \sqrt{3}b/2$ on a BCC lattice. Note that the radius diverges at low attraction. A shoulder forms around the superlight regions (part of the curves when both attractions are comparable $U \sim V$).

4.3.6   Estimation of Transition Temperature

In this section, we redirect our attention back to ultra-cold atoms in optical lattices. As mentioned in Chapter 1, advancement in quantum technologies makes it possible to implement Hubbard models in a clean and precise manner. We also recall that the onsite and intersite interactions can be made attractive or repulsive: implying that phenomena like superconductivity and superfluidity could be simulated and observed experimentally.

At sufficiently low temperature, Bose-Einstein condensation of bound pairs may take place on the optical lattice for well-separated, weakly-interacting, local pairs (i.e. a dilute system). The BEC transition temperature can be calculated from the Bose integral:

$$\frac{n_b}{\Omega_{\text{site}}} = \int \frac{d^3 \boldsymbol{P}}{(2\pi)^3} \frac{1}{\exp[(E_{\boldsymbol{P}} - E_0)/k_B T_{\text{BEC}}] - 1} \tag{4.108}$$

where n_b is the number of pairs per lattice site, Ω_{site} is the volume of the Wigner–Seitz cell, k_B is Boltzmann's constant, T_{BEC} is the BEC transition temperature, and the pair dispersion $E_{\boldsymbol{P}}$ is used in this expression. At low energies, the behaviour of the pair dispersion is parabolic, as can be seen in Figure 4.5.

The Bose–Einstein distribution decreases rapidly when $E_{\boldsymbol{P}} - E_0 > T_{\text{BEC}}$. This means that only $\boldsymbol{P}$ points where $E_{\boldsymbol{P}} \lesssim k_B T_{\text{BEC}}$ contribute to the integral. For pair dispersions that are parabolic (i.e. consistent with an effective mass approximation) up to energy scales comparable with $k_B T_{\text{BEC}}$, the transition temperature is:

$$T_{\text{BEC}} \approx \frac{3.31 \hbar^2}{m_b^* k_B} \left(\frac{n_b}{\Omega_{\text{site}}} \right)^{2/3} \tag{4.109}$$

where m_b^* is the pair mass, $\hbar$ is the reduced Planck's constant, and $\Omega_{\text{site}} = b^3/2$ for a BCC lattice. Note that n_b is the number of pairs per site and should not be confused with the particle density, which is $n_b/\Omega_{\text{site}} = 2n_b/b^3$.

A four laser scheme can be used to construct a BCC optical lattice (see scheme A from Table 1 of Ref. [102]), for which $b/\lambda_{\text{beam}} = \sqrt{3}/2$. Then $\Omega_{\text{site}} = 3^{3/2} \lambda_{\text{beam}}^3/16$, so

we can re-write (4.109) in terms of the laser beam wavelength λ_{beam}, as

$$T_{\text{BEC}} = 7.01 \frac{n_b^{2/3} \hbar^2}{m_b^* k_B \lambda_{\text{beam}}^2}. \tag{4.110}$$

In the following, we assume either a red laser with wavelength 650 nm or a blue laser with wavelength 450 nm, and fermionic ^{6}Li atoms. Equations (4.109) and (4.110) are valid when pairs are dilute and weakly interacting. This means both that (1) n_b must be small, and (2) that the pair wavefunctions should not overlap strongly, else these equations need to be corrected. We also require that pairs exist before condensation such that $T_{\text{BEC}} < T_\Delta$, where $T_\Delta = \Delta/k_B$ is a characteristic pairing temperature and $\Delta = 2\varepsilon_0 - E_0$ (where ε_0 is the energy of a free particle with zero momentum, E_0 is the energy of a bound pair).

We can estimate the maximum n_b for which T_{BEC} is consistent with the effective mass approximation in the following way: If we express the effective pair hopping t_{eff}, in terms of the effective mass via $m_b^* = \hbar^2/2b^2 t_{\text{eff}}$, Equation (4.110) becomes

$$T_{\text{BEC}} = 10.52 \frac{n_b^{2/3} t_{\text{eff}}}{k_B}. \tag{4.111}$$

Typical pair dispersions have parabolic behaviour up to at least $E_{\boldsymbol{P}} \sim t_{\text{eff}}$. We set an upper bound that $k_B T_{\text{BEC}} \lesssim t_{\text{eff}}$ for the effective mass approximation to be reasonable. This leads to the estimate that $n_b \lesssim 10.52^{-3/2} = 0.0293$ for T_{BEC} to be consistent with the effective mass approximation.

The hopping in a sinusoidal optical lattice can be estimated [32] to be

$$t \approx \frac{h^2}{2\sqrt{\pi} M a^2} \left(\frac{V_0}{E_r}\right)^{3/4} \exp\left[-2\left(\frac{V_0}{E_r}\right)^{1/2}\right] \tag{4.112}$$

where a is the nearest-neighbour distance, V_0 is the depth of the lattice potential, E_r is the recoil energy and M is the atomic mass of the atoms. According to Ref. [32], this is accurate to $\sim$10% for $V_0/E_r \gtrsim 15$, and $\sim$15% for $V_0/E_r \gtrsim 10$. The recoil energy E_r is

given as

$$E_r = \frac{h^2}{8Ma^2} \qquad . \tag{4.113}$$

We use $V_0/E_r = 10$, thus, the hopping energy t scales as $\sim 10^{-12}$ electron-volt for ^{6}Li atoms. Using Equation (4.112), one can express the bare mass

$$m_0 = \frac{\hbar^2}{2b^2 t} \tag{4.114}$$

in terms of the atomic mass M as

$$m_0 \approx \frac{Ma^2}{4b^2\pi^{3/2}} \left(\frac{E_r}{V_0}\right)^{3/4} \exp\left[2\left(\frac{V_0}{E_r}\right)^{1/2}\right] \tag{4.115}$$

For BCC lattice, $a = \sqrt{3}b/2$, which means that $a^2/b^2 = 3/4$. Hence,

$$m_0 \approx \frac{3M}{16\pi^{3/2}} \left(\frac{E_r}{V_0}\right)^{3/4} \exp\left[2\left(\frac{V_0}{E_r}\right)^{1/2}\right] \tag{4.116}$$

The condition on overlap is whether pairs of radius $R' = \alpha r^*$ and density n_b can fit into space, i.e. that $8n_b R'^3/3 < 1$. The constant α should be sufficiently large that overlap of the exponentially decaying tails of the pair wavefunction are small. We suggest taking $\alpha = 5$. At higher densities we expect that pairs will start to interact and overlap and that would lead to many-body corrections that cause the transition temperature to level out and then fall as pairs begin to interact strongly and other phases are encountered (and potentially clusters form [103, 104, 105]).

We examine the transition temperature for fixed value of n_b, noting that there is a peak associated with the superlight behaviour of pairs (Figures 4.13a and 4.13b). The coloured regions of the plots indicate cases where the value of n_b is compatible with the conditions on pair overlap. Also, the dotted regions imply that the binding temperature T_Δ is lower than the estimated condensation temperature T_{BEC}, hence, the bound state cannot Bose condense. In order to probe the T_{BEC} of non-overlapping pairs with superlight characteristics (i.e. the peak in T_{BEC}) in an optical lattice setting, the
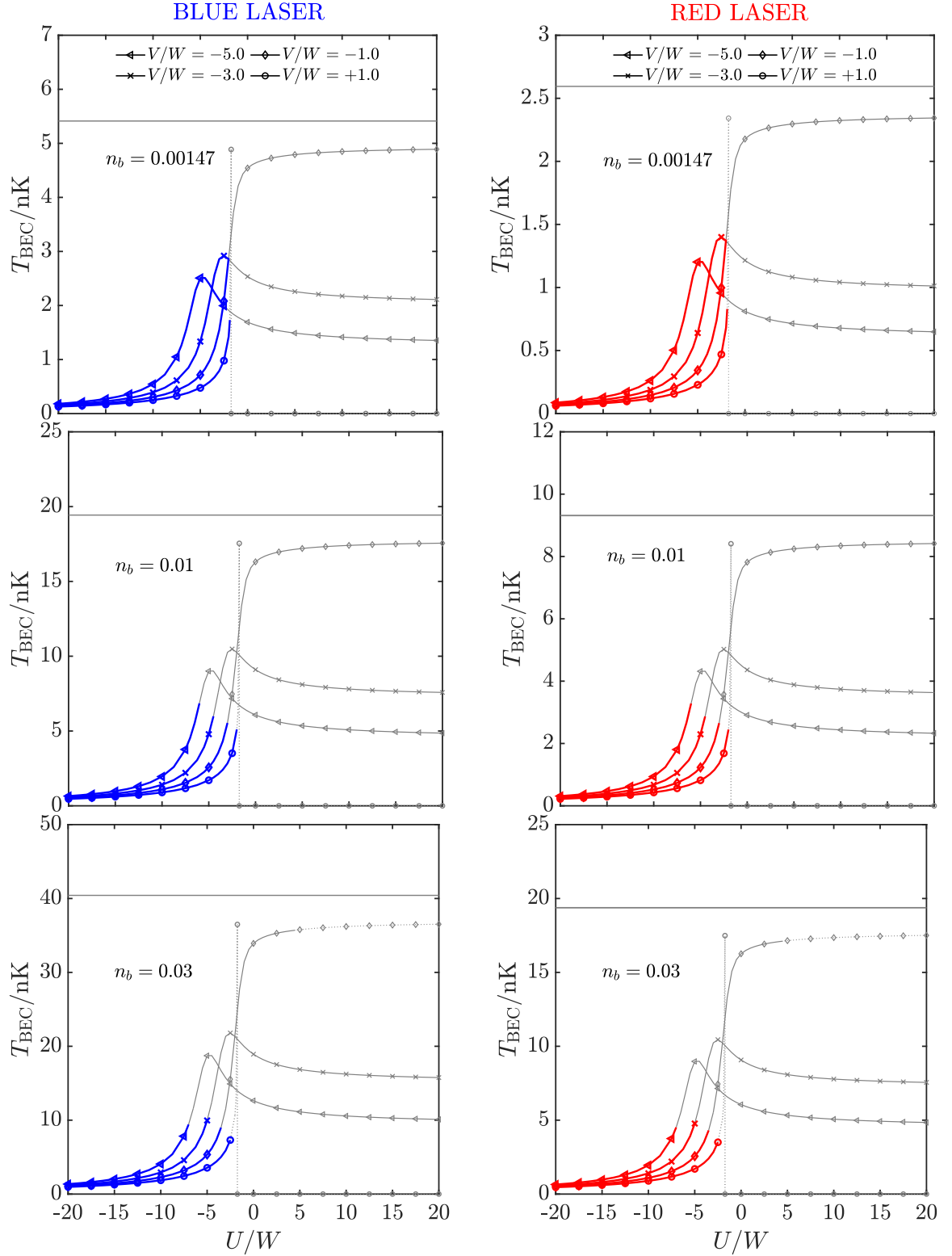
Figure 4.13a: BEC transition temperatures for ^{6}Li atoms in BCC lattices formed with blue and red lasers. Here, V is fixed while U is varied. The coloured regions in the plots indicate cases where the value of n_b is compatible with the conditions on pair overlap. The horizontal lines in each panel are the corresponding T_{BEC} value for $m^* = 2m_0$. The dotted regions imply that $T_\Delta < T_{\mathrm{BEC}}$ i.e. the pair is formed below the condensation temperature.
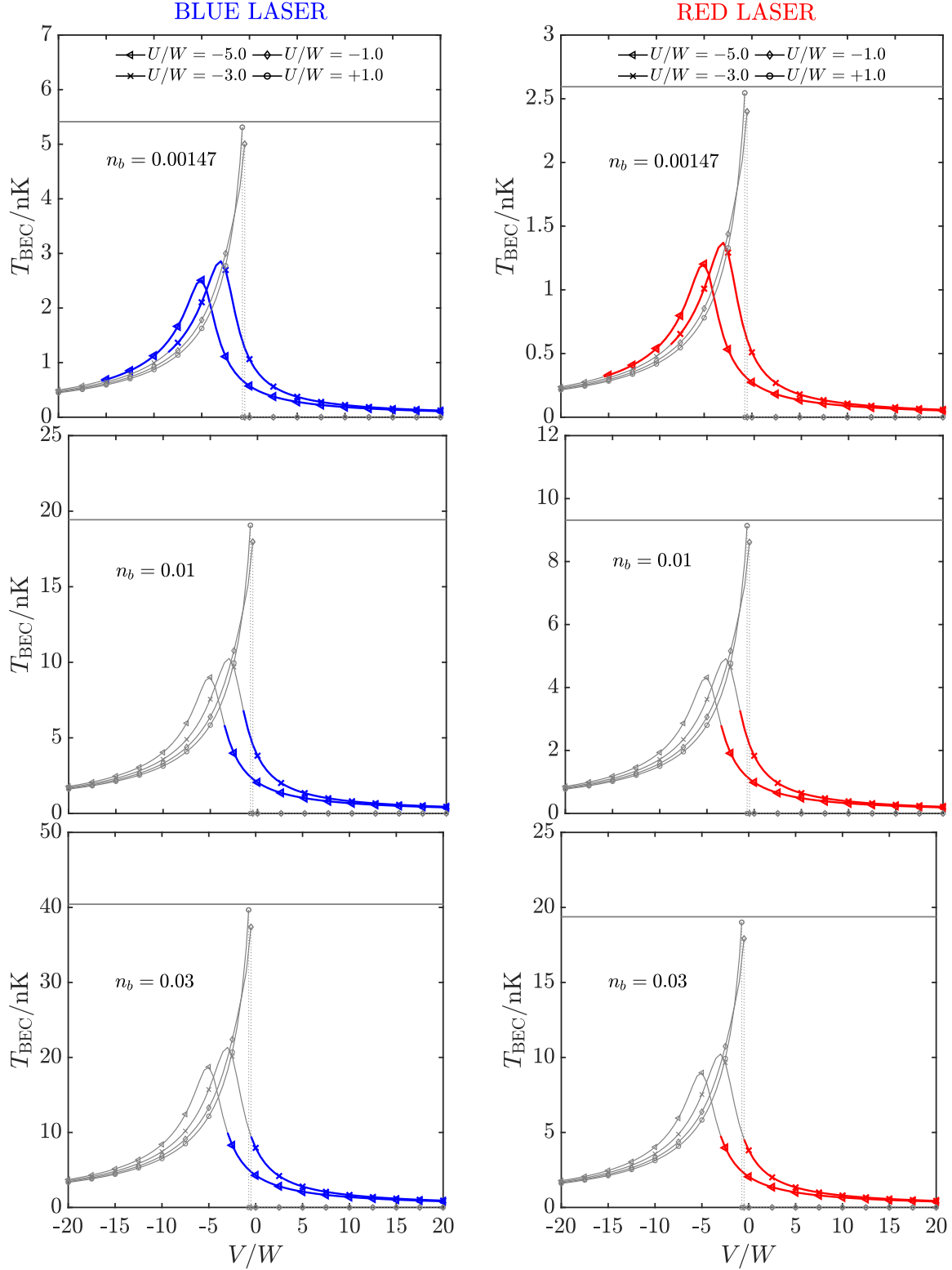
Figure 4.13b: BEC transition temperatures for ^{6}Li atoms in BCC lattices formed with blue and red lasers. Here, U is fixed while V is varied. The coloured regions in the plots indicate cases where the value of n_b is compatible with the conditions on pair overlap. The horizontal lines in each panel are the corresponding T_{BEC} value for $m^* = 2m_0$. The dotted regions imply that $T_\Delta < T_{\text{BEC}}$ i.e. the pair is formed below the condensation temperature.

number of pairs has to be low (say $n_b \sim 0.0015$). In that case, the superlight behaviour occurs at roughly 3 nK.

4.4   Discussion

The formation and condensation of fermion pairs in cold atom quantum simulators (optical lattice) with BCC structure have been investigated. We make calculations of BEC transition temperatures and other pair properties.

To examine pair properties in the dilute limit, we have solved the two-particle Schrödinger equation to analytically compute the critical interactions required for binding, pair total energy, mass, radius, and transition temperatures. Using group theory analysis, we identified the different pair symmetries and diagonalised the secular equations. Furthermore, we constructed BZ dispersions of bound pairs. We note the uniqueness of the H point which shares some similarities with the Dirac points in graphene. At the H point: (a) surprisingly, particles can bind with very small attractions U or V, (b) pairs formed in the limit of equal onsite and intersite attractions have very high degeneracy where all bands cross. By performing second-order perturbation calculations, the dispersion results were validated in the strong coupling limits. We also found that local pairs formed in BCC optical lattices can have light masses. By considering fermionic ^{6}Li atoms, we estimated Bose-Einstein condensation of non-overlapping pairs to occur around 10 nK.

The mass of a bound pair becomes superlight when U and V are of similar magnitude and both attractive. In this regime, the pair is highly mobile with graphene-like dispersion characteristics and can move freely through the optical lattice without the need to access high-energy intermediate states. This low mass state corresponds to a change

from onsite pairs to intersite pairs and leads to a peak in the transition temperature. Superlight states have been predicted to lead to high superconducting transition temperatures [69], and they are of particular interest in electron-phonon systems where a single particle's mass is greatly enhanced due to retarded self-interaction effect. The ability to examine superlight behaviour and the properties of pairs in BCC lattices is of interest because there are no previous calculations regarding pairing on a BCC optical lattice. We note that pairs form above the condensation temperature, thus, pair properties are accessible at higher temperatures.

Chapter 5

Superlight States for High-T_c Superconductivity in FCC Lattices

5.1 Summary

This chapter has a similar structure to Chapter 4 since they both present solutions to the UV model but in distinct lattices, and the lattice of consideration in this chapter is more complex. This chapter is structured as follows: After solving the (anti-)symmetrised Schödinger equation of two fermions in an FCC lattice in Section 5.2, the properties of the two bound particles, as well as the Bose-Einstein condensation of pairs are then reported in Section 5.3. Lastly, this chapter concludes with a discussion in Section 5.4.

5.2   Preliminaries

Unlike in the simple cubic and BCC lattices, the two-particle problem in an FCC lattice is harder. Partly due to its complicated structure and the larger coordination number. The 12 nearest-neighbour sites of an FCC lattice is shown in Figure 5.1. The vectors in an FCC unit cell, expressed in terms of the lattice constant b, are $(0,0,0)$, $(\frac{b}{2}, \frac{b}{2}, 0)$, $(-\frac{b}{2}, -\frac{b}{2}, 0)$, $(\frac{b}{2}, -\frac{b}{2}, 0)$, $(-\frac{b}{2}, \frac{b}{2}, 0)$, $(0, \frac{b}{2}, \frac{b}{2})$, $(0, -\frac{b}{2}, -\frac{b}{2})$, $(0, \frac{b}{2}, -\frac{b}{2})$, $(0, -\frac{b}{2}, \frac{b}{2})$, $(\frac{b}{2}, 0, \frac{b}{2})$, $(-\frac{b}{2}, 0, -\frac{b}{2})$, $(\frac{b}{2}, 0, -\frac{b}{2})$, and $(-\frac{b}{2}, 0, \frac{b}{2})$.
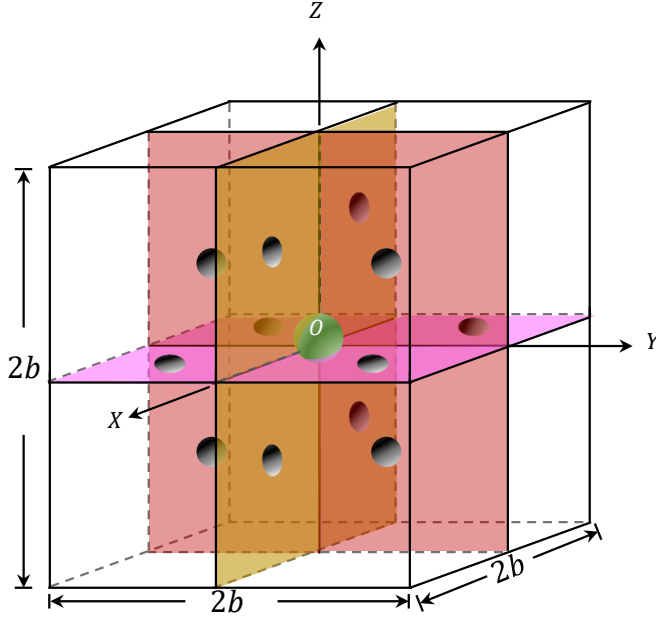
Figure 5.1: Visualising the 12 nearest-neighbour sites (grey oval circles) with respect to a central lattice site (green circle) in an FCC lattice.

We derived the (anti-)symmetrised solution in Chapter 3 to be

$$(E - \varepsilon_{\boldsymbol{k}_1} - \varepsilon_{\boldsymbol{k}_2})\phi^{\pm}_{\boldsymbol{k}_1\boldsymbol{k}_2} = \frac{1}{N}\sideset{}{'}\sum_{\boldsymbol{q}\boldsymbol{a}_{\pm}} \hat{V}_{\boldsymbol{a}_{\pm}} \left\{ e^{i(\boldsymbol{q}-\boldsymbol{k}_1)\,\boldsymbol{a}_{\pm}} \pm e^{i(\boldsymbol{q}-\boldsymbol{k}_2)\,\boldsymbol{a}_{\pm}} \right\} \phi^{\pm}_{\boldsymbol{q},\boldsymbol{k}_1+\boldsymbol{k}_2-\boldsymbol{q}} \qquad (5.1)$$

where the singlet and triplet wave function is respectively $\phi^{+}_{\boldsymbol{q},\boldsymbol{k}_1+\boldsymbol{k}_2-\boldsymbol{q}}$ and $\phi^{-}_{\boldsymbol{q},\boldsymbol{k}_1+\boldsymbol{k}_2-\boldsymbol{q}}$. In an FCC lattice, the free-particle dispersion is

$$\varepsilon_{\boldsymbol{k}} = -\sum_{\boldsymbol{a}} t\,e^{i\boldsymbol{k}\cdot\boldsymbol{a}} = -4t\left[\cos\frac{k_x b}{2}\cdot\cos\frac{k_y b}{2} + \cos\frac{k_y b}{2}\cdot\cos\frac{k_z b}{2} + \cos\frac{k_x b}{2}\cdot\cos\frac{k_z b}{2}\right] \qquad (5.2)$$

As required, we define the vector sets $\{\boldsymbol{a}_+\}$ and $\{\boldsymbol{a}_-\}$ to split symmetric and anti-symmetric states, and then substitute them into Equation (5.1) to give (7×7) and (6×6) matrices for the singlets and triplet states, respectively. For example *

$$\{\boldsymbol{a}_+\} = \{\boldsymbol{a}_0^+, \boldsymbol{a}_1^+, \boldsymbol{a}_2^+, \boldsymbol{a}_3^+, \boldsymbol{a}_4^+, \boldsymbol{a}_5^+, \boldsymbol{a}_6^+\} \tag{5.3}$$

$$= \{(0,0,0), (\frac{b}{2}, \frac{b}{2}, 0), (0, \frac{b}{2}, \frac{b}{2}), (\frac{b}{2}, 0, \frac{b}{2}), (\frac{b}{2}, -\frac{b}{2}, 0), (0, \frac{b}{2}, -\frac{b}{2}), (-\frac{b}{2}, 0, \frac{b}{2})\} \tag{5.4}$$

$$\{\boldsymbol{a}_-\} = \{\boldsymbol{a}_1^-, \boldsymbol{a}_2^-, \boldsymbol{a}_3^-, \boldsymbol{a}_4^-, \boldsymbol{a}_5^-, \boldsymbol{a}_6^-\} \tag{5.5}$$

$$= \{(\frac{b}{2}, \frac{b}{2}, 0), (0, \frac{b}{2}, \frac{b}{2}), (\frac{b}{2}, 0, \frac{b}{2}), (\frac{b}{2}, -\frac{b}{2}, 0), (0, \frac{b}{2}, -\frac{b}{2}), (-\frac{b}{2}, 0, \frac{b}{2})\} \tag{5.6}$$

### 5.2.1   Solution for Singlets

For the singlets, we make use of the vectors $\{\boldsymbol{a}_+\}$ in Equation (5.1) † to obtain

$$
\begin{aligned}
(E - \varepsilon_{\boldsymbol{k}_1} - \varepsilon_{\boldsymbol{k}_2})\phi_{\boldsymbol{k}_1\boldsymbol{k}_2}^+ = & \frac{1}{N}\sum_{\boldsymbol{q}} \left[\frac{1}{2}U(e^{i(\boldsymbol{q}-\boldsymbol{k}_1)\boldsymbol{a}_0^+} + e^{i(\boldsymbol{q}-\boldsymbol{k}_2)\boldsymbol{a}_0^+}) + V(e^{i(\boldsymbol{q}-\boldsymbol{k}_1)\boldsymbol{a}_1^+} + e^{i(\boldsymbol{q}-\boldsymbol{k}_2)\boldsymbol{a}_1^+}) \right. \\
& + V(e^{i(\boldsymbol{q}-\boldsymbol{k}_1)\boldsymbol{a}_2^+} + e^{i(\boldsymbol{q}-\boldsymbol{k}_2)\boldsymbol{a}_2^+}) + V(e^{i(\boldsymbol{q}-\boldsymbol{k}_1)\boldsymbol{a}_3^+} + e^{i(\boldsymbol{q}-\boldsymbol{k}_2)\boldsymbol{a}_3^+}) \\
& + V(e^{i(\boldsymbol{q}-\boldsymbol{k}_1)\boldsymbol{a}_4^+} + e^{i(\boldsymbol{q}-\boldsymbol{k}_2)\boldsymbol{a}_4^+}) + V(e^{i(\boldsymbol{q}-\boldsymbol{k}_1)\boldsymbol{a}_5^+} + e^{i(\boldsymbol{q}-\boldsymbol{k}_2)\boldsymbol{a}_5^+}) \\
& \left. + V(e^{i(\boldsymbol{q}-\boldsymbol{k}_1)\boldsymbol{a}_6^+} + e^{i(\boldsymbol{q}-\boldsymbol{k}_2)\boldsymbol{a}_6^+}) \right]\phi_{\boldsymbol{q},\boldsymbol{k}_1+\boldsymbol{k}_2-\boldsymbol{q}}^+ \\
= & \frac{1}{N}\sum_{\boldsymbol{q}} \left[U + V\,e^{i(\frac{q_x}{2}+\frac{q_y}{2})}(e^{-i\boldsymbol{k}_1\boldsymbol{a}_1^+} + e^{-i\boldsymbol{k}_2\boldsymbol{a}_1^+}) \right. \\
& + V\,e^{i(\frac{q_y}{2}+\frac{q_z}{2})}(e^{-i\boldsymbol{k}_1\boldsymbol{a}_2^+} + e^{-i\boldsymbol{k}_2\boldsymbol{a}_2^+}) \\
& + V\,e^{i(\frac{q_x}{2}+\frac{q_z}{2})}(e^{-i\boldsymbol{k}_1\boldsymbol{a}_3^+} + e^{-i\boldsymbol{k}_2\boldsymbol{a}_3^+}) \\
& + V\,e^{i(\frac{q_x}{2}-\frac{q_y}{2})}(e^{-i\boldsymbol{k}_1\boldsymbol{a}_4^+} + e^{-i\boldsymbol{k}_2\boldsymbol{a}_4^+}) \\
& + V\,e^{i(\frac{q_y}{2}-\frac{q_z}{2})}(e^{-i\boldsymbol{k}_1\boldsymbol{a}_5^+} + e^{-i\boldsymbol{k}_2\boldsymbol{a}_5^+}) \\
& \left. + V\,e^{i(-\frac{q_x}{2}+\frac{q_z}{2})}(e^{-i\boldsymbol{k}_1\boldsymbol{a}_6^+} + e^{-i\boldsymbol{k}_2\boldsymbol{a}_6^+}) \right]\phi_{\boldsymbol{q},\boldsymbol{k}_1+\boldsymbol{k}_2-\boldsymbol{q}}^+
\end{aligned}
$$

$$\tag{5.7}$$

---

*As before, no member of a set is related by inversion and $\boldsymbol{a}_0^+$ belongs to the singlets.
†We require that $\boldsymbol{a}_+ = \boldsymbol{0}$ term must be multiplied by $\frac{1}{2}$ to account for double occupancy.

If we substitute the following basis functions

$$\Phi_0^+(\boldsymbol{P}) = \frac{1}{N}\sum_{\boldsymbol{q}} \phi_{\boldsymbol{q},\boldsymbol{P}-\boldsymbol{q}}^+ \,, \quad \Phi_1^+(\boldsymbol{P}) = \frac{1}{N}\sum_{\boldsymbol{q}} e^{i(\frac{q_x}{2}+\frac{q_y}{2})} \phi_{\boldsymbol{q},\boldsymbol{P}-\boldsymbol{q}}^+ \,,$$

$$\Phi_2^+(\boldsymbol{P}) = \frac{1}{N}\sum_{\boldsymbol{q}} e^{i(\frac{q_y}{2}+\frac{q_z}{2})} \phi_{\boldsymbol{q},\boldsymbol{P}-\boldsymbol{q}}^+ \,, \quad \Phi_3^+(\boldsymbol{P}) = \frac{1}{N}\sum_{\boldsymbol{q}} e^{i(\frac{q_x}{2}+\frac{q_z}{2})} \phi_{\boldsymbol{q},\boldsymbol{P}-\boldsymbol{q}}^+ \,,$$

$$\Phi_4^+(\boldsymbol{P}) = \frac{1}{N}\sum_{\boldsymbol{q}} e^{i(\frac{q_x}{2}-\frac{q_y}{2})} \phi_{\boldsymbol{q},\boldsymbol{P}-\boldsymbol{q}}^+ \,, \quad \Phi_5^+(\boldsymbol{P}) = \frac{1}{N}\sum_{\boldsymbol{q}} e^{i(\frac{q_y}{2}-\frac{q_z}{2})} \phi_{\boldsymbol{q},\boldsymbol{P}-\boldsymbol{q}}^+ \,, \tag{5.8}$$

$$\Phi_6^+(\boldsymbol{P}) = \frac{1}{N}\sum_{\boldsymbol{q}} e^{i(-\frac{q_x}{2}+\frac{q_z}{2})} \phi_{\boldsymbol{q},\boldsymbol{P}-\boldsymbol{q}}^+$$

where $\boldsymbol{P} = \boldsymbol{k}_1 + \boldsymbol{k}_2$, into Equation (5.7) to arrive at the generalised expression

$$\phi_{\boldsymbol{k}_1\boldsymbol{k}_2}^+ = \frac{1}{(E-\varepsilon_{\boldsymbol{k}_1}-\varepsilon_{\boldsymbol{k}_2})}\left\{ U\Phi_0^+(\boldsymbol{P}) + V\,\Phi_1^+(\boldsymbol{P})(e^{-i\boldsymbol{k}_1\boldsymbol{a}_1^+}+e^{-i\boldsymbol{k}_2\boldsymbol{a}_1^+}) \right.$$

$$+ V\,\Phi_2^+(\boldsymbol{P})(e^{-i\boldsymbol{k}_1\boldsymbol{a}_2^+}+e^{-i\boldsymbol{k}_2\boldsymbol{a}_2^+}) + V\,\Phi_3^+(\boldsymbol{P})(e^{-i\boldsymbol{k}_1\boldsymbol{a}_3^+}+e^{-i\boldsymbol{k}_2\boldsymbol{a}_3^+})$$

$$+ V\,\Phi_4^+(\boldsymbol{P})(e^{-i\boldsymbol{k}_1\boldsymbol{a}_4^+}+e^{-i\boldsymbol{k}_2\boldsymbol{a}_4^+}) + V\,\Phi_5^+(\boldsymbol{P})(e^{-i\boldsymbol{k}_1\boldsymbol{a}_5^+}+e^{-i\boldsymbol{k}_2\boldsymbol{a}_5^+}) \tag{5.9}$$

$$\left. + V\,\Phi_6^+(\boldsymbol{P})(e^{-i\boldsymbol{k}_1\boldsymbol{a}_6^+}+e^{-i\boldsymbol{k}_2\boldsymbol{a}_6^+}) \right\}$$

Applying Equation (5.9) to each basis function $\Phi_0^+(\boldsymbol{P}),\Phi_1^+(\boldsymbol{P})...\ \Phi_6^+(\boldsymbol{P})$ and redefining $q_j = q_j' + \frac{P_j}{2}$ would yield the seven distinct equations below.

$$\Phi_0^+(\boldsymbol{P}) = \frac{1}{N}\sum_{\boldsymbol{q}'} \frac{1}{E-\varepsilon_{\frac{P}{2}+\boldsymbol{q}'}-\varepsilon_{\frac{P}{2}-\boldsymbol{q}'}}\left\{ U\Phi_0^+(\boldsymbol{P}) \right.$$

$$+ V\Phi_1^+(\boldsymbol{P})\,e^{-i(\frac{P_x}{4}+\frac{P_y}{4})}\left[e^{i(\frac{q_x'}{2}+\frac{q_y'}{2})}+e^{-i(\frac{q_x'}{2}+\frac{q_y'}{2})}\right]$$

$$+ V\Phi_2^+(\boldsymbol{P})\,e^{-i(\frac{P_y}{4}+\frac{P_z}{4})}\left[e^{i(\frac{q_y'}{2}+\frac{q_z'}{2})}+e^{-i(\frac{q_y'}{2}+\frac{q_z'}{2})}\right]$$

$$+ V\Phi_3^+(\boldsymbol{P})\,e^{-i(\frac{P_x}{4}+\frac{P_z}{4})}\left[e^{i(\frac{q_x'}{2}+\frac{q_z'}{2})}+e^{-i(\frac{q_x'}{2}+\frac{q_z'}{2})}\right] \tag{5.10}$$

$$+ V\Phi_4^+(\boldsymbol{P})\,e^{-i(\frac{P_x}{4}-\frac{P_y}{4})}\left[e^{i(\frac{q_x'}{2}-\frac{q_y'}{2})}+e^{-i(\frac{q_x'}{2}-\frac{q_y'}{2})}\right]$$

$$+ V\Phi_5^+(\boldsymbol{P})\,e^{-i(\frac{P_y}{4}-\frac{P_z}{4})}\left[e^{i(\frac{q_y'}{2}-\frac{q_z'}{2})}+e^{-i(\frac{q_y'}{2}-\frac{q_z'}{2})}\right]$$

$$\left. + V\Phi_6^+(\boldsymbol{P})\,e^{-i(-\frac{P_x}{4}+\frac{P_z}{4})}\left[e^{i(-\frac{q_x'}{2}+\frac{q_z'}{2})}+e^{-i(-\frac{q_x'}{2}+\frac{q_z'}{2})}\right] \right\}$$

$$\tilde{\Phi}_0^+(\boldsymbol{P}) = U\mathcal{G}_{000}(\boldsymbol{P})\tilde{\Phi}_0^+(\boldsymbol{P}) + V\Big[\mathcal{G}_{110}(\boldsymbol{P}) + \mathcal{G}_{\bar{1}\bar{1}0}(\boldsymbol{P})\Big]\tilde{\Phi}_1^+(\boldsymbol{P})$$

$$+ V\Big[\mathcal{G}_{011}(\boldsymbol{P}) + \mathcal{G}_{0\bar{1}\bar{1}}(\boldsymbol{P})\Big]\tilde{\Phi}_2^+(\boldsymbol{P}) + V\Big[\mathcal{G}_{101}(\boldsymbol{P}) + \mathcal{G}_{\bar{1}0\bar{1}}(\boldsymbol{P})\Big]\tilde{\Phi}_3^+(\boldsymbol{P})$$

$$+ V\Big[\mathcal{G}_{1\bar{1}0}(\boldsymbol{P}) + \mathcal{G}_{\bar{1}10}(\boldsymbol{P})\Big]\tilde{\Phi}_4^+(\boldsymbol{P}) + V\Big[\mathcal{G}_{01\bar{1}}(\boldsymbol{P}) + \mathcal{G}_{0\bar{1}1}(\boldsymbol{P})\Big]\tilde{\Phi}_5^+(\boldsymbol{P})$$

$$+ V\Big[\mathcal{G}_{\bar{1}01}(\boldsymbol{P}) + \mathcal{G}_{10\bar{1}}(\boldsymbol{P})\Big]\tilde{\Phi}_6^+(\boldsymbol{P}) \tag{5.11}$$

$$\tilde{\Phi}_1^+(\boldsymbol{P}) = U\tilde{\Phi}_0^+(\boldsymbol{P})\mathcal{G}_{110}(\boldsymbol{P}) + V\Big[\mathcal{G}_{000}(\boldsymbol{P}) + \mathcal{G}_{220}(\boldsymbol{P})\Big]\tilde{\Phi}_1^+(\boldsymbol{P}) + V\Big[\mathcal{G}_{10\bar{1}}(\boldsymbol{P}) + \mathcal{G}_{121}(\boldsymbol{P})\Big]\tilde{\Phi}_2^+(\boldsymbol{P})$$

$$+ V\Big[\mathcal{G}_{01\bar{1}}(\boldsymbol{P}) + \mathcal{G}_{211}(\boldsymbol{P})\Big]\tilde{\Phi}_3^+(\boldsymbol{P}) + V\Big[\mathcal{G}_{020}(\boldsymbol{P}) + \mathcal{G}_{200}(\boldsymbol{P})\Big]\tilde{\Phi}_4^+(\boldsymbol{P})$$

$$+ V\Big[\mathcal{G}_{101}(\boldsymbol{P}) + \mathcal{G}_{12\bar{1}}(\boldsymbol{P})\Big]\tilde{\Phi}_5^+(\boldsymbol{P}) + V\Big[\mathcal{G}_{21\bar{1}}(\boldsymbol{P}) + \mathcal{G}_{011}(\boldsymbol{P})\Big]\tilde{\Phi}_6^+(\boldsymbol{P}) \tag{5.12}$$

$$\tilde{\Phi}_2^+(\boldsymbol{P}) = U\tilde{\Phi}_0^+(\boldsymbol{P})\mathcal{G}_{011}(\boldsymbol{P}) + V\Big[\mathcal{G}_{\bar{1}01}(\boldsymbol{P}) + \mathcal{G}_{121}(\boldsymbol{P})\Big]\tilde{\Phi}_1^+(\boldsymbol{P}) + V\Big[\mathcal{G}_{000}(\boldsymbol{P}) + \mathcal{G}_{022}(\boldsymbol{P})\Big]\tilde{\Phi}_2^+(\boldsymbol{P})$$

$$+ V\Big[\mathcal{G}_{\bar{1}10}(\boldsymbol{P}) + \mathcal{G}_{112}(\boldsymbol{P})\Big]\tilde{\Phi}_3^+(\boldsymbol{P}) + V\Big[\mathcal{G}_{\bar{1}21}(\boldsymbol{P}) + \mathcal{G}_{101}(\boldsymbol{P})\Big]\tilde{\Phi}_4^+(\boldsymbol{P})$$

$$+ V\Big[\mathcal{G}_{002}(\boldsymbol{P}) + \mathcal{G}_{020}(\boldsymbol{P})\Big]\tilde{\Phi}_5^+(\boldsymbol{P}) + V\Big[\mathcal{G}_{110}(\boldsymbol{P}) + \mathcal{G}_{\bar{1}12}(\boldsymbol{P})\Big]\tilde{\Phi}_6^+(\boldsymbol{P}) \tag{5.13}$$

$$\tilde{\Phi}_3^+(\boldsymbol{P}) = U\tilde{\Phi}_0^+(\boldsymbol{P})\mathcal{G}_{101}(\boldsymbol{P}) + V\Big[\mathcal{G}_{0\bar{1}1}(\boldsymbol{P}) + \mathcal{G}_{211}(\boldsymbol{P})\Big]\tilde{\Phi}_1^+(\boldsymbol{P}) + V\Big[\mathcal{G}_{1\bar{1}0}(\boldsymbol{P}) + \mathcal{G}_{112}(\boldsymbol{P})\Big]\tilde{\Phi}_2^+(\boldsymbol{P})$$

$$+ V\Big[\mathcal{G}_{000}(\boldsymbol{P}) + \mathcal{G}_{202}(\boldsymbol{P})\Big]\tilde{\Phi}_3^+(\boldsymbol{P}) + V\Big[\mathcal{G}_{011}(\boldsymbol{P}) + \mathcal{G}_{2\bar{1}1}(\boldsymbol{P})\Big]\tilde{\Phi}_4^+(\boldsymbol{P})$$

$$+ V\Big[\mathcal{G}_{1\bar{1}2}(\boldsymbol{P}) + \mathcal{G}_{110}(\boldsymbol{P})\Big]\tilde{\Phi}_5^+(\boldsymbol{P}) + V\Big[\mathcal{G}_{200}(\boldsymbol{P}) + \mathcal{G}_{002}(\boldsymbol{P})\Big]\tilde{\Phi}_6^+(\boldsymbol{P}) \tag{5.14}$$

$$\tilde{\Phi}_4^+(\boldsymbol{P}) = U\tilde{\Phi}_0^+(\boldsymbol{P})\mathcal{G}_{1\bar{1}0}(\boldsymbol{P}) + V\Big[\mathcal{G}_{0\bar{2}0}(\boldsymbol{P}) + \mathcal{G}_{200}(\boldsymbol{P})\Big]\tilde{\Phi}_1^+(\boldsymbol{P}) + V\Big[\mathcal{G}_{1\bar{2}\bar{1}}(\boldsymbol{P}) + \mathcal{G}_{101}(\boldsymbol{P})\Big]\tilde{\Phi}_2^+(\boldsymbol{P})$$

$$+ V\Big[\mathcal{G}_{0\bar{1}\bar{1}}(\boldsymbol{P}) + \mathcal{G}_{2\bar{1}1}(\boldsymbol{P})\Big]\tilde{\Phi}_3^+(\boldsymbol{P}) + V\Big[\mathcal{G}_{000}(\boldsymbol{P}) + \mathcal{G}_{2\bar{2}0}(\boldsymbol{P})\Big]\tilde{\Phi}_4^+(\boldsymbol{P})$$

$$+ V\Big[\mathcal{G}_{1\bar{2}1}(\boldsymbol{P}) + \mathcal{G}_{10\bar{1}}(\boldsymbol{P})\Big]\tilde{\Phi}_5^+(\boldsymbol{P}) + V\Big[\mathcal{G}_{2\bar{1}\bar{1}}(\boldsymbol{P}) + \mathcal{G}_{0\bar{1}1}(\boldsymbol{P})\Big]\tilde{\Phi}_6^+(\boldsymbol{P}) \tag{5.15}$$

$$\tilde{\Phi}_5^+(\boldsymbol{P}) = U\tilde{\Phi}_0^+(\boldsymbol{P})\mathcal{G}_{01\bar{1}}(\boldsymbol{P}) + V\Big[\mathcal{G}_{\bar{1}0\bar{1}}(\boldsymbol{P}) + \mathcal{G}_{12\bar{1}}(\boldsymbol{P})\Big]\tilde{\Phi}_1^+(\boldsymbol{P}) + V\Big[\mathcal{G}_{00\bar{2}}(\boldsymbol{P}) + \mathcal{G}_{020}(\boldsymbol{P})\Big]\tilde{\Phi}_2^+(\boldsymbol{P})$$

$$+ V\Big[\mathcal{G}_{\bar{1}1\bar{2}}(\boldsymbol{P}) + \mathcal{G}_{110}(\boldsymbol{P})\Big]\tilde{\Phi}_3^+(\boldsymbol{P}) + V\Big[\mathcal{G}_{\bar{1}2\bar{1}}(\boldsymbol{P}) + \mathcal{G}_{10\bar{1}}(\boldsymbol{P})\Big]\tilde{\Phi}_4^+(\boldsymbol{P})$$

$$+ V\Big[\mathcal{G}_{000}(\boldsymbol{P}) + \mathcal{G}_{02\bar{2}}(\boldsymbol{P})\Big]\tilde{\Phi}_5^+(\boldsymbol{P}) + V\Big[\mathcal{G}_{11\bar{2}}(\boldsymbol{P}) + \mathcal{G}_{\bar{1}10}(\boldsymbol{P})\Big]\tilde{\Phi}_6^+(\boldsymbol{P})$$

$$(5.16)$$

$$\tilde{\Phi}_6^+(\boldsymbol{P}) = U\tilde{\Phi}_0^+(\boldsymbol{P})\mathcal{G}_{\bar{1}01}(\boldsymbol{P}) + V\Big[\mathcal{G}_{\bar{2}\bar{1}1}(\boldsymbol{P}) + \mathcal{G}_{011}(\boldsymbol{P})\Big]\tilde{\Phi}_1^+(\boldsymbol{P}) + V\Big[\mathcal{G}_{\bar{1}\bar{1}0}(\boldsymbol{P}) + \mathcal{G}_{\bar{1}12}(\boldsymbol{P})\Big]\tilde{\Phi}_2^+(\boldsymbol{P})$$

$$+ V\Big[\mathcal{G}_{\bar{2}00}(\boldsymbol{P}) + \mathcal{G}_{002}(\boldsymbol{P})\Big]\tilde{\Phi}_3^+(\boldsymbol{P}) + V\Big[\mathcal{G}_{\bar{2}11}(\boldsymbol{P}) + \mathcal{G}_{0\bar{1}1}(\boldsymbol{P})\Big]\tilde{\Phi}_4^+(\boldsymbol{P})$$

$$+ V\Big[\mathcal{G}_{\bar{1}\bar{1}2}(\boldsymbol{P}) + \mathcal{G}_{\bar{1}10}(\boldsymbol{P})\Big]\tilde{\Phi}_5^+(\boldsymbol{P}) + V\Big[\mathcal{G}_{000}(\boldsymbol{P}) + \mathcal{G}_{\bar{2}02}(\boldsymbol{P})\Big]\tilde{\Phi}_6^+(\boldsymbol{P})$$

$$(5.17)$$

The newly introduced functions, $\tilde{\Phi}_i^+(\boldsymbol{P}) = e^{\frac{-i}{2}(\boldsymbol{P}\boldsymbol{a}_i^+)}\Phi_i^+$ (where $i = 0, 1, ...6$), have phase factors which provide information about the centre-of-mass motion of the bound state. Furthermore, $\mathcal{G}$ represents the Green's function of the FCC lattice and is defined as

$$\mathcal{G}_{l,m,n}(\boldsymbol{P}) = \frac{1}{N}\sum_{\boldsymbol{q}'}\frac{e^{i(l\frac{q_x'}{2} + m\frac{q_y'}{2} + n\frac{q_z'}{2})}}{E - \varepsilon_{\frac{\boldsymbol{P}}{2}+\boldsymbol{q}'} - \varepsilon_{\frac{\boldsymbol{P}}{2}-\boldsymbol{q}'}} = -\int_{-2\pi}^{2\pi}\int_{-2\pi}^{2\pi}\int_{-2\pi}^{2\pi}\frac{dq_x'dq_y'dq_z'}{(4\pi)^3}\frac{\cos\left(l\frac{q_x'}{2} + m\frac{q_y'}{2} + n\frac{q_z'}{2}\right)}{|E| + \varepsilon_{\frac{\boldsymbol{P}}{2}+\boldsymbol{q}'} + \varepsilon_{\frac{\boldsymbol{P}}{2}-\boldsymbol{q}'}}$$

$$(5.18)$$

where l, m, and $n \in [0, \pm1, \pm2]$.

Combining Equations (5.11)–(5.17) gives the matrix equation below for all singlets at arbitrary momentum

$$\begin{bmatrix} U\mathcal{G}_{000} & V(\mathcal{G}_{110} + \mathcal{G}_{\bar{1}\bar{1}0}) & V(\mathcal{G}_{011} + \mathcal{G}_{0\bar{1}\bar{1}}) & V(\mathcal{G}_{101} + \mathcal{G}_{\bar{1}0\bar{1}}) & V(\mathcal{G}_{1\bar{1}0} + \mathcal{G}_{\bar{1}10}) & V(\mathcal{G}_{01\bar{1}} + \mathcal{G}_{0\bar{1}1}) & V(\mathcal{G}_{\bar{1}01} + \mathcal{G}_{10\bar{1}}) \\ U\mathcal{G}_{110} & V(\mathcal{G}_{000} + \mathcal{G}_{220}) & V(\mathcal{G}_{10\bar{1}} + \mathcal{G}_{121}) & V(\mathcal{G}_{01\bar{1}} + \mathcal{G}_{211}) & V(\mathcal{G}_{020} + \mathcal{G}_{200}) & V(\mathcal{G}_{101} + \mathcal{G}_{12\bar{1}}) & V(\mathcal{G}_{21\bar{1}} + \mathcal{G}_{011}) \\ U\mathcal{G}_{011} & V(\mathcal{G}_{\bar{1}01} + \mathcal{G}_{121}) & V(\mathcal{G}_{000} + \mathcal{G}_{022}) & V(\mathcal{G}_{\bar{1}10} + \mathcal{G}_{112}) & V(\mathcal{G}_{\bar{1}21} + \mathcal{G}_{101}) & V(\mathcal{G}_{002} + \mathcal{G}_{020}) & V(\mathcal{G}_{110} + \mathcal{G}_{\bar{1}12}) \\ U\mathcal{G}_{101} & V(\mathcal{G}_{0\bar{1}1} + \mathcal{G}_{211}) & V(\mathcal{G}_{1\bar{1}0} + \mathcal{G}_{112}) & V(\mathcal{G}_{000} + \mathcal{G}_{202}) & V(\mathcal{G}_{011} + \mathcal{G}_{2\bar{1}1}) & V(\mathcal{G}_{1\bar{1}2} + \mathcal{G}_{110}) & V(\mathcal{G}_{200} + \mathcal{G}_{002}) \\ U\mathcal{G}_{1\bar{1}0} & V(\mathcal{G}_{0\bar{2}0} + \mathcal{G}_{200}) & V(\mathcal{G}_{12\bar{1}} + \mathcal{G}_{101}) & V(\mathcal{G}_{01\bar{1}} + \mathcal{G}_{2\bar{1}1}) & V(\mathcal{G}_{000} + \mathcal{G}_{2\bar{2}0}) & V(\mathcal{G}_{1\bar{2}1} + \mathcal{G}_{10\bar{1}}) & V(\mathcal{G}_{2\bar{1}1} + \mathcal{G}_{0\bar{1}1}) \\ U\mathcal{G}_{01\bar{1}} & V(\mathcal{G}_{\bar{1}0\bar{1}} + \mathcal{G}_{12\bar{1}}) & V(\mathcal{G}_{00\bar{2}} + \mathcal{G}_{0\bar{2}0}) & V(\mathcal{G}_{\bar{1}1\bar{2}} + \mathcal{G}_{110}) & V(\mathcal{G}_{\bar{1}2\bar{1}} + \mathcal{G}_{10\bar{1}}) & V(\mathcal{G}_{000} + \mathcal{G}_{02\bar{2}}) & V(\mathcal{G}_{11\bar{2}} + \mathcal{G}_{\bar{1}10}) \\ U\mathcal{G}_{\bar{1}01} & V(\mathcal{G}_{\bar{2}\bar{1}1} + \mathcal{G}_{011}) & V(\mathcal{G}_{\bar{1}\bar{1}0} + \mathcal{G}_{\bar{1}12}) & V(\mathcal{G}_{\bar{2}00} + \mathcal{G}_{002}) & V(\mathcal{G}_{\bar{2}11} + \mathcal{G}_{0\bar{1}1}) & V(\mathcal{G}_{\bar{1}\bar{1}2} + \mathcal{G}_{\bar{1}10}) & V(\mathcal{G}_{000} + \mathcal{G}_{\bar{2}02}) \end{bmatrix}\begin{bmatrix} \tilde{\Phi}_0^+ \\ \tilde{\Phi}_1^+ \\ \tilde{\Phi}_2^+ \\ \tilde{\Phi}_3^+ \\ \tilde{\Phi}_4^+ \\ \tilde{\Phi}_5^+ \\ \tilde{\Phi}_6^+ \end{bmatrix} = \begin{bmatrix} \tilde{\Phi}_0^+ \\ \tilde{\Phi}_1^+ \\ \tilde{\Phi}_2^+ \\ \tilde{\Phi}_3^+ \\ \tilde{\Phi}_4^+ \\ \tilde{\Phi}_5^+ \\ \tilde{\Phi}_6^+ \end{bmatrix}$$

$$(5.19)$$

5.2.2 Solution for Triplets

For the triplets, we substitute $\{\mathbf{a}_-\}$ in Equation (5.1), to obtain

$$
\begin{aligned}
(E - \varepsilon_{\mathbf{k}_1} - \varepsilon_{\mathbf{k}_2})\phi^-_{\mathbf{k}_1\mathbf{k}_2} = & \frac{1}{N}\sum_{\mathbf{q}}\Bigg[V\, e^{i(\frac{q_x}{2}+\frac{q_y}{2})}(e^{-i\mathbf{k}_1\mathbf{a}_1^-} - e^{-i\mathbf{k}_2\mathbf{a}_1^-}) \\
& + V\, e^{i(\frac{q_y}{2}+\frac{q_z}{2})}(e^{-i\mathbf{k}_1\mathbf{a}_2^-} - e^{-i\mathbf{k}_2\mathbf{a}_2^-}) \\
& + V\, e^{i(\frac{q_x}{2}+\frac{q_z}{2})}(e^{-i\mathbf{k}_1\mathbf{a}_3^-} - e^{-i\mathbf{k}_2\mathbf{a}_3^-}) \\
& + V\, e^{i(\frac{q_x}{2}-\frac{q_y}{2})}(e^{-i\mathbf{k}_1\mathbf{a}_4^-} - e^{-i\mathbf{k}_2\mathbf{a}_4^-}) \\
& + V\, e^{i(\frac{q_y}{2}-\frac{q_z}{2})}(e^{-i\mathbf{k}_1\mathbf{a}_5^-} - e^{-i\mathbf{k}_2\mathbf{a}_5^-}) \\
& + V\, e^{i(-\frac{q_x}{2}+\frac{q_z}{2})}(e^{-i\mathbf{k}_1\mathbf{a}_6^-} - e^{-i\mathbf{k}_2\mathbf{a}_6^-})\Bigg]\phi^-_{\mathbf{q},\mathbf{k}_1+\mathbf{k}_2-\mathbf{q}}
\end{aligned}
\tag{5.20}
$$

We also define the following basis functions for the spin-triplets:

$$
\Phi_1^-(\mathbf{P}) = \frac{1}{N}\sum_{\mathbf{q}} e^{i(\frac{q_x}{2}+\frac{q_y}{2})}\,\phi^-_{\mathbf{q},\mathbf{P}-\mathbf{q}}\,, \quad \Phi_2^-(\mathbf{P}) = \frac{1}{N}\sum_{\mathbf{q}} e^{i(\frac{q_y}{2}+\frac{q_z}{2})}\,\phi^-_{\mathbf{q},\mathbf{P}-\mathbf{q}}
$$

$$
\Phi_3^-(\mathbf{P}) = \frac{1}{N}\sum_{\mathbf{q}} e^{i(\frac{q_x}{2}+\frac{q_z}{2})}\,\phi^-_{\mathbf{q},\mathbf{P}-\mathbf{q}}\,, \quad \Phi_4^-(\mathbf{P}) = \frac{1}{N}\sum_{\mathbf{q}} e^{i(\frac{q_x}{2}-\frac{q_y}{2})}\,\phi^-_{\mathbf{q},\mathbf{P}-\mathbf{q}}
\tag{5.21}
$$

$$
\Phi_5^-(\mathbf{P}) = \frac{1}{N}\sum_{\mathbf{q}} e^{i(\frac{q_y}{2}-\frac{q_z}{2})}\,\phi^-_{\mathbf{q},\mathbf{P}-\mathbf{q}}\,, \quad \Phi_6^-(\mathbf{P}) = \frac{1}{N}\sum_{\mathbf{q}} e^{i(-\frac{q_x}{2}+\frac{q_z}{2})}\,\phi^-_{\mathbf{q},\mathbf{P}-\mathbf{q}}
$$

After some algebra, we arrive at

$$
\begin{aligned}
\Phi_1^-(\mathbf{P}) = & \frac{1}{N}\sum_{\mathbf{q}'}\frac{1}{E - \varepsilon_{\frac{\mathbf{P}}{2}+\mathbf{q}'} - \varepsilon_{\frac{\mathbf{P}}{2}-\mathbf{q}'}}\Bigg\{ V\Phi_1^-(\mathbf{P})\Big[1 - e^{2i(\frac{q_x'}{2}+\frac{q_y'}{2})}\Big] \\
& + V\Phi_2^-(\mathbf{P})\, e^{i(\frac{P_x}{4}-\frac{P_z}{4})}\Big[e^{i(\frac{q_x'}{2}-\frac{q_z'}{2})} - e^{i(\frac{q_x'}{2}+2(\frac{q_y'}{2})+\frac{q_z'}{2})}\Big] \\
& + V\Phi_3^-(\mathbf{P})\, e^{i(\frac{P_y}{4}-\frac{P_z}{4})}\Big[e^{i(\frac{q_y'}{2}-\frac{q_z'}{2})} - e^{i(2(\frac{q_x'}{2})+\frac{q_y'}{2}+\frac{q_z'}{2})}\Big] \\
& + V\Phi_4^-(\mathbf{P})e^{2i(\frac{P_y}{4})}\Big[e^{2i(\frac{q_y'}{2})} - e^{2i(\frac{q_x'}{2})}\Big] \\
& + V\Phi_5^-(\mathbf{P})\, e^{i(\frac{P_x}{4}+\frac{P_z}{4})}\Big[e^{i(\frac{q_x'}{2}+\frac{q_z'}{2})} - e^{i(\frac{q_x'}{2}+2(\frac{q_y'}{2})-\frac{q_z'}{2})}\Big] \\
& + V\Phi_6^-(\mathbf{P})\, e^{i(2(\frac{P_x}{4})+\frac{P_y}{4}-\frac{P_z}{4})}\Big[e^{i(2(\frac{q_x'}{2})+\frac{q_y'}{2}-\frac{q_z'}{2})} - e^{i(\frac{q_y'}{2}+\frac{q_z'}{2})}\Big]\Bigg\}
\end{aligned}
\tag{5.22}
$$

So we have

$$
\begin{aligned}
\tilde{\Phi}_1^-(\boldsymbol{P}) =& V\Big[\mathcal{G}_{000}(\boldsymbol{P}) - \mathcal{G}_{220}(\boldsymbol{P})\Big]\tilde{\Phi}_1^-(\boldsymbol{P}) + V\Big[\mathcal{G}_{10\bar{1}}(\boldsymbol{P}) - \mathcal{G}_{121}(\boldsymbol{P})\Big]\tilde{\Phi}_2^-(\boldsymbol{P}) \\
&+ V\Big[\mathcal{G}_{01\bar{1}}(\boldsymbol{P}) - \mathcal{G}_{211}(\boldsymbol{P})\Big]\tilde{\Phi}_3^-(\boldsymbol{P}) + V\Big[\mathcal{G}_{020}(\boldsymbol{P}) - \mathcal{G}_{200}(\boldsymbol{P})\Big]\tilde{\Phi}_4^-(\boldsymbol{P}) \\
&+ V\Big[\mathcal{G}_{101}(\boldsymbol{P}) - \mathcal{G}_{12\bar{1}}(\boldsymbol{P})\Big]\tilde{\Phi}_5^-(\boldsymbol{P}) + V\Big[\mathcal{G}_{21\bar{1}}(\boldsymbol{P}) - \mathcal{G}_{011}\Big]\tilde{\Phi}_6^-(\boldsymbol{P})
\end{aligned}
\tag{5.23}
$$

$$
\begin{aligned}
\tilde{\Phi}_2^-(\boldsymbol{P}) =& V\Big[\mathcal{G}_{\bar{1}01}(\boldsymbol{P}) - \mathcal{G}_{121}(\boldsymbol{P})\Big]\tilde{\Phi}_1^-(\boldsymbol{P}) + V\Big[\mathcal{G}_{000}(\boldsymbol{P}) - \mathcal{G}_{022}(\boldsymbol{P})\Big]\tilde{\Phi}_2^-(\boldsymbol{P}) \\
&+ V\Big[\mathcal{G}_{\bar{1}10}(\boldsymbol{P}) - \mathcal{G}_{112}(\boldsymbol{P})\Big]\tilde{\Phi}_3^-(\boldsymbol{P}) + V\Big[\mathcal{G}_{\bar{1}21}(\boldsymbol{P}) - \mathcal{G}_{101}(\boldsymbol{P})\Big]\tilde{\Phi}_4^-(\boldsymbol{P}) \\
&+ V\Big[\mathcal{G}_{002}(\boldsymbol{P}) - \mathcal{G}_{020}(\boldsymbol{P})\Big]\tilde{\Phi}_5^-(\boldsymbol{P}) + V\Big[\mathcal{G}_{110}(\boldsymbol{P}) - \mathcal{G}_{\bar{1}12}(\boldsymbol{P})\Big]\tilde{\Phi}_6^-(\boldsymbol{P})
\end{aligned}
\tag{5.24}
$$

$$
\begin{aligned}
\tilde{\Phi}_3^-(\boldsymbol{P}) =& V\Big[\mathcal{G}_{0\bar{1}1}(\boldsymbol{P}) - \mathcal{G}_{211}(\boldsymbol{P})\Big]\tilde{\Phi}_1^-(\boldsymbol{P}) + V\Big[\mathcal{G}_{1\bar{1}0}(\boldsymbol{P}) - \mathcal{G}_{112}(\boldsymbol{P})\Big]\tilde{\Phi}_2^-(\boldsymbol{P}) \\
&+ V\Big[\mathcal{G}_{000}(\boldsymbol{P}) - \mathcal{G}_{202}(\boldsymbol{P})\Big]\tilde{\Phi}_3^-(\boldsymbol{P}) + V\Big[\mathcal{G}_{011}(\boldsymbol{P}) - \mathcal{G}_{2\bar{1}1}(\boldsymbol{P})\Big]\tilde{\Phi}_4^-(\boldsymbol{P}) \\
&+ V\Big[\mathcal{G}_{1\bar{1}2}(\boldsymbol{P}) - \mathcal{G}_{110}(\boldsymbol{P})\Big]\tilde{\Phi}_5^-(\boldsymbol{P}) + V\Big[\mathcal{G}_{200}(\boldsymbol{P}) - \mathcal{G}_{002}(\boldsymbol{P})\Big]\tilde{\Phi}_6^-(\boldsymbol{P})
\end{aligned}
\tag{5.25}
$$

$$
\begin{aligned}
\tilde{\Phi}_4^-(\boldsymbol{P}) =& V\Big[\mathcal{G}_{0\bar{2}0}(\boldsymbol{P}) - \mathcal{G}_{200}(\boldsymbol{P})\Big]\tilde{\Phi}_1^-(\boldsymbol{P}) + V\Big[\mathcal{G}_{1\bar{2}\bar{1}}(\boldsymbol{P}) - \mathcal{G}_{101}(\boldsymbol{P})\Big]\tilde{\Phi}_2^-(\boldsymbol{P}) \\
&+ V\Big[\mathcal{G}_{0\bar{1}\bar{1}}(\boldsymbol{P}) - \mathcal{G}_{2\bar{1}1}(\boldsymbol{P})\Big]\tilde{\Phi}_3^-(\boldsymbol{P}) + V\Big[\mathcal{G}_{000}(\boldsymbol{P}) - \mathcal{G}_{2\bar{2}0}(\boldsymbol{P})\Big]\tilde{\Phi}_4^-(\boldsymbol{P}) \\
&+ V\Big[\mathcal{G}_{1\bar{2}1}(\boldsymbol{P}) - \mathcal{G}_{10\bar{1}}(\boldsymbol{P})\Big]\tilde{\Phi}_5^-(\boldsymbol{P}) + V\Big[\mathcal{G}_{2\bar{1}\bar{1}}(\boldsymbol{P}) - \mathcal{G}_{0\bar{1}1}(\boldsymbol{P})\Big]\tilde{\Phi}_6^-(\boldsymbol{P})
\end{aligned}
\tag{5.26}
$$

$$
\begin{aligned}
\tilde{\Phi}_5^-(\boldsymbol{P}) =& V\Big[\mathcal{G}_{\bar{1}0\bar{1}}(\boldsymbol{P}) - \mathcal{G}_{12\bar{1}}(\boldsymbol{P})\Big]\tilde{\Phi}_1^-(\boldsymbol{P}) + V\Big[\mathcal{G}_{00\bar{2}}(\boldsymbol{P}) - \mathcal{G}_{020}(\boldsymbol{P})\Big]\tilde{\Phi}_2^-(\boldsymbol{P}) \\
&+ V\Big[\mathcal{G}_{\bar{1}1\bar{2}}(\boldsymbol{P}) - \mathcal{G}_{110}(\boldsymbol{P})\Big]\tilde{\Phi}_3^-(\boldsymbol{P}) + V\Big[\mathcal{G}_{\bar{1}2\bar{1}}(\boldsymbol{P}) - \mathcal{G}_{10\bar{1}}(\boldsymbol{P})\Big]\tilde{\Phi}_4^-(\boldsymbol{P}) \\
&+ V\Big[\mathcal{G}_{000}(\boldsymbol{P}) - \mathcal{G}_{02\bar{2}}(\boldsymbol{P})\Big]\tilde{\Phi}_5^-(\boldsymbol{P}) + V\Big[\mathcal{G}_{11\bar{2}}(\boldsymbol{P}) - \mathcal{G}_{\bar{1}10}(\boldsymbol{P})\Big]\tilde{\Phi}_6^-(\boldsymbol{P})
\end{aligned}
\tag{5.27}
$$

$$
\begin{aligned}
\tilde{\Phi}_6^-(\boldsymbol{P}) =& V\Big[\mathcal{G}_{\bar{2}\bar{1}1}(\boldsymbol{P}) - \mathcal{G}_{011}(\boldsymbol{P})\Big]\tilde{\Phi}_1^-(\boldsymbol{P}) + V\Big[\mathcal{G}_{\bar{1}\bar{1}0}(\boldsymbol{P}) - \mathcal{G}_{\bar{1}12}(\boldsymbol{P})\Big]\tilde{\Phi}_2^-(\boldsymbol{P}) \\
&+ V\Big[\mathcal{G}_{\bar{2}00}(\boldsymbol{P}) - \mathcal{G}_{002}(\boldsymbol{P})\Big]\tilde{\Phi}_3^-(\boldsymbol{P}) + V\Big[\mathcal{G}_{\bar{2}11}(\boldsymbol{P}) - \mathcal{G}_{0\bar{1}1}(\boldsymbol{P})\Big]\tilde{\Phi}_4^-(\boldsymbol{P}) \\
&+ V\Big[\mathcal{G}_{\bar{1}\bar{1}2}(\boldsymbol{P}) - \mathcal{G}_{\bar{1}10}(\boldsymbol{P})\Big]\tilde{\Phi}_5^-(\boldsymbol{P}) + V\Big[\mathcal{G}_{000}(\boldsymbol{P}) - \mathcal{G}_{\bar{2}02}(\boldsymbol{P})\Big]\tilde{\Phi}_6^-(\boldsymbol{P})
\end{aligned}
\tag{5.28}
$$

The same steps which apply for the singlets apply here too. Hence, the combined self-consistency equations for all triplets is

$$
\begin{bmatrix}
V(\mathcal{G}_{000} - \mathcal{G}_{220}) & V(\mathcal{G}_{10\bar{1}} - \mathcal{G}_{121}) & V(\mathcal{G}_{01\bar{1}} - \mathcal{G}_{211}) & V(\mathcal{G}_{020} - \mathcal{G}_{200}) & V(\mathcal{G}_{101} - \mathcal{G}_{12\bar{1}}) & V(\mathcal{G}_{21\bar{1}} - \mathcal{G}_{011}) \\
V(\mathcal{G}_{\bar{1}01} - \mathcal{G}_{121}) & V(\mathcal{G}_{000} - \mathcal{G}_{022}) & V(\mathcal{G}_{\bar{1}10} - \mathcal{G}_{112}) & V(\mathcal{G}_{\bar{1}21} - \mathcal{G}_{101}) & V(\mathcal{G}_{002} - \mathcal{G}_{020}) & V(\mathcal{G}_{110} - \mathcal{G}_{\bar{1}12}) \\
V(\mathcal{G}_{0\bar{1}1} - \mathcal{G}_{211}) & V(\mathcal{G}_{1\bar{1}0} - \mathcal{G}_{112}) & V(\mathcal{G}_{000} - \mathcal{G}_{202}) & V(\mathcal{G}_{011} - \mathcal{G}_{2\bar{1}1}) & V(\mathcal{G}_{1\bar{1}2} - \mathcal{G}_{110}) & V(\mathcal{G}_{200} - \mathcal{G}_{002}) \\
V(\mathcal{G}_{0\bar{2}0} - \mathcal{G}_{200}) & V(\mathcal{G}_{1\bar{2}\bar{1}} - \mathcal{G}_{101}) & V(\mathcal{G}_{0\bar{1}\bar{1}} - \mathcal{G}_{2\bar{1}1}) & V(\mathcal{G}_{000} - \mathcal{G}_{2\bar{2}0}) & V(\mathcal{G}_{1\bar{2}1} - \mathcal{G}_{10\bar{1}}) & V(\mathcal{G}_{2\bar{1}\bar{1}} - \mathcal{G}_{0\bar{1}1}) \\
V(\mathcal{G}_{\bar{1}0\bar{1}} - \mathcal{G}_{12\bar{1}}) & V(\mathcal{G}_{00\bar{2}} - \mathcal{G}_{0\bar{2}0}) & V(\mathcal{G}_{\bar{1}1\bar{2}} - \mathcal{G}_{110}) & V(\mathcal{G}_{\bar{1}2\bar{1}} - \mathcal{G}_{10\bar{1}}) & V(\mathcal{G}_{000} - \mathcal{G}_{02\bar{2}}) & V(\mathcal{G}_{11\bar{2}} - \mathcal{G}_{\bar{1}10}) \\
V(\mathcal{G}_{\bar{2}\bar{1}1} - \mathcal{G}_{011}) & V(\mathcal{G}_{\bar{1}\bar{1}0} - \mathcal{G}_{\bar{1}12}) & V(\mathcal{G}_{\bar{2}00} - \mathcal{G}_{002}) & V(\mathcal{G}_{\bar{2}11} - \mathcal{G}_{0\bar{1}1}) & V(\mathcal{G}_{\bar{1}\bar{1}2} - \mathcal{G}_{\bar{1}10}) & V(\mathcal{G}_{000} - \mathcal{G}_{\bar{2}02})
\end{bmatrix}
\begin{bmatrix}
\tilde{\Phi}_1^+ \\ \tilde{\Phi}_2^+ \\ \tilde{\Phi}_3^+ \\ \tilde{\Phi}_4^+ \\ \tilde{\Phi}_5^+ \\ \tilde{\Phi}_6^+
\end{bmatrix}
=
\begin{bmatrix}
\tilde{\Phi}_1^+ \\ \tilde{\Phi}_2^+ \\ \tilde{\Phi}_3^+ \\ \tilde{\Phi}_4^+ \\ \tilde{\Phi}_5^+ \\ \tilde{\Phi}_6^+
\end{bmatrix}
$$

$$(5.29)$$

where $\mathcal{G}_{lmn}$ are the Green's functions defined in Equation (5.18). Equations (5.19) and (5.29) are the respective eigenequations that are solved to obtain pair properties for the singlets and triplets. With the size of these matrices, it is easy to tell that there will be more bound states in the FCC lattice as compared to the BCC lattice. The properties of two fermions in an FCC lattice will be discussed next.

5.3 Pair Properties

The characteristic properties of fermion pair in FCC lattices are reported in this section. In the following order, we: (1) calculate the *total energy* of the pair with different symmetries; (2) construct a *pairing diagram* for binding analysis; (3) calculate the *dispersion characteristics* of bound pairs in the FCC BZ; (4) calculate the pair *effective mass* at various attraction strengths; (5) evaluate the *effective radius* of a bound *s*-state; and (6) estimate the *BEC transition temperatures* at which *s*-wave pairs may Bose condense in the low-density limit.

5.3.1 Total Energy

In the present study, we can tell if two particles are bound or not by inspecting the total energy of the pair. Although, a bound state can form only if there is sufficient potential

U or V to bind the particles. One of the consequential advantages of Equations (5.19) and (5.29) is that we can determine the total energy of a pair at an arbitrary $\boldsymbol{P}$.

5.3.1.1   Energy of an Unbound Pair at $\boldsymbol{P} = 0$

The minimum energy of a free particle (also the half-bandwidth W) in an FCC lattice can be determined from Equation (5.1) to be $\varepsilon_{\min} \equiv W = -12t$, when $\boldsymbol{k} = 0$. Therefore, the total energy of *two* free-particles, each at zero momentum, is $-24t$. By implication, we can say that for the case of *zero* total momentum ($\boldsymbol{P} = 0$), the energy of the system equals the bandwidth $-24t$.

5.3.1.2   Energy of a Bound Pair at $\boldsymbol{P} = 0$

If there is a strong enough attractive potential to bind the particles, the energy of the system drops below the energy of *two* unbound free particles. To calculate the total energy at *zero* pair momentum, we set $\boldsymbol{P} = 0$ in Equation (5.19). The Γ point which is at the centre of the FCC BZ corresponds to momentum $\boldsymbol{P} = 0$. At this point of the zone, the FCC lattice possesses O_h point symmetry, thus, we can apply our group theory analysis.

Simplification at the Γ point

At the Γ point where $(P_x = P_y = P_z = 0)$, the Green's function in Equation (5.18) becomes

$$
\begin{aligned}
\mathcal{G}_{lmn}(0) &= \frac{1}{N} \sum_{\boldsymbol{q'}} \frac{e^{i(l\frac{q'_x}{2} + m\frac{q'_y}{2} + n\frac{q'_z}{2})}}{E - 2\varepsilon_{\boldsymbol{q'}}} \\
&= -\int_{-2\pi}^{2\pi}\int_{-2\pi}^{2\pi}\int_{-2\pi}^{2\pi} \frac{dq'_x dq'_y dq'_z}{(4\pi)^3} \frac{\cos\left(l\frac{q'_x}{2}\right)\,\cos\left(m\frac{q'_y}{2}\right)\,\cos\left(n\frac{q'_z}{2}\right)}{|E| + 2\varepsilon_{\boldsymbol{q'}}} \\
&= -\frac{1}{(2\pi)^3}\int_{-\pi}^{\pi}\int_{-\pi}^{\pi}\int_{-\pi}^{\pi} \frac{\cos(lq''_x)\cos(mq''_y)\cos(nq''_z)}{|E| + 2\varepsilon_{\boldsymbol{q''}}} dq''_x\, dq''_y dq''_z \quad : \quad (q''_j = \frac{q'_j}{2})
\end{aligned}
$$
(5.30)

where $\varepsilon_{\boldsymbol{q}''} = -4t\left\{\cos(q''_x)\cos(q''_y) + \cos(q''_x)\cos(q''_z) + \cos(q''_y)\cos(q''_z)\right\}$. Because some of the Green's functions are numerically identical due to symmetry properties [106], we may then use the simplifications below

$$\mathcal{G}_{000} = \mathcal{G}_0$$

$$\mathcal{G}_{110} = \mathcal{G}_{101} = \mathcal{G}_{011} = \mathcal{G}_{\bar{1}01} = \mathcal{G}_{0\bar{1}1} = \mathcal{G}_{10\bar{1}} = \mathcal{G}_{\bar{1}0\bar{1}} = \mathcal{G}_{0\bar{1}\bar{1}} = \mathcal{G}_{01\bar{1}} = \mathcal{G}_{\bar{1}10} = \mathcal{G}_{1\bar{1}0} = \mathcal{G}_{\bar{1}\bar{1}0} \equiv \mathcal{G}_1$$

$$\mathcal{G}_{220} = \mathcal{G}_{022} = \mathcal{G}_{202} = \mathcal{G}_{2\bar{2}0} = \mathcal{G}_{02\bar{2}} = \mathcal{G}_{\bar{2}02} \equiv \mathcal{G}_2$$

$$\mathcal{G}_{200} = \mathcal{G}_{020} = \mathcal{G}_{002} = \mathcal{G}_{\bar{2}00} = \mathcal{G}_{0\bar{2}0} = \mathcal{G}_{00\bar{2}} \equiv \mathcal{G}_3$$

$$\mathcal{G}_{211} = \mathcal{G}_{121} = \mathcal{G}_{112} = \mathcal{G}_{\bar{2}11} = \mathcal{G}_{1\bar{2}1} = \mathcal{G}_{11\bar{2}} = \mathcal{G}_{\bar{1}\bar{1}2} = ... \equiv \mathcal{G}_4$$

$$(5.31)$$

to modify our dispersion matrices (5.19) and (5.29) respectively as :

$$\underbrace{\begin{bmatrix} U\mathcal{G}_0 & 2V\mathcal{G}_1 & 2V\mathcal{G}_1 & 2V\mathcal{G}_1 & 2V\mathcal{G}_1 & 2V\mathcal{G}_1 & 2V\mathcal{G}_1 \\ U\mathcal{G}_1 & V(\mathcal{G}_0+\mathcal{G}_2) & V(\mathcal{G}_1+\mathcal{G}_4) & V(\mathcal{G}_1+\mathcal{G}_4) & 2V\mathcal{G}_3 & V(\mathcal{G}_1+\mathcal{G}_4) & V(\mathcal{G}_4+\mathcal{G}_1) \\ U\mathcal{G}_1 & V(\mathcal{G}_1+\mathcal{G}_4) & V(\mathcal{G}_0+\mathcal{G}_2) & V(\mathcal{G}_1+\mathcal{G}_4) & V(\mathcal{G}_4+\mathcal{G}_1) & 2V\mathcal{G}_3 & V(\mathcal{G}_1+\mathcal{G}_4) \\ U\mathcal{G}_1 & V(\mathcal{G}_1+\mathcal{G}_4) & V(\mathcal{G}_1+\mathcal{G}_4) & V(\mathcal{G}_0+\mathcal{G}_2) & V(\mathcal{G}_1+\mathcal{G}_4) & V(\mathcal{G}_4+\mathcal{G}_1) & 2V\mathcal{G}_3 \\ U\mathcal{G}_1 & 2V\mathcal{G}_3 & V(\mathcal{G}_4+\mathcal{G}_1) & V(\mathcal{G}_1+\mathcal{G}_4) & V(\mathcal{G}_0+\mathcal{G}_2) & V(\mathcal{G}_4+\mathcal{G}_1) & V(\mathcal{G}_4+\mathcal{G}_1) \\ U\mathcal{G}_1 & V(\mathcal{G}_1+\mathcal{G}_4) & 2V\mathcal{G}_3 & V(\mathcal{G}_4+\mathcal{G}_1) & V(\mathcal{G}_4+\mathcal{G}_1) & V(\mathcal{G}_0+\mathcal{G}_2) & V(\mathcal{G}_4+\mathcal{G}_1) \\ U\mathcal{G}_1 & V(\mathcal{G}_4+\mathcal{G}_1) & V(\mathcal{G}_1+\mathcal{G}_4) & 2V\mathcal{G}_3 & V(\mathcal{G}_4+\mathcal{G}_1) & V(\mathcal{G}_4+\mathcal{G}_1) & V(\mathcal{G}_0+\mathcal{G}_2) \end{bmatrix}}_{\hat{H}_{singlet}} \underbrace{\begin{bmatrix} \Phi_0^+ \\ \Phi_1^+ \\ \Phi_2^+ \\ \Phi_3^+ \\ \Phi_4^+ \\ \Phi_5^+ \\ \Phi_6^+ \end{bmatrix}}_{\hat{\Phi}_{singlet}} = \underbrace{\begin{bmatrix} \Phi_0^+ \\ \Phi_1^+ \\ \Phi_2^+ \\ \Phi_3^+ \\ \Phi_4^+ \\ \Phi_5^+ \\ \Phi_6^+ \end{bmatrix}}_{\hat{\Phi}_{singlet}}$$

$$(5.32)$$

$$\underbrace{\begin{bmatrix} V(\mathcal{G}_0-\mathcal{G}_2) & V(\mathcal{G}_1-\mathcal{G}_4) & V(\mathcal{G}_1-\mathcal{G}_4) & 0 & V(\mathcal{G}_1-\mathcal{G}_4) & V(\mathcal{G}_4-\mathcal{G}_1) \\ V(\mathcal{G}_1-\mathcal{G}_4) & V(\mathcal{G}_0-\mathcal{G}_2) & V(\mathcal{G}_1-\mathcal{G}_4) & V(\mathcal{G}_4-\mathcal{G}_1) & 0 & V(\mathcal{G}_1-\mathcal{G}_4) \\ V(\mathcal{G}_1-\mathcal{G}_4) & V(\mathcal{G}_1-\mathcal{G}_4) & V(\mathcal{G}_0-\mathcal{G}_2) & V(\mathcal{G}_1-\mathcal{G}_4) & V(\mathcal{G}_4-\mathcal{G}_1) & 0 \\ 0 & V(\mathcal{G}_4-\mathcal{G}_1) & V(\mathcal{G}_1-\mathcal{G}_4) & V(\mathcal{G}_0-\mathcal{G}_2) & V(\mathcal{G}_4-\mathcal{G}_1) & V(\mathcal{G}_4-\mathcal{G}_1) \\ V(\mathcal{G}_1-\mathcal{G}_4) & 0 & V(\mathcal{G}_4-\mathcal{G}_1) & V(\mathcal{G}_4-\mathcal{G}_1) & V(\mathcal{G}_0-\mathcal{G}_2) & V(\mathcal{G}_4-\mathcal{G}_1) \\ V(\mathcal{G}_4-\mathcal{G}_1) & V(\mathcal{G}_1-\mathcal{G}_4) & 0 & V(\mathcal{G}_4-\mathcal{G}_1) & V(\mathcal{G}_4-\mathcal{G}_1) & V(\mathcal{G}_0-\mathcal{G}_2) \end{bmatrix}}_{\hat{H}_{triplet}} \underbrace{\begin{bmatrix} \Phi_1^- \\ \Phi_2^- \\ \Phi_3^- \\ \Phi_4^- \\ \Phi_5^- \\ \Phi_6^- \end{bmatrix}}_{\hat{\Phi}_{triplet}} = \underbrace{\begin{bmatrix} \Phi_1^- \\ \Phi_2^- \\ \Phi_3^- \\ \Phi_4^- \\ \Phi_5^- \\ \Phi_6^- \end{bmatrix}}_{\hat{\Phi}_{triplet}} \quad (5.33)$$

Note that $\tilde{\Phi}_i^{\pm} \equiv \Phi_i^{\pm}$ since $\boldsymbol{P} = 0$. The matrices above form the eigenequation

$$\hat{H}_{s,t}\,\hat{\Phi}_{s,t} = \mu_{s,t}\,\hat{\Phi}_{s,t} \tag{5.34}$$

where $\hat{H}_s$ and $\hat{H}_t$ are the singlet and triplet dispersion matrices, $\hat{\Phi}_s$ and $\hat{\Phi}_t$ are the singlet and triplet eigenvectors, and μ_s and μ_t being the corresponding eigenvalues, respectively.

To find the pair energy, we select E, compute $\mathcal{G}$, and then μ. A true pair state corresponds to $\mu = 1$. Thus, all pair energies can be found by adjusting E and searching for $\mu = 1$ using standard binary search algorithms.
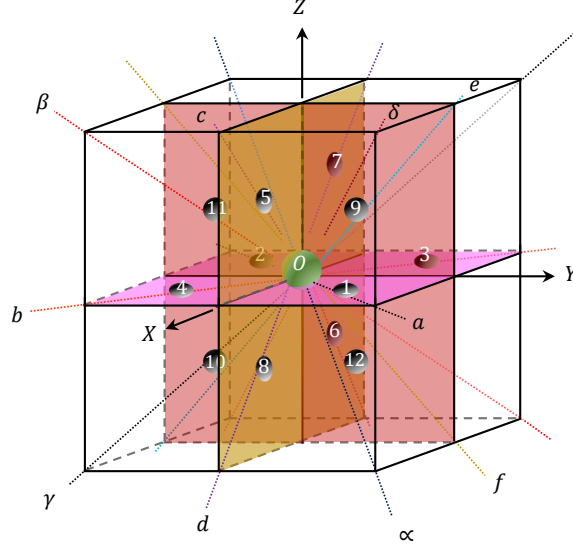
Figure 5.2: A basic FCC lattice showing the axes for the O_h operations. The axes are $OX, OY, OZ, Oa, Ob, Oc, Od, Oe, Of, O\alpha, O\beta, O\gamma$, and $O\delta$. The numbers $1, 2, \ldots, 12$ represent nearest-neighbour lattice sites.

Application of Group Theory

In addition to the simplification of the Green's functions, one can take further advantage of this high symmetry point. We follow the procedure explained in Section 3.4.7 of Chapter 3. The symmetry operations are those belonging to the O_h point group. The resulting output from each step will follow.

Step 1: If we label the lattice sites according to Figure 5.2 and then perform the 48 symmetry operations, we can find the character of the input representation (reducible reps.).

Step 2: We obtain the irreducible representations (irred. reps.) by selecting the non-zero representations in the last column of Table 5.1. Finally, the sought irred. reps. for

O_h group	E	$8C_2$	$3C_3$	$6C_4$	$6C_5$	C_6	$8C_7$	$3C_8$	$6C_9$	$6C_{10}$		
Red. rep (Γ_t^{fcc})	12	0	0	0	2	0	0	4	0	2	$\sum$	$\sum/48$
A_{1g}	12	0	0	0	12	0	0	12	0	12	48	1
A_{2g}	12	0	0	0	-12	0	0	12	0	-12	0	0
E_g	24	0	0	0	0	0	0	24	0	0	48	1
T_{1g}	36	0	0	0	-12	0	0	-12	0	-12	0	0
T_{2g}	36	0	0	0	12	0	0	-12	0	12	48	1
A_{1u}	12	0	0	0	12	0	0	-12	0	-12	0	0
A_{2u}	12	0	0	0	-12	0	0	-12	0	12	0	0
E_u	24	0	0	0	0	0	0	-24	0	0	0	0
T_{1u}	36	0	0	0	-12	0	0	12	0	12	48	1
T_{2u}	36	0	0	0	12	0	0	12	0	-12	48	1

Table 5.1: Constructing irreducible representation from O_h point group using the reduction formula in the FCC lattice. The symmetry classes and the matrices for irreducible representations of each symmetry operation are provided in Appendix B.

both the singlet and triplet states are respectively

$$\Gamma_{singlet}^{fcc} = A_{1g} \oplus E_g \oplus T_{2g} \tag{5.35}$$

$$\Gamma_{triplet}^{fcc} = T_{1u} \oplus T_{2u} \tag{5.36}$$

We note that A_{1g} is s-symmetrical, E_g ($d_{x^2-y^2}$ and $d_{2z^2-x^2-y^2}$) and T_{2g} (d_{xy}, d_{xz} and d_{yz}) are of d-symmetry, T_{1u} (p_x, p_y and p_z) has p-symmetry whilst T_{2u} ($f_{x[z^2-y^2]}$, $f_{y[z^2-x^2]}$ and $f_{z[x^2-y^2]}$) forms the f- symmetric states. We define an example of symmetrised linear combinations for the singlets as

$$\chi^{A_{1g}} = \Phi_1^+ + \Phi_2^+ + \Phi_3^+ + \Phi_4^+ + \Phi_3^5 + \Phi_6^+ \tag{5.37}$$

$$\chi^{T_{2g}} = \begin{cases} \Phi_1^+ - \Phi_4^+ \\[2mm] \Phi_3^+ - \Phi_6^+ \\[2mm] \Phi_2^+ - \Phi_5^+ \end{cases} \qquad\qquad \chi^{E_g} = \begin{cases} \Phi_1^+ - 2\Phi_2^+ + \Phi_3^+ + \Phi_4^+ - 2\Phi_5^+ + \Phi_6^+ \\[2mm] \Phi_1^+ - \Phi_3^+ + \Phi_4^+ - \Phi_6^+ \end{cases}$$

$$\tag{5.38}$$

and for the triplets as

$$\chi^{T_{1u}} = \begin{cases} \Phi_1^- + \Phi_2^- - \Phi_4^- + \Phi_5^- \\[2mm] \Phi_1^- + \Phi_3^- + \Phi_4^- - \Phi_6^- \\[2mm] -\Phi_2^- - \Phi_3^- + \Phi_5^- - \Phi_6^- \end{cases} \qquad \chi^{T_{2u}} = \begin{cases} \Phi_2^- - \Phi_3^- - \Phi_5^- - \Phi_6^- \\[2mm] \Phi_1^- - \Phi_3^- + \Phi_4^- + \Phi_6^- \\[2mm] \Phi_1^- - \Phi_2^- - \Phi_4^- - \Phi_5^- \end{cases} \tag{5.39}$$

Step 3: Next, we combine Equation (5.37) with Φ_0^+ (the onsite basis), to arrive at a complete orthogonal basis [‡,§]

$$\hat{\Phi}_s = \begin{bmatrix} \Phi_0 \\ \Phi_s \\ \Phi_{d_1} \\ \Phi_{d_2} \\ \Phi_{d_3} \\ \Phi_{d_4} \\ \Phi_{d_5} \end{bmatrix} = \begin{bmatrix} 1 & 0 & 0 & 0 & 0 & 0 & 0 \\ 0 & 1 & 1 & 1 & 1 & 1 & 1 \\ 0 & 1 & 0 & 0 & -1 & 0 & 0 \\ 0 & 0 & 0 & 1 & 0 & 0 & -1 \\ 0 & 0 & 1 & 0 & 0 & -1 & 0 \\ 0 & 1 & -2 & 1 & 1 & -2 & 1 \\ 0 & 1 & 0 & -1 & 1 & 0 & -1 \end{bmatrix} \begin{bmatrix} \Phi_0^+ \\ \Phi_1^+ \\ \Phi_2^+ \\ \Phi_3^+ \\ \Phi_4^+ \\ \Phi_5^+ \\ \Phi_6^+ \end{bmatrix} \equiv \hat{\chi}_s \begin{bmatrix} \Phi_0^+ \\ \Phi_1^+ \\ \Phi_2^+ \\ \Phi_3^+ \\ \Phi_4^+ \\ \Phi_5^+ \\ \Phi_6^+ \end{bmatrix} \tag{5.40}$$

[‡]We have omitted the normalisation factors of the new symmetrised basis.

[§]The subscript s has been used twice: $\hat{\Phi}_s$ means all possible singlet states $(s, d, \dots)$ while Φ_s means an extended s-state.

$$
\hat{\Phi}_t =
\begin{bmatrix}
\Phi_{p_1} \\
\Phi_{p_2} \\
\Phi_{p_3} \\
\Phi_{f_1} \\
\Phi_{f_2} \\
\Phi_{f_3}
\end{bmatrix}
=
\begin{bmatrix}
1 & 1 & 0 & -1 & 1 & 0 \\
1 & 0 & 1 & 1 & 0 & -1 \\
0 & -1 & -1 & 0 & 1 & -1 \\
0 & 1 & -1 & 0 & -1 & -1 \\
1 & 0 & -1 & 1 & 0 & 1 \\
1 & -1 & 0 & -1 & -1 & 0
\end{bmatrix}
\begin{bmatrix}
\Phi_1^- \\
\Phi_2^- \\
\Phi_3^- \\
\Phi_4^- \\
\Phi_5^- \\
\Phi_6^-
\end{bmatrix}
\equiv \hat{\chi}_t
\begin{bmatrix}
\Phi_1^- \\
\Phi_2^- \\
\Phi_3^- \\
\Phi_4^- \\
\Phi_5^- \\
\Phi_6^-
\end{bmatrix}
\tag{5.41}
$$

The matrices $\hat{\chi}_i$ (where $i = s, t$) are independent unitary matrices that help to diagonalise the problem.

Step 4: Using the similarity transformation as in Equation, (4.37), we block-diagonalise the Hamiltonians $\hat{H}_s$ and $\hat{H}_t$. The respective block-diagonal dispersion relations are

$$
\begin{bmatrix}
U\mathcal{G}_0 & 2V\mathcal{G}_1 & 0 & 0 & 0 & 0 & 0 \\
6U\mathcal{G}_1 & \mathcal{K}_s & 0 & 0 & 0 & 0 & 0 \\
0 & 0 & \mathcal{K}_{d_{T_{2g}}} & 0 & 0 & 0 & 0 \\
0 & 0 & 0 & \mathcal{K}_{d_{T_{2g}}} & 0 & 0 & 0 \\
0 & 0 & 0 & 0 & \mathcal{K}_{d_{T_{2g}}} & 0 & 0 \\
0 & 0 & 0 & 0 & 0 & \mathcal{K}_{d_{E_g}} & 0 \\
0 & 0 & 0 & 0 & 0 & 0 & \mathcal{K}_{d_{E_g}}
\end{bmatrix}
\begin{bmatrix}
\Phi_0 \\
\Phi_s \\
\Phi_{d_1} \\
\Phi_{d_2} \\
\Phi_{d_3} \\
\Phi_{d_4} \\
\Phi_{d_5}
\end{bmatrix}
=
\begin{bmatrix}
\Phi_0 \\
\Phi_s \\
\Phi_{d_1} \\
\Phi_{d_2} \\
\Phi_{d_3} \\
\Phi_{d_4} \\
\Phi_{d_5}
\end{bmatrix}
\tag{5.42}
$$

$$
\begin{bmatrix}
\mathcal{K}_p & 0 & 0 & 0 & 0 & 0 \\
0 & \mathcal{K}_p & 0 & 0 & 0 & 0 \\
0 & 0 & \mathcal{K}_p & 0 & 0 & 0 \\
0 & 0 & 0 & \mathcal{K}_f & 0 & 0 \\
0 & 0 & 0 & 0 & \mathcal{K}_f & 0 \\
0 & 0 & 0 & 0 & 0 & \mathcal{K}_f
\end{bmatrix}
\begin{bmatrix}
\Phi_{p_1} \\
\Phi_{p_2} \\
\Phi_{p_3} \\
\Phi_{f_1} \\
\Phi_{f_2} \\
\Phi_{f_3}
\end{bmatrix}
=
\begin{bmatrix}
\Phi_{p_1} \\
\Phi_{p_2} \\
\Phi_{p_3} \\
\Phi_{f_1} \\
\Phi_{f_2} \\
\Phi_{f_3}
\end{bmatrix}
\tag{5.43}
$$

where

$$\mathcal{K}_s = V(\mathcal{G}_0 + 4\mathcal{G}_1 + \mathcal{G}_2 + 2\mathcal{G}_3 + 4\mathcal{G}_4) \tag{5.44}$$

$$\mathcal{K}_{d_{T_{2g}}} = V(\mathcal{G}_0 + \mathcal{G}_2 - 2\mathcal{G}_3) = 1 \tag{5.45}$$

$$\mathcal{K}_{d_{E_g}} = V(\mathcal{G}_0 - 2\mathcal{G}_1 + \mathcal{G}_2 + 2\mathcal{G}_3 - 2\mathcal{G}_4) = 1 \tag{5.46}$$

$$\mathcal{K}_p = V(\mathcal{G}_0 + 2\mathcal{G}_1 - \mathcal{G}_2 - 2\mathcal{G}_4) = 1 \tag{5.47}$$

$$\mathcal{K}_f = V(\mathcal{G}_0 - 2\mathcal{G}_1 - \mathcal{G}_2 + 2\mathcal{G}_4) = 1 \tag{5.48}$$

These are the solutions to the two-body problem at zero temperature and pressure. The 2×2 block in Equation (5.42) corresponds to the s-symmetrical state, the next three 1×1 blocks are triply degenerate d- states of T_{2g} symmetry, and the last two 1×1 are doubly degenerate d- states with the E_g symmetry. In the case of triplet states in Equation (5.43), the p- and f- states are 3-fold degenerate and they belong to the T_{1u} and T_{2u} symmetry, respectively.
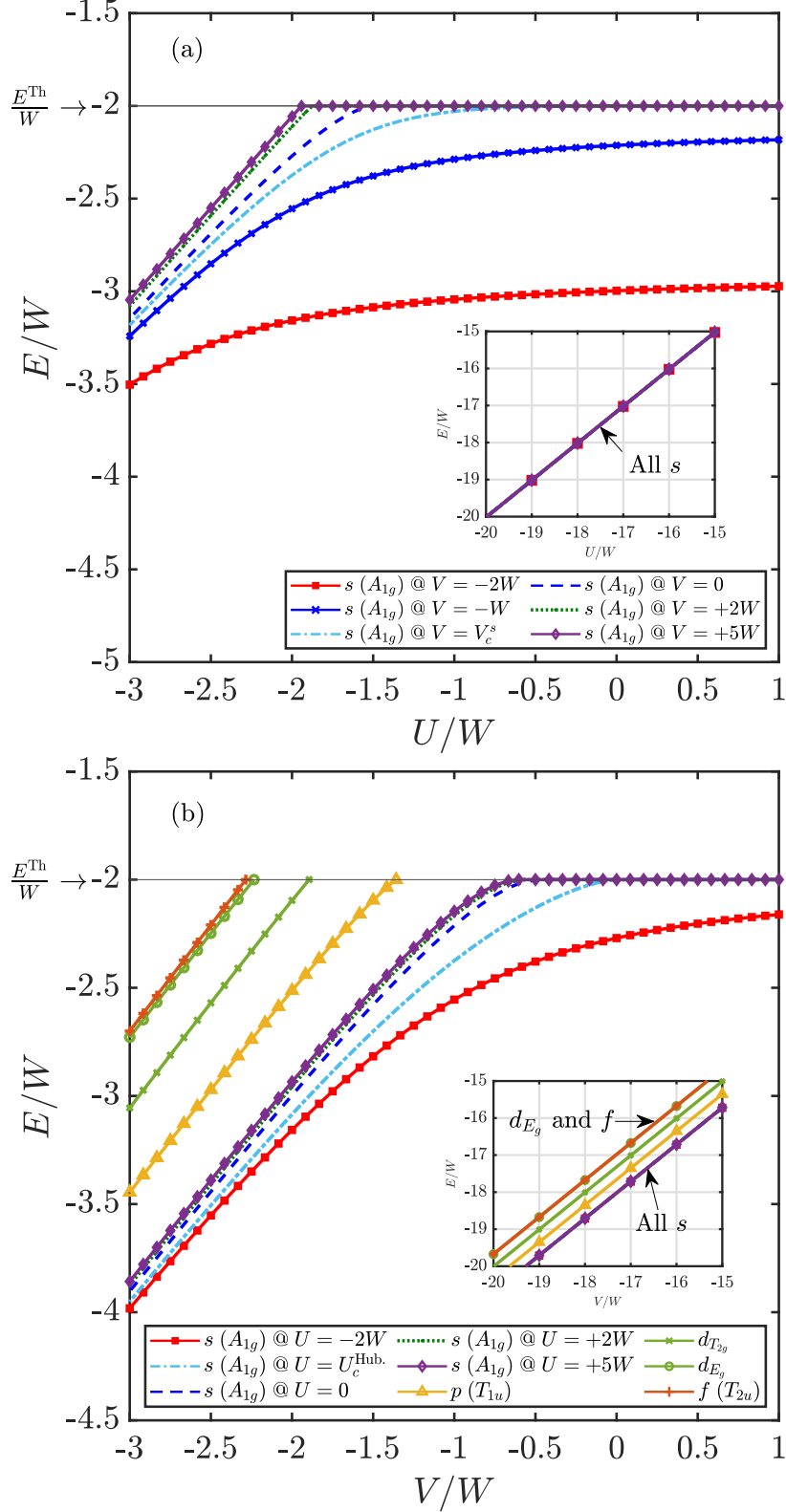
Figure 5.3: The total energy of pairs for (a) the s-states only, and (b) all states of various symmetries. The critical attractions for the s-state are $U_c^{\text{Hub.}}(V=0)=-1.4874W$ and $V_c^s(U=0)=-0.4836W$. All states except the s-state are unaffected by U. The excited states (p, $d_{T_{2g}}$, d_{E_g} and f) only appear at strongly attractive V. At very large attractions U and V, all s-states have similar values (insets of panels (a) and (b)). For large intersite attraction, $V \to -\infty$, the d_{E_g} and f states have approximately the same energies and are indiscernible: inset of panel (b).

The plot in Figure 5.3 shows the total energy of all the different pair symmetries found in the FCC lattice. We note that there is a plateau at $-2W$ when the particles are not bound. Whereas there is a transition into a bound state when the plot drops below $-2W$. At zero momentum, the ground state pair is of s symmetry.

A critical attraction must be reached before the formation of any bound state. At very large attractions U and V, the s-states have very similar values (insets of Figure 5.3a and 5.3b). In Figure 5.3b, the s-states are formed at relatively weak intersite attractions V compared to other states. Additionally, for very strong attractive V, the energies of all the pair symmetries are separated by an energy of order t: except for the d_{E_g}- and f- states that have approximately the same energies and are therefore indiscernible when plotted (inset of Figure 5.3b). Note that the labels $d_{T_{2g}}$ and d_{E_g} are d-states with T_{2g} and E_g symmetries respectively. The separation of states at large attractive V is a consequence of the superlight effect. We emphasise that at $\boldsymbol{P} = 0$, the degeneracy of the p-, $d_{T_{2g}}$-, d_{E_g}-, and f- states is three-fold, three-fold, two-fold, and three-fold, respectively, as identified by the group theory analysis.

5.3.2 Binding Criteria

We evaluate the minimum binding threshold for the formation of a bound state at zero pair momentum. With the diagonalised equations (5.42) and (5.43), the different pair symmetries are given by:

$$s: \quad \begin{vmatrix} 1 - U\mathcal{G}_0 & -2V\mathcal{G}_1 \\ -6U\mathcal{G}_1 & 1 - \mathcal{K}_s \end{vmatrix} = 0 \tag{5.49}$$

$$d_{T_{2g}}: \quad 1 - \mathcal{K}_{d_{T_{2g}}} = 0 \tag{5.50}$$

$$d_{E_g}: \quad 1 - \mathcal{K}_{d_{E_g}} = 0 \tag{5.51}$$

$$p: \quad 1 - \mathcal{K}_p = 0 \tag{5.52}$$

$$f: \quad 1 - \mathcal{K}_f = 0 \tag{5.53}$$

A phase diagram that shows where bound pairs form can be constructed by setting $E \to -2W = -24t$ in the expressions (5.49)–(5.53) above. Following Ref. [107], the exact solution of the Green's functions (5.31) for $E = -24t$ are

$$\mathcal{G}_0 = -\frac{\sqrt{3}K_0^2}{8\pi^2 t} = \frac{-0.056027549298548}{t} \tag{5.54}$$

$$\mathcal{G}_1 = \frac{1}{24t} - \frac{\sqrt{3}K_0^2}{8\pi^2 t} = \frac{1}{24t} + \mathcal{G}_0 \tag{5.55}$$

$$\mathcal{G}_2 = -\frac{9\sqrt{3}K_0^2}{8\pi^2 t} - \frac{3}{4t\sqrt{3}K_0^2} + \frac{2}{3t} = 9\mathcal{G}_0 + \frac{3}{32\pi^2 t^2 \mathcal{G}_0} + \frac{2}{3t} \tag{5.56}$$

$$\mathcal{G}_3 = \frac{\sqrt{3}K_0^2}{24\pi^2 t} - \frac{1}{8t\sqrt{3}K_0^2} = \frac{1}{64\pi^2 t^2 \mathcal{G}_0} - \frac{\mathcal{G}_0}{3} \tag{5.57}$$

$$\mathcal{G}_4 = \frac{\sqrt{3}K_0^2}{24\pi^2 t} + \frac{1}{4t\sqrt{3}K_0^2} - \frac{1}{12t} = -\frac{\mathcal{G}_0}{3} - \frac{1}{32\pi^2 t^2 \mathcal{G}_0} - \frac{1}{12t} \tag{5.58}$$

where $K_0 = K\left(\frac{\sqrt{3}-1}{2\sqrt{2}}\right) = 1.598142002112540$ is the complete elliptic integral of the first kind. The binding condition for the s-state is obtained by expanding Equation (5.49).

Doing this, we have

$$V_c^s \leq V(U) = \frac{U\mathcal{G}_0 - 1}{U\mathcal{G}_0\mathcal{C} - \mathcal{C} - 12U\mathcal{G}_1^2} \tag{5.59}$$

where $\mathcal{C} = \mathcal{G}_0 + 4\mathcal{G}_1 + \mathcal{G}_2 + 2\mathcal{G}_3 + 4\mathcal{G}_4 = 12\mathcal{G}_0 + \frac{1}{2t} = -0.172330591582576/t$.

From Equation (5.59), the critical attractions to bind pairs into s-symmetric states in

certain limits are

$$V_c^s(U = 0) = -5.80280025...t \tag{5.60}$$

$$V_c^s(U \to +\infty) = -7.8028002504...t \tag{5.61}$$

$$U_c(V = 0) = -17.84836232388...t \tag{5.62}$$

$$U_c(V \to +\infty) = -24t \tag{5.63}$$

Similarly, for the non-s states, we obtain the following critical attractions

$$V_c^{d_{T_{2g}}} = -22.734195989010747t \tag{5.64}$$

$$V_c^{d_{E_g}} = -26.810644276320041t \tag{5.65}$$

$$V_c^p = -16.302567033831927t \tag{5.66}$$

$$V_c^f = -27.416574191996979t \tag{5.67}$$

To construct the binding diagram in Figure 5.4, we vary the interaction strengths U

and V, and note when the total energy drops slightly below $-2W$. The non-s-symmetric

states (i.e. p-, $d_{T_{2g}}$-, d_{E_g}- and f- states) are insensitive to U. In comparison to other

lattices with lower coordination numbers, pairs require stronger attractions for their for-

mation in the FCC lattice. This is due to the increase in kinetic energy with coordination

number.

We measure the critical attractions above relative to the half-bandwidth energy.

The required potential to create bound onsite pairs with no intersite interaction is

$U_c^{\text{Hub.}}(V{=}0) \approx -1.4874W$ (the negative Hubbard model, $V{=}0$). This is a slightly greater

attraction relative to the simple cubic [73] and body-centred cubic (Chapter 4, section

4.3.2) lattices. On the other hand, the critical attraction to form an intersite s-state

with no onsite interaction is $V_c^s(U{=}0) \approx -0.4836W$. Furthermore, the s-states in the

limit of infinite repulsions are analysed. The onsite s-state is guaranteed to form if

$U_c^{\text{Hub.}}(V{\to}{+}\infty) \le -2W$. Similarly, $V_c^s({+}\infty) \le -0.6502W$ will certainly bind an extended

s-state when U is infinite. The non-s pairs have critical intersite binding strength V_c^p

$\approx -1.3586W$, $V_c^{d_{T_{2g}}} \approx -1.8945W$, $V_c^{d_{E_g}} \approx -2.2342W$, $V_c^f \approx -2.2847W$.
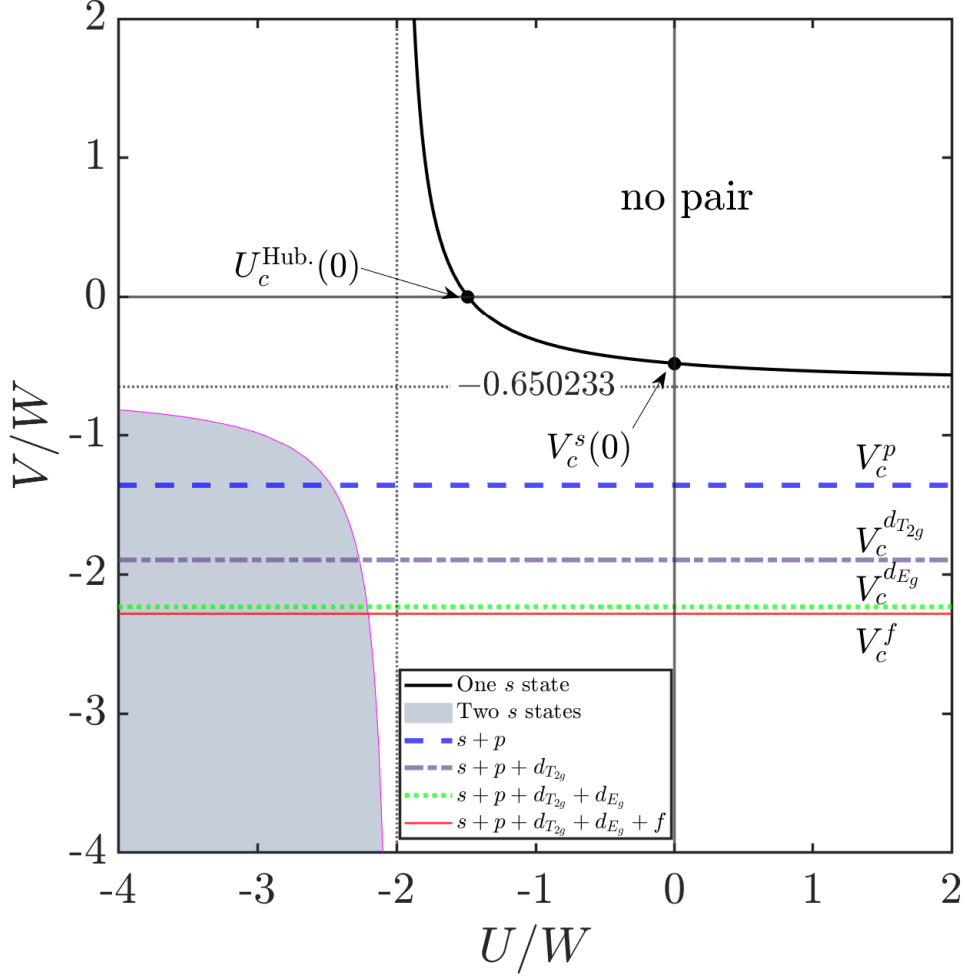
Figure 5.4: Binding diagram showing pair formation at $\boldsymbol{P} = 0$ in an FCC lattice. The black curved line is the boundary that separates bound from unbound s-symmetry pairs, the grey shaded region enclosed by the magenta solid line indicates a region with two s-states, the blue thick dashed line represents the onset of triply degenerate p-states, the purple dash-dotted line shows the binding of a triple degenerate d-symmetry pair of T_{2g} symmetry (labelled $d_{T_{2g}}$), the green dotted line is the line below which two d-wave pairs with E_g symmetry start to form (labelled d_{E_g}) and the red solid line indicates the formation of triply-degenerate f pairs. An s-state is guaranteed to form for attractions equal to or stronger than $U = -2W$, $V = -0.65023W$.

To examine the effect of the coordination number (alternatively referred to as the number of nearest-neighbour sites) on the binding strength in 3D lattices, we compare the critical attractions in the simple cubic, BCC and FCC lattices. Noting that the respective half-bandwidths are $W_{\mathrm{SC}} = 6t$, $W_{\mathrm{BCC}} = 8t$, and $W_{\mathrm{FCC}} = 12t$, the summary of this comparison is given in Table 5.2. First and foremost, it is evident that the number of paired states increases with the coordination number. Secondly, there are similarities in the minimal thresholds for creating pairs on these 3D lattices. A striking commonality found in these systems is that an onsite attraction equal to the bandwidth energy in each lattice will adequately form a well-bound onsite pair in the limit of infinitely large intersite repulsion. In contrast, however, an intersite attraction that is stronger than the bandwidth would be required to bind two fermions into highly energetic states (d_{E_g}- and f- states) in the FCC lattice.

Pairing symmetry	Binding parameter	Minimum attraction required		
		SC	BCC	FCC
s-wave	$U(V{=}0)$	$-1.3189W_{\mathrm{SC}}$	$-1.4355W_{\mathrm{BCC}}$	$-1.4874W_{\mathrm{FCC}}$
	$U(V{=}{+}\infty)$	$-2W_{\mathrm{SC}}$	$-2W_{\mathrm{BCC}}$	$-2W_{\mathrm{FCC}}$
	$V(U{=}0)$	$-0.6455W_{\mathrm{SC}}$	$-0.6358W_{\mathrm{BCC}}$	$-0.4836W_{\mathrm{FCC}}$
	$V(U{=}{+}\infty)$	$-0.9789W_{\mathrm{SC}}$	$-0.8858W_{\mathrm{BCC}}$	$-0.6502W_{\mathrm{FCC}}$
p-wave (A_{2u})	V	$-1.5885W_{\mathrm{SC}}$	$-1.5828W_{\mathrm{BCC}}$	$-1.3586W_{\mathrm{FCC}}$
d-wave (T_{2g})	V		$-1.8804W_{\mathrm{BCC}}$	$-1.8945W_{\mathrm{FCC}}$
d-wave (E_g)	V	$-1.8034W_{\mathrm{SC}}$		$-2.2342W_{\mathrm{FCC}}$
f-wave (T_{2u})	V		$-1.9639W_{\mathrm{BCC}}$	$-2.2847W_{\mathrm{FCC}}$

Table 5.2: Comparing critical binding strengths at $\boldsymbol{P} = 0$, $T = 0$ in 3D cubic lattices (simple cubic, body-centred cubic, and face-centred cubic). $W_{\mathrm{SC}} = 6t$, $W_{\mathrm{BCC}} = 8t$, and $W_{\mathrm{FCC}} = 12t$ are the respective half-bandwidths. We note that there are more pairing states in the FCC lattice than the other lattices.

5.3.3   Dispersion

Here, we calculate the dispersion of bound pairs in the first BZ of the FCC lattice. We recall from the last section that V must be attractively greater than the bandwidth energy (i.e $V < -2.2847W$) to observe the excited states. We begin with the dispersions obtained from the secular equations (5.19) and (5.29). Next, we compare perturbation theory calculations and the dispersions.

Figure 5.5 shows the characteristic dispersion for intersite paired states (using the secular equations) whereby U is repulsive and V is attractive: a very common scenario found in many materials. Also, we construct the dispersion of pairs in the limit of competing attractive interactions (i.e. $|U| = |V|$) in Figure 5.6. In both figures, degeneracies are lifted away from the Γ point, and there is mixing and crossing of states, making it difficult to specify pair symmetries. Our method aids the explicit classification of the singlet and triplet states.

In addition to having more bound states when U is attractive, there is a considerable modification in the shape of the singlets between Figures 5.5 and 5.6. For example in Figure 5.6 and along the Γ-X line, a high singlet energy drops drastically to almost coincide with the lowest singlet energy at the X point - this behaviour is absent in Figure 5.5 where U is repulsive and is not due to the increase in V. Similarly, a slight discrepancy can be noticed in the U-Γ direction. Whereas the general form of the triplets is not altered in both plots since the dispersion matrix, Equation (5.29), does not contain U, but their energies scale with the strength of V.
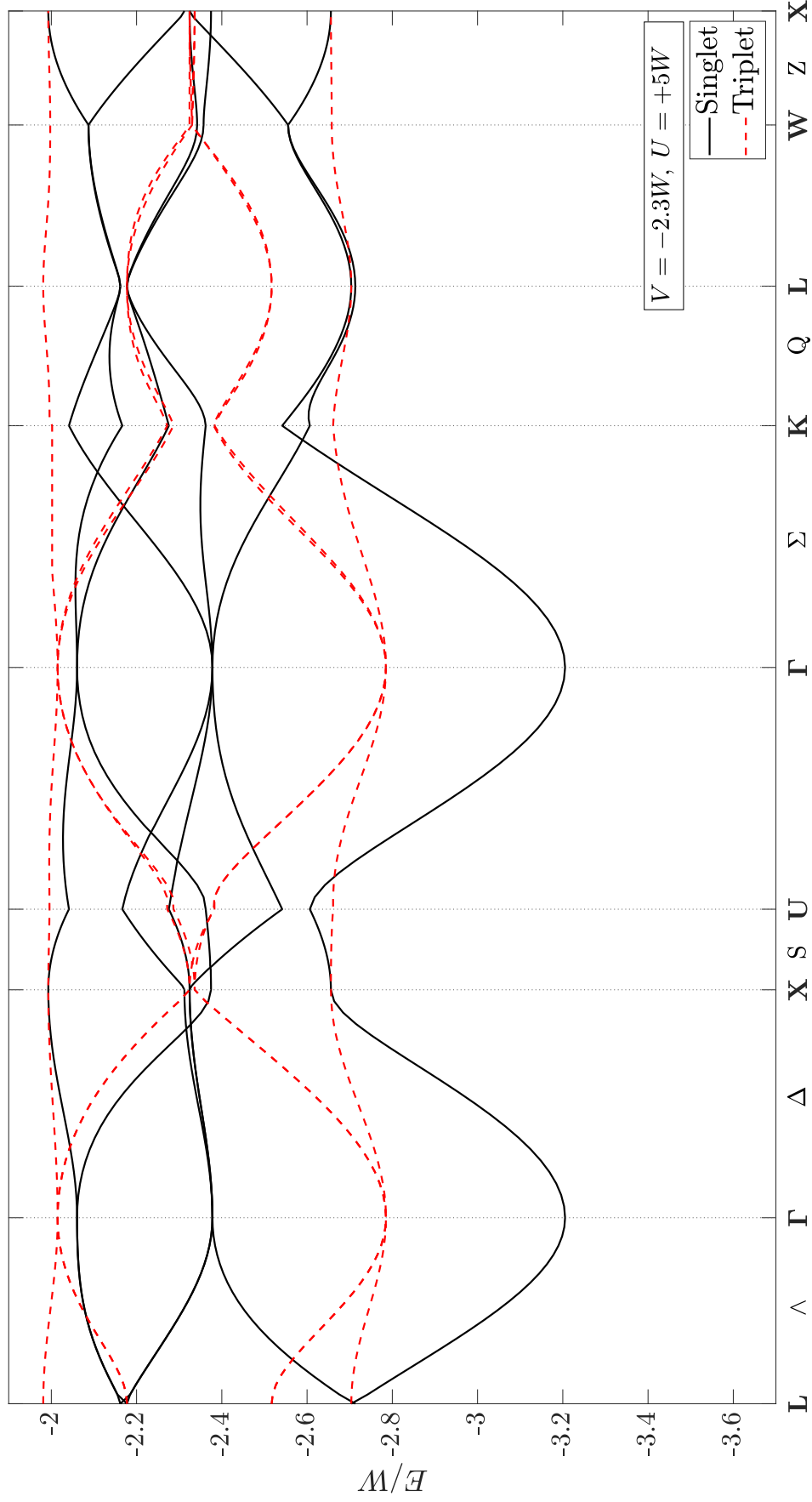
Figure 5.5: Dispersion in FCC Brillouin zone with repulsive Hubbard interaction $U = +5W$ and attractive intersite interaction $V = -2.3W$ calculated using Equations (5.19) and (5.29).
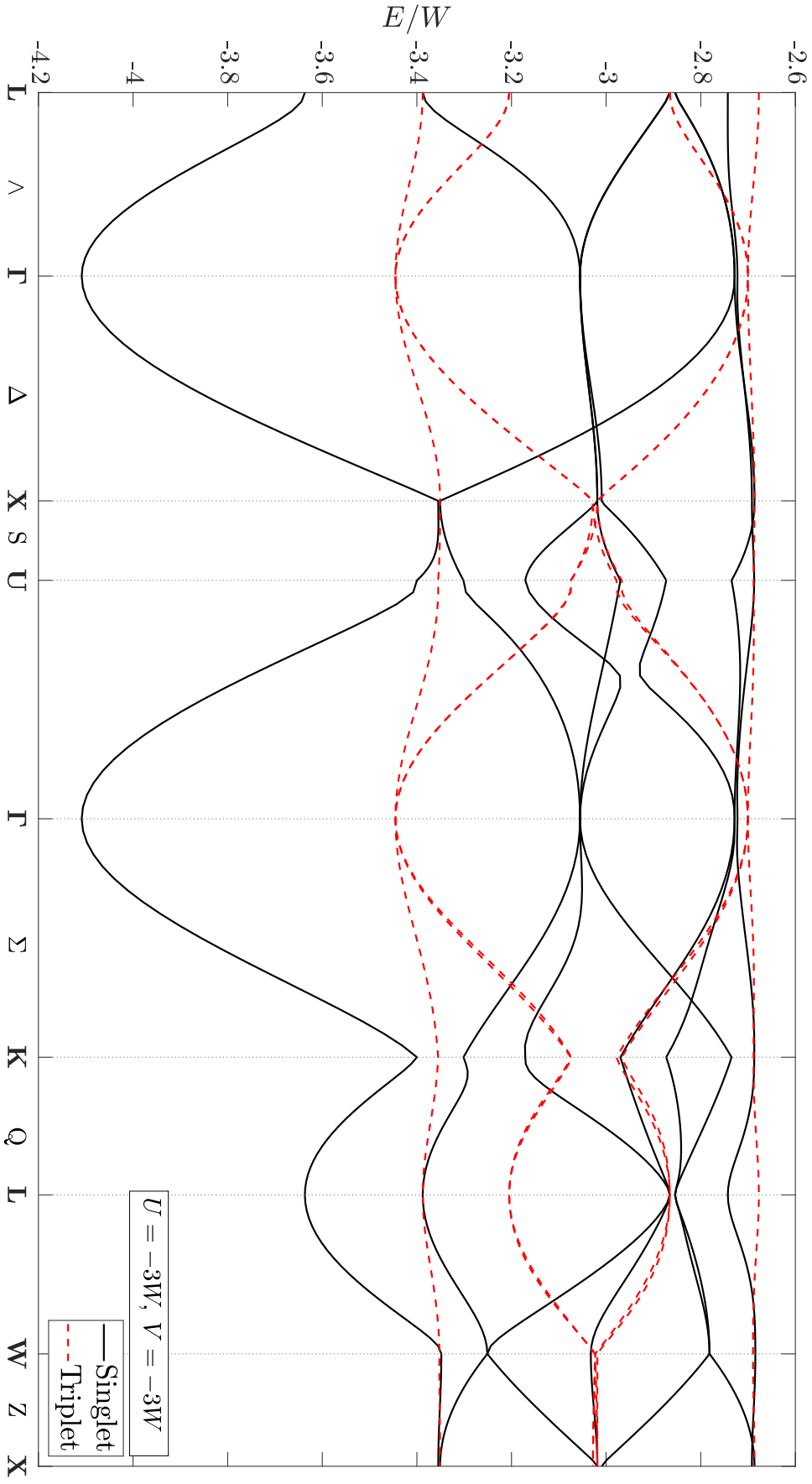
Figure 5.6: Dispersion with similar attractions calculated from the dispersion equations (5.19) and (5.29). The onsite and intersite interactions are both equal and attractive $U = V = -3W$.

5.3.3.1 Perturbation Theory Calculations

We perform perturbation calculations in the strong-coupling limits and present the dispersion results. The perturbation is the hopping of particles. We first perform this treatment in the strongly attractive Hubbard limit: $U \to -\infty$, $|U| \gg t$, $V = 0$. In this case, there has to be two hops for the pair to bind again after initially breaking. Secondly, we find the secular Hamiltonian due to the perturbation in the limit of strong repulsive onsite interaction but strongly attractive intersite interaction: $U \to +\infty$, $V < 0$, $|V| \gg t$. In this case, the movement of pairs is a first-order effect in t because of the FCC lattice structure.
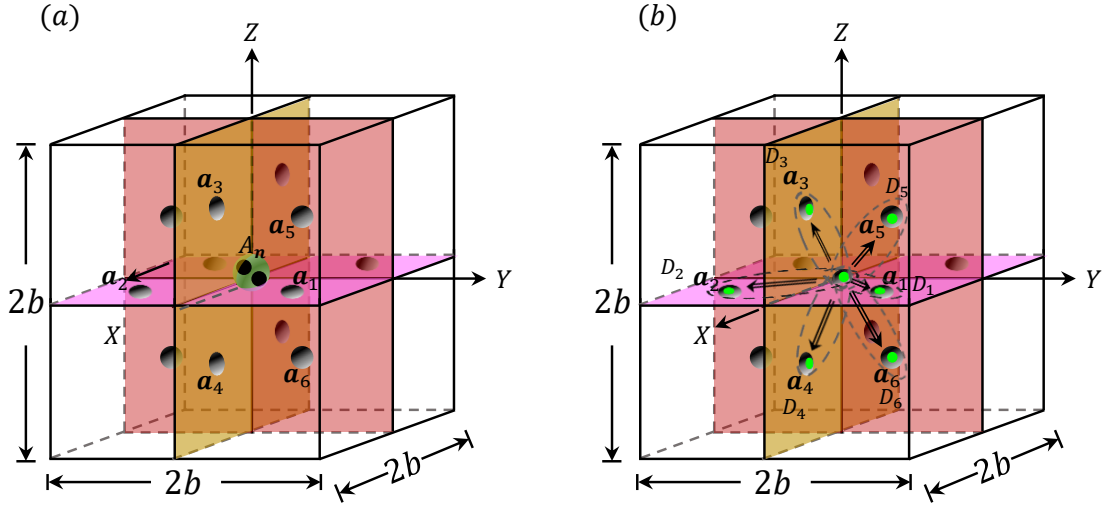
Figure 5.7: FCC nearest-neighbour vectors and dimer basis for (a) Initial configuration $A_{\boldsymbol{n}}$, the small black circles represent the two electrons. (b) Intersite attraction - D_1, D_2, D_3, D_4, D_5, and D_6 are pre-defined intersite configurations. In (b), the small green circles represent electrons, the dashed oval depicts a bound state, we use the central lattice site as the anchor point, the double-line arrow shows the anchor direction used to analyse the hopping of triplet states. The need for the anchor is to help resolve the sign problem arising from particle exchange.

Before we proceed, we shall define *six* dimer basis vectors (see Figure 5.7b):

$$
\begin{aligned}
\boldsymbol{a}_1 &= \left\{ \frac{b}{2}, \frac{b}{2}, 0 \right\}, \quad \boldsymbol{a}_2 = \left\{ \frac{b}{2}, -\frac{b}{2}, 0 \right\}, \quad \boldsymbol{a}_3 = \left\{ \frac{b}{2}, 0, \frac{b}{2} \right\}, \\
\boldsymbol{a}_4 &= \left\{ \frac{b}{2}, 0, -\frac{b}{2} \right\}, \quad \boldsymbol{a}_5 = \left\{ 0, \frac{b}{2}, \frac{b}{2} \right\}, \quad \boldsymbol{a}_6 = \left\{ 0, \frac{b}{2}, -\frac{b}{2} \right\}
\end{aligned}
\tag{5.68}
$$

where b is the lattice constant. Next, we define the Fourier-space vectors below

$$A_{\boldsymbol{n}} = \sum_{\boldsymbol{P}} e^{i\boldsymbol{P}\boldsymbol{n}} A_{\boldsymbol{P}} \ , \qquad A_{\boldsymbol{n}+\boldsymbol{a}} = \sum_{\boldsymbol{P}} e^{i\boldsymbol{P}(\boldsymbol{n}+\boldsymbol{a})} A_{\boldsymbol{P}} = e^{i\boldsymbol{P}\boldsymbol{a}} A_{\boldsymbol{n}} \tag{5.69}$$

where $\boldsymbol{P}$ is the pair total momentum.

Strongly bound onsite pair

In the limit of large attractive U, $V = 0$, $|U| \gg t$, the energy due to perturbation is proportional to t^2/U. If the initial configuration is $A_{\boldsymbol{n}}$ as in Figure 5.7a, then the perturbed Hamiltonian matrix is

$$\hat{H}' \cdot A_{\boldsymbol{n}} = -\frac{24t^2}{|U|} A_{\boldsymbol{n}} - \frac{2t^2}{|U|}(A_{\boldsymbol{n}+\boldsymbol{a}_1} + A_{\boldsymbol{n}-\boldsymbol{a}_1} + A_{\boldsymbol{n}+\boldsymbol{a}_2} + A_{\boldsymbol{n}-\boldsymbol{a}_2} + A_{\boldsymbol{n}+\boldsymbol{a}_3} + A_{\boldsymbol{n}-\boldsymbol{a}_3}$$
$$+ A_{\boldsymbol{n}+\boldsymbol{a}_4} + A_{\boldsymbol{n}-\boldsymbol{a}_4} + A_{\boldsymbol{n}+\boldsymbol{a}_5} + A_{\boldsymbol{n}-\boldsymbol{a}_5} + A_{\boldsymbol{n}+\boldsymbol{a}_6} + A_{\boldsymbol{n}-\boldsymbol{a}_6}) \tag{5.70}$$

Next, we substitute Equation (5.69) in Equation (5.70) to have

$$E_{\boldsymbol{n}}^{(2)} = -\frac{24t^2}{|U|} - \frac{2t^2}{|U|}(e^{i\boldsymbol{P}\boldsymbol{a}_1} + e^{-i\boldsymbol{P}\boldsymbol{a}_1} + e^{i\boldsymbol{P}\boldsymbol{a}_2} + e^{-i\boldsymbol{P}\boldsymbol{a}_2} + e^{i\boldsymbol{P}\boldsymbol{a}_3} + e^{-i\boldsymbol{P}\boldsymbol{a}_3}$$
$$+ e^{i\boldsymbol{P}\boldsymbol{a}_4} + e^{-i\boldsymbol{P}\boldsymbol{a}_4} + e^{i\boldsymbol{P}\boldsymbol{a}_5} + e^{-i\boldsymbol{P}\boldsymbol{a}_5} + e^{i\boldsymbol{P}\boldsymbol{a}_6} + e^{-i\boldsymbol{P}\boldsymbol{a}_6}) \tag{5.71}$$
$$= -\frac{24t^2}{|U|} - \frac{8t^2}{|U|}\left[\cos\frac{P_x b}{2} \cdot \cos\frac{P_y b}{2} + \cos\frac{P_x b}{2} \cdot \cos\frac{P_z b}{2} + \cos\frac{P_y b}{2} \cdot \cos\frac{P_z b}{2}\right]$$

Hence, the bound state in this limit has the dispersion of the form

$$E(\boldsymbol{P}) = -|U| - \frac{8t^2}{|U|}\left[3 + \cos\frac{P_x b}{2} \cdot \cos\frac{P_y b}{2} + \cos\frac{P_x b}{2} \cdot \cos\frac{P_z b}{2} + \cos\frac{P_y b}{2} \cdot \cos\frac{P_z b}{2}\right] \tag{5.72}$$

where the first term is the strong coupling unperturbed energy, and the rest is the energy due to perturbation.

We plot the result obtained from Equation (5.19) versus Equation (5.72) in Figure 5.8. Both results are in good agreement except at the Γ and K points where there is less than 2.5% and 0.6% energy difference at those points respectively. The difference in energy reduces as the attraction U is further increased. We note that in this limit, the bound pair moves like a *dressed* free particle in the FCC BZ.
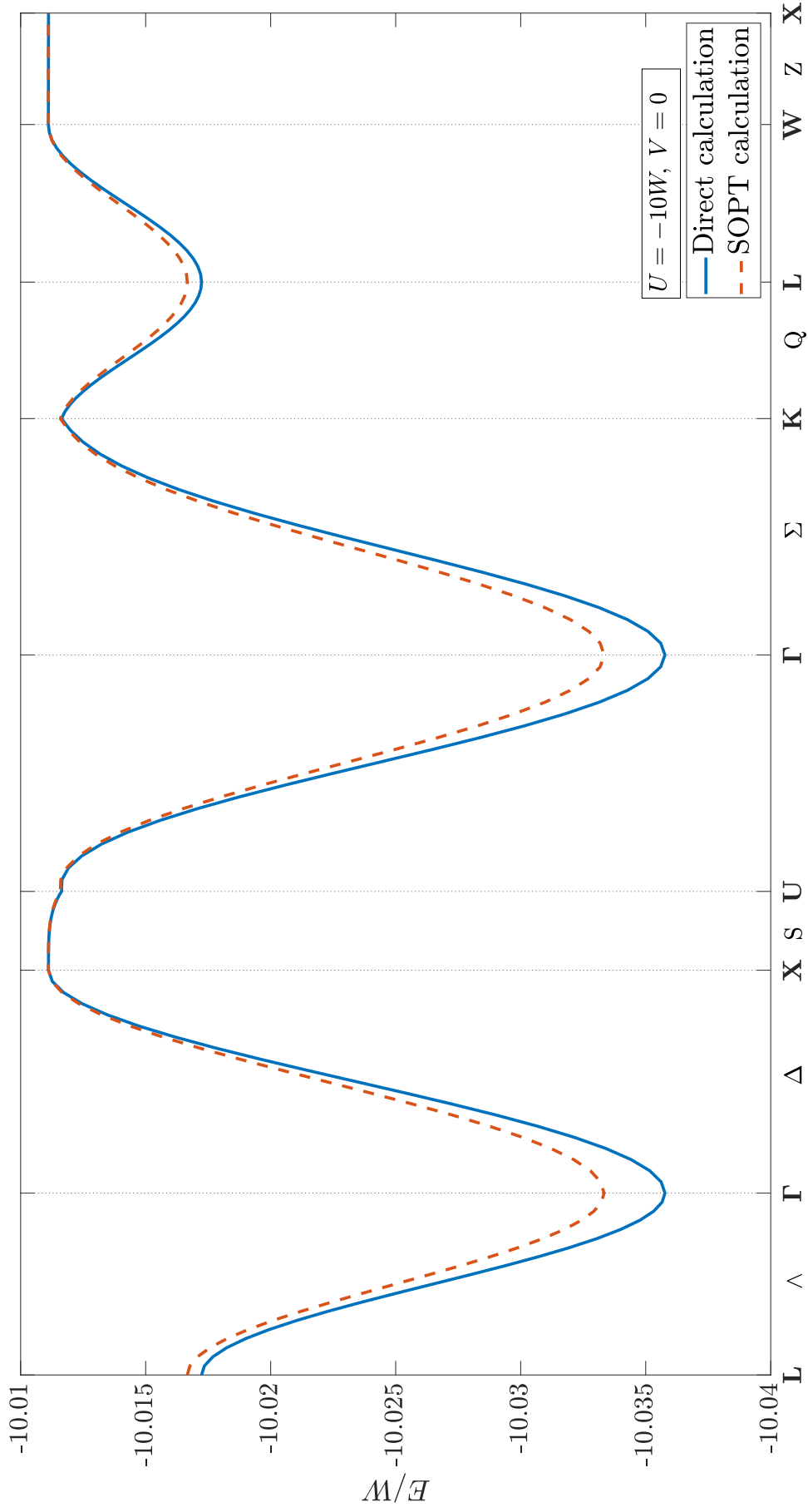
Figure 5.8: Comparing the dispersion of strongly bound onsite pair ($U = -10W$, $V = 0$) obtained from Equation (5.19) against second-order perturbation theory calculation Equation (5.72). The blue solid line is the direct calculation and the red dashed line is for the SOPT result. There is consistency in both results.

Strongly bound pairs requiring intersite attraction

In the limit $U = +\infty$, $V < 0$, $V \gg t$, the pair is made of two particles occupying a pair of nearest-neighbours with the zero-order binding energy as $-|V|$. If we introduce a first-order perturbation H', then the energy gained due to perturbation is the expectation value of the perturbed Hamiltonian which is $-t$. With the dimer basis defined earlier, we can declare the configurations for the singlets and triplets respectively as

$$D^s_{i,\boldsymbol{n}} = \frac{1}{\sqrt{2}} \left(|\uparrow\rangle_{\boldsymbol{n}} |\downarrow\rangle_{\boldsymbol{n}+\boldsymbol{a}_i} + |\downarrow\rangle_{\boldsymbol{n}} |\uparrow\rangle_{\boldsymbol{n}+\boldsymbol{a}_i} \right) \quad , \tag{5.73}$$

$$D^t_{i,\boldsymbol{n}} = |\uparrow\rangle_{\boldsymbol{n}} |\uparrow\rangle_{\boldsymbol{n}+\boldsymbol{a}_i} \tag{5.74}$$

where for the triplet states, $D^t_{i,\boldsymbol{n}} = -D^t_{i,\boldsymbol{n}-\boldsymbol{a}_i}$. Unlike in the BCC lattice, the perturbation is first-order in the FCC lattice due to its structural advantage. Using Equation (5.73), the first-order Hamiltonian matrix for the singlet states is

$$\hat{H}' D_{1,\boldsymbol{n}} = -t \left(D_{3,\boldsymbol{n}} + D_{3,\boldsymbol{n}+\boldsymbol{a}_6} \right) - t \left(D_{4,\boldsymbol{n}} + D_{4,\boldsymbol{n}+\boldsymbol{a}_5} \right) - t \left(D_{5,\boldsymbol{n}} + D_{5,\boldsymbol{n}+\boldsymbol{a}_4} \right) - t \left(D_{6,\boldsymbol{n}} + D_{6,\boldsymbol{n}+\boldsymbol{a}_3} \right)$$

$$\tag{5.75}$$

$$\hat{H}' D_{2,\boldsymbol{n}} = -t \left(D_{3,\boldsymbol{n}} + D_{3,\boldsymbol{n}-\boldsymbol{a}_5} \right) - t \left(D_{4,\boldsymbol{n}} + D_{4,\boldsymbol{n}-\boldsymbol{a}_6} \right) - t \left(D_{5,\boldsymbol{n}+\boldsymbol{a}_2} + D_{5,\boldsymbol{n}-\boldsymbol{a}_5} \right) - t \left(D_{6,\boldsymbol{n}+\boldsymbol{a}_2} + D_{6,\boldsymbol{n}-\boldsymbol{a}_6} \right)$$

$$\tag{5.76}$$

$$\hat{H}' D_{3,\boldsymbol{n}} = -t \left(D_{1,\boldsymbol{n}} + D_{1,\boldsymbol{n}-\boldsymbol{a}_6} \right) - t \left(D_{2,\boldsymbol{n}} + D_{2,\boldsymbol{n}+\boldsymbol{a}_5} \right) - t \left(D_{5,\boldsymbol{n}} + D_{5,\boldsymbol{n}+\boldsymbol{a}_2} \right) - t \left(D_{6,\boldsymbol{n}+\boldsymbol{a}_3} + D_{6,\boldsymbol{n}-\boldsymbol{a}_6} \right)$$

$$\tag{5.77}$$

$$\hat{H}' D_{4,\boldsymbol{n}} = -t \left(D_{1,\boldsymbol{n}} + D_{1,\boldsymbol{n}+\boldsymbol{a}_2} \right) - t \left(D_{2,\boldsymbol{n}} + D_{2,\boldsymbol{n}+\boldsymbol{a}_6} \right) - t \left(D_{5,\boldsymbol{n}-\boldsymbol{a}_5} + D_{5,\boldsymbol{n}+\boldsymbol{a}_4} \right) - t \left(D_{6,\boldsymbol{n}} + D_{6,\boldsymbol{n}+\boldsymbol{a}_2} \right)$$

$$\tag{5.78}$$

$$\hat{H}' D_{5,\boldsymbol{n}} = -t \left(D_{1,\boldsymbol{n}} + D_{1,\boldsymbol{n}-\boldsymbol{a}_4} \right) - t \left(D_{2,\boldsymbol{n}-\boldsymbol{a}_2} + D_{2,\boldsymbol{n}+\boldsymbol{a}_5} \right) - t \left(D_{3,\boldsymbol{n}} + D_{3,\boldsymbol{n}-\boldsymbol{a}_2} \right) - t \left(D_{4,\boldsymbol{n}-\boldsymbol{a}_4} + D_{4,\boldsymbol{n}+\boldsymbol{a}_5} \right)$$

$$\tag{5.79}$$

$$\hat{H}' D_{6,\boldsymbol{n}} = -t \left(D_{1,\boldsymbol{n}} + D_{1,\boldsymbol{n}-\boldsymbol{a}_3} \right) - t \left(D_{2,\boldsymbol{n}-\boldsymbol{a}_2} + D_{2,\boldsymbol{n}+\boldsymbol{a}_6} \right) - t \left(D_{3,\boldsymbol{n}+\boldsymbol{a}_6} + D_{3,\boldsymbol{n}-\boldsymbol{a}_3} \right) - t \left(D_{4,\boldsymbol{n}} + D_{4,\boldsymbol{n}-\boldsymbol{a}_2} \right)$$

$$\tag{5.80}$$

Applying a Fourier transform, one obtains the consistency equation below

$$
\begin{bmatrix}
E(\boldsymbol{P})+|V| & 0 & t(1+e^{i\boldsymbol{P}\boldsymbol{a}_6}) & t(1+e^{i\boldsymbol{P}\boldsymbol{a}_5}) & t(1+e^{i\boldsymbol{P}\boldsymbol{a}_4}) & t(1+e^{i\boldsymbol{P}\boldsymbol{a}_3}) \\
0 & E(\boldsymbol{P})+|V| & t(1+e^{-i\boldsymbol{P}\boldsymbol{a}_5}) & t(1+e^{-i\boldsymbol{P}\boldsymbol{a}_6}) & t(e^{i\boldsymbol{P}\boldsymbol{a}_2}+e^{-i\boldsymbol{P}\boldsymbol{a}_5}) & t(e^{i\boldsymbol{P}\boldsymbol{a}_2}+e^{-i\boldsymbol{P}\boldsymbol{a}_6}) \\
t(1+e^{-i\boldsymbol{P}\boldsymbol{a}_6}) & t(1+e^{i\boldsymbol{P}\boldsymbol{a}_5}) & E(\boldsymbol{P})+|V| & 0 & t(1+e^{i\boldsymbol{P}\boldsymbol{a}_2}) & t(e^{i\boldsymbol{P}\boldsymbol{a}_3}+e^{-i\boldsymbol{P}\boldsymbol{a}_6}) \\
t(1+e^{-i\boldsymbol{P}\boldsymbol{a}_5}) & t(1+e^{i\boldsymbol{P}\boldsymbol{a}_6}) & 0 & E(\boldsymbol{P})+|V| & t(e^{i\boldsymbol{P}\boldsymbol{a}_4}+e^{-i\boldsymbol{P}\boldsymbol{a}_5}) & t(1+e^{i\boldsymbol{P}\boldsymbol{a}_2}) \\
t(1+e^{-i\boldsymbol{P}\boldsymbol{a}_4}) & t(e^{i\boldsymbol{P}\boldsymbol{a}_5}+e^{-i\boldsymbol{P}\boldsymbol{a}_2}) & t(1+e^{-i\boldsymbol{P}\boldsymbol{a}_2}) & t(e^{i\boldsymbol{P}\boldsymbol{a}_5}+e^{-i\boldsymbol{P}\boldsymbol{a}_4}) & E(\boldsymbol{P})+|V| & 0 \\
t(1+e^{-i\boldsymbol{P}\boldsymbol{a}_3}) & t(e^{i\boldsymbol{P}\boldsymbol{a}_6}+e^{-i\boldsymbol{P}\boldsymbol{a}_2}) & t(e^{i\boldsymbol{P}\boldsymbol{a}_6}+e^{-i\boldsymbol{P}\boldsymbol{a}_3}) & t(1+e^{-i\boldsymbol{P}\boldsymbol{a}_2}) & 0 & E(\boldsymbol{P})+|V|
\end{bmatrix}
\begin{bmatrix}
D_{1,n} \\ D_{2,n} \\ D_{3,n} \\ D_{4,n} \\ D_{5,n} \\ D_{6,n}
\end{bmatrix}
= 0
$$

$$(5.81)$$

where $E(\boldsymbol{P})$ are the singlet pair energies at pair momentum $\boldsymbol{P}$.

Similarly, we obtain the first-order Hamiltonian matrix for the triplets as

$$\hat{H}' D_{1,\boldsymbol{n}} = -t\left(D_{3,\boldsymbol{n}}+D_{3,\boldsymbol{n}+\boldsymbol{a}_6}\right) - t\left(D_{4,\boldsymbol{n}}+D_{4,\boldsymbol{n}+\boldsymbol{a}_5}\right) - t\left(D_{5,\boldsymbol{n}}+D_{5,\boldsymbol{n}+\boldsymbol{a}_4}\right) - t\left(D_{6,\boldsymbol{n}}+D_{6,\boldsymbol{n}+\boldsymbol{a}_3}\right)$$

$$(5.82)$$

$$\hat{H}' D_{2,\boldsymbol{n}} = -t\left(D_{3,\boldsymbol{n}}+D_{3,\boldsymbol{n}-\boldsymbol{a}_5}\right) - t\left(D_{4,\boldsymbol{n}}+D_{4,\boldsymbol{n}-\boldsymbol{a}_6}\right) + t\left(D_{5,\boldsymbol{n}+\boldsymbol{a}_2}+D_{5,\boldsymbol{n}-\boldsymbol{a}_5}\right) + t\left(D_{6,\boldsymbol{n}+\boldsymbol{a}_2}+D_{6,\boldsymbol{n}-\boldsymbol{a}_6}\right)$$

$$(5.83)$$

$$\hat{H}' D_{3,\boldsymbol{n}} = -t\left(D_{1,\boldsymbol{n}}+D_{1,\boldsymbol{n}-\boldsymbol{a}_6}\right) - t\left(D_{2,\boldsymbol{n}}+D_{2,\boldsymbol{n}+\boldsymbol{a}_5}\right) - t\left(D_{5,\boldsymbol{n}}+D_{5,\boldsymbol{n}+\boldsymbol{a}_2}\right) + t\left(D_{6,\boldsymbol{n}+\boldsymbol{a}_3}+D_{6,\boldsymbol{n}-\boldsymbol{a}_6}\right)$$

$$(5.84)$$

$$\hat{H}' D_{4,\boldsymbol{n}} = -t\left(D_{1,\boldsymbol{n}}+D_{1,\boldsymbol{n}+\boldsymbol{a}_2}\right) - t\left(D_{2,\boldsymbol{n}}+D_{2,\boldsymbol{n}+\boldsymbol{a}_6}\right) + t\left(D_{5,\boldsymbol{n}-\boldsymbol{a}_5}+D_{5,\boldsymbol{n}+\boldsymbol{a}_4}\right) - t\left(D_{6,\boldsymbol{n}}+D_{6,\boldsymbol{n}+\boldsymbol{a}_2}\right)$$

$$(5.85)$$

$$\hat{H}' D_{5,\boldsymbol{n}} = -t\left(D_{1,\boldsymbol{n}}+D_{1,\boldsymbol{n}-\boldsymbol{a}_4}\right) + t\left(D_{2,\boldsymbol{n}-\boldsymbol{a}_2}+D_{2,\boldsymbol{n}+\boldsymbol{a}_5}\right) - t\left(D_{3,\boldsymbol{n}}+D_{3,\boldsymbol{n}-\boldsymbol{a}_2}\right) + t\left(D_{4,\boldsymbol{n}-\boldsymbol{a}_4}+D_{4,\boldsymbol{n}+\boldsymbol{a}_5}\right)$$

$$(5.86)$$

$$\hat{H}' D_{6,\boldsymbol{n}} = -t\left(D_{1,\boldsymbol{n}}+D_{1,\boldsymbol{n}-\boldsymbol{a}_3}\right) + t\left(D_{2,\boldsymbol{n}-\boldsymbol{a}_2}+D_{2,\boldsymbol{n}+\boldsymbol{a}_6}\right) + t\left(D_{3,\boldsymbol{n}+\boldsymbol{a}_6}+D_{3,\boldsymbol{n}-\boldsymbol{a}_3}\right) - t\left(D_{4,\boldsymbol{n}}+D_{4,\boldsymbol{n}-\boldsymbol{a}_2}\right)$$

$$(5.87)$$

and the their energies $E(\boldsymbol{P})$ are determined from the equation below

$$
\begin{bmatrix}
E(\boldsymbol{P})+|V| & 0 & t(1+e^{i\boldsymbol{Pa}_6}) & t(1+e^{i\boldsymbol{Pa}_5}) & t(1+e^{i\boldsymbol{Pa}_4}) & t(1+e^{i\boldsymbol{Pa}_3}) \\
0 & E(\boldsymbol{P})+|V| & t(1+e^{-i\boldsymbol{Pa}_5}) & t(1+e^{-i\boldsymbol{Pa}_6}) & -t(e^{i\boldsymbol{Pa}_2}+e^{-i\boldsymbol{Pa}_5}) & -t(e^{i\boldsymbol{Pa}_2}+e^{-i\boldsymbol{Pa}_6}) \\
t(1+e^{-i\boldsymbol{Pa}_6}) & t(1+e^{i\boldsymbol{Pa}_5}) & E(\boldsymbol{P})+|V| & 0 & t(1+e^{i\boldsymbol{Pa}_2}) & -t(e^{i\boldsymbol{Pa}_3}+e^{-i\boldsymbol{Pa}_6}) \\
t(1+e^{-i\boldsymbol{Pa}_5}) & t(1+e^{i\boldsymbol{Pa}_6}) & 0 & E(\boldsymbol{P})+|V| & -t(e^{i\boldsymbol{Pa}_4}+e^{-i\boldsymbol{Pa}_5}) & t(1+e^{i\boldsymbol{Pa}_2}) \\
t(1+e^{-i\boldsymbol{Pa}_4}) & -t(e^{i\boldsymbol{Pa}_5}+e^{-i\boldsymbol{Pa}_2}) & t(1+e^{-i\boldsymbol{Pa}_2}) & -t(e^{i\boldsymbol{Pa}_5}+e^{-i\boldsymbol{Pa}_4}) & E(\boldsymbol{P})+|V| & 0 \\
t(1+e^{-i\boldsymbol{Pa}_3}) & -t(e^{i\boldsymbol{Pa}_6}+e^{-i\boldsymbol{Pa}_2}) & -t(e^{i\boldsymbol{Pa}_6}+e^{-i\boldsymbol{Pa}_3}) & t(1+e^{-i\boldsymbol{Pa}_2}) & 0 & E(\boldsymbol{P})+|V|
\end{bmatrix}
\begin{bmatrix}
D_{1,n} \\ D_{2,n} \\ D_{3,n} \\ D_{4,n} \\ D_{5,n} \\ D_{6,n}
\end{bmatrix} = 0
$$

$$(5.88)$$

We note that the Equations (5.81) and (5.88) are similar except for sign changes in some of the matrix elements. The result from the perturbation theory calculation is shown in Figure 5.9a and is compared with the direct UV calculations: using Equations (5.19) and (5.29), in Figure 5.9b. Both results are in good agreement albeit there is a high level of degeneracy in the perturbation calculations.
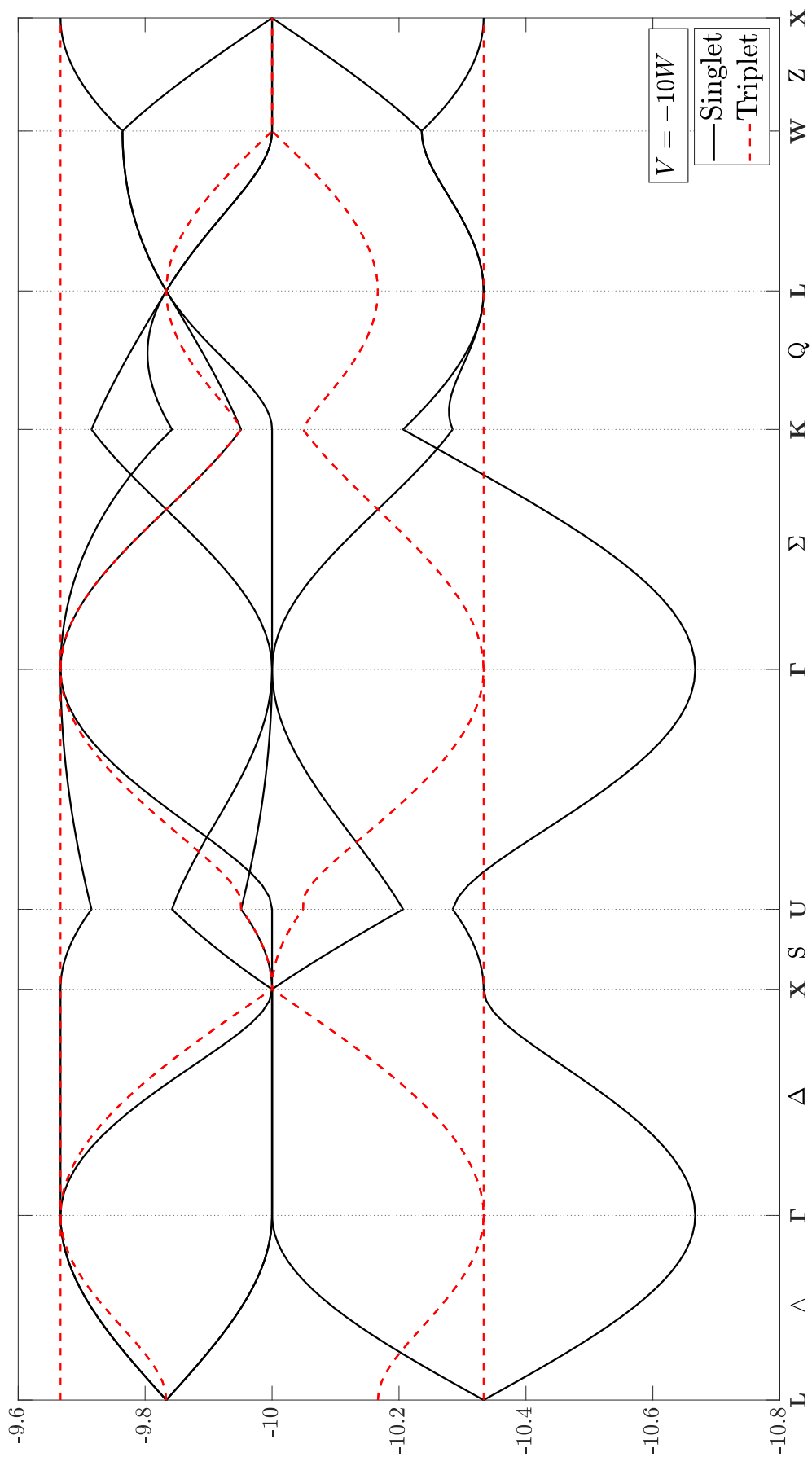
Figure 5.9a: Plot of dispersion from perturbation theory calculations on FCC for $V = -10W$, $U = +\infty$.
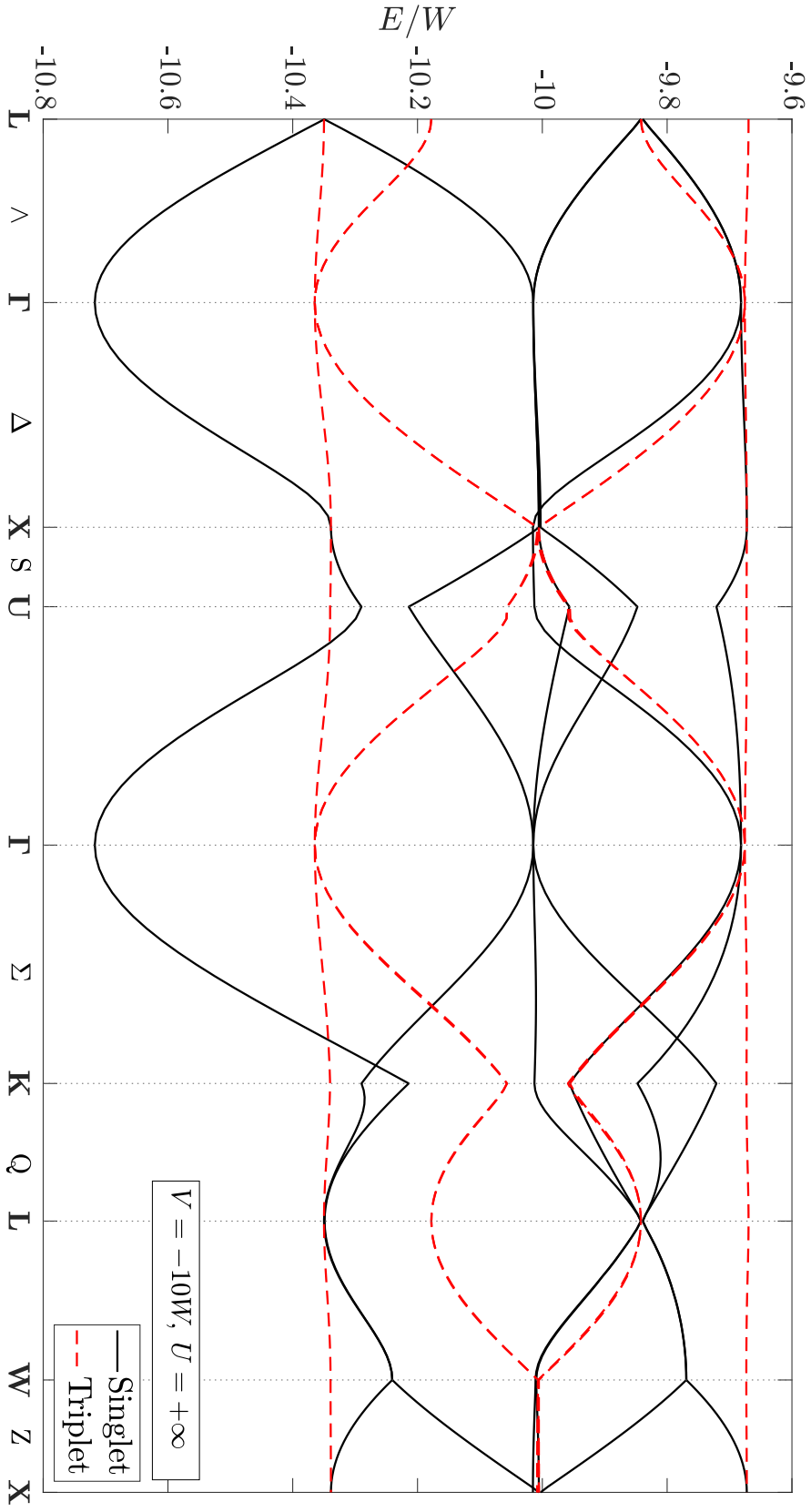
Figure 5.9b: Dispersion plot of pairs in FCC at strong intersite coupling and infinite onsite repulsion from direct UV calculation $V = -10W$, $U = +\infty$.

5.3.4 Effective Mass

For the effective mass, we use Equation (4.106) defined in Chapter 4 and the mass for pair in the FCC lattice can be seen in Figure 5.10.

In some lattices (e.g. rectangular ladder [81], simple cubic [73], and BCC [Chapter 4]), a superlight itinerant state is formed only when U and V are nearly equal and are both attractive which enhances the mobility of the pair via a single hop. However, for superlight pairs in staggered ladder [69] and triangular lattices [74], attractive onsite attraction is not required: a condition that is closer to physical systems which typically have onsite repulsion. The FCC lattice, due to its structure, is special and belongs to the latter group.

In the limit where the intersite interaction is attractive and dominant $V \to -\infty$, the pair mass does not increase infinitely (Figure 5.10b) but is only *six times* heavier than a single particle's (i.e. $m^* = 6m_0$, see derivation in the next section). This result shows the *superlight* nature of pairs in the FCC lattice because the energy and the movement of the pair only linearly depend on t. Similar *low*–mass states were reported in lower dimensions (Refs. [74, 81]) at very strong attractive V. Superlight pair movement is depicted in Figure 5.11 and during motion, the pair's total energy remains unchanged in all configurations.

On the other hand, in the limit where the onsite attraction is largely dominant $U \to -\infty$ and V is small or repulsive, the mass of the bound pair increases infinitely. In this case, the pair movement has a second-order effect in the hopping parameter t.
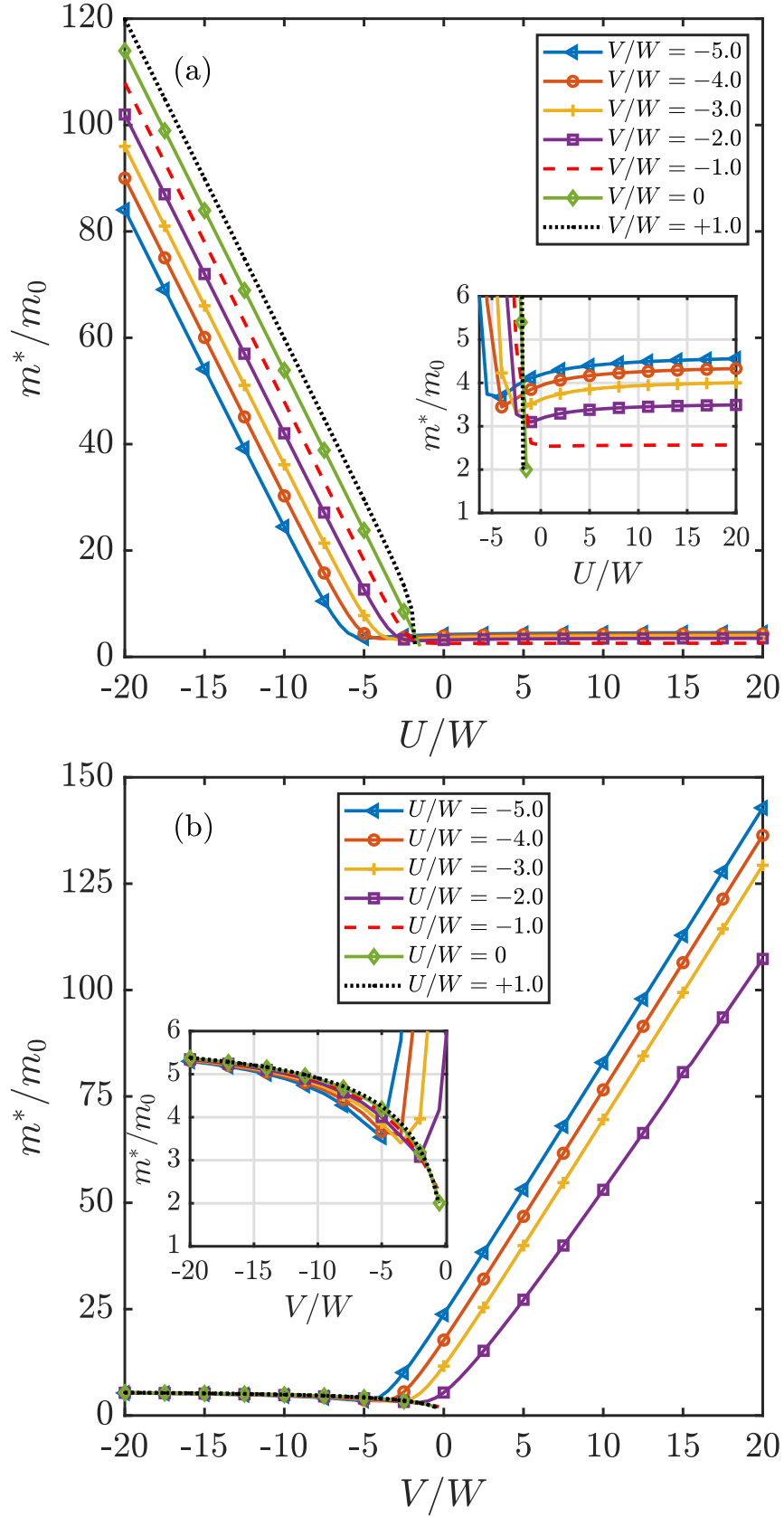
Figure 5.10: The pair mass expressed in the unit of a *free* particle mass. $m_0 = \hbar^2/(2b^2 t)$ is the bare mass of one free particle in the FCC lattice (see derivation in Appendix B).
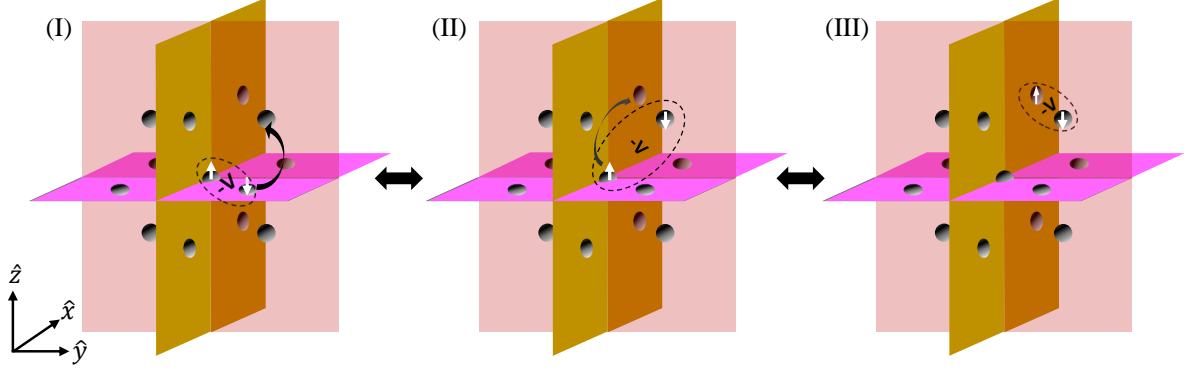
Figure 5.11: Superlight states move by first-order hops in the FCC lattice. The white vertical arrow represents an electron with its spin, each small grey circle is a lattice site (only the 13 sites of interest shown), the dashed oval represents a bound state through an attractive V and the two-way arrow implies that the configurations are degenerate. The key feature here is that the pair is itinerant as long as the intersite interaction is sufficiently attractive. Unlike in other 3D lattices where first-order superlight states are only attainable via an attractive U, a superlight state in the FCC lattice depicts a physical system where the Coulomb repulsion is large and pair movement does not require U.

5.3.4.1   Limiting Behaviour for Superlight Pair Mass

We use the dispersion equation (5.81) to derive the mass of the singlet in the limit $V \to -\infty$. It is sufficient to evaluate the energy $E(\boldsymbol{P})$ at small $\boldsymbol{P}$. Utilising the isotropic property of cubic dispersion relations close to the Γ point, we can set $\boldsymbol{P} = (P_x, 0, 0)$ and expand Equation (5.81) to arrive at

$$E^3(E - 4t)\left[E^2 + 4tE - 16t^2\left(1 + \cos\frac{P_x b}{2}\right)\right] = 0 \,, \tag{5.89}$$

The above expression gives the dispersion of six pair bands along the P_x direction where the lowest band is

$$E_1(P_x) = -2t\left(1 + \sqrt{5 + 4\cos\frac{P_x b}{2}}\right). \tag{5.90}$$

If we expand Equation (5.90) at small P_x, one obtains

$$E_1(P_x b \ll 1) \approx -2t\left[1 + 3\left(1 - \frac{(P_x b)^2}{18}\right)^{1/2}\right]$$

$$\approx -8t + \frac{1}{6}t(P_x b)^2 \equiv E_0 + \frac{\hbar^2 P_x^2}{2m^*} \,, \tag{5.91}$$

wherefrom we can extract the pair mass as

$$m^* = \frac{3\hbar^2}{tb^2} = 6m_0 \ .$$

(5.92)

5.3.5   Radius

The effective radius has been calculated using the relation defined in Equation (4.107) and the procedure described in Section 4.3.5 of Chapter 4 applies too.

The size of the pair diverges near the threshold energy $(E \to E^{\mathrm{Th}})$ because the pair is weakly bound and the pair wave function spreads over distant lattice sites. If the particles unbind, the size of the pair becomes infinite whereas it shrinks as the attraction increases. When V is strongly attractive and dominates over U, we see the formation of a local intersite pair. A bound pair is local if its size is on the order of the lattice parameter. In contrast, if the Hubbard attraction is very strong and dominant, an onsite pair is formed. We notice a shoulder-like shape in the radius when the onsite and intersite attractions are comparable. When the attractions are comparable, there is a random fluctuation in the pair's configuration i.e. it can easily switch between onsite and intersite configurations.
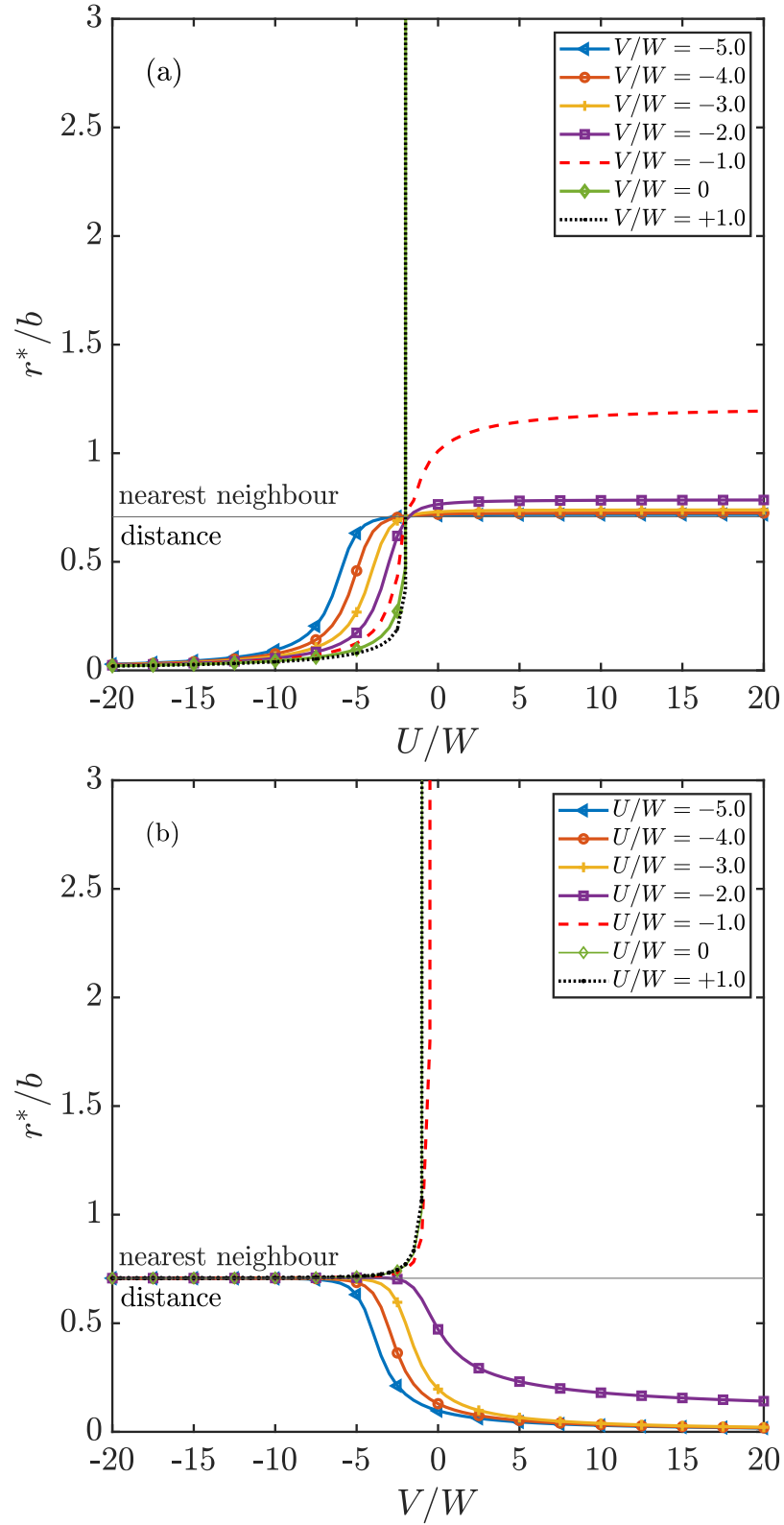
Figure 5.12: Effective radius for various U and V. The thin solid horizontal lines represent the nearest-neighbour distance $a = b/\sqrt{2}$ on a FCC lattice. Note that the radius diverges at low attraction. A shoulder forms when both attractions are comparable $U \sim V$.

5.3.6   Estimation of Transition Temperature

In this section, we examine if superlight pairs in an FCC lattice could Bose-condense at significant transition temperatures in a low-density system. As before (refer to Section 4.3.6), the transition temperature is given by the approximation:

$$T_{BEC} = \frac{3.31\hbar^2}{\bar{m}m_0 k_B} \left(\frac{n_b}{\Omega_{\text{site}}}\right)^{2/3} \tag{5.93}$$

where m_b^* is the pair mass (m_0 is the mass of a free particle and the dimensionless mass $\bar{m} = m^*/m_0$), $\Omega_{\text{site}} = b^3/4$ is the volume of the Wigner–Seitz cell for the FCC lattice, and n_b is the number of pairs per lattice site. For our calculation, we use an exemplar lattice constant $b = 14.24$Å (consistent with the FCC fullerides, although we note that electrons are not dilute in fullerides).

The transition temperatures for fixed n_b are plotted in Figures 5.13a and 5.13b. For condensation to take place, there must be pairs. This means that pairs must exist above T_{BEC}, i.e. $T_{\text{BEC}} < T_\Delta$, where $T_\Delta = \Delta/k_B$ is the pairing temperature and the binding energy is $\Delta = 2\varepsilon_0 - E_0$. The hopping parameter $t = 0.04$eV has been chosen to be consistent with fulleride superconductors [17] to set the energy scale. The maximum n_b for which T_{BEC} is consistent with the effective mass approximation is estimated to be approximately 0.015. We adopt a similar requirement to that used in Chapter 4 where pairs of radius $R' = \alpha r^*$ can fit into space without overlapping, i.e. that $n_b 16 R'^3/3 < 1$. We also assign the value $\alpha = 5$ to minimise the overlap of wave functions of different pairs. For the lowest n_b considered in this study, superlight pairs can yield a transition temperature up to 30 K (see Figures 5.13a and 5.13b for $n_b = 0.0015$). When n_b is increased, the transition temperature goes up but these superlight pairs begin to overlap. Nonetheless, this calculation predicts a transition temperature up to 70 K when $n_b = 0.015$ which is consistent with the overlap condition above.
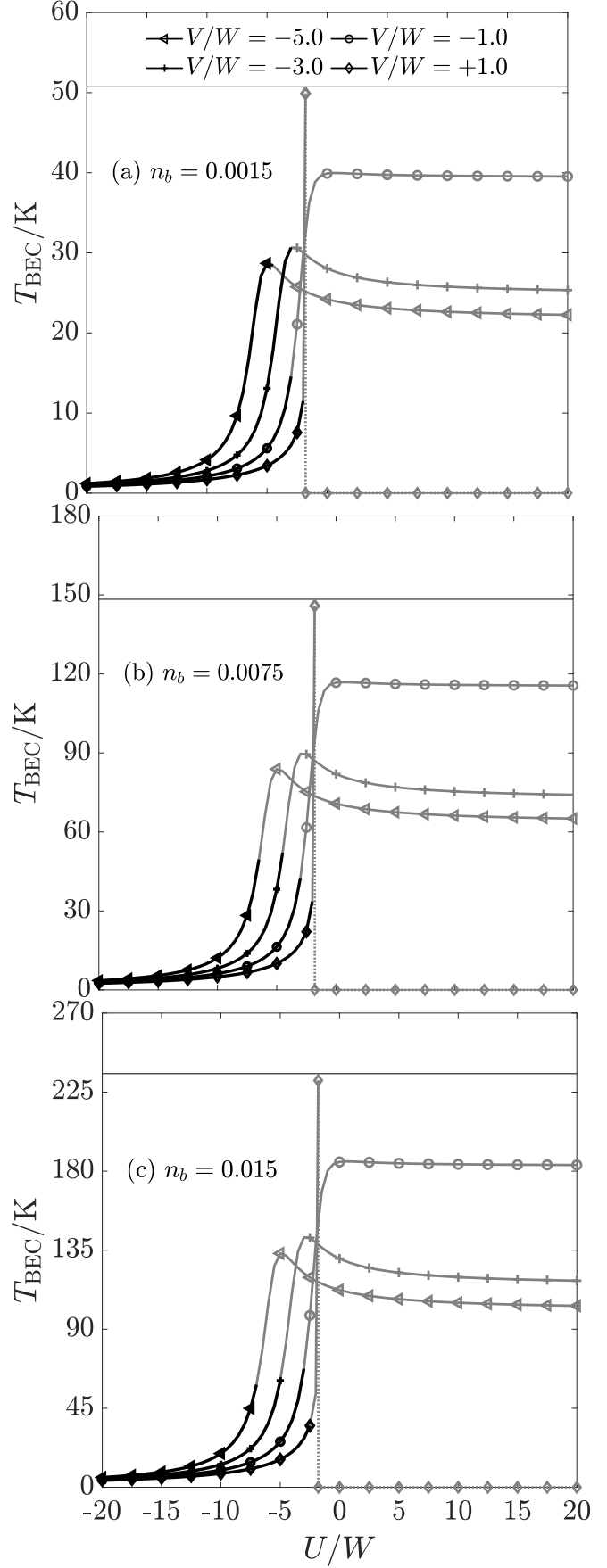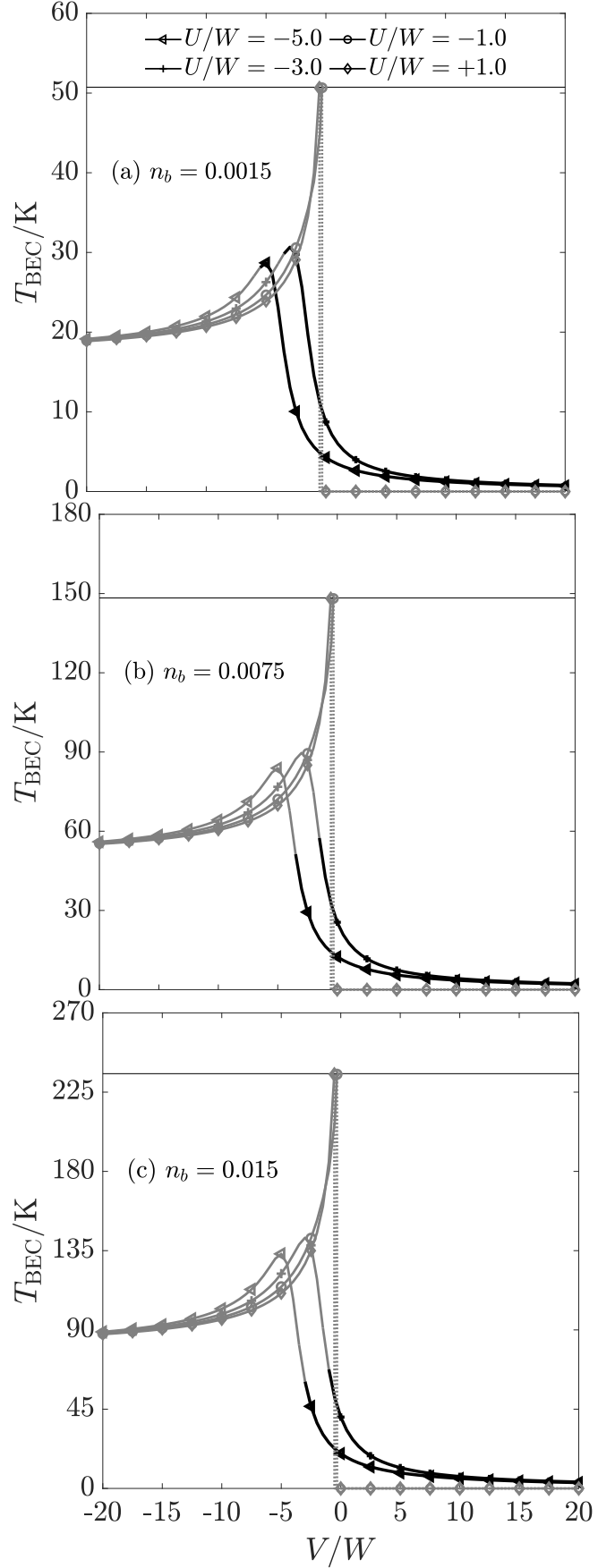
Figure 5.13a: Plots of BEC transition temperature for bound pairs with an increasing number of pairs per site n_b, and V is fixed while U is varied. The dark regions of the curves indicate cases where the value of n_b is compatible with the conditions that the pair do not overlap. We observe a peak in T_{BEC} in the superlight regimes. The horizontal line in each panel is the corresponding T_{BEC} value for $m^* = 2m_0$. The dotted regions imply that $T_\Delta < T_{\mathrm{BEC}}$ i.e. the pair is formed below the condensation temperature or where there are no bound pairs to form condensates.

Figure 5.13b: Plots of BEC transition temperature for bound pairs with an increasing number of pairs per site n_b, and U is fixed while V is varied. The dark regions indicate cases where the value of n_b is compatible with the conditions that the pair do not overlap. We observe a peak in T_{BEC} in the superlight regimes. The horizontal line in each panel is the corresponding T_{BEC} value for $m^* = 2m_0$. The dotted regions imply that $T_\Delta < T_{\mathrm{BEC}}$ i.e. the pair is formed below the condensation temperature or where there are no bound pairs to form condensates.

5.4 Discussion

We have studied the formation and the characteristic properties of fermion pairs in an FCC lattice. At the same, the consequences as to whether such pairs can Bose-condense in the dilute limit are also examined.

We found superlight local pairs forming in the FCC lattice. When the intersite attraction becomes infinitely large, there is no significant impact on the pair mass; the bound pair is just six times heavier than a single particle mass. The FCC lattice is the 3D analogue of the triangular and staggered lattices in the sense that pairs formed on these lattices are superlight and can move freely via a single hop even in the strong coupling limit $V \rightarrow -\infty$. For the dispersion of pairs where the intersite interaction is considered attractive, the singlet states show a slightly different behaviour between the cases of attractive and repulsive U. Degenerate perturbation calculations were used to validate the dispersion results in the strong coupling limits.

When conditions on overlap are maintained to keep pairs dilute and weakly interacting, the transition temperature is predicted to be as high as 70 K. This work has shown that small pairs formed in FCC lattice are much lighter than pairs in the simple cubic and body-centred cubic lattices by an order of magnitude. Consequentially, we propose that FCC systems with infinite Hubbard U repulsion and moderate intersite attraction V would be a good place to search for high-temperature superconductivity. We note that transition temperatures predicted here are similar to those in FCC fulleride materials (albeit fullerides are not dilute).

Chapter 6

Bipolaronic Pairing in A_3C_{60} Solids

6.1 Summary

This chapter has been motivated by the complex nature of the A_3C_{60} compounds. These are interesting materials with surprising behaviours, particularly as they sit at the intersection of conventional and unconventional superconductivity. We approach the problem of electron pairing in these compounds using the UV formalism. We start with a brief recap of the relevant interactions in these compounds and discuss how an appropriate Hamiltonian that captures the essential physics could be established. Then, we perform a canonical transformation to derive an effective UV Hamiltonian. Next, we study the properties of two electrons in the two distinct structures of cesium-doped fullerides (Cs_3C_{60}). Finally, we discuss the consequences of the structural difference on the properties of bound pairs and on their transition temperatures.

6.2 Preliminaries

In addition to the bandwidth, other relevant interaction parameters considered in the theoretical treatment of electrical conductivity in the doped fullerides are the onsite Coulomb repulsion, Hund's coupling, and the Jahn-Teller effect (JTE arising from the C_{60} vibron modes). As the onsite correlation is large in these materials, the Coulomb interaction suppresses the hopping of electrons to and from different C_{60} molecules. In the normal state of a trivalent-doped fulleride (A_3C_{60}) solid, the Hund's distribution rule favours high-spin states when electrons are donated by the alkali atoms to the C_{60} molecules (accordingly, the donated electrons must singly occupy the three different orbital levels of t_{1u} with parallel spins). However, the intramolecular vibrations resulting from the Jahn-Teller distortion create an effective attraction between electrons located on the same C_{60} molecule despite the strong Coulomb repulsion. The latter favours the formation of a local singlet pair [108] (i.e. two electrons with anti-parallel spins occupy the same orbital level and the third electron occupies one of the remaining two orbitals of the t_{1u} levels).

In the present work, we assume the following. (1) Each C_{60} molecule forms a lattice site where an electron is located. (2) We consider a single band approximation [109] to this problem and thus interorbital exchange interactions are neglected. (3) The JTE dominates over Hund's coupling [108], making it possible to create an onsite singlet pair. With these simplifications, we can derive an effective UV Hamiltonian where some underlying physics of bipolarons in A_3C_{60} solids can be understood. Our goal is to examine structural effects on the bipolaron properties of cesium-doped fulleride (Cs_3C_{60}) since it has two structural phases (BCC and FCC). The derivation of the Hamiltonian will be discussed next.

6.3   The Hamiltonian

For the alkali-doped fulleride compounds (A_3C_{60}), we consider a Hamiltonian of the form

$$H = H_{\text{el}} + H_{\text{ph}} + H_{\text{el}-\text{ph}} \tag{6.1}$$

where the first term is the Hamiltonian describing the electron subsystem, the second term is the phonon subsystem that describes the vibration of the C_{60} molecules (vibrons) and the alkali atoms, and the third term accounts for the coupling of electrons to the phonons in the system. We will treat each term in more detail in the following sections.

6.3.1   The Electron Subsystem

With Cs_3C_{60} in mind and to minimise the number of free parameters, we introduce the scaled Coulomb coupling, $\tilde{V}$, which is related to the intersite electron-electron interaction $V = \tilde{V}/b$, where b is the lattice parameter. This form of interaction means that there is just a single parameter to vary which is identical (or at least very similar) within the different structures of Cs_3C_{60} (BCC and FCC). The Hamiltonian is

$$H_{\text{el}} = -\sum_{\langle ii' \rangle} t_{ii'} \hat{c}_i^\dagger \hat{c}_{i'} + \frac{U_{\text{H}}}{2} \sum_i \hat{n}_{i\uparrow} \hat{n}_{i\downarrow} + \frac{1}{2} \sum_{ij} \frac{\tilde{V}_{ij}}{b} \hat{n}_i \hat{n}_j \tag{6.2}$$

where the first term is the tight-binding term describing the hopping of electrons between nearest-neighbour C_{60} sites i and j, the second term is the onsite Coulomb interaction between two electrons located at site i, and the last term describes the intersite Coulomb potential experienced by two electrons on nearest-neighbour sites i and j.

6.3.2 Phonon and Vibron Hamiltonians

The phonon subsystem contains the vibrational modes (vibrons) of the C_{60} molecules and the vibration of the alkali atoms. The Hamiltonian reads

$$H_{\text{ph}} = \hbar\omega_C \sum_i \hat{a}_i^\dagger \hat{a}_i + \hbar\omega_A \sum_{j\nu} \hat{d}_{j\nu}^\dagger \hat{d}_{j\nu} \tag{6.3}$$

where $\hat{a}$ and $\hat{a}^\dagger$ are phonon operators for the C_{60} molecules, and $\hat{d}$ and $\hat{d}^\dagger$ are phonon operators for the alkali atoms. ω_C and ω_A are the frequency of vibration for the C_{60} molecule and alkali atom respectively. The index j is used uniquely for the alkali sites.

6.3.3 Electron Coupling with Vibrons and Phonons

The electrons donated by the alkali atoms are strongly coupled to the *two A_g* and *eight H_g* intramolecular phonons (vibrons). The nature of the electron-phonon coupling affects the direction and magnitude of orbital distortion but does not cause the splitting of the orbital degeneracy [18]. However, only one of the H_g modes (which is five-fold degenerate) is responsible for the JTE [110]. To write our electron-phonon Hamiltonian for the Cs_3C_{60} solid, we need to bear in mind: Firstly, the stoichiometric difference in its two structural phases. Secondly, the polarisation of the underlying lattice. In addition to the intramolecular phonons from the C_{60} molecules, the positions of the cesium atoms introduce additional polarisation in the lattice which may enhance or hinder the effective interaction with a phonon experienced by an electron. This polarisation effect will be taken into account when considering the respective Hamiltonian equation for the BCC and FCC systems. What this means is that we allow for the possibility that electrons on C_{60} molecules can interact via phonons on Cs sites since they can modify the local

JT modes [111]. Thus the full electron-phonon interaction is:

$$H_{\text{el-ph}} = g \sum_i \hat{c}_i^\dagger \hat{c}_i (\hat{a}_i^\dagger + \hat{a}_i) + \sum_{ij,\nu} \frac{g'_{ij,CA}}{b^2} \hat{c}_i^\dagger \hat{c}_i (\hat{d}_{\text{A},j\nu}^\dagger + \hat{d}_{\text{A},j\nu}) \hat{\boldsymbol{r}}_{ij} \cdot \boldsymbol{\eta}_\nu \tag{6.4}$$

$$= g \sum_i \hat{c}_i^\dagger \hat{c}_i (\hat{a}_i^\dagger + \hat{a}_i) + \sum_{ij,\nu} \frac{\tilde{g}_{ij\nu}}{b^2} \hat{c}_i^\dagger \hat{c}_i (\hat{d}_{\text{A},j\nu}^\dagger + \hat{d}_{\text{A},j\nu}) \tag{6.5}$$

where the first term is a Holstein-like coupling between an electron and a phonon on the same C_{60} site, which is used as an approximation to the JT coupling [112, 113]. The second term is the coupling between an electron and vibration modes of the cesium atoms. Note that $\tilde{g}_{ij\nu} = g'_{ij,CA} \hat{\boldsymbol{r}}_{ij} \cdot \boldsymbol{\eta}_\nu$. Calculation of $\hat{\boldsymbol{r}}_{ij} \cdot \boldsymbol{\eta}$ is specific to the lattice and the orientation of the phonon modes and will be discussed later. $\boldsymbol{\eta}_\nu$ is the polarisation of mode ν. We assume that these polarisations are orthogonal. Here, $\hat{a}^\dagger$ create vibrons on fullerene sites and $\hat{d}^\dagger$ create phonons on the alkali sites.

Now that all the sub-Hamiltonians in Equation (6.1) have been declared, we turn to the derivation of the UV Hamiltonian for these compounds.

6.4   Derivation of UV Model for Cs_3C_{60} Solids

In this section, we will discuss a step-by-step procedure for the derivation of an effective UV Hamiltonian using a canonical transformation. We note that the Hamiltonian in Equation (6.1) contains seven terms if the subset Hamiltonians are combined.

6.4.1   Applying a Canonical Transformation

We use the Lang–Firsov canonical transformation to derive an effective UV model in the limit that the phonon frequency is large. To do this, we perform a canonical operation below with a unitary operator S. The essence of this operation is to decouple the EPI

terms in Equation (6.1).

$$\tilde{H} = e^S \, H \, e^{-S} = H + [S, H] + \frac{1}{2!}[S, [S, H]] + \ldots \tag{6.6}$$

where the original Hamiltonian, in full, is

$$H = -\sum_{\langle ii' \rangle} t_{ii'} \hat{c}_i^\dagger \hat{c}_{i'} + \frac{U_H}{2} \sum_i \hat{n}_{i\uparrow} \hat{n}_{i\downarrow} + \sum_{\langle ii' \rangle} \frac{\tilde{V}_{ii'}}{b} \hat{n}_i \hat{n}_{i'} + \sum_{ij} g\delta_{ij} \hat{c}_i^\dagger \hat{c}_i (\hat{a}_j^\dagger + \hat{a}_j)$$
$$+ \sum_{ij,\nu} \frac{\tilde{g}_{ij\nu}}{b^2} \hat{c}_i^\dagger \hat{c}_i (\hat{d}_{j\nu}^\dagger + \hat{d}_{j\nu}) + \hbar\omega_C \sum_j \hat{a}_j^\dagger \hat{a}_j + \hbar\omega_A \sum_{j\nu} \hat{d}_{j\nu}^\dagger \hat{d}_{j\nu} \tag{6.7}$$

The operator S in Equation (6.6) takes the form

$$S = \sum_{ij,\nu} \frac{\tilde{g}_{ij\nu}}{b^2 \hbar\omega_A} \hat{c}_i^\dagger \hat{c}_i (\kappa \hat{d}_{j\nu}^\dagger - \kappa \hat{d}_{j\nu}) + \sum_{ij} \frac{g_{ij}}{\hbar\omega_C} \hat{c}_i^\dagger \hat{c}_i (\kappa \hat{a}_j^\dagger - \kappa \hat{a}_j) \tag{6.8}$$

where κ is a scaling parameter and $g_{ij} = g\delta_{ij}$ in the second term.

The electron and phonon operators are also transformed as follows

$$\hat{c}_i \rightarrow \tilde{c}_i = e^S \hat{c}_i e^{-S} \tag{6.9}$$

$$\hat{d}_{j\nu} \rightarrow \tilde{d}_{j\nu} = e^S \hat{d}_{j\nu} e^{-S} \tag{6.10}$$

$$\hat{a}_j \rightarrow \tilde{a}_j = e^S \hat{a}_j e^{-S} \tag{6.11}$$

Then the transformed operators are obtained by solving a set of differential equations

$$\frac{\partial \tilde{c}_i}{\partial \kappa} = \frac{\partial \tilde{c}_i}{\partial S} \cdot \frac{\partial S}{\partial \kappa} \tag{6.12}$$

$$\frac{\partial \tilde{d}_j}{\partial \kappa} = \frac{\partial \tilde{d}_j}{\partial S} \cdot \frac{\partial S}{\partial \kappa} \tag{6.13}$$

$$\frac{\partial \tilde{a}_j}{\partial \kappa} = \frac{\partial \tilde{a}_j}{\partial S} \cdot \frac{\partial S}{\partial \kappa} \tag{6.14}$$

From Equation (6.8), we have that

$$\frac{\partial S}{\partial \kappa} = \sum_{ij,\nu} \frac{\tilde{g}_{ij\nu}}{b^2 \hbar\omega_A} \hat{c}_i^\dagger \hat{c}_i (\hat{d}_{j\nu}^\dagger - \hat{d}_{j\nu}) + \sum_{ij} \frac{g\delta_{ij}}{\hbar\omega_C} \hat{c}_i^\dagger \hat{c}_i (\hat{a}_j^\dagger - \hat{a}_j) \tag{6.15}$$

Using Equation (6.9) in (6.12), we get

$$\frac{\partial \tilde{c}_i}{\partial \kappa} = e^S \sum_i [\hat{c}_i^\dagger \hat{c}_i, \hat{c}_i] \left\{ \sum_{j\nu} \frac{\tilde{g}_{ij\nu}}{b^2 \hbar\omega_A} (\hat{d}_{j\nu}^\dagger - \hat{d}_{j\nu}) + \sum_j \frac{g\delta_{ij}}{\hbar\omega_C} (\hat{a}_j^\dagger - \hat{a}_j) \right\} e^{-S}$$
$$= -\hat{c}_i \left[\sum_{j\nu} \frac{\tilde{g}_{ij\nu}}{b^2 \hbar\omega_A} (\hat{d}_{j\nu}^\dagger - \hat{d}_{j\nu}) + \sum_j \frac{g\delta_{ij}}{\hbar\omega_C} (\hat{a}_j^\dagger - \hat{a}_j) \right] \tag{6.16}$$

If we take the limits $\kappa \to 1$, we arrive at

$$\hat{c}_i \to \tilde{c}_i = \hat{c}_i \exp\left[-\sum_{j\nu} \frac{\tilde{g}_{ij\nu}}{b^2 \hbar \omega_A}(\hat{d}_{j\nu}^\dagger - \hat{d}_{j\nu}) - \sum_j \frac{g\delta_{ij}}{\hbar \omega_C}(\hat{a}_j^\dagger - \hat{a}_j) \right] \tag{6.17}$$

So that its conjugate operator is given as

$$\hat{c}_i^\dagger \to \tilde{c}_i^\dagger = \hat{c}_i^\dagger \exp\left[\sum_{j\nu} \frac{\tilde{g}_{ij\nu}}{b^2 \hbar \omega_A}(\hat{d}_{j\nu}^\dagger - \hat{d}_{j\nu}) + \sum_j \frac{g\delta_{ij}}{\hbar \omega_C}(\hat{a}_j^\dagger - \hat{a}_j) \right] \tag{6.18}$$

Similarly, we solve Equations (6.13) and (6.14) using (6.10) and (6.11), respectively, to arrive at the transformed operators

$$\hat{d}_{j\nu} \to \tilde{d}_{j\nu} = \hat{d}_{j\nu} - \sum_{i\nu} \frac{\tilde{g}_{ij\nu}}{b^2 \hbar \omega_A}\hat{c}_i^\dagger \hat{c}_i \quad , \qquad \hat{d}_{j\nu}^\dagger \to \tilde{d}_j^\dagger = \hat{d}_j^\dagger - \sum_{i\nu} \frac{\tilde{g}_{ij\nu}}{b^2 \hbar \omega_A}\hat{c}_i^\dagger \hat{c}_i \tag{6.19}$$

and

$$\hat{a}_j \to \tilde{a}_j = \hat{a}_j - \sum_i \frac{g\delta_{ij}}{\hbar \omega_C}\hat{c}_i^\dagger \hat{c}_i \quad , \qquad \hat{a}_j^\dagger \to \tilde{a}_j^\dagger = \hat{a}_j^\dagger - \sum_i \frac{g\delta_{ij}}{\hbar \omega_C}\hat{c}_i^\dagger \hat{c}_i \tag{6.20}$$

From Equation (6.6), we have

$$\begin{aligned}
\tilde{H} = &-\sum_{\langle ii' \rangle} t_{ii'} \tilde{c}_i^\dagger \tilde{c}_{i'} + \frac{U_H}{2}\sum_i \tilde{n}_{i\uparrow}\tilde{n}_{i\downarrow} + \frac{1}{2}\sum_{\langle ii' \rangle} \frac{\tilde{V}_{ii'}}{b}\tilde{n}_i\tilde{n}_{i'} + g\sum_i \tilde{c}_i^\dagger \tilde{c}_i(\tilde{a}_i^\dagger + \tilde{a}_i) \\
&+ \sum_{ij,\nu} \frac{\tilde{g}_{ij\nu}}{b^2}\tilde{c}_i^\dagger \tilde{c}_i(\tilde{d}_{j\nu}^\dagger + \tilde{d}_{j\nu}) + \hbar \omega_C \sum_i \tilde{a}_i^\dagger \tilde{a}_i + \hbar \omega_A \sum_{j\nu} \tilde{d}_{j\nu}^\dagger \tilde{d}_{j\nu}
\end{aligned} \tag{6.21}$$

Treating each term separately for convenience and substituting the transformed operators (6.17)–(6.20), we get

1st term:

$$\begin{aligned}
-\sum_{\langle ii' \rangle} t_{ii'} \tilde{c}_i^\dagger \tilde{c}_{i'} = &-\sum_{\langle ii' \rangle} t_{ii'} \hat{c}_i^\dagger \hat{c}_{i'} \exp\left[\sum_{j\nu} \frac{\tilde{g}_{ij\nu}}{b^2 \hbar \omega_A}(\hat{d}_{j\nu}^\dagger - \hat{d}_{j\nu}) + \sum_j \frac{g\delta_{ij}}{\hbar \omega_C}(\hat{a}_j^\dagger - \hat{a}_j) \right] \\
&\times \exp\left[-\sum_{j\nu} \frac{\tilde{g}_{i'j\nu}'}{b^2 \hbar \omega_A}(\hat{d}_{j\nu}^\dagger - \hat{d}_{j\nu}) - \sum_j \frac{g'\delta_{i'j}}{\hbar \omega_C}(\hat{a}_j^\dagger - \hat{a}_j) \right] \\
= &-\sum_{\langle ii' \rangle} \tilde{t}_{ii'} \hat{c}_i^\dagger \hat{c}_{i'}
\end{aligned}$$

where

$$\begin{aligned}
\tilde{t}_{ii'} = t_{ii'} &\exp\left[\sum_{j\nu} \frac{\tilde{g}_{ij\nu}}{b^2 \hbar \omega_A}(\hat{d}_{j\nu}^\dagger - \hat{d}_{j\nu}) + \sum_j \frac{g\delta_{ij}}{\hbar \omega_C}(\hat{a}_j^\dagger - \hat{a}_j) \right] \\
&\times \exp\left[-\sum_{j\nu} \frac{\tilde{g}_{i'j\nu}'}{b^2 \hbar \omega_A}(\hat{d}_{j\nu}^\dagger - \hat{d}_{j\nu}) - \sum_j \frac{g'\delta_{i'j}}{\hbar \omega_C}(\hat{a}_j^\dagger - \hat{a}_j) \right]
\end{aligned} \tag{6.22}$$

2nd term:

$$\frac{U_\text{H}}{2} \sum_i \tilde{n}_{i\uparrow}\tilde{n}_{i\downarrow} = \frac{U_\text{H}}{2} \sum_i \tilde{c}_{i\uparrow}^\dagger \tilde{c}_{i\uparrow}\tilde{c}_{i\downarrow}^\dagger \tilde{c}_{i\downarrow} = \frac{U_\text{H}}{2} \sum_i \hat{c}_{i\uparrow}^\dagger \hat{c}_{i\uparrow}\hat{c}_{i\downarrow}^\dagger \hat{c}_{i\downarrow} = \frac{U_\text{H}}{2} \sum_i \hat{n}_{i\uparrow}\hat{n}_{i\downarrow}$$

3rd term:

$$\frac{1}{2} \sum_{\langle ii'\rangle} \frac{\tilde{V}_{ii'}}{b} \tilde{n}_i\tilde{n}_j = \frac{1}{2} \sum_{\langle ii'\rangle} \frac{\tilde{V}_{ij}}{b} \tilde{c}_i^\dagger \tilde{c}_i\tilde{c}_{i'}^\dagger \tilde{c}_{i'} = \frac{1}{2} \sum_{\langle ii'\rangle} \frac{\tilde{V}_{ii'}}{b} \hat{c}_i^\dagger \hat{c}_i\hat{c}_{i'}^\dagger \hat{c}_{i'} = \frac{1}{2} \sum_{\langle ii'\rangle} \frac{\tilde{V}_{ii'}}{b} \hat{n}_i\hat{n}_{i'}$$

4th term:

$$\sum_{ij} g\delta_{ij}\tilde{c}_i^\dagger \tilde{c}_i(\tilde{a}_j^\dagger + \tilde{a}_j) = \sum_{ij} g\delta_{ij}\hat{c}_i^\dagger \hat{c}_i\left(\hat{a}_j^\dagger + \hat{a}_j - 2\sum_{i'} \frac{g\delta_{i'j}}{\hbar\omega_C}\hat{c}_{i'}^\dagger \hat{c}_{i'} \right)$$

5th term:

$$\sum_{ij,\nu} \frac{\tilde{g}_{ij\nu}}{b^2} \tilde{c}_i^\dagger \tilde{c}_i(\tilde{d}_{j\nu}^\dagger + \tilde{d}_{j\nu}) = \sum_{ij,\nu} \frac{\tilde{g}_{ij\nu}}{b^2} \hat{c}_i^\dagger \hat{c}_i\left(\hat{d}_{j\nu}^\dagger + \hat{d}_{j\nu} - 2\sum_{i'\nu} \frac{\tilde{g}_{i'j\nu}}{b^2\hbar\omega_A}\hat{c}_{i'}^\dagger \hat{c}_{i'} \right)$$

6th term:

$$\hbar\omega_C \sum_j \tilde{a}_j^\dagger \tilde{a}_j = \hbar\omega_C \sum_j \left[\hat{a}_j^\dagger \hat{a}_j - \sum_i \frac{g\delta_{ij}}{\hbar\omega_C}\hat{c}_i^\dagger \hat{c}_i(\hat{a}_i^\dagger + \hat{a}_i) + \sum_{ii'} \frac{g\delta_{ij}g\delta_{i'j}}{(\hbar\omega_C)^2}\hat{c}_i^\dagger \hat{c}_i\hat{c}_{i'}^\dagger \hat{c}_{i'} \right]$$

7th term:

$$\hbar\omega_A \sum_{j\nu} \tilde{d}_{j\nu}^\dagger \tilde{d}_{j\nu} = \hbar\omega_A \sum_{j\nu} \left[d_{j\nu}^\dagger \hat{d}_{j\nu} - \sum_{i\nu} \frac{\tilde{g}_{ij\nu}}{b^2\hbar\omega_A}\hat{c}_i^\dagger \hat{c}_i(d_{j\nu}^\dagger + \hat{d}_{j\nu}) \right.$$
$$\left. + \left(\frac{1}{b^2\hbar\omega_A} \right)^2 \sum_{ii'\nu} \tilde{g}_{ij\nu}\tilde{g}_{i'j\nu}\hat{c}_i^\dagger \hat{c}_i c_{i'}^\dagger \hat{c}_{i'} \right]$$

Hence, the fully transformed Hamiltonian is

$$\tilde{H} = -\sum_{\langle ii'\rangle} \tilde{t}_{ii'}\hat{c}_i^\dagger \hat{c}_{i'} + \frac{U_\text{H}}{2} \sum_i \hat{n}_{i\uparrow}\hat{n}_{i\downarrow} + \frac{1}{2} \sum_{\langle ii'\rangle} \frac{\tilde{V}_{ii'}}{b} \hat{n}_i\hat{n}_{i'} - \frac{1}{\hbar\omega_C} \sum_{ii'j} g\delta_{ij}g\delta_{i'j}\hat{c}_i^\dagger \hat{c}_i c_{i'}^\dagger \hat{c}_{i'}$$
$$-\frac{1}{b^4\hbar\omega_A} \sum_{ii'j\nu} \tilde{g}_{ij\nu}\tilde{g}_{i'j\nu}\hat{c}_i^\dagger \hat{c}_i c_{i'}^\dagger \hat{c}_{i'} + \hbar\omega_C \sum_j \hat{a}_j^\dagger \hat{a}_j + \hbar\omega_A \sum_{j\nu} \hat{d}_j^\dagger \hat{d}_j \tag{6.23}$$

We recall that $\tilde{g}_{ij\nu} \equiv g'_{\text{ij},CA}\hat{r}_{ij} \cdot \boldsymbol{\eta}_\nu$, thus

$$\tilde{H} = -\sum_{\langle ii'\rangle} \tilde{t}_{ii'}\hat{c}_i^\dagger \hat{c}_{i'} + \frac{U_\text{H}}{2} \sum_i \hat{n}_{i\uparrow}\hat{n}_{i\downarrow} + \frac{1}{2} \sum_{\langle ii'\rangle} \frac{\tilde{V}_{ii'}}{b} \hat{n}_i\hat{n}_{i'} - \frac{1}{\hbar\omega_C} \sum_{ii'j} g\delta_{ij}g\delta_{i'j}\hat{c}_i^\dagger \hat{c}_i\hat{c}_{i'}^\dagger \hat{c}_{i'}$$
$$-\frac{1}{b^4\hbar\omega_A} \sum_{ii'j\nu} g'_{ij,CA}g'_{i'j,CA}\, \hat{c}_i^\dagger \hat{c}_i\hat{c}_{i'}^\dagger \hat{c}_{i'}(\hat{r}_{ij} \cdot \boldsymbol{\eta}_\nu)(\hat{r}_{i'j} \cdot \boldsymbol{\eta}_\nu) \tag{6.24}$$
$$+ \hbar\omega_C \sum_j \hat{a}_j^\dagger \hat{a}_j + \hbar\omega_A \sum_{j\nu} \hat{d}_{j\nu}^\dagger \hat{d}_{j\nu}$$

6.4.1.1   Transformed Hamiltonian in the Atomic Limit

In the limit $\tilde{t} \to 0$ where electrons are considered static, only the phonon-related terms
are activated. If we let

$$\frac{g\delta_{ij}}{\hbar\omega_C} \to \bar{g}_C = \frac{f_{ij}\delta_{ij}}{\hbar\omega_C\sqrt{2M\hbar\omega_C}} \tag{6.25}$$

and

$$\frac{\tilde{g}_{ij\nu}}{b^2\hbar\omega_A} \to \bar{g}_\nu = \frac{f'_{ij\nu}}{\hbar\omega_A\sqrt{2M\hbar\omega_A}}, \tag{6.26}$$

the EPI terms (4th and 5th terms in 6.23) become

$$-\sum_{ii'j}\frac{f_{ij}f_{i'j}}{2M\hbar^2\omega_C^2}\hat{n}_i\hat{n}_{i'} - \sum_{ii'j\nu}\frac{f'_{ij\nu}f'_{i'j\nu}}{2M\hbar^2\omega_A^2}\hat{n}_i\hat{n}_{i'} \tag{6.27}$$

We then define functions relating to the molecular vibrons and alkali phonon, polaron
self-energy and the dimensionless coupling parameter respectively as

$$\Phi^C_{ii'} = \sum_j f_{ij}f_{i'j} \qquad , \tag{6.28}$$

$$\Phi^A_{ii'\nu} = \sum_{j\nu} f'_{ij\nu}f'_{i'j\nu} \qquad : \quad \{f'_{ij\nu} = (\hat{\boldsymbol{r}}_{ij}\cdot\boldsymbol{\eta}_\nu)\,e^{-r_{ij}/R_{\mathrm{sc}}}/r_{ij}^3\} \quad , \tag{6.29}$$

$$E_p = \frac{1}{2M\hbar^2\omega^2}\sum_i f_i^2 = \frac{\Phi_{00}}{2M\hbar^2\omega^2} \quad , \tag{6.30}$$

$$\lambda = \frac{\Phi_{00}}{2MW\hbar^2\omega^2} \tag{6.31}$$

where W is the half-bandwidth. We emphasise that the summation in Equation (6.29)
runs over all modes of the alkali phonon. The expression for $f'_{ij\nu}$ is of the Fröhlich form
[93], where R_{sc} (expressed in units of the lattice vector $|\boldsymbol{a}|$ and ranges from $0 \to \infty$) is
the screening radius that controls the effect of the alkali phonon-mediated interaction
(from short- to long-range), r_{ij} is the separation distance between a C_{60} ball at site i
and an alkali ion at site j. The EPI terms can be re-written as

$$-\sum_{ii'}\lambda_C W\frac{\Phi^C_{ii'}}{\Phi^C_{00}}\hat{n}_i\hat{n}_{i'} - \sum_{ii'\nu}\lambda'W\frac{\Phi^A_{ii'\nu}}{\Phi^A_{00\nu}}\hat{n}_i\hat{n}_{i'} \tag{6.32}$$

where λ_C and λ' are the dimensionless coupling parameter of electrons with the C_{60} and the alkali ion (A) phonons respectively. Taking the atomic limit of Equation (6.23), the transformed Hamiltonian is thus

$$\tilde{H}_{\text{at}} = -\sum_{ii'} \lambda_C W \frac{\Phi^C_{ii'}}{\Phi^C_{00}} \hat{n}_i \hat{n}_{i'} - \sum_{ii'\nu} \lambda' W \frac{\Phi^A_{ii'\nu}}{\Phi^A_{00\nu}} \hat{n}_i \hat{n}_{i'} + \hbar\omega_C \sum_j \hat{a}^\dagger_j \hat{a}_j + \hbar\omega_A \sum_{j\nu} \hat{d}^\dagger_{j\nu} \hat{d}_{j\nu} \quad (6.33)$$

6.4.1.2 Transforming the Tight-Binding Hamiltonian

Examining the tight-binding Hamiltonian (first term in Equation (6.23)), we have

$$\tilde{H}_{\text{tb}} = -\sum_{\langle ii'\rangle} t_{ii'} \tilde{c}^\dagger_i \tilde{c}_{i'} \rightarrow -\sum_{\langle ii'\rangle} \tilde{t}_{ii'} \hat{c}^\dagger_i \hat{c}_{i'} \quad (6.34)$$

where, from Equation (6.22), the renormalised hopping integral $\tilde{t}$ corresponding to the kinetic term of a polaron (*dressed* electron) is

$$\tilde{t}_{ii'} = t_{ii'} \exp\left[\sum_{j\nu} \bar{g}_\nu(\hat{d}^\dagger_{j\nu} - \hat{d}_{j\nu}) + \sum_j \bar{g}_C(\hat{a}^\dagger_j - \hat{a}_j)\right] \times \exp\left[-\sum_{j\nu} \bar{g}'_\nu(\hat{d}^\dagger_{j\nu} - \hat{d}_{j\nu}) - \sum_j \bar{g}'_C(\hat{a}^\dagger_j - \hat{a}_j)\right]$$
$$(6.35)$$

where $\bar{g}_C = \frac{f_{ij}\delta_{ij}}{\hbar\omega_C\sqrt{2M\hbar\omega_C}}$, $\bar{g}'_C = \frac{f_{i'j}\delta_{i'j}}{\hbar\omega_C\sqrt{2M\hbar\omega_C}}$, $\bar{g}_\nu = \frac{f'_{ij\nu}}{\hbar\omega_A\sqrt{2M\hbar\omega_A}}$, and $\bar{g}'_\nu = \frac{f'_{i'j\nu}}{\hbar\omega_A\sqrt{2M\hbar\omega_A}}$. It is immediately obvious that there are still electron-phonon couplings via $\tilde{t}_{ii'}$. These can be eliminated by rearranging the exponent and then taking the near anti-adiabatic limit (i.e. finite phonon frequency). To do this, we make use of the identity $e^A e^B = e^{A+B} e^{[A,B]/2}$, where this relation holds if A and B commute. For the moment, let $A = \sum_{j\nu} \bar{g}_\nu(\hat{d}^\dagger_{j\nu} - \hat{d}_{j\nu}) + \sum_j \bar{g}_C(\hat{a}^\dagger_j - \hat{a}_j)$ and $B = -\sum_{j\nu} \bar{g}'_\nu(\hat{d}^\dagger_{j\nu} - \hat{d}_{j\nu}) - \sum_j \bar{g}'_C(\hat{a}^\dagger_j - \hat{a}_j)$. Thus, we have $A + B = \sum_{j\nu}(\bar{g}_\nu - \bar{g}'_\nu)(\hat{d}^\dagger_{j\nu} - \hat{d}_{j\nu}) + \sum_j(\bar{g}_C - \bar{g}'_C)(\hat{a}^\dagger_j - \hat{a}_j)$, and $[A, B] = 0$. So,

$$\tilde{t}_{ii'} = t_{ii'} \exp\left[\left[\sum_{j\nu}(\bar{g}_\nu - \bar{g}'_\nu)\hat{d}^\dagger_{j\nu} + \sum_j(\bar{g}_C - \bar{g}'_C)\hat{a}^\dagger_j\right] - \left[\sum_{j\nu}(\bar{g}_\nu - \bar{g}'_\nu)\hat{d}_{j\nu} + \sum_j(\bar{g}_C - \bar{g}'_C)\hat{a}_j\right]\right]$$
$$(6.36)$$

Reusing the identity $e^{A+B} = e^A e^B e^{-[A,B]/2}$ again, where

$$A = \left[\sum_{j\nu}(\bar{g}_\nu - \bar{g}'_\nu)\hat{d}^\dagger_{j\nu} + \sum_j(\bar{g}_C - \bar{g}'_C)\hat{a}^\dagger_j\right] \text{ and } B = -\left[\sum_{j\nu}(\bar{g}_\nu - \bar{g}'_\nu)\hat{d}_{j\nu} + \sum_j(\bar{g}_C - \bar{g}'_C)\hat{a}_j\right].$$

It follows that

$$[A, B] = -\sum_{j\nu}(\bar{g}_\nu - \bar{g}'_\nu)^2[\hat{d}^\dagger_{j\nu}, \hat{d}_{j\nu}] - \sum_{jj'\nu}(\bar{g}_\nu - \bar{g}'_\nu)(\bar{g}_C - \bar{g}'_C)[\hat{d}^\dagger_{j'\nu}, \hat{a}_j]$$

$$- \sum_{jj'\nu}(\bar{g}_C - \bar{g}'_C)(\bar{g}_\nu - \bar{g}'_\nu)[\hat{a}^\dagger_j, \hat{d}_{j'\nu}] - \sum_j(\bar{g}_C - \bar{g}'_C)^2[\hat{a}^\dagger_j, \hat{a}_j]$$

$$= \sum_{j\nu}(\bar{g}_\nu - \bar{g}'_\nu)^2 + \sum_j(\bar{g}_C - \bar{g}'_C)^2$$

$$= \sum_{j\nu}\left\{\frac{f'^2_{ij\nu}}{\hbar\omega_A} - 2\frac{f'_{ij\nu}f'_{i'j\nu}}{\hbar\omega_A} + \frac{f'^2_{i'j\nu}}{\hbar\omega_A}\right\} \cdot \frac{1}{2M\hbar^2\omega_A^2} + \sum_j\left\{\frac{f^2_{ij}}{\hbar\omega_C} - 2\frac{f_{ij}f_{i'j}}{\hbar\omega_C} + \frac{f^2_{i'j}}{\hbar\omega_C}\right\} \cdot \frac{1}{2M\hbar^2\omega_C^2}$$

$$= \frac{2\lambda'W}{\hbar\omega_A}\left(1 - \frac{\Phi^A_{ii'\nu}}{\Phi^A_{00\nu}}\right) + \frac{2\lambda_C W}{\hbar\omega_C}\left(1 - \frac{\Phi^C_{ii'}}{\Phi^C_{00}}\right)$$

$$\tag{6.37}$$

$$\therefore -[A, B]/2 = -\frac{\lambda'W}{\hbar\omega_A}\left(1 - \frac{\Phi^A_{ii'\nu}}{\Phi^A_{00\nu}}\right) - \frac{\lambda_C W}{\hbar\omega_C}\left(1 - \frac{\Phi^C_{ii'}}{\Phi^C_{00}}\right) \tag{6.38}$$

The final expression for the renormalised hopping integral $\tilde{t}_{ii'}$ is

$$\tilde{t} = t_{ii'}\exp\left[-\frac{\lambda'W}{\hbar\omega_A}\left(1 - \frac{\Phi^A_{ii'\nu}}{\Phi^A_{00\nu}}\right) - \frac{\lambda_C W}{\hbar\omega_C}\left(1 - \frac{\Phi^C_{ii'}}{\Phi^C_{00}}\right)\right] \times$$

$$\exp\left[\sum_{j\nu}(\bar{g}_\nu - \bar{g}'_\nu)\hat{d}^\dagger_{j\nu} + \sum_j(\bar{g}_C - \bar{g}'_C)\hat{a}^\dagger_j\right] \times \exp\left[-\sum_{j\nu}(\bar{g}_\nu - \bar{g}'_\nu)\hat{d}_{j\nu} - \sum_j(\bar{g}_C - \bar{g}'_C)\hat{a}_j\right]$$

$$\tag{6.39}$$

An advantage of taking the finite frequency limit of this transformation is that the phonon degrees of freedom are integrated out. Thus, we have an effective UV Hamiltonian for the alkali-doped fullerides as

$$H_{\text{eff}} = \sum_{\langle\boldsymbol{n},\boldsymbol{a}\rangle\sigma}\tilde{t}_{\boldsymbol{a}}\,\hat{c}^\dagger_{\boldsymbol{n}+\boldsymbol{a},\sigma}\,\hat{c}_{\boldsymbol{n}\sigma} + U\sum_{\boldsymbol{n}}\hat{\rho}_{\boldsymbol{n}\uparrow}\,\hat{\rho}_{\boldsymbol{n}\downarrow} + \sideset{}{'}\sum_{\langle\boldsymbol{n},\boldsymbol{a}\rangle}V_{\boldsymbol{a}}\,\hat{\rho}_{\boldsymbol{n}+\boldsymbol{a}}\,\hat{\rho}_{\boldsymbol{n}} \tag{6.40}$$

where the first two terms are the standard Hubbard Hamiltonian and the third term describes the intersite electron-electron interaction. Note that $\boldsymbol{a}$ is the nearest-neighbour lattice vector which should not be confused with the lattice constant b, and the prime in the last summation implies that $\boldsymbol{a} = 0$ is excluded from summation. U and V are renormalised potentials defined as

$$U = \frac{U_H}{2} - W(\lambda_C + \lambda') \tag{6.41}$$

$$V_{\boldsymbol{a}} = \frac{\tilde{V}}{2a} - W\left[\lambda'\frac{\Phi_\nu^A(0,\boldsymbol{a})}{\Phi_\nu^A(0,0)}\right] \tag{6.42}$$

The Hamiltonian (6.40) is solved to obtain the properties of two bound electrons in the Cs_3C_{60} solids. We will compare these properties in both BCC and FCC lattices, and then discuss their consequences in the next sections.

6.5 Bipolaron Properties in the BCC and FCC forms of Cs_3C_{60} Solids

We derived an effective Hamiltonian for Cs_3C_{60} in the previous section. Now, we will determine some characteristic properties of two electrons in the two structures of the solid. Then, these properties will be compared and contrasted to examine the effects of the underlying lattice structure.

6.5.1 Polarisation Effects and the Φ Functions

Here, we demonstrate how the polarisation $(\hat{\boldsymbol{r}}_{ij} \cdot \boldsymbol{\eta}_\nu)$ is computed both in the BCC and FCC lattices. We also examine implications for the the function $\Phi_\nu^A(\mathbf{i}, \mathbf{i}')$ in the respective lattices.

6.5.1.1 Computation of $(\hat{\boldsymbol{r}}_{ij} \cdot \boldsymbol{\eta}_\nu)(\hat{\boldsymbol{r}}_{i'j} \cdot \boldsymbol{\eta}_\nu)$

We will calculate the polarisation separately in the BCC and FCC lattices. For convenience, we set the lattice constant to unity in both lattices.

BCC Lattice

Intersite: two electrons occupying two different but neighbouring C_{60} sites

As depicted in Figure 6.1, if the coordinate of the central C_{60} molecule is $(0, 0, 0)$, and that labelled "**A**" is $(\frac{1}{2}, \frac{-1}{2}, \frac{1}{2})$, then, the three Cs ions labelled "1","2","3" - with respective coordinates $(0, \frac{-1}{2}, \frac{1}{4})$, $(\frac{1}{4}, 0, \frac{1}{2})$, $(\frac{1}{2}, \frac{-1}{4}, 0)$ - connect the two C_{60} molecules in consideration. We define a vector of the form $\hat{\boldsymbol{r}}_{ij} = C_{\mathbf{i}}\hat{C}s_{\mathbf{j}}$ which represents the separation between the C_{60} molecule at site i and a cesium ion at site j. Then, we find the dot products using Cartesian coordinates. Examples are given below for the C_{60} at site **A** and the three
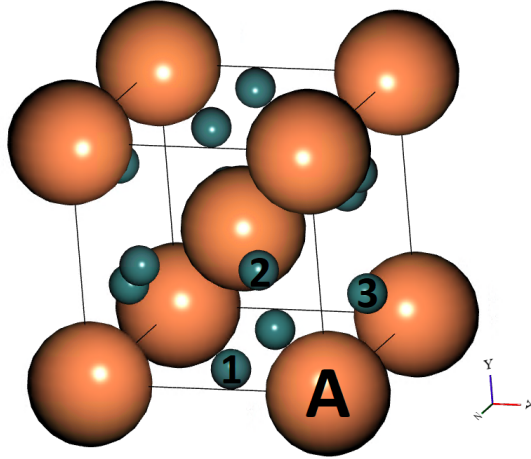
Figure 6.1: Annotated BCC structure of the Cs_3C_{60}. The small green balls represent the cesium atoms and the big brown balls represent the C_{60} molecules. For consideration of effective interaction, we assume one electron is located at the central C_{60} ball and another electron at the C_{60} labelled A. The closest cesium atoms connecting the central ball and ball A are the small green balls labelled 1, 2, 3.

nearest cesium ions (treating a single Cs ion at a time).

ION 1 (Cs_1):

$C_A\hat{C}s_1 = \frac{4}{\sqrt{5}}(\frac{-1}{2}, 0, \frac{-1}{4}) \implies C_A\hat{C}s_1 \cdot \hat{x}_{mode} = \frac{-2}{\sqrt{5}}; C_A\hat{C}s_1 \cdot \hat{y}_{mode} = 0; C_A\hat{C}s_1 \cdot \hat{z}_{mode} = \frac{-1}{\sqrt{5}}.$

$C_o\hat{C}s_1 = \frac{4}{\sqrt{5}}(0, \frac{-1}{2}, \frac{1}{4}) \implies C_o\hat{C}s_1 \cdot \hat{x}_{mode} = 0; C_o\hat{C}s_1 \cdot \hat{y}_{mode} = \frac{-2}{\sqrt{5}}; C_o\hat{C}s_1 \cdot \hat{z}_{mode} = \frac{1}{\sqrt{5}}$

So, $|C_A\hat{C}s_1 \cdot C_o\hat{C}s_1|_{mode} = |(C_A\hat{C}s_1 \cdot \hat{x}) \cdot (C_o\hat{C}s_1 \cdot \hat{x})|_{mode} + |(C_A\hat{C}s_1 \cdot \hat{y}) \cdot (C_o\hat{C}s_1 \cdot \hat{y})|_{mode} +$

$|(C_A\hat{C}s_1 \cdot \hat{z}) \cdot (C_o\hat{C}s_1 \cdot \hat{z})|_{mode} = \frac{-1}{5}.$

ION 2 (Cs_2):

$C_A\hat{C}s_2 = \frac{4}{\sqrt{5}}(\frac{-1}{4}, \frac{1}{2}, 0) \implies C_A\hat{C}s_2 \cdot \hat{x}_{mode} = \frac{-1}{\sqrt{5}}; C_A\hat{C}s_2 \cdot \hat{y}_{mode} = \frac{2}{\sqrt{5}}; C_A\hat{C}s_2 \cdot \hat{z}_{mode} = 0.$

$C_o\hat{C}s_2 = \frac{4}{\sqrt{5}}(\frac{1}{4}, 0, \frac{1}{2}) \implies C_o\hat{C}s_2 \cdot \hat{x}_{mode} = \frac{1}{\sqrt{5}}; C_o\hat{C}s_2 \cdot \hat{y}_{mode} = 0; C_o\hat{C}s_2 \cdot \hat{z}_{mode} = \frac{2}{\sqrt{5}}$

$\therefore |C_A\hat{C}s_2 \cdot C_o\hat{C}s_2|_{mode} = \frac{-1}{5}.$

ION 3 (Cs_3):

$C_A\hat{C}s_3 = \frac{4}{\sqrt{5}}(0, \frac{1}{4}, \frac{-1}{2}) \implies C_A\hat{C}s_3 \cdot \hat{x}_{mode} = 0; C_A\hat{C}s_3 \cdot \hat{y}_{mode} = \frac{1}{\sqrt{5}}; C_A\hat{C}s_3 \cdot \hat{z}_{mode} = \frac{-2}{\sqrt{5}}.$

$C_o\hat{C}s_3 = \frac{4}{\sqrt{5}}(\frac{1}{2}, \frac{-1}{4}, 0) \implies C_o\hat{C}s_3 \cdot \hat{x}_{mode} = \frac{2}{\sqrt{5}}; C_o\hat{C}s_3 \cdot \hat{y}_{mode} = \frac{-1}{\sqrt{5}}; C_o\hat{C}s_3 \cdot \hat{z}_{mode} = 0.$

$\therefore |C_A\hat{C}s_3 \cdot C_o\hat{C}s_3|_{mode} = \frac{-1}{5}$

We see from above that between a pair of C_{60} neighbours, the effective interaction due to the (orthogonal) vibrations of the nearest alkali ions is

$$\sum_{n=1}^{3} |(C_{\mathbf{A}}\hat{C}s_n \cdot \{\hat{x}, \hat{y}, \hat{z}\}) \cdot (C_{\mathbf{o}}\hat{C}s_n \cdot \{\hat{x}, \hat{y}, \hat{z}\})|_{\text{mode}} = |(C_{\mathbf{A}}\hat{C}s_1 \cdot \hat{x}) \cdot (C_{\mathbf{o}}\hat{C}s_1 \cdot \hat{x})|$$

$$+ |(C_{\mathbf{A}}\hat{C}s_1 \cdot \hat{y}) \cdot (C_{\mathbf{o}}\hat{C}s_1 \cdot \hat{y})| + |(C_{\mathbf{A}}\hat{C}s_1 \cdot \hat{z}) \cdot (C_{\mathbf{o}}\hat{C}s_1 \cdot \hat{z})|$$

$$+ |(C_{\mathbf{A}}\hat{C}s_2 \cdot \hat{x}) \cdot (C_{\mathbf{o}}\hat{C}s_2 \cdot \hat{x})| + |(C_{\mathbf{A}}\hat{C}s_2 \cdot \hat{y}) \cdot (C_{\mathbf{o}}\hat{C}s_2 \cdot \hat{y})| \qquad (6.43)$$

$$+ |(C_{\mathbf{A}}\hat{C}s_2 \cdot \hat{z}) \cdot (C_{\mathbf{o}}\hat{C}s_2 \cdot \hat{z})| + |(C_{\mathbf{A}}\hat{C}s_3 \cdot \hat{x}) \cdot (C_{\mathbf{o}}\hat{C}s_3 \cdot \hat{x})|$$

$$+ |(C_{\mathbf{A}}\hat{C}s_3 \cdot \hat{y}) \cdot (C_{\mathbf{o}}\hat{C}s_3 \cdot \hat{y})| + |(C_{\mathbf{A}}\hat{C}s_3 \cdot \hat{z}) \cdot (C_{\mathbf{o}}\hat{C}s_3 \cdot \hat{z})| = \frac{-3}{5}$$

Onsite: two electrons occupying the same C_{60} site

Similarly, we compute for the case of two electrons at the central site in Figure 6.1

$$\sum_{n=1}^{12} |(C_{\mathbf{o}}\hat{C}s_n \cdot \{\hat{x}, \hat{y}, \hat{z}\}) \cdot (C_{\mathbf{o}}\hat{C}s_n \cdot \{\hat{x}, \hat{y}, \hat{z}\})|_{\text{mode}}$$

However, it should be noted that in the BCC Cs_3C_{60} unit cell, all the Cs ions are equidistant from the central C_{60} molecule, therefore all the 12 ions would participate in the onsite case and not just 3 ions as in the case of the intersite. Depending on how they are labelled, we can find the coordinates and perform the summation as before. We will only illustrate here the result from the vibrational modes of the Cs ion labelled "1" in Figure 6.1.

$$|(C_{\mathbf{o}}\hat{C}s_1 \cdot \hat{x}) \cdot (C_{\mathbf{o}}\hat{C}s_1 \cdot \hat{x})|_{\text{mode}} + |(C_{\mathbf{o}}\hat{C}s_1 \cdot \hat{y}) \cdot (C_{\mathbf{o}}\hat{C}s_1 \cdot \hat{y})|_{\text{mode}} + |(C_{\mathbf{o}}\hat{C}s_1 \cdot \hat{z}) \cdot (C_{\mathbf{o}}\hat{C}s_1 \cdot \hat{z})|_{\text{mode}} =$$

1.

It immediately becomes obvious that all the surrounding balls will contribute the same weight. Thus, the overall contribution is $12 \times 1 = 12$. We note here that between two electrons situated onsite, the overall effect from the vibrations of the nearest alkali

ions on these electrons is positive (attractive) whilst for intersite electrons at nearest-neighbour C$_{60}$ balls, the overall contribution from the alkali ions is negative (repulsive).

In summary, in the BCC phase of a Cs$_3$C$_{60}$ solid, the effective interaction between two electrons interacting via the Cs vibrational modes is

- repulsive (negative, $\rightarrow \frac{-3}{5}$) when the electrons occupy nearest-neighbour sites, and

- attractive (positive with a weight N, where $N = 12$ is the total number of nearest Cs ions) for onsite configuration.
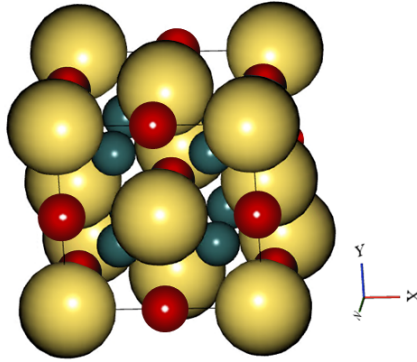

Figure 6.2: The structure of the Cs$_3$C$_{60}$ in its FCC phase. There are four cesium atoms connecting two C$_{60}$ molecules: 2 green balls at the tetrahedral sites and 2 red balls at the octahedral sites.

FCC Lattice

Intersite: two electrons occupying two different but neighbouring C$_{60}$ sites

Just as in the BCC case above, we will similarly determine the effective interaction between electrons on two C$_{60}$ molecules (Figure 6.2). We use a central C$_{60}$ molecule at $(0, 0, 0)$ and a neighbouring C$_{60}$ molecules at position **A** $(\frac{1}{2}, \frac{1}{2}, 0)$. For the chosen C$_{60}$ molecules, the two closest Cs ions (green balls) are at coordinates $(\frac{1}{4}, \frac{1}{4}, \frac{1}{4})$ and $(\frac{1}{4}, \frac{1}{4}, \frac{-1}{4})$ respectively, while the next two (red balls) ions have their respective coordinates as $(\frac{1}{2}, 0, 0)$ and $(0, \frac{1}{2}, 0)$.

ION 1: green Cs

$C_A\hat{C}s_1 = \frac{4}{\sqrt{3}}(\frac{-1}{4}, \frac{-1}{4}, \frac{1}{4}) \implies C_A\hat{C}s_1 \cdot \hat{x}_{mode} = \frac{-1}{\sqrt{3}}$; $C_A\hat{C}s_1 \cdot \hat{y}_{mode} = \frac{-1}{\sqrt{3}}$; $C_A\hat{C}s_1 \cdot \hat{z}_{mode} = \frac{1}{\sqrt{3}}$.

$C_o\hat{C}s_1 = \frac{4}{\sqrt{3}}(\frac{1}{4}, \frac{1}{4}, \frac{1}{4}) \implies C_o\hat{C}s_1 \cdot \hat{x}_{mode} = \frac{1}{\sqrt{3}}$; $C_o\hat{C}s_1 \cdot \hat{y}_{mode} = \frac{1}{\sqrt{3}}$; $C_o\hat{C}s_1 \cdot \hat{z}_{mode} = \frac{1}{\sqrt{3}}$

So, $|C_A\hat{C}s_1 \cdot C_o\hat{C}s_1|_{mode} = |(C_A\hat{C}s_1 \cdot \hat{x}) \cdot (C_o\hat{C}s_1 \cdot \hat{x})|_{mode} + |(C_A\hat{C}s_1 \cdot \hat{y}) \cdot (C_o\hat{C}s_1 \cdot \hat{y})|_{mode} +$

$|(C_A\hat{C}s_1 \cdot \hat{z}) \cdot (C_o\hat{C}s_1 \cdot \hat{z})|_{mode} = \frac{-1}{3}$.

ION 2: green Cs

$C_A\hat{C}s_2 = \frac{4}{\sqrt{3}}(\frac{-1}{4}, \frac{-1}{4}, \frac{-1}{4}) \implies C_A\hat{C}s_2 \cdot \hat{x}_{mode} = \frac{-1}{\sqrt{3}}$; $C_A\hat{C}s_2 \cdot \hat{y}_{mode} = \frac{-1}{\sqrt{3}}$; $C_A\hat{C}s_2 \cdot \hat{z}_{mode} =$

$\frac{-1}{\sqrt{3}}$.

$C_o\hat{C}s_2 = \frac{4}{\sqrt{3}}(\frac{1}{4}, \frac{1}{4}, \frac{-1}{4}) \implies C_o\hat{C}s_2 \cdot \hat{x}_{mode} = \frac{1}{\sqrt{3}}$; $C_o\hat{C}s_2 \cdot \hat{y}_{mode} = \frac{1}{\sqrt{3}}$; $C_o\hat{C}s_2 \cdot \hat{z}_{mode} = \frac{-1}{\sqrt{3}}$

$\therefore |C_A\hat{C}s_2 \cdot C_o\hat{C}s_2|_{mode} = \frac{-1}{3}$.

ION 3: red Cs

$C_A\hat{C}s_3 = 2(0, \frac{-1}{2}, 0) \implies C_A\hat{C}s_3 \cdot \hat{x}_{mode} = 0$; $C_A\hat{C}s_3 \cdot \hat{y}_{mode} = -1$; $C_A\hat{C}s_3 \cdot \hat{z}_{mode} = 0$.

$C_o\hat{C}s_3 = 2(\frac{1}{2}, 0, 0) \implies C_o\hat{C}s_3 \cdot \hat{x}_{mode} = 1$; $C_o\hat{C}s_3 \cdot \hat{y}_{mode} = 0$; $C_o\hat{C}s_3 \cdot \hat{z}_{mode} = 0$.

$\therefore |C_A\hat{C}s_3 \cdot C_o\hat{C}s_3|_{mode} = 0$

ION 4: red Cs

$C_A\hat{C}s_4 = 2(\frac{-1}{2}, 0, 0) \implies C_A\hat{C}s_4 \cdot \hat{x}_{mode} = -1$; $C_A\hat{C}s_4 \cdot \hat{y}_{mode} = 0$; $C_A\hat{C}s_4 \cdot \hat{z}_{mode} = 0$.

$C_o\hat{C}s_4 = 2(0, \frac{1}{2}, 0) \implies C_o\hat{C}s_4 \cdot \hat{x}_{mode} = 0$; $C_o\hat{C}s_4 \cdot \hat{y}_{mode} = 1$; $C_o\hat{C}s_4 \cdot \hat{z}_{mode} = 0$.

$\therefore |C_A\hat{C}s_4 \cdot C_o\hat{C}s_4|_{mode} = 0$

Clearly from above, the effective interaction between two electrons sitting on two neighbouring sites taking account of polarisation is

$$\sum_{n=1}^{4} |(C_A\hat{C}s_n \cdot \{\hat{x}, \hat{y}, \hat{z}\}) \cdot (C_o\hat{C}s_n \cdot \{\hat{x}, \hat{y}, \hat{z}\})|_{mode} = \frac{-2}{3}$$

which is interpreted as repulsive. The alkali ions on a direct line between the coordinates (i.e. at octahedral sites) play no role at all in intersite consideration.

Onsite: two electrons occupying the same C_{60} site

In the FCC phase of the cesium-doped fulleride, when two onsite electrons interact via the cesium vibration, only the closest ions (8 at the tetrahedral sites) have significant contributions.

$$\sum_{n=1}^{8} |(C_{\mathbf{o}}\hat{C}s_{n} \cdot \{\hat{x}, \hat{y}, \hat{z}\}) \cdot (C_{\mathbf{o}}\hat{C}s_{n} \cdot \{\hat{x}, \hat{y}, \hat{z}\})|_{\text{mode}} = 8$$

We may conclude that the polarisation effect on effective interactions in an FCC unit cell for electrons on

- different (nearest-neighbour) sites is repulsive $\rightarrow \frac{-2}{3}$

- the same site creates an attraction with a weight N, where $N = 8$.

The above illustrations are done only for few ions within a unit cell. In our work, we have numerically computed the effective interaction between the two electrons via the Φ function defined in Equation (6.29).

6.5.1.2   The Φ Function and Screening Effect

Next, we investigate the functions, Φ defined in Equation (6.29). For a finite-size lattice, the net effect of the cesium phonons is calculated by summing all contributions from the cesium ions in the entire lattice. We plot the ratio of the intersite $\Phi_{\nu}^{A}(0, \boldsymbol{a})$ to the onsite function $\Phi_{\nu}^{A}(0, 0)$ as a function of the screening radius R_{sc} in Figure 6.3 for both lattices. The first conclusion that can be drawn is that the interaction is higher for onsite interactions than intersite interactions (at least *ten times* stronger) in both lattices. It should be noted that only the cesium atoms closest to the doubly occupied site are used to compute $\Phi_{\nu}^{A}(0, 0)$. Secondly, short-range screening brings about a net repulsive interaction (negative ratio). Thus it has an inhibiting effect on pair formation. On the other hand, for screening radii beyond the nearest-neighbour distance $|\boldsymbol{a}|$, the net interaction force between two particles is attractive (positive ratio) which may favour the formation

of light pairs. Long-range effects become saturated at a screening distance of about $15|\boldsymbol{a}|$ in both lattices. Hence, this means that increasing the screening radius further will not modify the attraction strength significantly.
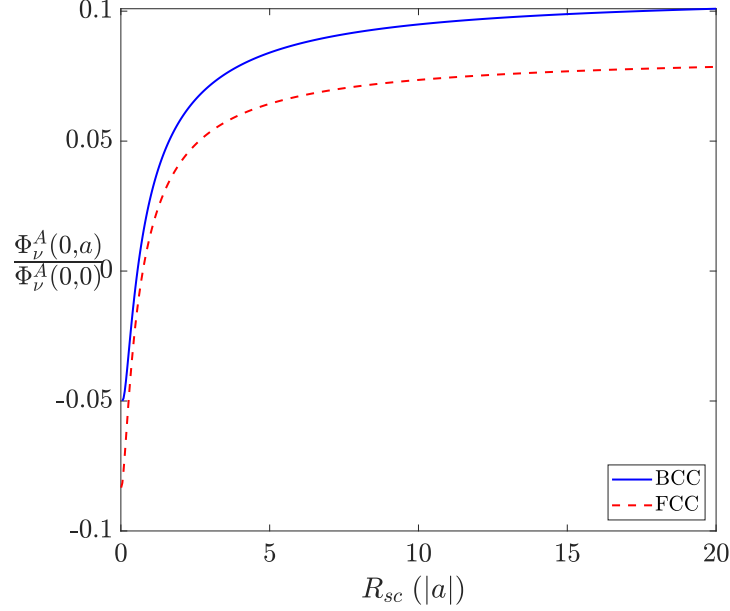

Figure 6.3: The ratio of the Φ functions in the BCC and FCC lattices of a Cs_3C_{60} solid. $\Phi^A(0, \boldsymbol{a})$ and $\Phi^A(0, 0)$ are the total *intersite* and *onsite* functions, respectively. Accordingly, positive (negative) value of the ratio means attraction (repulsion). The interaction becomes attractive when the screening radius approaches the distance between the two nearest C_{60} molecules. Superlight pairs could result from the long-range contributions.

6.5.2 UV Model for Cs_3C_{60} Solids

In the last section, we demonstrated how the electron-electron interaction functions Φ mediated by the alkali phonons in the Hamiltonian (6.24) can be computed. The instantaneous interaction between electrons resulting from Cs phonon exchange is

$$H_{\text{el}-\text{el}}^{\text{inst}} = \sum_{ii'} \tilde{\Phi}_{ii'} \hat{c}_i^\dagger \hat{c}_i \hat{c}_{i'}^\dagger \hat{c}_{i'} \tag{6.44}$$

where $\tilde{\Phi}_{00} = -(\lambda_C + \lambda')W$, and $\tilde{\Phi}_{nn'} = Q_{nn'}\tilde{\lambda}_A W : [\lambda_C = g^2/(\hbar\omega_C W); \lambda' = g'^2/(b^4\hbar\omega_A W)]$, g is the electron-phonon matrix element due to the C_{60} vibron modes and g' is the electron-phonon matrix element due to the phonon mode of an alkali ion. The value of $Q_{nn'}$ is determined depending on whether the interaction is short or long range. The Hamiltonian (6.40) is solved as standard UV with dispersion matrices of the form (4.15) and (5.19) for the BCC and FCC, respectively. The difference, however, lies in the expressions for the interaction parameters U and V. Unlike in Chapters 4 and 5, here, these interaction parameters depend on the vibrational properties of the alkali ions (Equations (6.41) and (6.42)).

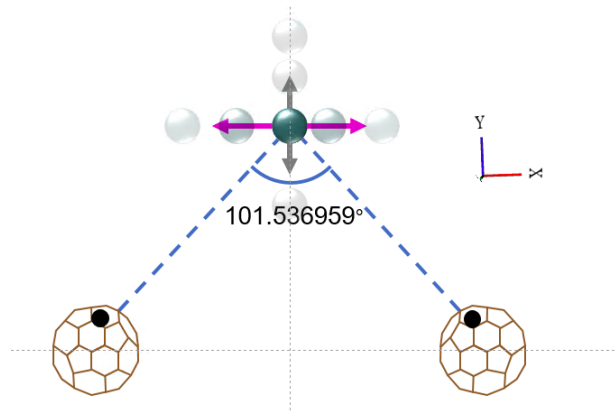

Figure 6.4: Electrons interacting with Cs vibrational modes in Cs_3C_{60} BCC. Two electrons (small black circles) on different C_{60} balls interact through the three phonon modes of Cs: along the x and y axes, the z−axis is out of the page. Note that the two C_{60} molecules are not in the xy plane, rather the diagram above has been drawn only for simplified visualisation.

6.5.2.1   Bipolaron Properties in the Distinct Structures of Cs_3C_{60}

It is important to note that the distances of the cesium ions from a central C_{60} molecule vary in the two structures of Cs_3C_{60}. In the BCC structure (Figure 6.1) for example, all the cesium ions (small green balls) are equidistant from the central C_{60} molecule. Also, it should be recalled that the angle between vectors connecting a cesium ion and two nearest C_{60} molecules is 101.5369° as seen in Figure 6.4. Unlike in the BCC phase, the cesium ions linking a pair of nearest C_{60} molecules in the FCC phase are at two inequivalent locations (i.e. nonequidistant from a central C_{60} molecule). Hence, the cesium ions are drawn in two colours (green and red balls) in the FCC structure (see Figure 6.2) where 4 cesium ions (2 red, 2 green balls) connect any nearest-neighbour C_{60} pair. Two of these four ions (i.e. the green balls) sitting at the tetrahedral positions are the closest, with the angle between vectors connecting Cs and C_{60} positions being 109.471220° while the remaining two (red balls which are slightly more distant) sit at the octahedral positions and separate the C_{60} molecules at 90°. For our calculations, the interaction parameters measured in eV (electron-volt) are taken from Ref. [114] as $U_{H,\text{BCC}} = 1.1$, $U_{H,\text{FCC}} = 1.07$, $V_{\text{BCC}} = 0.31$, $V_{\text{FCC}} = 0.3$, $W_{\text{BCC}} = 0.6$, and $W_{\text{FCC}} = 0.4$, respectively. The respective $\tilde{V}$ is obtained by multiplying V with the lattice parameter in each structure of the Cs_3C_{60} solid.

As mentioned before, the solution to Equation (6.40) is that of a typical UV problem, except for the definitions of U and V. Thus, we will apply the same method as we did in Chapters 4 and 5. The total energy and effective mass of the pair are reported below.

a. **Total Energy**

We explore the parameter space for bipolaron formation in the two structural phases of Cs_3C_{60} by varying the phonon coupling due to the vibrons λ_C and due to cesium phonons λ', as well as the screening radius R_{sc}. This allows us to determine if and when the particles bind. ε_0 in the respective lattice is the total energy of two unbound particles at zero momentum.

Firstly, we found that the formation of a bound state is easier in the BCC structure than in the FCC structure of Cs_3C_{60}. The critical value of the parameters required for pairing was determined. In the BCC structure, an intermediate vibron coupling $\lambda_C \sim 0.5$ is sufficient to bind onsite pair (though weakly) when the alkali phonon coupling is $\lambda' \sim 2.9$ and at a screening radius $R_{sc} \sim 4.6|\boldsymbol{a}|$. Whereas the same vibron coupling ($\lambda_C \sim 0.5$) cannot create a bound pair in the FCC phase which is mainly due to the larger lattice constant. Instead, a coupling of about unity $\lambda_C \approx 1$ is required for the onset of a weakly bound bipolaron which occurs via long-range interaction $R_{sc} \approx 15|\boldsymbol{a}|$ when $\lambda' \approx 3.25$ in the FCC.

In Figure 6.5, we show the bound state energy in both lattices with vibron coupling $\lambda_C = 1$, and at a range of λ' and R_{sc} parameters. At this vibron coupling, the onset of a weakly bound onsite bipolaron in the BCC lattice is found at $\lambda' \approx 2.33$ and at a screening radius of $R_{sc} \approx 4.45|\boldsymbol{a}|$. This value of alkali coupling λ' is consistent with the result in Ref. [115] for K_3C_{60}. We note that K_3C_{60} has an FCC structure and even a larger lattice constant. In both lattices, increasing λ' further results in a strongly bound onsite bipolaron as $R_{sc} \to 0$.

For λ' value of 3.5, the effect of the screening radius is more pronounced in the FCC plot. As the screening radius increases from zero, the energy of the pair significantly drops, and further increase beyond $R_{sc} = 12|\boldsymbol{a}|$ does not change the energy much.
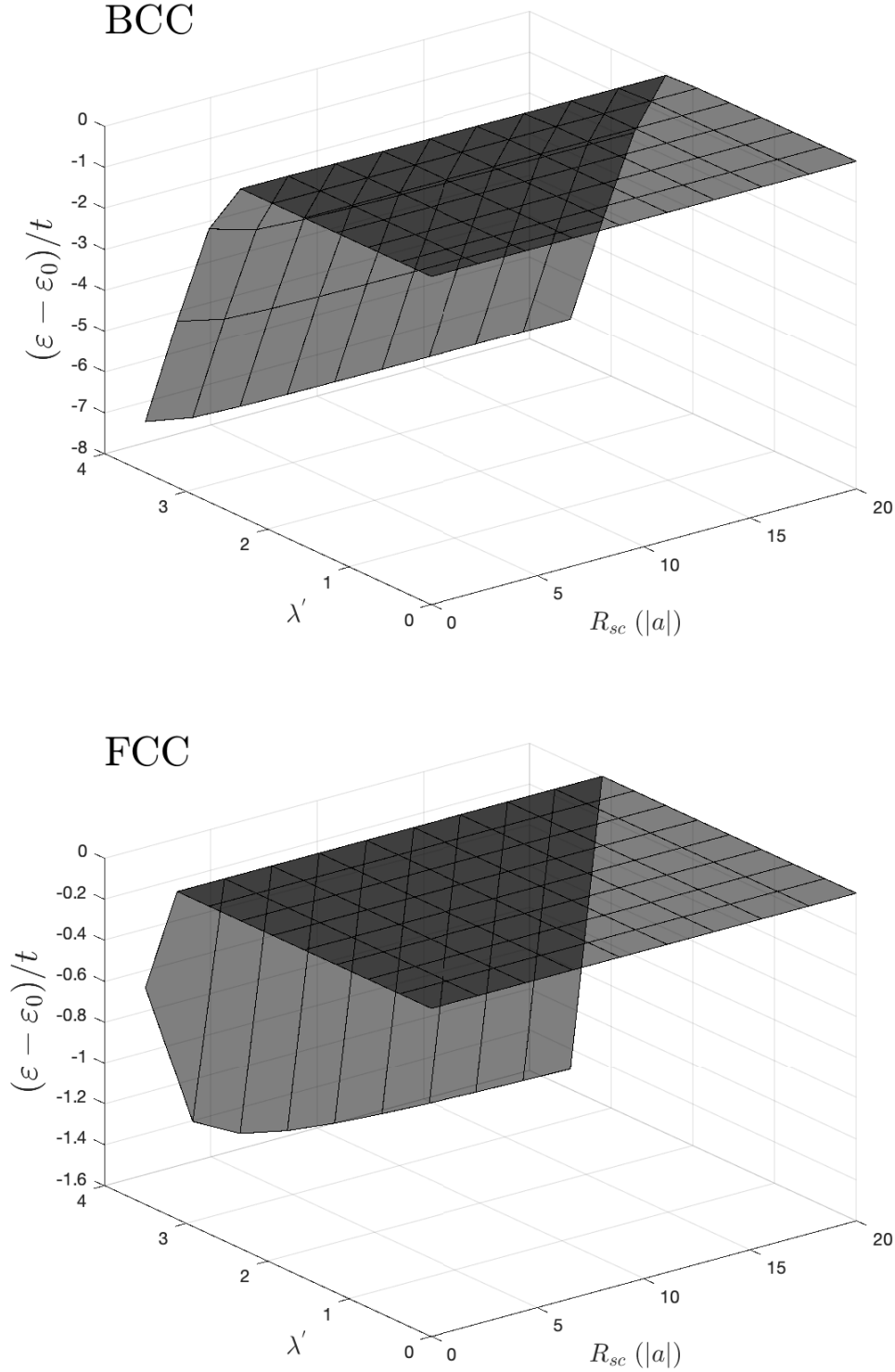
Figure 6.5: Total bipolaron energy as a function of the screening radius R_{sc} and the coupling to Cs phonons λ' at C_{60} vibron coupling of $\lambda_C = 1$ in (a) BCC and (b) FCC structures of Cs_3C_{60}. ϵ_0 is the total energy of two unbound free electrons, thus, the electrons are unbound in the flat regions where $\varepsilon = \varepsilon_0$. Note that $\varepsilon_0 = -16t$ and $\varepsilon_0 = -24t$ is the ground state energy of two free particle in the BCC and FCC lattices respectively. The particles begin to bind at $\lambda' \approx 2.33$ in the BCC and at $\lambda' \approx 3.25$ in the FCC lattice, respectively.

b. **Mass**

We also calculate the effective mass of the bipolaron m^*, measured in the unit of a free lattice electron (polaron) m_0 in both lattices. The masses are plotted in Figure 6.6. At low λ' when the particles are not bound, the bipolaron mass equals $2m_0$ (twice the mass of lattice electron), and hence is not shown. We only plot the parameter space where the particles begin to bind.

Overall, the bipolaron is heavier in the BCC phase as compared to the FCC phase. This is because there is a higher polarisation due to the Cs atoms in the BCC phase, and hence the Φ function (Figure 6.3) contributes a greater net attraction. The effective mass increases as the alkali phonon coupling λ' increases in both lattices. However, the effect of screening shows contrasting behaviours in these lattices. For significant regions of the parameter space, there is a decline in the effective mass in the BCC phase when the screening radius R_{sc} increases. Conversely, in the FCC phase, the bipolaron mass increases with R_{sc}. This difference in the behaviour of bipolaron mass would have a significant impact on the condensation temperature of bipolarons in the respective lattices.
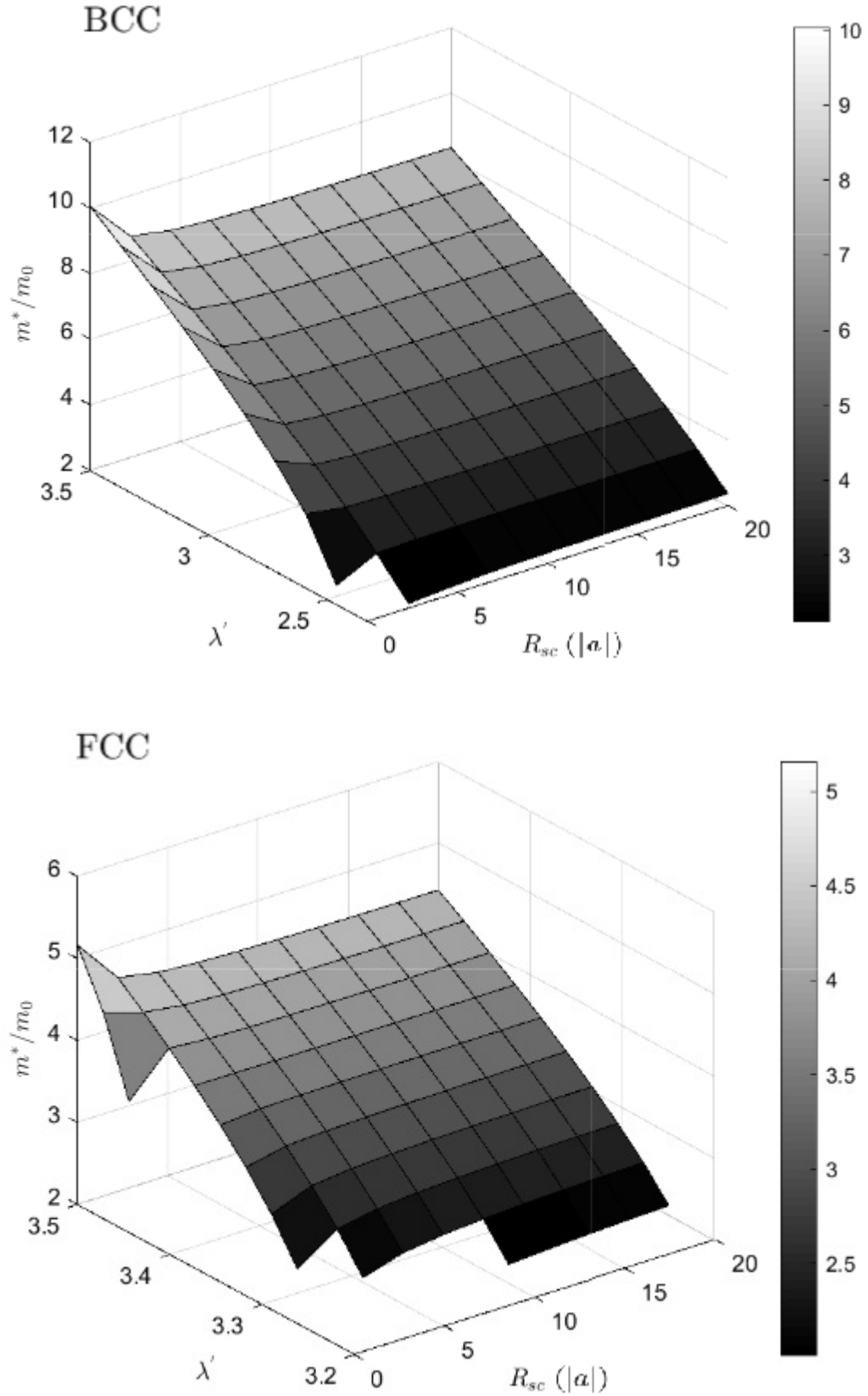
Figure 6.6: Bipolaron mass m^* in the BCC and FCC phases of Cs_3C_{60} at $\lambda_C = 1$. m_0 is the mass of lattice electron (polaron) in the respective lattice.

6.6 Discussion

We have developed an effective UV Hamiltonian to study the pairing mechanism in the alkali-doped fullerides and then obtained properties of bound electrons specifically in the two structural phases (BCC and FCC) of Cs_3C_{60}. Based on our findings, a few remarks can be made:

- Within the parameter space, the two electrons are bound onto onsite bipolaron.

- Smaller attraction (via λ_C and λ') is required to bind two particles in the BCC phase compared to the FCC phase. This means that forming of a tightly bound, local pair is more favourable in the Cs_3C_{60} solid with a BCC (A15) structure.

- Beside the attractive interaction created by C_{60} vibrons, our result suggests that additionally relevant attractions could be generated when the vibration of the cesium ions are taken into account.

- There is significant effect of long-range interactions in these solids. As bipolarons in the BCC phase are found to be heavier in this work, one would expect the FCC phase with lighter mass to yield a higher Bose-Einstein condensation temperature. However, experiments [19, 20] have proved otherwise. We note that there are opposing behaviours of bipolaron mass in the two structural phases with increasing screening radius.

Even though the bipolarons are lighter in the FCC phase at short screening distance, a very strong coupling (which leads to heavy pair taking account of a polaron mass) is required to bind them. Our conclusion is that: Since local pairs can be formed in the BCC phase at weak to moderate coupling and their masses (which will be similar to the FCC) can further reduce with long-range effects, then, they may Bose-condense at high

temperatures. This result might provide a useful explanation as to why a higher T_c is observed in the BCC phase of a Cs_3C_{60} solid or open new ideas for understanding the superconducting mechanism in the alkali-doped fulleride family.

Chapter 7

QMC Simulations on BCC and FCC Lattices

7.1 Summary

In this chapter, we study the properties of bipolarons in the BCC and FCC lattices in the adiabatic regime using the continuous-time quantum Monte Carlo algorithm introduced in Chapter 3. Here, we study the effects of the EPIs on the bipolaron properties. The preliminary discussion briefly introduces the two types of interaction of interest in this study: the Holstein-Hubbard and the near-neighbour interaction (extended Holstein-Hubbard model, EHHM). For this project, an update was made to the QMC code in order to effectively capture loops due to triple kinks in an FCC lattice. So, we will discuss how the new update is implemented in the code. Then, we report the results for simulations carried out at low phonon frequency (which can be used to examine retardation effects) while varying the EPI and Coulomb interaction strengths. We end this chapter with a discussion of our findings.
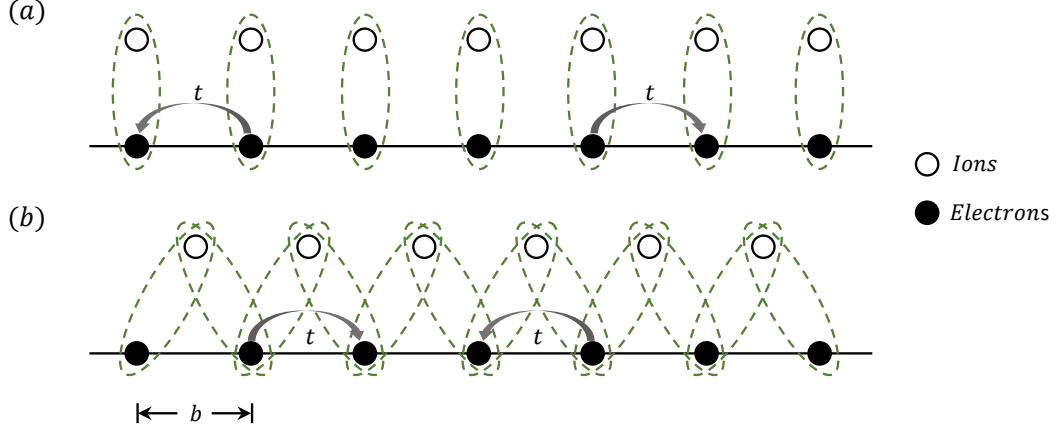
Figure 7.1: One-dimensional schematic of (a) the Holstein-Hubbard model and (b) the extended Holstein-Hubbard model with near-neighbour EPI. The filled circles, empty circles and dashed oval circles represent the electron Wannier orbitals, lattice ions, and nonzero electron-phonon coupling, respectively. The nearest-neighbour electron sites have overlapping orbitals such that an electron can hop via t, and b is the lattice constant. Adapted from Ref. [70].

7.2 Preliminaries

Bipolarons formed in the Holstein-Hubbard model (HHM) [57, 116] and those formed in an extended Holstein-Hubbard model (EHHM) [70] consist of two polarons that can bind into a stable singlet state when the exchange of phonons overcomes Coulomb repulsion. These categories of bipolarons differ in the spatial extent of their EPI. As shown in Figure 7.1, the nature of the EPI in the former model is site-local (electron located at the vibrating atomic site) whereas the latter has a long-range EPI (of near-neighbour type). In the local HHM, we note that even though the phonon-mediated attraction between two polarons on different sites is zero, an intersite Coulomb repulsion V could still be present (as considered in this study). To our knowledge, there is not yet a numerical study of bipolaron properties, neither in the BCC nor the FCC lattice.

In this work, we placed two fermions in a $20 \times 20 \times 20$ box (BCC and FCC lattices, respectively), and then simulations were carried out at a normalised phonon frequency of $\bar{\omega} = \hbar\omega/t = 1$ and inverse temperature $\bar{\beta} = 1/k_B T = 20$ for a range of Coulomb

repulsion (U and V) and coupling constant λ. The interaction parameters U and V are scaled by the lattice half-bandwidths W. We adopted twisted boundary condition on paths to estimate the mass. The procedure for the simulation has been summarised in Section 3.6.1. Measurements are done every few Monte Carlo steps and for each data point, the error bars are displayed as 3 standard deviations. Where the error bars are not visible it means they are too small to be apparent on the scale of the plot.

7.3 Triple Update on FCC Lattice

Due to the geometry of the FCC lattice, it is possible that a bound bipolaron returns to an initial configuration after three consecutive hops of one of the particles. Hence, it is important to use detailed balance to derive updates with this property to be used in the Metropolis algorithm. We note that this update is only applied to one of the two electron paths. The procedure and implementation of the triple update in the QMC code is as follows:

1. We use the weighting scheme, detailed in Appendix A, to select a path with equal probability 1/2.

2. A combination of three kinks that is suitable for this update is determined. For example, a kink is selected from the 12 possible kinks (the number of nearest-neighbour sites) and we label it l_1. Then, we choose two other kinks (l_2 and l_3) such that $l_1 + l_2 + l_3 = 0$. Satisfying this condition means that the particle returns to its initial site after three hops.

3. We choose insertion or removal of the (three) kinks with equal probability 1/2.

4. If insertion is chosen in step 4, we select the imaginary times τ_1, τ_2, τ_3 for the new

kinks with equal probability $1/\bar{\beta}$ from the interval $[0, \bar{\beta})$. The Metropolis condition is given as:

$$P_{\text{add}}(\tau_1, \tau_2, \tau_3) = \min\left\{1, \frac{t\bar{\beta}}{N_{l_1}+1}\frac{t\bar{\beta}}{N_{l_2}+1}\frac{t\bar{\beta}}{N_{l_3}+1} \cdot e^{A(D)-A(C)}\right\} \qquad (7.1)$$

where C and D are the initial and final configurations, respectively. $A(C)$ and $A(D)$ are the bipolaron actions in both initial and final configurations. N_{l_i} $(i = 1, 2, 3)$ is the number of kinks of type l_i before the addition update (i.e. in the initial configuration, C).

5. On the other hand, if removal of kinks is selected in step 4, there are two possibilities. The first is to check whether the kink types l_1, l_2, and l_3 chosen from step 3 already exist in the initial configuration. If any of those selected kinks does not exist in the current path, the acceptance probability is zero and the update is aborted. Otherwise, provided that there is at least one of each kink type, the removal at imaginary times τ_1, τ_2, τ_3 is carried out with the acceptance probability:

$$P_{\text{remove}}(\tau_1, \tau_2, \tau_3) = \min\left\{1, \frac{N_{l_1}}{t\bar{\beta}}\frac{N_{l_2}}{t\bar{\beta}}\frac{N_{l_3}}{t\bar{\beta}} \cdot e^{A(C)-A(D)}\right\} \qquad (7.2)$$

where N_{l_i} $(i = 1, 2, 3)$ is the number of kinks of type l_i before removal.

7.4 Bipolaron Properties

This section splits into two parts because we studied two types of singlet bipolarons (in the HHM and EHHM as mentioned above) - treating one at a time. The measured properties of the bipolarons in both the BCC and FCC lattices include the ground state energy, the total number of excited phonons, the effective mass, and the bipolaron radius.

7.4.1 Holstein-Hubbard Model (HHM) Bipolarons

For the majority of the simulations of Holstein-Hubbard model (HHM) bipolarons found in the literature (e.g. [61, 70, 72, 73, 117, 118]), only the Hubbard U is retained in the model Hamiltonian whilst the intersite Coulomb interaction V is usually ignored. However, in this work, we include both the onsite and intersite Coulomb interaction terms in the Hamiltonian Equation (2.27) and consider only the physical case for which both U and V are repulsive. We have also considered this scenario so as to mimic the fulleride compounds where repulsive U and V, as well as EPI are present. V is small in the fullerides [24], and this will be the case in our simulations.

7.4.1.1 Total Energy of HHM Bipolarons

The energy of the HHM bipolarons, expressed in terms of the half-bandwidth W, in both the BCC and FCC lattices is depicted in Figure 7.2. In both lattices, the polarons do not bind when $\lambda = 0$ as expected of two free-electrons experiencing repulsive Coulomb interactions. If U and/or V are present while $\lambda = 0$, the simulation of the two-particle HHM directly maps onto the UV model (see Chapters 4 and 5). Thus, we have used the QMC code (in the $\lambda = 0$ limit) to validate our analytic results and vice-versa. However, when the phonon coupling is turned on, its effect is seen as the particles begin to bind via lattice phonons. The energy curve (Figure 7.2) is sloped for a bound (onsite)

bipolaron while it remains flat when there is insufficient phonon interaction to overcome the Coulomb repulsions. The effect of small repulsive V is that the probability of forming an intersite bipolaron is further diminished.

In the strong coupling limit, the energy of the onsite bipolaron is given as [72]

$$E/W = U/W - 4\lambda \quad , \tag{7.3}$$

which is also plotted as dashed lines in Figure 7.2. Upon lowering U or increasing λ, the energy of the HHM bipolaron rapidly approaches the limiting behaviour of a strongly bound onsite pair. A large onsite repulsion U is required to break the pairing as the electron-phonon coupling increases. For both BCC and FCC lattices, the energies (measured in W) are qualitatively similar and neither system is significantly modified due to small intersite repulsion.
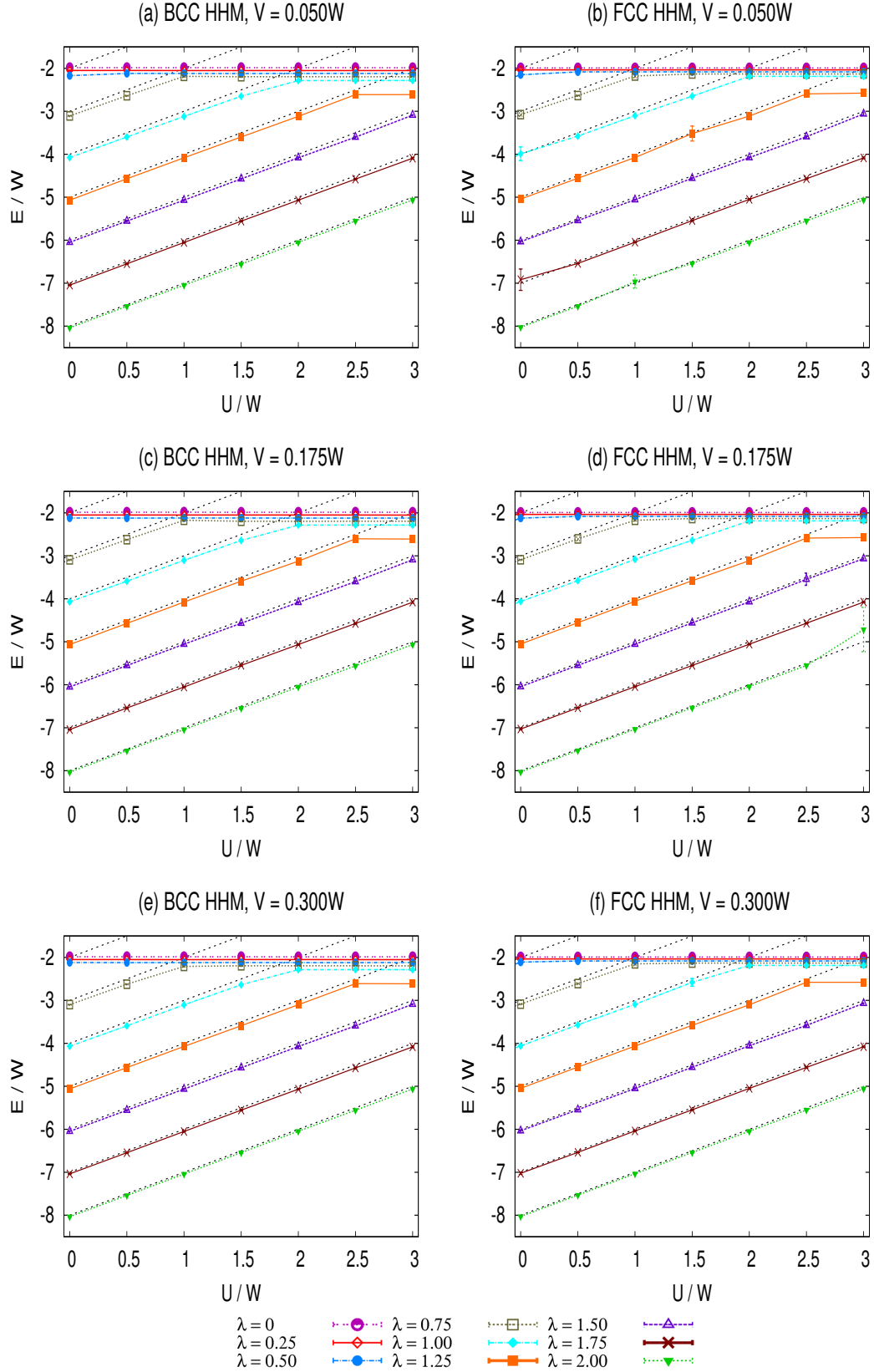
Figure 7.2: Total singlet energy of the Holstein-Hubbard model (HHM) bipolaron obtained from the continuous-time QMC simulation in the BCC and FCC lattices at various U and small repulsive V. Panels (a), (c), and (e) on the left are for singlet bipolarons in the BCC lattice and panels on the right (b), (d), (f) are for singlet bipolarons in the FCC lattice. The first, second and third row corresponds to cases where $V = 0.05W$, $V = 0.175W$, and $V = 0.3W$, respectively. Dashed lines running diagonally are the energy of onsite bipolarons in the strong coupling limit.

7.4.1.2   Number of Phonons for HHM Bipolarons

To further investigate the HHM bipolarons, we plot the number of phonons, N_{ph} associated with the phonon cloud within which the polarons are confined as a function of U, V and λ (Figure 7.3). For $\lambda = 0$, there are no phonons in the system. However, when electron-phonon interactions are switched on in these systems, the number of phonons becomes non-zero regardless of whether a bound state is formed or not.

As the repulsive Hubbard U is slowly decreased, there is a sharp increase in the number of associated phonons signifying the formation of a bound state. We observe a linear increase in the number of phonons as the electron-phonon coupling strength increases. In the strong-coupling limit, $N_{\mathrm{ph}} = 4\lambda z$ for HHM bipolarons [72]. Once the onsite bipolaron is formed, each curve remains flat upon reducing U and approaches the strong-coupling limit (represented by the black arrows on the left in Figure 7.3). This implies that the number of excited phonons in the system is unaffected by any change in U after pairing has occurred and the convergence improves as λ increases.

There is a clear distinction in the number of excited phonons surrounding the electrons in the BCC lattice as compared to the FCC lattice - though the curves are similar in form. An interesting feature is observed at $\lambda = 1$ and for $U \geq 2$ where there are no bound states (i.e. 2 free polarons). The number of phonons appear to be greater in the BCC lattice with around twice as many as in the FCC lattice. In the region of bound onsite pairs, however, the number of phonons is significantly higher in the latter. Thus, the possibility of binding pairs could be higher in the FCC lattice than the BCC lattice due to the presence of more phonons. We will examine in the next section whether the increased number of phonons causes the bipolarons to be heavier in the FCC lattice. The effect of increasing the intersite Coulomb interaction V is only noticeable in the BCC lattice (see Figures 7.3a, 7.3c and 7.3e for $0.5 \lesssim \lambda \lesssim 0.75$ and $U \leq W$).
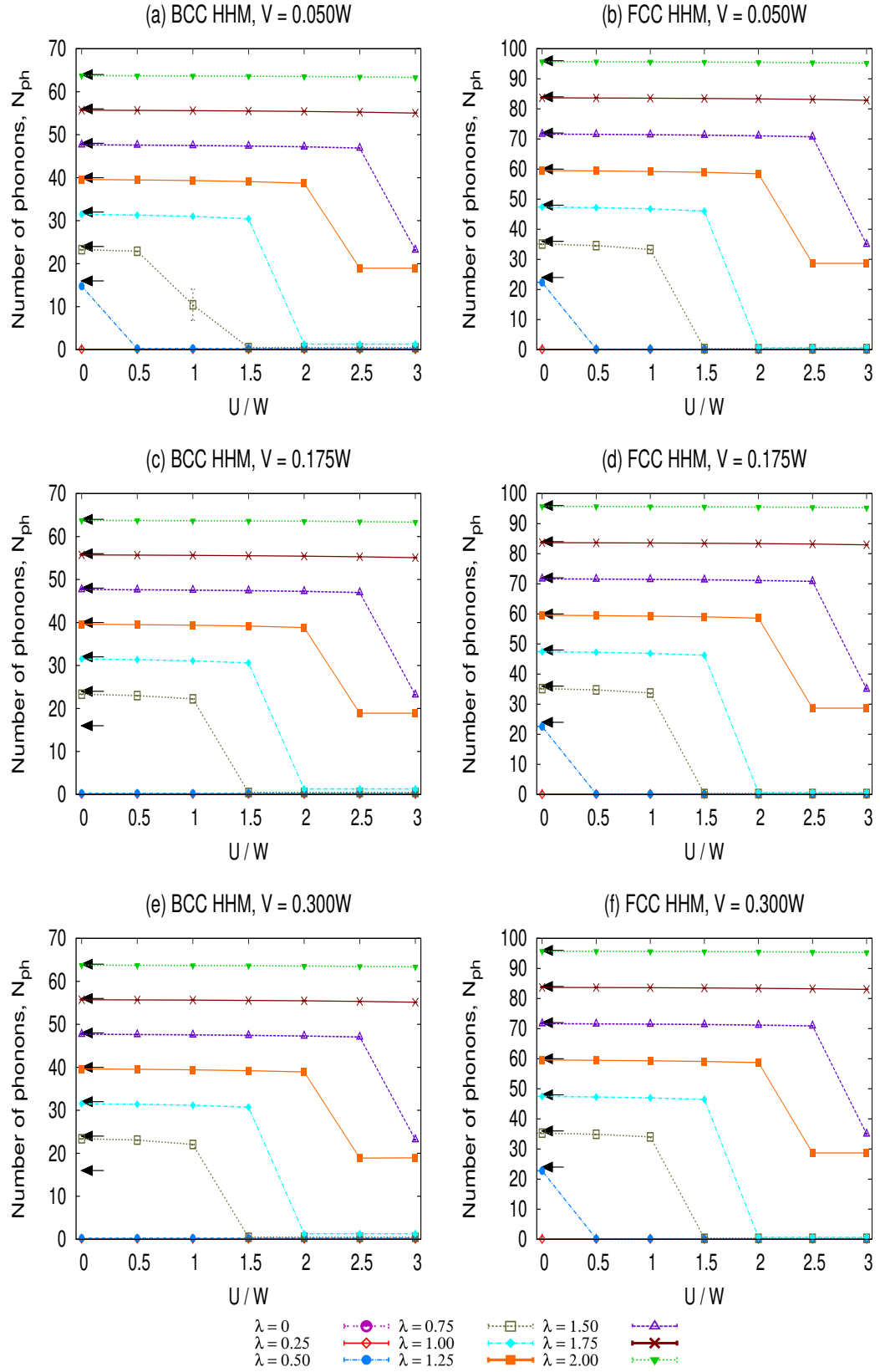
Figure 7.3: The number of excited phonons for HHM bipolarons in both the BCC and FCC lattices. Results are obtained from the simulation of singlet bipolarons in the presence of intersite repulsions.

7.4.1.3   Inverse Effective Mass of HHM Bipolarons

The next property we examine is the effective mass of the HHM bipolarons. Figure 7.4 shows the inverse bipolaron mass (expressed in units of non-interacting electron mass, m_0) in the BCC and FCC lattices. Low (high) values along the vertical axis of the plots in Figure 7.4 implies that the bipolaron is heavy (light). Bipolarons are heavy for lower U and are conversely light for large U. We note that the change from unbound to bound bipolaron properties is very abrupt, similar to the number of phonons discussed above. In such a crossover region, the pair mass becomes very heavy when particles bind, hence the inverse mass becomes very small.

In both BCC and FCC systems, the pair becomes very heavy for $\lambda > 1$. The effect of the finite size lattice can be observed in the calculation of the mass when $\lambda = 0$ where there are no phonons to bind the particles, and as such the pair mass should be twice the mass of free lattice electron (i.e. $m_0/m^* \approx 0.45$ when it should be 0.5 in an infinite lattice). As there are more phonons in the FCC lattice, bound FCC bipolarons are relatively heavier - for example, compare the inverse mass for $\lambda = 0.5$, $U < W$, and $V > 0.05W$ in both lattices. Again, the effects of an intersite repulsion V can be seen only in the BCC lattice in the region $U \leq W$ and $0.5 \lesssim \lambda < 0.75$. For an unbound pair at large U and $\lambda = 1$, the FCC pair appears to be lighter than the BCC one.
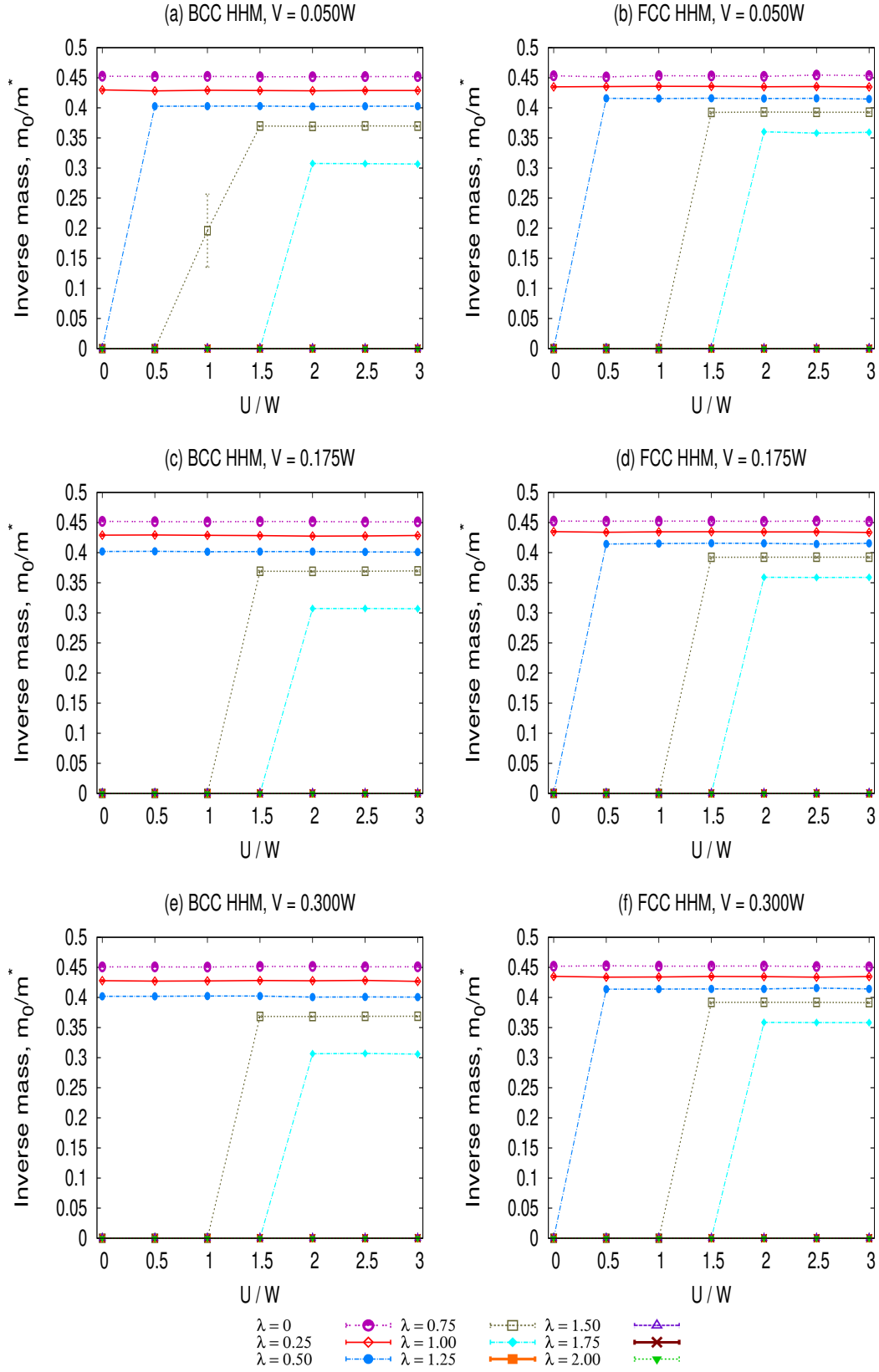
Figure 7.4: Inverse mass of Holstein-Hubbard model (HHM) bipolarons in the BCC and FCC lattices in the presence of intersite repulsions. The effect of changing V on the inverse mass is only noticeable in the BCC case when V goes above $0.05W$. Within the QMC calculations, inverse mass is zero unless visible on the linear scale.

7.4.1.4   Inverse Radius of HHM Bipolarons

The inverse radius of HHM bipolarons is plotted in Figure 7.5. We see the contraction of large two unbound polarons into a small bound bipolaron as the electron-phonon coupling is increased. Higher values in the plot correspond smaller pair radius. There are quantitative differences in the size of bound pairs in the considered lattices. Bipolarons in the FCC lattice are significantly smaller as compared to the BCC counterpart for all values of U. When V and λ are fixed, and U is varied, there is an abrupt drop in the inverse bipolaron radius at the transition from bound to the unbound states in both systems. This substantial increase in pair radius (i.e. low inverse radius) upon increasing U is because the Coulomb repulsion breaks the pairing and prohibits the onsite occupation of the particles. We also note that the effect of increasing V is noticed only in the BCC lattice at $\lambda \sim 0.5 - 0.75$.

The total energy, number of phonons, effective mass and size of the HHM bipolaron have been examined above. The same properties for bipolarons formed in the extended Holstein-Hubbard model (EHHM) will be explored in the next section.
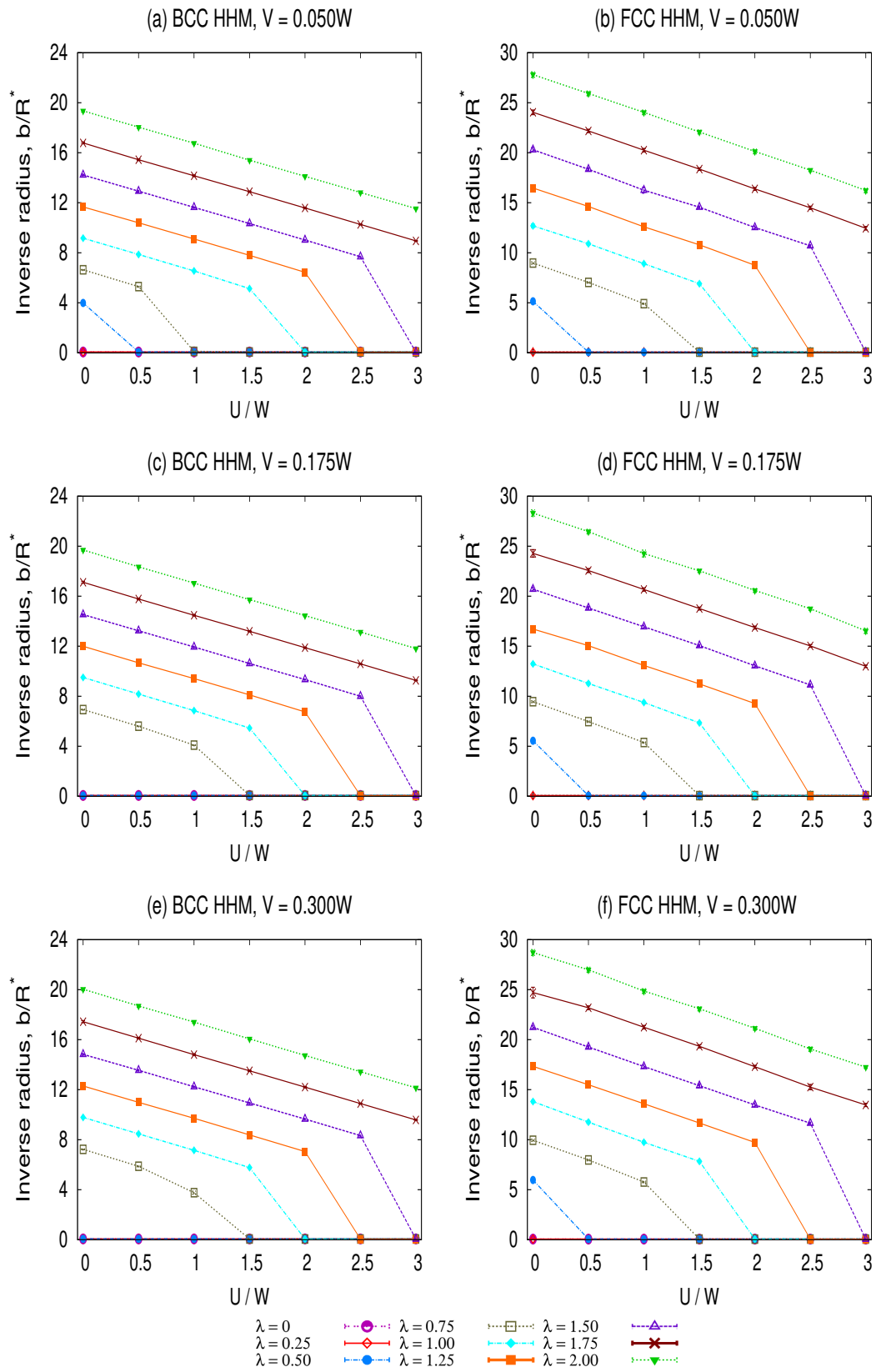
Figure 7.5: Holstein-Hubbard model (HHM) bipolaron inverse radius in the BCC and FCC lattices in the presence of intersite repulsions. For $\lambda = 0.5$, the effect of changing V can be identified in the BCC lattice.

7.4.2   Extended Holstein-Hubbard Model (EHHM) Bipolarons

We now turn to the simulation of extended Holstein-Hubbard model (EHHM) bipolarons with nearest-neighbour phonon interactions (NNPIs). We define γ, the strength of interaction, which is the ratio of the phonon-mediated interaction between two particles occupying the nearest-neighbour sites as

$$\gamma = \frac{\Phi_{0a}}{\Phi_{00}} \quad , \tag{7.4}$$

where a is the nearest-neighbour distance. Note that $a = \sqrt{3}b/2$ in the BCC lattice, and $a = \sqrt{2}b/2$ for FCC lattice, where b is the lattice constant. For this study, we have chosen $\gamma = 0.5$. We may alternatively refer to EHHM bipolaron as intersite bipolaron or simply as near-neighbour bipolaron (NNB). It has been demonstrated (in other simple systems) that NNPIs give the most important contributions to the properties of bipolarons [70, 71, 72, 73]. Furthermore, the suppression in the optical absorption spectrum of multipolaron systems increases with lattice dimensionality due to the screening of long-range EPI [57]. Hence, no Frölich tail is expected in 3D lattices. More so, the properties of bipolaron formed from near-neighbour EPI show no effect due to repulsive intersite Coulomb interaction as long as $V < W$ [69]. In this work, we will examine the intrinsic properties of pairs from NNPIs for $V = 0$ in the BCC and FCC lattices.

7.4.2.1   Total Energy of EHHM Bipolarons

Short-range EPI favours the formation of both onsite (when U is small and λ is large) and intersite bipolarons, and the bipolaron total energy is shown in Figure 7.6. There is a smoother transition from an unbound to a weakly bound state at small coupling $\lambda \leq 0.5$, compared to the HHM bipolarons. Upon increasing λ, a well bound state is formed even at finite U. This is because intersite bipolarons are unaffected by large

Hubbard U.

Singlet bipolaron energy in the two lattices (BCC and FCC) are quantitatively similar when measured in terms of the respective lattice half-bandwidths. The limiting behaviour of strongly bound onsite bipolaron at $U \gg \lambda W$ is given as [72]

$$E/W = -2\lambda(1 + \gamma) \quad , \tag{7.5}$$

and this value is represented by arrows at the right-hand side of the plots in Figure 7.6. The crossover from intersite to strongly bound onsite bipolaron requires that λ is large and that the Hubbard U is small. Note how the curves approach the limiting behaviour of strongly bound onsite bipolaron very slowly in comparison to the HHM bipolaron (refer to Figure 7.2).
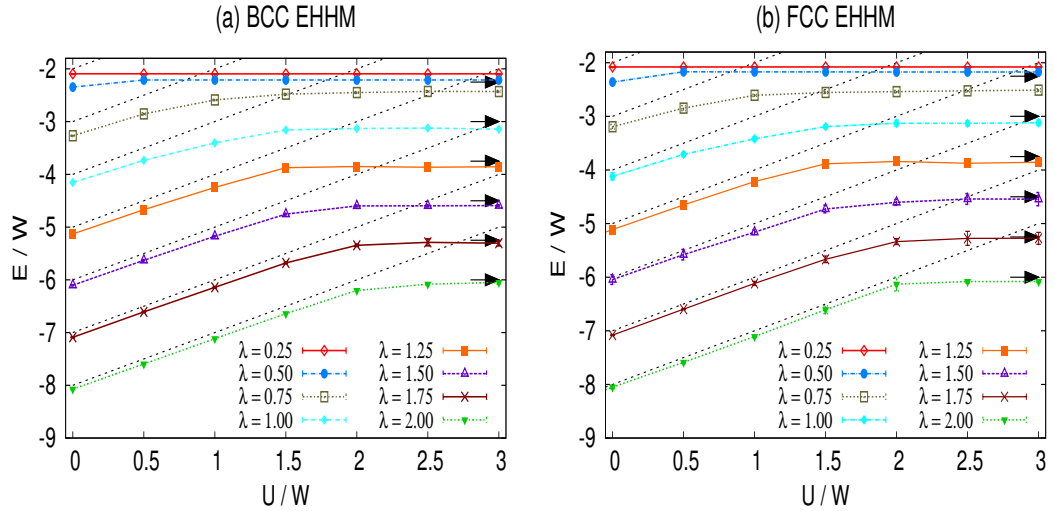

Figure 7.6: Total singlet energy of extended Holstein-Hubbard model (EHHM) bipolarons obtained from the continuous-time QMC simulation in the BCC lattice (left) and the FCC lattice (right) at different coupling constant λ and repulsive U.

7.4.2.2 Number of Phonons for EHHM Bipolarons

The effect of the EPI in the EHHM is also apparent in the number of phonons associated with the bipolaron (Figure 7.7). Similar to the energy of singlet EHHM bipolarons, the number of phonons at the transition from onsite to intersite bipolarons changes smoothly and slowly approaches the limit of strongly bound onsite pairs (arrows on the left in Figure 7.7). For comparison, in the region of $U > W$ and $0.5 < \lambda < 1$, the number of phonons is higher in the EHHM than in the HHM by several orders of magnitude. This indicates that bound states can be found in the EHHM at intermediate coupling for Hubbard U greater than the half-bandwidth ($U > W$).

Figure 7.7 also shows that there are more phonons associated with the bipolaron in the FCC lattice which suggests that the chance of bipolarons forming via nearest-neighbour interaction is greater in the FCC lattice than in the BCC lattice (this is also true for HHM bipolarons, see Section 7.4.1.2). As was the case for HHM bipolarons, the presence of more phonons could lead to the formation of heavy EHHM bipolarons as we shall see in the next section. For phonon energy $\hbar\omega = t$, the number of phonons associated with the strongly-coupled intersite bipolaron is given as $N_{\mathrm{ph}} = 2\lambda z(1+\gamma)$ [72]. Our QMC result is also in good agreement with the strong-coupling behaviour (arrow on the right in Figure 7.7) as λ increases.
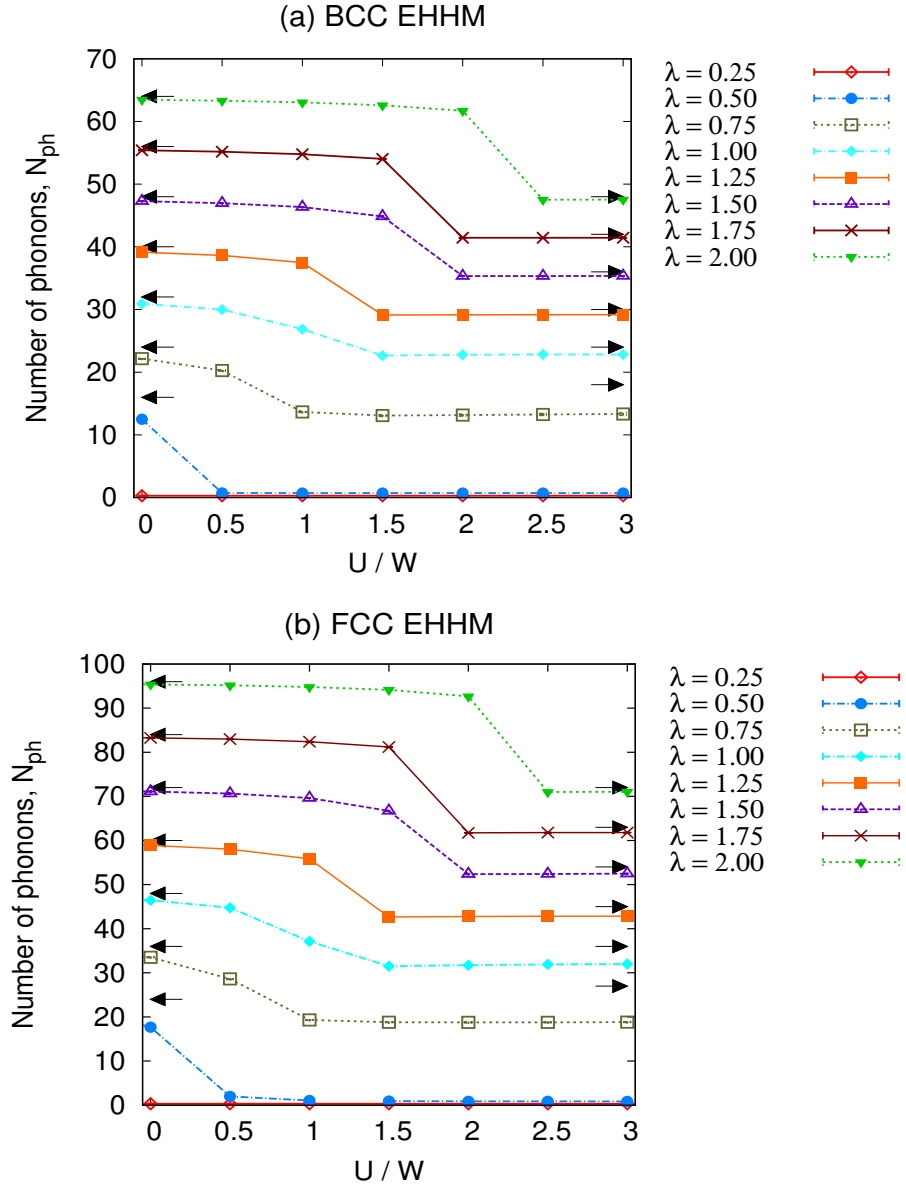
Figure 7.7: Plots showing the number of phonons for EHHM bipolarons in the BCC and FCC lattices obtained from the continuous-time QMC simulation with repulsive Hubbard interaction U.

7.4.2.3   Inverse Effective Mass of EHHM Bipolarons

The inverse mass of the EHHM bipolarons is shown in Figure 7.8. The inverse mass decreases (i.e. increase in mass) as λ increases and the plots appear similar for both lattices. To visualise any difference between the bipolaron masses, we plot the inverse mass in a logarithmic scale (Figure 7.9).

From Figure 7.9, the onsite bound bipolaron in the FCC lattice quickly gets heavier by orders of magnitude as compared to the BCC counterpart when λ is increased. This is not surprising because, in the FCC lattice; (1) the mass of each polaron that forms the bipolaron sharply increases (i.e. decrease in the inverse mass) for $\lambda > 1$ [93], and (2) we see in the last section that there are more phonons in the FCC system responsible for binding the two polarons (see Figure 7.7). In comparison to the HHM case, there are bound EHHM bipolarons at large U, although it initially seems that the HHM bipolaron is lighter, in practice, in the HHM case these are two free polarons. At low U where particles form an onsite pair, the HHM bipolarons have relatively larger masses (evident when the inverse mass are plotted in a log scale) than the EHHM bipolarons.

In the BCC case, maxima are observed in the log scale plots (Figure 7.9) for $\lambda > 0.75$ where the pair mass first decreases (i.e. increase in the inverse mass) as the Hubbard U increases, and the mass gets heavier again (i.e. lowered inverse mass) with further increment in U. This feature shows the superlight behaviour of bipolarons in the BCC lattice where the effective U becomes an approximate attractive intersite interaction similar in size to the effective V (from Equation (2.59) $\tilde{U} \sim U - 4W\lambda \sim V \approx -2W\lambda$) - thus allowing the pair to move via single hop without breaking the pairing. At first glance, the superlight behaviour in the FCC lattice does not seem obvious. However, if we carefully examine the mass for large U and $0.75 \lesssim \lambda \lesssim 1.25$, we see that the FCC bipolaron is lighter than the BCC bipolaron by at least an order of magnitude.
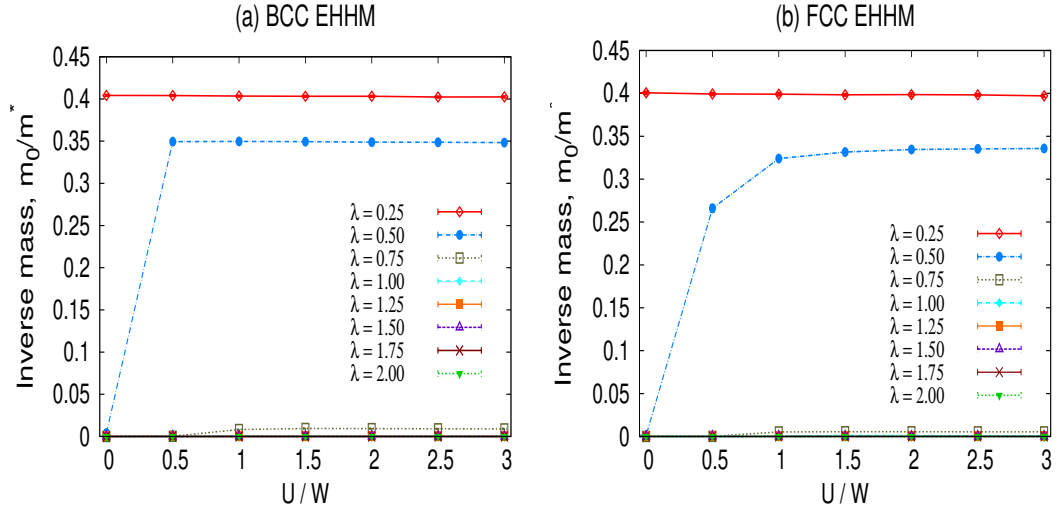
Figure 7.8: Inverse mass of EHHM bipolarons in the BCC and FCC lattices (linear scale). For λ values beyond 0.6, it becomes difficult to see data on the linear scale. Hence, we make a plot of the same data in the logarithmic scale in Figure 7.9 below.

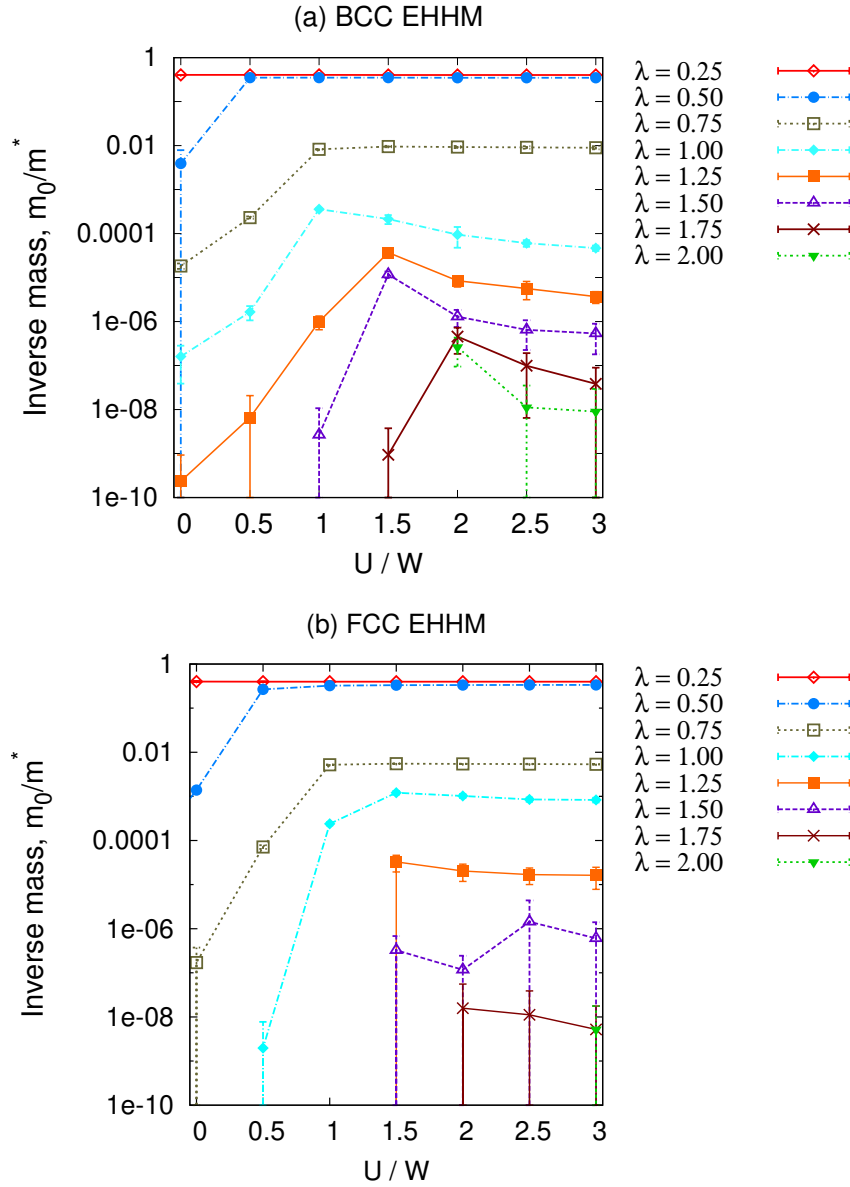**Figure 7.9:** Inverse mass of EHHM bipolarons in the BCC and FCC lattices plotted using log scales. For the majority of the parameter space, bipolarons formed in the FCC lattice are heavier than those in the BCC lattice. This could be mainly due to the presence of more phonons in the FCC lattice (Figure 7.7).

7.4.2.4 Inverse Radius of EHHM Bipolarons

We plot the inverse radius of the EHHM bipolarons in Figure 7.10. As the coupling constant λ increases and U decreases, bipolarons in both lattices become smaller (quantitatively different radius though). This is so because the electron-phonon attraction dominates over the small Coulomb screening. At strong λ and large U, we see the formation of intersite bipolarons, where the bipolaron size tends to the nearest-neighbour distance. In comparison to the HHM bipolarons, the inverse radius of onsite bipolarons from the EHHM (i.e. at low U) is twice as large in the examined λ range. This means that the onsite HHM bipolarons are about half the size of onsite EHHM bipolarons.
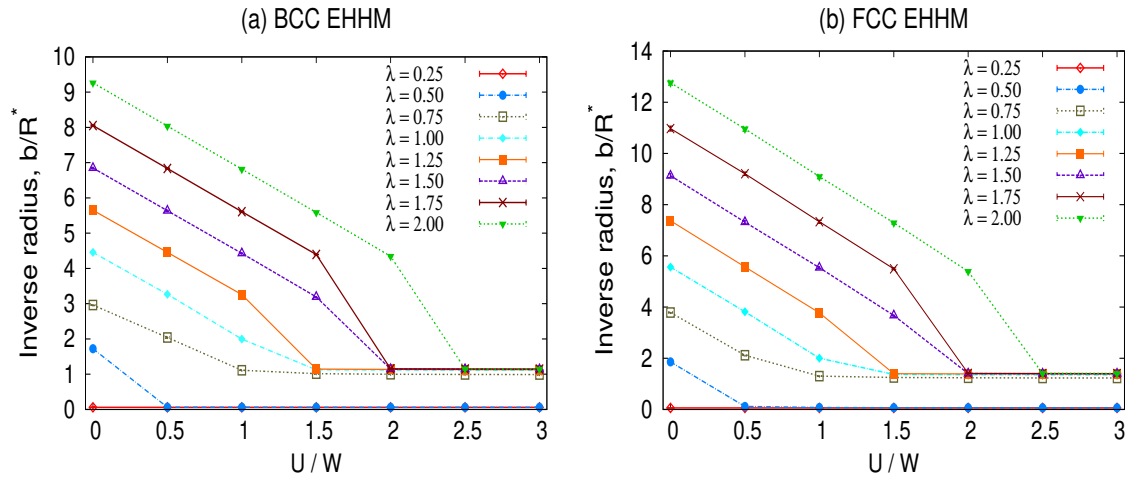

Figure 7.10: Inverse radius of EHHM bipolaron in the BCC and FCC lattices obtained from QMC simulation.

7.5   Discussion

Using a QMC simulation algorithm, we have studied the Holstein-Hubbard and extended Holstein-Hubbard models applied to two interacting particles in the presence of phonon-mediated attractions. The simulation was carried out for two electrons in the BCC and FCC lattices. A key difference between HHM and EHHM bipolarons is that the transition between bound and unbound states is sharp in the former while it is smooth in the latter. Strongly bound EHHM bipolarons have both onsite and intersite states whereas HHM bipolarons only show onsite characteristics.

The energy of the HHM and EHHM bipolarons are similar for $U \lesssim 1.5$ and large λ (i.e. onsite bipolarons). At larger U, however, they have qualitatively different behaviours: EHHM bipolarons can be well bound and stable at large U due to the near-neighbour phonon attraction. There is no qualitative difference in the total energy of bipolarons in both the BCC and FCC lattices for a specific model.

Our results also show that the number of phonons associated with the bipolaron is not dictated by the dimensionality of the lattice, but perhaps the lattice coordination number. The number of phonons in both models (HHM and EHHM) quantitatively differ over a wide region of parameter space. We found that there are more phonons present in the FCC lattice which suggests an increased chance of binding two polarons as compared to the BCC lattice. This behaviour (more phonons in the FCC lattice) was observed in both models (HHM and EHHM).

Another benefit of the QMC simulation is that we can examine the effect of phonon retardation on the properties of bipolarons. At low phonon frequencies (as considered in this work), the retardation effect is expected to be significant. For well bound onsite pairs with a coupling strength of $\lambda \gtrsim 0.5$, pairs on the BCC lattice are lighter by

orders of magnitude as compared to the FCC lattice. Whereas for well bound intersite pairs at intermediate electron-phonon coupling, the FCC is lighter by at least an order of magnitude. Such a near-neighbour bipolaron in the FCC lattice displays superlight behaviour (i.e. the pair moves by first order hops) as U becomes infinitely large. On the other hand, pairs in the BCC lattice become superlight in the region of U of around half- to full-bandwidth of the lattice. For a wide range of parameter space studied, we may conclude that the mass of the FCC pairs is mainly due to the presence of more phonons which enhances polaron effects.

Although the FCC pairs are quite heavy, they have a relatively small size when compared to the BCC pairs. In the entire parameter space, the size of the HHM and EHHM bipolarons are clearly different with HHM bipolarons being smaller. EHHM bipolarons are intersite (on the order of the nearest-neighbour separation) at $U > W$ and $\lambda \geq 0.75$.

Part III

CONCLUSIONS

Chapter 8

Conclusions

During this study, we have explored the behaviour of strongly interacting fermions in three-dimensional systems (BCC and FCC) with a focus on the A_3C_{60} (fulleride) compounds. These compounds, among many other materials, are suitable for studying correlated behaviour of electrons and, by extension, for investigating the link(s) between conventional and unconventional superconductivity. The main goal of this research was to investigate the mechanism(s) of superfluidity and superconductivity in strongly correlated systems. Part I (Chapters 1, 2 and 3) of this thesis reviewed the theoretical backgrounds of strong correlation in fermionic systems, the fullerides compounds, and the methodology used in this work. In Part II, we reported our findings and the summary is given below. (For detailed discussions, please refer to Sections 4.4, 5.4, 6.6 and 7.5, respectively.)

We have presented exact solutions (Chapters 4 and 5) of the two-body problem in both BCC and FCC lattices in the anti-adiabatic (i.e. high-phonon frequency) limit. The parameter space for the formation of bound pairs in both lattices was examined and binding diagrams were constructed. Binding diagrams provide the conditions for identifying paired and unpaired regions within the parameter space. The stability of

the pairs was analysed, and properties including the effective mass and radius were also calculated. In these lattices, we found the pairs to be small and light at the same time. We showed that bound electrons in an FCC lattice can be highly itinerant and have potential for high-temperature superconductivity. In addition, we predict the onset of superfluidity in a quantum simulator with fermionic lithium-6 atom occurring at temperatures up to 10 nK.

Furthermore, we developed an effective UV Hamiltonian for the fullerides in Chapter 6. The critical electron-phonon coupling (arising from the alkali atoms) that is required for bipolaron pairing has been reported and we have shown that two polarons bind at a smaller coupling in the BCC phase in comparison to the FCC phase. Our result also suggests that there may be long-range (attractive) contributions from the vibration of the alkali atoms. Even though the pairs in the FCC structure of the fullerides have lighter masses upon binding, the BCC structure in contrast has a higher transition temperature [19] which may be due to the long-range interactions (reduction of the effective mass with long-range contributions) reported in this work. This result shows that the underlying structure and the positions of the alkali atoms in these solids play important roles in the observed superconducting behaviours.

Lastly, using a QMC simulation in Chapter 7, the direct interplay of phonon coupling between two polarons was also examined away from the anti-adiabatic limit. It was found that bipolarons form at moderate coupling constants in both the BCC and FCC lattices. Results for nearest-neighbour phonon interactions (NNPIs) show a smoother transition and the bipolarons are well bound (more stable) in a wide parameter range as compared to their Holstein counterpart. The bound state in an FCC lattice is lighter than BCC pairs for the Holstein case, whereas the BCC bound pairs are typically lighter than the FCC pairs in case of NNPIs. Bound onsite pairs in the EHHM have less mass (by several

orders of magnitude) in comparison to their HHM counterparts. We also found superlight behaviour of bound pairs in both lattices but the question as to whether increases in mass due to polaron effects would dominate over any increase in the mobility of the pair was not investigated. In the FCC lattice, the pair are smaller than the BCC pairs in both Holstein and NNPI cases.

The summary of our results above has shown that, pairs formed on these lattices are promising candidates for high-temperature superconductivity, as bound electrons can be both small and light. These features are the prerequisites for Bose-Einstein condensation to take place with potentially high-transition temperatures.

Future Work

Due to time constraints for this PhD research, there were other considerations which could not be investigated. Therefore, we suggest them for future work. Our suggestions include the following.

- Examining long-range UV model in 3D systems: We have only limited the interactions between the electrons to nearest-neighbour sites. Meanwhile, it would be of great interest to explore the effects of the next-nearest-neighbour interactions such that a long-range UV model can be investigated. As for most lattices with dimension $d > 1$, the nearest-neighbour distances are often comparable to the next-nearest-neighbour distances, hence, adding these terms to the UV calculations may have significant impact on the properties of the pairs in 3D systems.

- Extending the QMC method to simulate multipolaron systems: QMC has the capability to simulate an interacting system with number of particles $N > 3$. Thus, it would be worthwhile to explore systems with additional particles. This

will provide an extra layer of understanding regarding the effects of many-body interaction.

- Studying other pair symmetries in more detail: This work mainly focused on the properties of the s-symmetric pairs and their condensates. Since there is experimental evidence of d-wave pairing in the cuprates and even a mixture with s- and p-wave symmetries, it will be important to examine and contrast other pairing symmetries in the 3D lattices.

- Investigating the effects of retardation on the mobility of superlight pairs: In this work, we have found that bound pairs can be heavy yet they may tunnel through the lattice with single hopping events. At this stage, we cannot make conclusive comments on whether polaron effects predominate over their mobility. Investigating this would be an interesting question to consider.

- Explore a multi-band UV model for the fulleride compounds: Although, we have made a single-band simplification in the derivation and the solution of the UV Hamiltonian for the fullerides (Equation 2.41) in Chapter 7, the fullerides are inherently multi-band systems. Hence, we suggest treating a similar Hamiltonian with multiple band considerations.

Part IV

APPENDICES

Appendix A

CTQMC Algorithm

Results from the continuous-time Monte Carlo (CTQMC) simulation of bipolarons on the BCC and FCC lattices were reported in Chapter 7. Following an introduction to the CTQMC in Section 3.6 of Chapter 3, we want to elaborate on some of the technicalities here.

A.1 Update Rules and Weighting Scheme

The electron paths are continuous in time and an electron hops between sites via kinks in its path. In an exchange configuration, our result is free from sign problem since we only studied singlet states. The selection of path, insertion or removal of kink, and choosing the kink type is implemented probabilistically. The kink type specifies the direction of particle's hop.

Kink insertion or removal is carried out in pairs so that the end configurations of the paths maintain their boundary conditions. We refer to kink insertions and/or removals as updates and there are rules for carrying out these updates for the simulation of two particles. Four binary updates were used:

1. Kinks of type l are added to or removed from each path.

2. Add or remove a kink of type l and its anti-kink $-l$ to or from one of the paths.

3. Insert a kink of type l to one path and remove another kink of the same type l from the same path. This update only works if there is at least one kink of type l on that path since there will no kink to remove if it is non-existent.

4. Insert a kink of type l from one path and remove an anti-kink $-l$ from the other path.

All the updates above were the existing rules prior to the commencement of this study. The detailed balance equations and Metropolis conditions for these updates can be found in Hague et al. 2007 (*J. Phys. Cond. Matt. 19, 255214*). In this work, I have added a new update rule which is reported in Section 7.3 of Chapter 7.

The summary of the probabilities for kink selection is given below.

- For N_k number of nearest-neighbours, we choose a kink type l with the probability $P_l = 1/N_k$ and its anti-kink l is determined.

- Since there are only two particles, we select one of the two paths as path A with a probability $1/2$ and label the other as path B.

- We choose a kink shift type with an equal probability $P_{\text{Shift}} = 1/2$. The kink shift can either be top shift (in the direction of l) or bottom shift (in the direction of $-l$).

- To remove the first kink of type l from a path A at imaginary time τ, do so with the probability $1/N_{Al}(I)$, where I is the initial configuration before removal.

- To remove the second kink of type l from path A, this is done with a probability $1/N_{Al}(I)$, where I represents the configuration before removal.

- The first kink of type l is inserted at time τ with probability density $p(\tau) = 1/\beta$.

- For the addition of the second kink of type l at time τ', do so with a probability density $p(\tau) = 1/\beta$.

- The shift type of the second kink is dependent on whether it is correlated or anti-correlated with the shift type of the first kink. The inter-path distance is unchanged for correlated insertion but changes for anti-correlated insertion.

Appendix B

Supplementary Materials

B.1   Classes of the O_h Point Group

The classes are listed below. C_{nj} denotes a proper rotation through $2\pi/n$ in the right-hand screw sense about the axis O_j. A superscript means that the rotation is performed in the left-hand screw sense. I implies spatial inversion.

E : the identity operation

$8C_2 = C_{3\alpha}, C_{3\beta}, C_{3\gamma}, C_{3\delta}, C_{3\alpha}^{-1}, C_{3\beta}^{-1}, C_{3\gamma}^{-1}, C_{3\delta}^{-1}$: 120° rotation about $O\alpha,\ O\beta,\ O\gamma,\ O\delta$ axes

$3C_3 = C_{2x}, C_{2y}, C_{2z}$: 180° rotation about $OX,\ OY,\ OZ$ axes

$6C_4 = C_{4x}, C_{4y}, C_{4z}, C_{4x}^{-1}, C_{4y}^{-1}, C_{4z}^{-1}$: 90° rotation about $OX,\ OY,\ OZ$ axes

$6C_5 = C_{2a}, C_{2b}, C_{2c}, C_{2d}, C_{2e}, C_{2f}$: 180° rotation about $Oa,\ Ob,\ Oc,\ Od,\ Oe,\ Of$ axes

$C_6 = i$: the inverse identity operation

$8C_7 = IC_{3\alpha}, IC_{3\beta}, IC_{3\gamma}, IC_{3\delta}, IC_{3\alpha}^{-1}, IC_{3\beta}^{-1}, IC_{3\gamma}^{-1}, IC_{3\delta}^{-1}$

$3C_8 = IC_{2x}, IC_{2y}, IC_{2z}$

$6C_9 = IC_{4x}, IC_{4y}, IC_{4z}, IC_{4x}^{-1}, IC_{4y}^{-1}, IC_{4z}^{-1}$

$6C_{10} = IC_{2a}, IC_{2b}, IC_{2c}, IC_{2d}, IC_{2e}, IC_{2f}$

The irreducible representation for each group element is given in Table B.1

$$E = \begin{bmatrix} 1 & 0 & 0 \\ 0 & 1 & 0 \\ 0 & 0 & 1 \end{bmatrix}, \quad C_{3\alpha} = \begin{bmatrix} 0 & 1 & 0 \\ 0 & 0 & -1 \\ -1 & 0 & 0 \end{bmatrix}, \quad C_{3\beta} = \begin{bmatrix} 0 & -1 & 0 \\ 0 & 0 & -1 \\ 1 & 0 & 0 \end{bmatrix}, \quad C_{3\gamma} = \begin{bmatrix} 0 & -1 & 0 \\ 0 & 0 & 1 \\ -1 & 0 & 0 \end{bmatrix},$$

$$C_{3\delta} = \begin{bmatrix} 0 & 1 & 0 \\ 0 & 0 & 1 \\ 1 & 0 & 0 \end{bmatrix}, \quad C_{3\alpha}^{-1} = \begin{bmatrix} 0 & 0 & -1 \\ 1 & 0 & 0 \\ 0 & -1 & 0 \end{bmatrix}, \quad C_{3\beta}^{-1} = \begin{bmatrix} 0 & 0 & 1 \\ -1 & 0 & 0 \\ 0 & -1 & 0 \end{bmatrix}, \quad C_{3\gamma}^{-1} = \begin{bmatrix} 0 & 0 & -1 \\ -1 & 0 & 0 \\ 0 & 1 & 0 \end{bmatrix},$$

$$C_{3\delta}^{-1} = \begin{bmatrix} 0 & 0 & 1 \\ 1 & 0 & 0 \\ 0 & 1 & 0 \end{bmatrix}, \quad C_{2x} = \begin{bmatrix} 1 & 0 & 0 \\ 0 & -1 & 0 \\ 0 & 0 & -1 \end{bmatrix}, \quad C_{2y} = \begin{bmatrix} -1 & 0 & 0 \\ 0 & 1 & 0 \\ 0 & 0 & -1 \end{bmatrix}, \quad C_{2z} = \begin{bmatrix} -1 & 0 & 0 \\ 0 & -1 & 0 \\ 0 & 0 & 1 \end{bmatrix},$$

$$C_{4x} = \begin{bmatrix} 1 & 0 & 0 \\ 0 & 0 & 1 \\ 0 & -1 & 0 \end{bmatrix}, \quad C_{4x}^{-1} = \begin{bmatrix} 1 & 0 & 0 \\ 0 & 0 & -1 \\ 0 & 1 & 0 \end{bmatrix}, \quad C_{4y} = \begin{bmatrix} 0 & 0 & -1 \\ 0 & 1 & 0 \\ 1 & 0 & 0 \end{bmatrix}, \quad C_{4y}^{-1} = \begin{bmatrix} 0 & 0 & 1 \\ 0 & 1 & 0 \\ -1 & 0 & 0 \end{bmatrix},$$

$$C_{4z} = \begin{bmatrix} 0 & 1 & 0 \\ -1 & 0 & 0 \\ 0 & 0 & 1 \end{bmatrix}, \quad C_{4z}^{-1} = \begin{bmatrix} 0 & -1 & 0 \\ 1 & 0 & 0 \\ 0 & 0 & 1 \end{bmatrix}, \quad C_{2a} = \begin{bmatrix} 0 & 1 & 0 \\ 1 & 0 & 0 \\ 0 & 0 & -1 \end{bmatrix}, \quad C_{2b} = \begin{bmatrix} 0 & -1 & 0 \\ -1 & 0 & 0 \\ 0 & 0 & -1 \end{bmatrix},$$

$$C_{2c} = \begin{bmatrix} 0 & 0 & 1 \\ 0 & -1 & 0 \\ 1 & 0 & 0 \end{bmatrix}, \quad C_{2d} = \begin{bmatrix} 0 & 0 & -1 \\ 0 & -1 & 0 \\ -1 & 0 & 0 \end{bmatrix}, \quad C_{2e} = \begin{bmatrix} -1 & 0 & 0 \\ 0 & 0 & 1 \\ 0 & 1 & 0 \end{bmatrix}, \quad C_{2f} = \begin{bmatrix} -1 & 0 & 0 \\ 0 & 0 & -1 \\ 0 & -1 & 0 \end{bmatrix},$$

$$i = \begin{bmatrix} -1 & 0 & 0 \\ 0 & -1 & 0 \\ 0 & 0 & -1 \end{bmatrix}, \quad IC_{3\alpha} = \begin{bmatrix} 0 & -1 & 0 \\ 0 & 0 & 1 \\ 1 & 0 & 0 \end{bmatrix}, \quad IC_{3\beta} = \begin{bmatrix} 0 & 1 & 0 \\ 0 & 0 & 1 \\ -1 & 0 & 0 \end{bmatrix}, \quad IC_{3\gamma} = \begin{bmatrix} 0 & 1 & 0 \\ 0 & 0 & -1 \\ 1 & 0 & 0 \end{bmatrix},$$

$$IC_{3\delta} = \begin{bmatrix} 0 & -1 & 0 \\ 0 & 0 & -1 \\ -1 & 0 & 0 \end{bmatrix}, \quad IC_{3\alpha}^{-1} = \begin{bmatrix} 0 & 0 & 1 \\ -1 & 0 & 0 \\ 0 & 1 & 0 \end{bmatrix}, \quad IC_{3\beta}^{-1} = \begin{bmatrix} 0 & 0 & -1 \\ 1 & 0 & 0 \\ 0 & 1 & 0 \end{bmatrix}, \quad IC_{3\gamma}^{-1} = \begin{bmatrix} 0 & 0 & 1 \\ 1 & 0 & 0 \\ 0 & -1 & 0 \end{bmatrix},$$

$$IC_{3\delta}^{-1} = \begin{bmatrix} 0 & 0 & -1 \\ -1 & 0 & 0 \\ 0 & -1 & 0 \end{bmatrix}, \quad IC_{2x} = \begin{bmatrix} -1 & 0 & 0 \\ 0 & 1 & 0 \\ 0 & 0 & 1 \end{bmatrix}, \quad IC_{2y} = \begin{bmatrix} 1 & 0 & 0 \\ 0 & -1 & 0 \\ 0 & 0 & 1 \end{bmatrix}, \quad IC_{2z} = \begin{bmatrix} 1 & 0 & 0 \\ 0 & 1 & 0 \\ 0 & 0 & -1 \end{bmatrix},$$

$$IC_{4x} = \begin{bmatrix} -1 & 0 & 0 \\ 0 & 0 & -1 \\ 0 & 1 & 0 \end{bmatrix}, \quad IC_{4x}^{-1} = \begin{bmatrix} -1 & 0 & 0 \\ 0 & 0 & 1 \\ 0 & -1 & 0 \end{bmatrix}, \quad IC_{4y} = \begin{bmatrix} 0 & 0 & 1 \\ 0 & -1 & 0 \\ -1 & 0 & 0 \end{bmatrix}, \quad IC_{4y}^{-1} = \begin{bmatrix} 0 & 0 & -1 \\ 0 & -1 & 0 \\ 1 & 0 & 0 \end{bmatrix},$$

$$IC_{4z} = \begin{bmatrix} 0 & -1 & 0 \\ 1 & 0 & 0 \\ 0 & 0 & -1 \end{bmatrix}, \quad IC_{4z}^{-1} = \begin{bmatrix} 0 & 1 & 0 \\ -1 & 0 & 0 \\ 0 & 0 & -1 \end{bmatrix}, \quad IC_{2a} = \begin{bmatrix} 0 & -1 & 0 \\ -1 & 0 & 0 \\ 0 & 0 & 1 \end{bmatrix}, \quad IC_{2b} = \begin{bmatrix} 0 & 1 & 0 \\ 1 & 0 & 0 \\ 0 & 0 & 1 \end{bmatrix},$$

$$IC_{2c} = \begin{bmatrix} 0 & 0 & -1 \\ 0 & 1 & 0 \\ -1 & 0 & 0 \end{bmatrix}, \quad IC_{2d} = \begin{bmatrix} 0 & 0 & 1 \\ 0 & 1 & 0 \\ 1 & 0 & 0 \end{bmatrix}, \quad IC_{2e} = \begin{bmatrix} 1 & 0 & 0 \\ 0 & 0 & -1 \\ 0 & -1 & 0 \end{bmatrix}, \quad IC_{2f} = \begin{bmatrix} 1 & 0 & 0 \\ 0 & 0 & 1 \\ 0 & 1 & 0 \end{bmatrix}.$$

Table B.1: The matrices for irreducible representations for the O_h group elements. C_{nj} are proper rotations, while i and IC_{nj} describe improper rotations [a].

[a]From Appendix C - Character Tables for the Crystallographic Point Groups in Ref. [86].

B.2 Bare Mass of *one* Free-Particle

From first principles, we derive the mass of *one* free particle on the BCC and FCC lattices respectively. We shall use the free particle dispersion relation below

$$\varepsilon_{\boldsymbol{k}} = -t \sum_{\boldsymbol{a}} e^{i\boldsymbol{k}\cdot\boldsymbol{a}} \tag{B.1}$$

B.2.1 One-Particle Mass in BCC Lattice

The dispersion for a particle on a BCC lattice is

$$\varepsilon_{\boldsymbol{k}} = -8t \; \cos\frac{k_x b}{2} \cdot \cos\frac{k_y b}{2} \cdot \cos\frac{k_z b}{2},$$

$$\varepsilon_0 = -8\,t \tag{B.2}$$

Expanding the dispersion for small $\boldsymbol{k}$, we get

$$\varepsilon_{\boldsymbol{k}} \approx -8t + b^2 t \left(k_x^2 + k_y^2 + k_z^2\right) + \mathcal{O}(k^4) \equiv \varepsilon_0 + \frac{\hbar^2}{2m_0}\left(k_x^2 + k_y^2 + k_z^2\right) \quad , \tag{B.3}$$

and by comparison, the mass of the free-particle is

$$m_0 = \frac{\hbar^2}{2b^2 t} \tag{B.4}$$

B.2.2 One-Particle Mass in FCC Lattice

The dispersion for a particle in a FCC lattice is

$$\varepsilon_{\boldsymbol{k}} = -4t \left[\cos\frac{k_x b}{2} \cdot \cos\frac{k_y b}{2} + \cos\frac{k_y b}{2} \cdot \cos\frac{k_z b}{2} + cos\frac{k_x b}{2} \cdot \cos\frac{k_z b}{2}\right]$$

$$\varepsilon_0 = -12t \tag{B.5}$$

Expanding the dispersion for small $\boldsymbol{k}$, we get

$$\varepsilon_{\boldsymbol{k}} \approx -12t + b^2 t \left(k_x^2 + k_y^2 + k_z^2\right) + \mathcal{O}(k^4) \equiv \varepsilon_0 + \frac{\hbar^2}{2m_0}\left(k_x^2 + k_y^2 + k_z^2\right) \quad , \tag{B.6}$$

and by comparison, the mass of the free particle in an FCC lattice is

$$m_0 = \frac{\hbar^2}{2b^2 t} \tag{B.7}$$

Appendix C

Publications

C.1   Publications and Author's Contribution

Paper I

Title: Fermion pairing in body-centered-cubic quantum simulators of extended Hubbard models.

Authors: G. D. Adebanjo, P. E. Kornilovitch, J. P. Hague.

Journal: Phys. Lett. A 418 (2021), p. 127704

Contribution: I performed all the calculations and jointly wrote the manuscript.

Paper II

Title: Superlight small pairs in face-centred-cubic extended Hubbard models.

Authors: G. D. Adebanjo, P. E. Kornilovitch, J. P. Hague.

Journal: Under peer review (pre-print https://arxiv.org/pdf/2109.03031.pdf).

Contribution: I performed the majority of the calculations and the manuscript was jointly written.

C.2 Proof of Publications

Contents lists available at ScienceDirect

Physics Letters A

www.elsevier.com/locate/pla

Fermion pairing in body-centered-cubic quantum simulators of extended Hubbard models

Ganiyu D. Adebanjo [a,*], P.E. Kornilovitch [b], J.P. Hague [a,*]

[a] *School of Physical Sciences, The Open University, Walton Hall, Milton Keynes, MK7 6AA, UK*
[b] *Department of Physics, Oregon State University, Corvallis, OR, 97331, USA*

ABSTRACT

We investigate formation and condensation of fermion pairs in cold-atom quantum simulators for extended Hubbard models (UV models) with body-centered-cubic (BCC) optical lattices in the dilute limit, predicting small and light pairs. Pair mass, radius, and binding conditions are calculated, and used to compute transition temperatures. We predict that: (a) local pairs form in BCC optical lattices and binding energies can be large; (b) for particular cases where onsite U and intersite V are attractive with similar size, pairs are both small and light; and (c) pairs of ^{6}Li atoms Bose–Einstein condense at temperatures of around 10 nK.

© 2021 Elsevier B.V. All rights reserved.

1. Introduction

Optical lattices with BCC structures can be formed using arrays of four laser beams [1], and are of interest for two reasons. Firstly, they have been largely neglected in the context of quantum simulators. Secondly, there are condensed matter systems of interest with BCC lattices that could benefit from the insight provided by quantum simulators, such as BCC A_3C_{60} superconductors, which have high transition temperatures (38K) [2]. The goal of this article is to discuss the properties of fermion pairs formed by extended Hubbard interactions in cold-atom quantum simulators with BCC lattices.

The ability to probe Hubbard models in clean and well-controlled systems [3] has been a major success of cold atom quantum simulators formed using optical lattices. Quantum simulators offer the possibility to implement Hubbard models, in a way that cannot be achieved in condensed matter. For example single-band Hubbard models can be implemented without the complications of interactions between multiple electronic bands [3]. Several milestones have been achieved using cold atoms in optical lattices, including observations of Mott transitions in repulsive Hubbard models [4,5]. The interactions in cold-atom quantum simulators can be tuned such that attractive Hubbard models can be studied, allowing local pairs to be observed [6,7].

A simple extension to the Hubbard model [8], known as the extended Hubbard model [9], or (in the low density limit) UV-model [10], includes an onsite Hubbard U and an intersite interaction V. The UV Hamiltonian is defined as:

$$H = \sum_{\langle \mathbf{n},\mathbf{a}\rangle\sigma} t_{\mathbf{a}}\, c^{\dagger}_{\mathbf{n}+\mathbf{a},\sigma}\, c_{\mathbf{n}\sigma} + U \sum_{\mathbf{n}} \hat{\rho}_{\mathbf{n}\uparrow}\, \hat{\rho}_{\mathbf{n}\downarrow} + \sum_{\langle \mathbf{n},\mathbf{a}\rangle} V\, \hat{\rho}_{\mathbf{n}+\mathbf{a}}\, \hat{\rho}_{\mathbf{n}} \tag{1}$$

where $c^{\dagger}_{\mathbf{n}\sigma}$ ($c_{\mathbf{n}\sigma}$) creates (annihilates) an atom of spin σ at site $\mathbf{n}$, $\hat{\rho}_{\mathbf{n}} = \hat{\rho}_{\mathbf{n}\uparrow} + \hat{\rho}_{\mathbf{n}\downarrow}$, where $\hat{\rho}_{\mathbf{n}\sigma}$ is the number operator for atoms on site $\mathbf{n}$ with spin σ, $\mathbf{a}$ the intersite lattice vector, $t_{\mathbf{a}}$ is the intersite hopping, U is the onsite interaction and V is the intersite interaction. Both U and V may be attractive or repulsive. For a BCC lattice, $|\mathbf{a}| = \frac{\sqrt{3}}{2}b$ where b is the lattice constant.

UV models are of interest because local Coulomb repulsion and an intersite effective attraction are key features of many unconventional superconductors [11]. The site-local Hubbard U is typically present in any superconductor with low kinetic energy. Since Coulomb repulsion is typically small between sites due to screening (especially in 3D) an effective intersite attraction or repulsion could arise due

---

* Corresponding authors.
  E-mail addresses: ganiyu.adebanjo@gmail.com (G.D. Adebanjo), jim.hague@open.ac.uk (J.P. Hague).

Superlight small pairs in face-centered-cubic extended Hubbard models

Ganiyu D. Adebanjo,[1] P.E. Kornilovitch,[2] and J.P. Hague[1]

[1]*School of Physical Sciences, The Open University, Walton Hall, Milton Keynes, MK7 6AA, UK*
[2]*Department of Physics, Oregon State University, Corvallis, OR, 97331, USA*
(Dated: September 8, 2021)

We exactly solve a two-particle UV model to explore the behavior of pairs in a face-centered cubic (FCC) lattice within an extended Hubbard model. The conditions for pair formation, pair mass, pair size, and the Bose-Einstein condensation (BEC) temperature are examined. Our results show that strongly bound, superlight and small pairs can be generated in the FCC lattice, which are much lighter than pairs in other 3D lattices. We estimate that such pairs can Bose condense at high temperatures even if the lattice constant is large. Therefore, in the search for materials with high superconducting transition temperatures, three-dimensional materials with an underlying FCC structure should be investigated due to the possibility of superlight small pairs.

I. INTRODUCTION

There are a number of low-dimensional systems within which superlight pair states can be realised, for example the staggered ladder [1], triangular lattice [2, 3] and quasi-two-dimensional hexagonal lattice [4]. Superlight pairs consist of two fermions bound onto neighbouring sites by a combination of strong intersite attraction and strong onsite repulsion. Such pairs can be light and small if it is possible to move to neighboring lattice sites via a single hop without breaking the pairing [1], so that the pair motion is a first order effect. In many materials there is a strong onsite Coulomb repulsion, so intersite pairs are formed via any intersite or long-range attraction, which could originate either from phonons or other more exotic mechanisms. Localized light states are of interest because of their potential to form Bose-Einstein condensates (BEC) at high temperatures.

Extended Hubbard models [5, 6] contain the essential interactions to realize superlight states. The Hamiltonian of an extended Hubbard model is defined as:

$$H = \sum_{\langle \boldsymbol{n},\boldsymbol{a}\rangle\sigma} t_{\boldsymbol{a}} \, c_{\boldsymbol{n}+\boldsymbol{a},\sigma}^{\dagger} \, c_{\boldsymbol{n}\sigma} + U \sum_{\boldsymbol{n}} \hat{\rho}_{\boldsymbol{n}\uparrow}\,\hat{\rho}_{\boldsymbol{n}\downarrow} + \sum_{\langle \boldsymbol{n},\boldsymbol{a}\rangle} V \hat{\rho}_{\boldsymbol{n}+\boldsymbol{a}}\hat{\rho}_{\boldsymbol{n}}$$

(1)

where $c_{\boldsymbol{n}\sigma}^{\dagger}$ ($c_{\boldsymbol{n}\sigma}$) creates (annihilates) an electron of spin σ at site $\boldsymbol{n}$, $\hat{\rho}_{\boldsymbol{n}} = \hat{\rho}_{\boldsymbol{n}\uparrow} + \hat{\rho}_{\boldsymbol{n}\downarrow}$, where $\hat{\rho}_{\boldsymbol{n}\sigma}$ is the number operator for electrons on site $\boldsymbol{n}$ with spin σ, $\boldsymbol{a}$ is the intersite lattice vector, $t_{\boldsymbol{a}}$ is the intersite hopping, U is the onsite interaction and V is the intersite interaction. Both U and V may be attractive or repulsive, although in most materials repulsive U is more likely due to the difficulties of overcoming the Hubbard U with attractive interactions, such as those due to electron-phonon interactions. In the low-density limit the model is also known as the UV model. Properties of local pairs, which can be used to estimate the Bose-Einstein condensation temperature, have been studied in simple systems using the UV model [4, 7–10]. If U is highly repulsive and V is attractive, then exceptionally mobile pairs (superlight states) can be realized on suitable lattices.

In the context of superlight small pairs, the face-centered cubic (FCC) lattice can be viewed as the 3D analogue of the 2D triangular lattice, in that electrons paired between near-neighbor sites can move with a single hop. This remarkable feature should result in a low effective pair mass which could in turn yield a higher transition temperature relative to other systems that lack it. This implies that electron pairing in the FCC lattice is a candidate for obtaining superlight states. To our knowledge, superlight pairs have not yet been examined in FCC systems. The complexity of the FCC lattice structure and increased number of nearest-neighbor sites complicate the calculation and we aim to fill this gap. An illustration of the superlight pair movement in an FCC lattice is shown in Fig. 1. As long as the intersite attraction is maintained, and there is sufficient Hubbard U to suppress on-site pairing, the pair can move easily through the lattice.

In spite of their ubiquity in condensed matter systems, FCC lattices are often overlooked within the correlated electrons community owing to their relative complexity compared to other lattices. Materials of interest with FCC lattices include the A_3C_{60} compounds: a family of molecular compounds with high transition temperature [11] (where A is an alkali metal e.g. K, Rb, Cs) which are predominantly FCC structured [12]. In addition to electron-phonon interactions [11] found in these alkali-doped compounds, strong correlation [13] is also prevalent. The presence of long-range phonon mediated interactions (e.g. the intermolecular modes [12, 14]) may lead to suitable conditions for extended Hubbard physics and superlight pairs, and even if they do not have a role in those compounds, might be relevant to other FCC materials.

This work aims to provide an exact solution of the two-electron problem in an FCC lattice. We calculate the critical potentials U_c (V_c) to bind particles into pairs, the system's total energy, the pair's size and mass, and BEC transition temperatures of pairs in the low-density (dilute) limit. The paper is organized as follows: We describe the model Hamiltonian and methodology used to solve the UV model in the dilute limit (Sec. II). In Sec. III, the properties of the formed pairs are reported. We conclude this work with a discussion in Sec. IV.

Bibliography

[1] H. K. Onnes. In: *Leiden Comm.* 120b, 122b, 124c (1911).

[2] J. Bardeen, L. N. Cooper, and J. R. Schrieffer. "Microscopic theory of supercon-
     ductivity". In: *Phys. Rev.* 106 (1957), pp. 162–164. DOI: `10.1103/PhysRev.106.`
     `162`.

[3] J. Bardeen, L. N. Cooper, and J. R. Schrieffer. "Theory of superconductivity".
     In: *Phys. Rev.* 108 (1957), pp. 1175–1204. DOI: `10.1103/PhysRev.108.1175`.

[4] J. G. Bednorz and K. A. Müller. "Possible high T_c superconductivity in the Ba-
     La-Cu-O system". In: *Zeitschrift für Physik B Cond. Matt.* 64.2 (1986), pp. 189–
     193. DOI: `10.1007/BF01303701`.

[5] L. D. Landau. In: *Sov. Phys. JETP* 3.920 (1957).

[6] S-S. Lee. "Recent developments in non-Fermi liquid theory". In: *Annual Rev.
     Cond. Matt. Phys.* 9.1 (2018), pp. 227–244. DOI: `10.1146/annurev-conmatphys-`
     `031016-025531`.

[7] J. Hubbard. "Electron correlations in narrow energy bands". In: *Proc. Royal Soc.
     London. Series A. Mathematical and Physical Sciences* 276.1365 (1963), pp. 238–
     257.

[8]   A. Georges, G. Kotliar, W. Krauth, and M. J. Rozenberg. "Dynamical mean-field theory of strongly correlated fermion systems and the limit of infinite dimensions". In: *Rev. Mod. Phys.* 68 (1996), pp. 13–125. DOI: `10.1103/RevModPhys.68.13`.

[9]   G. Kotliar, S. Y. Savrasov, K. Haule, V. S. Oudovenko, O. Parcollet, and C. A. Marianetti. "Electronic structure calculations with dynamical mean-field theory". In: *Rev. Mod. Phys.* 78 (2006), pp. 865–951. DOI: `10.1103/RevModPhys.78.865`.

[10]   L. Taillefer. "Scattering and pairing in cuprate superconductors". In: *Annual Rev. Cond. Matt. Phys.* 1.1 (2010), pp. 51–70. DOI: `10.1146/annurev-conmatphys-070909-104117`.

[11]   M. H. Anderson, J. R. Ensher, M. R. Matthews, C. E. Wieman, and E. A. Cornell. "Observation of Bose-Einstein condensation in a dilute atomic vapor". In: *Science* 269.5221 (1995), pp. 198–201. DOI: `10.1126/science.269.5221.198`.

[12]   T. Bourdel, L. Khaykovich, J. Cubizolles, J. Zhang, F. Chevy, M. Teichmann, L. Tarruell, S. J. J. M. F. Kokkelmans, and C. Salomon. "Experimental study of the BEC-BCS crossover region in lithium 6". In: *Phys. Rev. Lett.* 93 (2004), p. 050401. DOI: `10.1103/PhysRevLett.93.050401`.

[13]   J. Wilks. *An Introduction to Liquid Helium.* Clarendon Press, Oxford, 1970.

[14]   J. Klaers, J. Schmitt, F. Vewinger, and M. Weitz. "Bose–Einstein condensation of photons in an optical microcavity". In: *Nature* 468.7323 (2010), pp. 545–548. DOI: `10.1038/nature09567`.

[15]   W. Krätschmer, L. D Lamb, K. Fostiropoulos, and D. R Huffman. "Solid C_{60}: a new form of carbon". In: *Nature* 347.6291 (1990), pp. 354–358. DOI: `10.1038/347354a0`.

[16] H. W. Kroto, J. R. Heath, S. C. O'Brien, R. F. Curl, and R. E. Smalley. "C_{60}: Buckminsterfullerene". In: *Nature* 318.6042 (1985), pp. 162–163. DOI: `10.1038/318162a0`.

[17] O. Gunnarsson. *Alkali-Doped Fullerides: Narrow-Band Solids with Unusual Properties*. World Scientific Publishing, Singapore, 2004.

[18] L. Forró and L. Mihály. "Electronic properties of doped fullerenes". In: *Rep. Prog. Phys.* 64.5 (2001), pp. 649–699. DOI: `10.1088/0034-4885/64/5/202`.

[19] A. Y. Ganin, Y. Takabayashi, Y. Z. Khimyak, S. Margadonna, A. Tamai, M. J. Rosseinsky, and K. Prassides. "Bulk superconductivity at 38 K in a molecular system". In: *Nature Mater.* 7.5 (2008), pp. 367–371. DOI: `10.1038/nmat2179`.

[20] A. Y. Ganin, Y. Takabayashi, P. Jeglič, D. Arčon, A. Potočnik, P. J. Baker, Y. Ohishi, M. T McDonald, M. D. Tzirakis, A. McLennan, et al. "Polymorphism control of superconductivity and magnetism in Cs_3C_{60} close to the Mott transition". In: *Nature* 466.7303 (2010), pp. 221–225. DOI: `10.1038/nature09120`.

[21] Y. Ihara, H. Alloul, P. Wzietek, D. Pontiroli, M. Mazzani, and M. Riccò. "NMR Study of the Mott transitions to superconductivity in the two Cs_3C_{60} phases". In: *Phys. Rev. Lett.* 104 (2010), p. 256402. DOI: `10.1103/PhysRevLett.104.256402`.

[22] O. Gunnarsson, E. Koch, and R. M. Martin. "Mott transition in degenerate Hubbard models: Application to doped fullerenes". In: *Phys. Rev. B* 54 (1996), R11026–R11029. DOI: `10.1103/PhysRevB.54.R11026`.

[23] R. W. Lof, M. A. Van Veenendaal, B. Koopmans, H. T. Jonkman, and G. A. Sawatzky. "Band gap, excitons, and Coulomb interaction in solid C_{60}". In: *Phys. Rev. Lett.* 68 (1992), pp. 3924–3927. DOI: `10.1103/PhysRevLett.68.3924`.

[24]   R. L. Martin and J. P. Ritchie. "Coulomb and exchange interactions in C_{60}^{n-}". In: *Phys. Rev. B* 48 (1993), pp. 4845–4849. DOI: 10.1103/PhysRevB.48.4845.

[25]   V. P. Antropov, O. Gunnarsson, and O. Jepsen. "Coulomb integrals and model Hamiltonians for C_{60}". In: *Phys. Rev. B* 46 (1992), pp. 13647–13650. DOI: 10.1103/PhysRevB.46.13647.

[26]   R. W. Lof, M. A. Van Veenendaal, B. Koopmans, A. Heessels, H. T. Jonkman, and G. A. Sawatzky. "Correlation effects in solid C_{60}". In: *Intl. J. Mod. Phys. B* 6.23n24 (1992), pp. 3915–3921. DOI: 10.1142/S0217979292002000.

[27]   P. A. Brühwiler, A. J. Maxwell, A. Nilsson, N. Mårtensson, and O. Gunnarsson. "Auger and photoelectron study of the Hubbard U in C_{60}, K_3C_{60} and K_6C_{60}". In: *Phys. Rev. B* 48 (1993), pp. 18296–18299. DOI: 10.1103/PhysRevB.48.18296.

[28]   H. Alloul, Y. Ihara, T. Mito, P. Wzietek, M. Aramini, D. Pontiroli, and M. Ricco. "NMR investigation of the pressure induced Mott transition to superconductivity in Cs_3C_{60} isomeric compounds". In: *J. Phys.: Conf. Series* 449 (2013), p. 012030. DOI: 10.1088/1742-6596/449/1/012030.

[29]   Y. Nomura, S. Sakai, M. Capone, and R. Arita. "Exotic s-wave superconductivity in alkali-doped fullerides". In: 28.15 (2016), p. 153001. DOI: 10.1088/0953-8984/28/15/153001.

[30]   M. Capone, M. Fabrizio, C. Castellani, and E. Tosatti. "Colloquium: Modeling the unconventional superconducting properties of expanded A_3C_{60} fullerides". In: *Rev. Mod. Phys.* 81 (2009), pp. 943–958. DOI: 10.1103/RevModPhys.81.943.

[31]   O. Gunnarsson. "Superconductivity in fullerides". In: *Rev. Mod. Phys.* 69 (1997), pp. 575–606. DOI: 10.1103/RevModPhys.69.575.

[32]   I. Bloch, J. Dalibard, and W. Zwerger. "Many-body physics with ultracold gases". In: *Rev. Mod. Phys.* 80 (2008), pp. 885–964. DOI: `10.1103/RevModPhys.80.885`.

[33]   L. Yuan, G. P. Wang, and X. Huang. "Arrangements of four beams for any Bravais lattice". In: *Opt. Lett.* 28.19 (2003), pp. 1769–1771. DOI: `10.1364/OL.28.001769`.

[34]   L-J. Lang, S-L. Zhang, K. T. Law, and Q. Zhou. "Weyl points and topological nodal superfluids in a face-centered-cubic optical lattice". In: *Phys. Rev. B* 96 (2017), p. 035145. DOI: `10.1103/PhysRevB.96.035145`.

[35]   H. J. Metcalf and P. Van der Straten. "Laser cooling and trapping of neutral atoms". In: *The Optics Encyclopedia*. American Cancer Society, 2007. ISBN: 9783527600441. DOI: `https://doi.org/10.1002/9783527600441.oe005`.

[36]   C. C. Bradley, C. A. Sackett, J. J. Tollett, and R. G. Hulet. "Evidence of Bose-Einstein condensation in an atomic gas with attractive interactions". In: *Phys. Rev. Lett.* 75 (1995), pp. 1687–1690. DOI: `10.1103/PhysRevLett.75.1687`.

[37]   C. Gross and I. Bloch. "Quantum simulations with ultracold atoms in optical lattices". In: *Science* 357.6355 (2017), pp. 995–1001. DOI: `10.1126/science.aal3837`.

[38]   L. Tarruell and L. Sanchez-Palencia. "Quantum simulation of the Hubbard model with ultracold fermions in optical lattices". In: *Comptes Rendus Physique* 19.6 (2018), pp. 365–393.

[39]   G. D. Adebanjo, P. E. Kornilovitch, and J. P. Hague. "Fermion pairing in body-centered-cubic quantum simulators of extended Hubbard models". In: *Phys. Lett. A* 418 (2021), p. 127704. DOI: `https://doi.org/10.1016/j.physleta.2021.127704`.

[40] G. D. Adebanjo, P. E. Kornilovitch, and J. P. Hague. "Superlight small pairs in face-centered-cubic extended Hubbard models with strong Coulomb repulsion". In: *arXiv preprint arXiv:2109.03031* (2021).

[41] C. Kittel and P. McEuen. *Introduction to Solid State Physics*. 8th Edition. Wiley, New York, 2005.

[42] J. C. Slater and G. F. Koster. "Simplified LCAO method for the periodic potential problem". In: *Phys. Rev.* 94 (1954), pp. 1498–1524. DOI: `10.1103/PhysRev.94.1498`.

[43] R. T. Scalettar, E. Y. Loh, J. E. Gubernatis, A. Moreo, S. R. White, D. J. Scalapino, R. L. Sugar, and E. Dagotto. "Phase diagram of the two-dimensional negative-U Hubbard model". In: *Phys. Rev. Lett.* 62 (1989), pp. 1407–1410. DOI: `10.1103/PhysRevLett.62.1407`.

[44] G. D. Watkins. "Negative-U properties for point defects in silicon". In: *MRS Proceedings* 2 (1980), p. 21. DOI: `10.1557/PROC-2-21`.

[45] N. F. Mott. "The basis of the electron theory of metals, with special reference to the transition metals". In: *Proc. Phys. Soc. A* 62.7 (1949), p. 416. DOI: `10.1088/0370-1298/62/7/303`.

[46] H. Bruus and K. Flensberg. *Many-Body Quantum Theory in Condensed Matter Physics: An Introduction*. Oxford University Press, Oxford, 2004.

[47] B. Monserrat, N. D. Drummond, and R. J. Needs. "Anharmonic vibrational properties in periodic systems: Energy, electron-phonon coupling, and stress". In: *Phys. Rev. B* 87.14 (2013), p. 144302. DOI: `10.1103/PhysRevB.87.144302`.

[48] H. Fröhlich. "Electrons in lattice fields". In: *Advances in Physics* 3.11 (1954), pp. 325–361. DOI: `10.1080/00018735400101213`.

[49] T. Holstein. "Studies of polaron motion: Part I & II". In: *Annals of Physics* 8.3 (1959), pp. 325–389. DOI: `https://doi.org/10.1016/0003-4916(59)90002-8`.

[50] J. Singh. "Lattice Vibrations: Phonon Scattering". In: *Electronic and Optoelectronic Properties of Semiconductor Structures*. Cambridge University Press, 2003, pp. 217–259. DOI: `10.1017/CBO9780511805745.008`.

[51] L. D. Landau. "Electron motion in crystal lattices". In: *Phys. Z. Sowjet.* 3 (1933), p. 664.

[52] S. I. Pekar. In: *Zh. Eksp. Teor. Fiz.* 16 (1946). *English translation* in Journal of Physics USSR 10, 341 (1946), p. 335.

[53] A. S. Alexandrov. *Theory of Superconductivity From Weak to Strong Coupling.* 1st Edition. CRC Press, 2003. DOI: `https://doi.org/10.1201/9781420033267`.

[54] A. Schirotzek, C-H Wu, A. Sommer, and M. W. Zwierlein. "Observation of Fermi polarons in a tunable Fermi liquid of ultracold atoms". In: *Phys. Rev. Lett.* 102 (2009), p. 230402. DOI: `10.1103/PhysRevLett.102.230402`.

[55] O. Grandstrand. *High Magnetic fields: Science and Technology.* Chapter: Theory of electron-phonon interactions in semiconductors. World Scientific, Singapore, 2003.

[56] J. T. Devreese. *Fröhlich Polarons. Lecture course including detailed theoretical derivations – 10th edition.* https://arxiv.org/pdf/1611.06122.pdf. 2020. arXiv: `1611.06122 [cond-mat.other]`.

[57] J. T. Devreese and A. S. Alexandrov. "Fröhlich polaron and bipolaron: recent developments". In: *Reports on Progress in Physics* 72.6 (2009), p. 066501. DOI: `10.1088/0034-4885/72/6/066501`. URL: `https://doi.org/10.1088/0034-4885/72/6/066501`.

[58] H. Fröhlich, H. Pelzer, and S. Zienau. "XX. Properties of slow electrons in polar materials". In: *The London, Edinburgh, and Dublin Philosophical Magazine and Journal of Science* 41.314 (1950), pp. 221–242. DOI: 10.1080/14786445008521794.

[59] A. S. Alexandrov and N. F. Mott. *Polarons and Bipolarons*. World Scientific, 1996.

[60] G. D. Mahan. *Many-particle physics*. 3rd Edition. Plenum Publishers, New York and London, 2000.

[61] A. Macridin, G. A. Sawatzky, and M. Jarrell. "Two-dimensional Hubbard-Holstein bipolaron". In: *Phys. Rev. B* 69 (2004), p. 245111. DOI: 10.1103/PhysRevB.69.245111.

[62] R. P. Feynman. "Slow Electrons in a Polar Crystal". In: *Phys. Rev.* 97 (1955), pp. 660–665. DOI: 10.1103/PhysRev.97.660.

[63] L. D. Landau and S. I. Pekar. "Effective mass of a polaron". In: *Zh. Eksp. Teor. Fiz* 18.5 (1948), pp. 419–423.

[64] S. J. Miyake. "The ground state of the optical polaron in the strong-coupling case". In: *Journal of the Physical Society of Japan* 41.3 (1976), pp. 747–752. DOI: 10.1143/JPSJ.41.747.

[65] C. Franchini, M. Reticcioli, M. Setvin, and U. Diebold. "Polarons in materials". In: *Nat. Rev. Mater.* 6 (2021), pp. 560–586. DOI: 10.1038/s41578-021-00289-w.

[66] Y. Natanzon, A. Azulay, and Y. Amouyal. "Evaluation of polaron transport in solids from first-principles". In: *Israel Journal of Chemistry* 60.8-9 (2020), pp. 768–786. DOI: https://doi.org/10.1002/ijch.201900101.

[67]   J. T. Devreese. "Optical properties of few and many Fröhlich polarons from 3D to 0D". In: *Polarons in Advanced Materials*. Chapter in Polarons in Advanced Materials A.S. Alexandrov Editor. Springer, 2007. DOI: `10.1017/CBO9780511805745.008`.

[68]   J. Bonča, S. A. Trugman, and I. Batistić. "Holstein polaron". In: *Phys. Rev. B* 60 (1999), pp. 1633–1642. DOI: `10.1103/PhysRevB.60.1633`.

[69]   J. P. Hague, P. E. Kornilovitch, J. H. Samson, and A. S. Alexandrov. "Superlight small bipolarons in the presence of a strong Coulomb repulsion". In: *Phys. Rev. Lett.* 98 (2007), p. 037002. DOI: `10.1103/PhysRevLett.98.037002`.

[70]   J. Bonča and S. A. Trugman. "Bipolarons in the extended Holstein Hubbard model". In: *Phys. Rev. B* 64 (9 2001), p. 094507. DOI: `10.1103/PhysRevB.64.094507`.

[71]   J. P. Hague and P. E. Kornilovitch. "Bipolarons from long-range interactions: Singlet and triplet pairs in the screened Hubbard-Fröhlich model on the chain". In: *Phys. Rev. B* 80 (2009), p. 054301. DOI: `10.1103/PhysRevB.80.054301`.

[72]   J. P. Hague and P. E. Kornilovitch. "Light and stable triplet bipolarons on square and triangular lattices". In: *Phys. Rev. B* 82 (2010), p. 094301. DOI: `10.1103/PhysRevB.82.094301`.

[73]   A. R. Davenport, J. P. Hague, and P. E. Kornilovitch. "Mobile small bipolarons on a three-dimensional cubic lattice". In: *Phys. Rev. B* 86 (2012), p. 035106. DOI: `10.1103/PhysRevB.86.035106`.

[74]   J. P. Hague, P. E. Kornilovitch, J. H. Samson, and A. S. Alexandrov. "Singlet and triplet bipolarons on the triangular lattice". In: *J. Phys. and Chem. Solids*

69.12 (2008). SNS2007, pp. 3304–3306. DOI: https://doi.org/10.1016/j.jpcs.2008.06.129.

[75]   A. S. Alexandrov, J. Ranninger, and S. Robaszkiewicz. "Bipolaronic supercon-ductivity: Thermodynamics, magnetic properties, and possibility of existence in real substances". In: *Phys. Rev. B* 33 (1986), pp. 4526–4542. DOI: 10.1103/PhysRevB.33.4526.

[76]   L. J. De Jongh. "A comparative study of (bi)polaronic (super)conductivity in high-and low-T_c superconducting oxides". In: *Physica C: Superconductivity* 152.2 (1988), pp. 171–216. DOI: https://doi.org/10.1016/0921-4534(88)90011-1.

[77]   A. S. Alexandrov and J. Ranninger. "Bipolaronic superconductivity". In: *Phys. Rev. B* 24 (1981), pp. 1164–1169. DOI: 10.1103/PhysRevB.24.1164.

[78]   B. K. Chakraverty. "Bipolarons and superconductivity". In: *J. Phys. France* 42.9 (1981), pp. 1351–1356. DOI: 10.1051/jphys:019810042090135100.

[79]   D. Emin and M. S. Hillery. "Formation of a large singlet bipolaron: Application to high-temperature bipolaronic superconductivity". In: *Phys. Rev. B* 39 (1989), p. 6575. DOI: 10.1103/PhysRevB.39.6575.

[80]   I. G. Lang and Y. A. Firsov. "Kinetic theory of semiconductors with low mobility". In: *Sov. Phys. JETP* 16.5 (1963), p. 1301.

[81]   J. P. Hague, P. E. Kornilovitch, J. H. Samson, and A. S. Alexandrov. "Superlight small bipolarons". In: *J. Phys.: Cond. Matt.* 19.25 (2007), p. 255214. DOI: 10.1088/0953-8984/19/25/255214.

[82]   P. Kornilovitch. "Enhanced stability of bound pairs at nonzero lattice momenta". In: *Phys. Rev. B* 69 (2004), p. 235110. DOI: 10.1103/PhysRevB.69.235110.

[83]   M. Bak. "Bound electron pairs on a triangular lattice in an extended Hubbard model". In: *Phys. Stat. Sol. B* 244 (2007), pp. 2421–2426. DOI: `https://doi.org/10.1002/pssb.200674603`.

[84]   J. P. Hague, P. E. Kornilovitch, and C. MacCormick. "Cold-atom quantum simulator to explore pairing, condensation, and pseudogaps in extended Hubbard-Holstein models". In: *Phys. Rev. A* 102 (2020), p. 033333. DOI: `10.1103/PhysRevA.102.033333`.

[85]   A. W. Joshi. *Elements of Group Theory for Physicists.* 4th Edition. New Age International, New Delhi, 1997.

[86]   J. F. Cornwell. *Group Theory in Physics: An Introduction.* Academic Press, California and London, 1997.

[87]   J. J. Sakurai and J. Napolitano. *Modern Quantum Mechanics.* 3rd Edition. Cambridge University Press, Cambridge, 2021.

[88]   B. Zwiebach. *8.06 Quantum Physics III: Video lectures on perturbation theory.* Massachusetts Institute of Technology: MIT OpenCourseWare. License: Creative Commons BY-NC-SA. URL: `https://ocw.mit.edu/courses/physics/8-06-quantum-physics-iii-spring-2018`.

[89]   S. Lakshmi-Bala. *Quantum Mechanics I: Lectures on perturbation theory.* Source: YouTube. URL: `https://www.youtube.com/watch?v=zdouC7ZNTJ0&t=312s`.

[90]   P. E. Kornilovitch. "Continuous-time quantum Monte Carlo algorithm for the lattice polaron". In: *Phys. Rev. Lett.* 81 (1998), pp. 5382–5385. DOI: `10.1103/PhysRevLett.81.5382`.

[91]   A. S. Alexandrov and P. E. Kornilovitch. "Mobile small polaron". In: *Phys. Rev. Lett.* 82 (1999), pp. 807–810. DOI: `10.1103/PhysRevLett.82.807`.

[92] P. E. Kornilovitch and E. R. Pike. "Polaron effective mass from Monte Carlo simulations". In: *Phys. Rev. B* 55 (1997), R8634–R8637. DOI: `10.1103/PhysRevB.55.R8634`.

[93] J. P. Hague, P. E. Kornilovitch, A. S. Alexandrov, and J. H. Samson. "Effects of lattice geometry and interaction range on polaron dynamics". In: *Phys. Rev. B* 73 (2006), p. 054303. DOI: `10.1103/PhysRevB.73.054303`.

[94] J. P. Hague, P. E. Kornilovitch, and A. S. Alexandrov. "Trapping of lattice polarons by impurities". In: *Phys. Rev. B* 78 (2008), p. 092302. DOI: `10.1103/PhysRevB.78.092302`.

[95] P. E. Kornilovitch. "Path-integral approach to lattice polarons". In: *J. Phys. Cond. Matt.* 19.25 (2007), p. 255213. DOI: `10.1088/0953-8984/19/25/255213`. URL: `https://doi.org/10.1088/0953-8984/19/25/255213`.

[96] K. Huang. *Introduction to Statistical Physics*. 2nd Edition. Taylor & Francis, London and New York, 2001. DOI: `https://doi.org/10.1201/9781439878132`.

[97] P. E. Spencer, J. H. Samson, P. E. Kornilovitch, and A. S. Alexandrov. "Effect of electron-phonon interaction range on lattice polaron dynamics: A continuous-time quantum Monte Carlo study". In: *Phys. Rev. B* 71 (2005), p. 184310. DOI: `10.1103/PhysRevB.71.184310`.

[98] G. S. Joyce. "Exact results for a body-centered cubic lattice Green's function with applications in lattice statistics. I". In: *J. Math. Phys.* 12.7 (1971), pp. 1390–1414. DOI: `10.1063/1.1665748`.

[99] C. N. R. Rao, K. Biswas, K. S. Subrahmanyam, and A. Govindaraj. "Graphene, the new nanocarbon". In: *J. Mater. Chem.* 19 (2009), pp. 2457–2469. DOI: `10.1039/B815239J`.

[100] D. R. Cooper, B. D'Anjou, N. Ghattamaneni, B. Harack, M. Hilke, A. Horth, N. Majlis, M. Massicotte, L. Vandsburger, E. Whiteway, et al. "Experimental review of graphene". In: *International Scholarly Research Notices* 2012 (2012). ISRN - Cond. Matt. Phys. DOI: 10.5402/2012/501686.

[101] Mathworks™. *N-D Fast Fourier Transform*. Matlab Mathematics User's Guide R2018b. URL: https://uk.mathworks.com/help/matlab/ref/fftn.html.

[102] L. Yuan, G. P. Wang, and X. Huang. "Arrangements of four beams for any Bravais lattice". In: *Opt. Lett.* 28.19 (2003), pp. 1769–1771. DOI: 10.1364/OL.28.001769.

[103] P. Kornilovitch. "Ferromagnetism and borromean binding in three-fermion clusters". In: *Phys. Rev. Lett.* 112 (2014), p. 077202. DOI: 10.1103/PhysRevLett.112.077202.

[104] P. E. Kornilovitch. "Stability of three-fermion clusters with finite range of attraction". In: *EPL (Europhys. Lett.)* 103.2 (2013), p. 27005. DOI: 10.1209/0295-5075/103/27005.

[105] P. Kornilovitch. "Trion formation and unconventional superconductivity in a three-dimensional model with short-range attraction". In: *Intl. J. Mod. Phys. B* 34.06 (2020), p. 2050042. DOI: 10.1142/S0217979220500423.

[106] T Morita. "Use of a recurrence formula in computing the lattice Green function". In: *Journal of Physics A: Mathematical and General* 8.4 (1975), pp. 478–489. DOI: 10.1088/0305-4470/8/4/008.

[107] M. L. Glasser and J Boersma. "Exact values for the cubic lattice Green functions". In: *Journal of Physics A: Mathematical and General* 33.28 (2000), p. 5017. DOI: 10.1088/0305-4470/33/28/306.

[108] K. V. Grigorishin. "The role of electron–vibron interaction and local pairing in conductivity and superconductivity of alkali-doped fullerides". In: *Physica C: Superconductivity and its Applications* 562 (2019), pp. 56–69. DOI: `https://doi.org/10.1016/j.physc.2018.12.001`.

[109] E. Cappelluti, P. Paci, C. Grimaldi, and L. Pietronero. "Relevance of multiband Jahn-Teller effects on the electron-phonon interaction in A_3C_{60}". In: *Phys. Rev. B* 72.5 (2005), p. 054521. DOI: `10.1103/PhysRevB.72.054521`.

[110] M. C. M. O'Brien and C. C. Chancey. "The Jahn–Teller effect: An introduction and current review". In: *American Journal of Physics* 61.8 (1993), pp. 688–697. DOI: `10.1119/1.17197`.

[111] Z. Huang, M. D. Albaqami, T. Sato, N. Iwahara, and L. F. Chibotaru. "Jahn-Teller effect in the cubic fullerides A_3C_{60}". In: *Phys. Rev. B* 103 (2021), p. 134102. DOI: `10.1103/PhysRevB.103.134102`.

[112] P. E. Kornilovitch. "Band structure of the Jahn-Teller polaron from quantum Monte Carlo". In: *Phys. Rev. Lett.* 84 (2000), pp. 1551–1554. DOI: `10.1103/PhysRevLett.84.1551`.

[113] S. El–Shawish, J. Bonča, Li-Chung Ku, and S. A. Trugman. "Numerical study of the $E \otimes e$ Jahn-Teller polaron and bipolaron". In: *Phys. Rev. B* 67 (2003), p. 014301. DOI: `10.1103/PhysRevB.67.014301`.

[114] Y. Nomura, K. Nakamura, and R. Arita. "Ab initio derivation of electronic low-energy models for C_{60} and aromatic compounds". In: *Phys. Rev. B* 85 (2012), p. 155452. DOI: `10.1103/PhysRevB.85.155452`.

[115] F. C. Zhang, M. Ogata, and T. M. Rice. "Attractive interaction and superconductivity for K_3C_{60}". In: *Phys. Rev. Lett.* 67 (1991), pp. 3452–3455. DOI: `10.1103/PhysRevLett.67.3452`.

[116] J. Bonča, T. Katrašnik, and S. A. Trugman. "Mobile bipolaron". In: *Phys. Rev. Lett.* 84 (14 2000), pp. 3153–3156. DOI: `10.1103/PhysRevLett.84.3153`.

[117] L. Proville and S. Aubry. "Small bipolarons in the 2-dimensional Holstein-Hubbard model. I. The adiabatic limit". In: *Eur. Phys. J. B* 11 (1999), pp. 41–58. DOI: `https://doi.org/10.1007/s100510050915`.

[118] M. Weber and M. Hohenadler. "Two-dimensional Holstein-Hubbard model: Critical temperature, Ising universality, and bipolaron liquid". In: *Phys. Rev. B* 98 (2018), p. 085405. DOI: `10.1103/PhysRevB.98.085405`.